The Role of Viscosity for Mixing and Transport Processes in Galaxy Clusters and Multiphase Gas

Tirso Marin Gilabert

München 2025

The Role of Viscosity for Mixing and Transport Processes in Galaxy Clusters and Multiphase Gas

Tirso Marin Gilabert

Dissertation
an der Fakultät für Physik
der Ludwig–Maximilians–Universität
München

vorgelegt von
Tirso Marin Gilabert
aus Alicante, Spain

München, den 11.06.2025

Erstgutachter: Prof. Dr. Klaus Dolag
Zweitgutachter: Prof. Dr. Volker Springel
Tag der mündlichen Prüfung: 22.07.2025

Zusammenfassung

Galaxienhaufen sind die größten gravitativ gebundenen und virialisierten Strukturen im Universum, und aufgrund ihrer extremen Bedingungen dienen sie als wertvolle Labore zur Erforschung kosmologischer und plasmaphysikalischer Prozesse. Die Verschmelzung von Galaxienhaufen oder die Aktivität des Active Galactic Nucleus (AGN) injiziert Energie räumlich großskalig, die in einem turbulenten Zerfall in kleinere Skalen übergeht und so Turbulenz im Intracluster Medium (ICM) erzeugt. Kürzlich gemachte Beobachtungen von Hitomi und XRISM zeigen jedoch unerwartet niedrige Turbulenzniveaus, was auf eine Unterdrückung der Turbulenz hindeutet. In dieser Arbeit untersuchen wir die Rolle der Viskosität bei der Regulierung von Mischungs- und Transportprozessen in Galaxienhaufen und in mehrphasigem astrophysikalischem Gas als einen zentralen Mechanismus zur Unterdrückung von Turbulenz. Ziel unserer Arbeit ist es, die regulierende Rolle der Viskosität durch den Einsatz fortschrittlicher numerischer Simulationen und theoretischer Analysen näher zu bestimmen.

Die Arbeit ist wie folgt gegliedert:

In Kapitel 1 führen wir die grundlegenden physikalischen Prozesse ein, die die Dynamik und Entwicklung von Galaxienhaufen bestimmen, und heben insbesondere die beobachteten Turbulenzniveaus hervor, die niedriger als erwartet ausfallen. Anschließend untersuchen wir in Kapitel 2 die Viskosität im Detail, wobei wir sowohl isotrope (Spitzer) als auch anisotrope (Braginskii) Beschreibungen betrachten und ihre jeweiligen Anwendungsbereiche erläutern.

Anschließend stellen wir in Kapitel 3 die verschiedenen Codes vor, die wir für unsere Simulationen verwenden: OpenGadget3, ein Smoothed Particle Hydrodynamics (SPH)-Code, der fortschrittliche Modelle für Gravitation, Hydrodynamik, Magneto-Hydrodynamik (MHD), und physikalische Viskosität enthält; Athena, ein eulerbasierter Gittercode, der auf die Erfassung detaillierter Fluiddynamik ausgelegt ist; und das Nachbearbeitungswerkzeug vortex-p, das zur Analyse von Geschwindigkeitsfeldern und zur Isolierung turbulenter Strukturen verwendet wird.

Nach der Einführung der Theorie und der numerischen Methoden untersuchen wir in Kapitel 4, wie physikalische Viskosität die Plasmadynamik verändert, indem sie scherkraftgetriebene Instabilitäten unterdrückt und Turbulenz in einem idealisierten Szenario dämpft. Mit dem SPH-Code OpenGadget3 analysieren wir die lineare Entwicklung der Kelvin-Helmholtz Instabilität (KHI) in verschiedenen Viskositätsszenarien. Die Simulationen bestätigen, dass Viskosität das Wachstum der KHI signifikant unterdrückt und einen kritischen Schwellenwert bei etwa 0.1% der klassischen Spitzer-Viskosität für unsere Anfangsbedingungen etabliert, ab dem die Instabilität vollständig gedämpft wird. Die numerische Viskosität, die der SPH-Implementierung innewohnt, erweist sich als deutlich geringer, was bestätigt, dass moderne

SPH-Methoden diese physikalischen Prozesse zuverlässig abbilden.

In Kapitel 5 erweitern wir die Analyse aus Kapitel 4, indem wir mit dem Code ATHENA die Abhängigkeit der kritischen Viskosität von der relativen Dichte und der Mach-Zahl des Mediums untersuchen. Darüber hinaus analysieren wir die nichtlinearen Eigenschaften einer mehrphasigen Gasumgebung und untersuchen, wie sich Viskosität auf Turbulenz und die Effizienz radiativer Kühlung auswirkt. In einer mehrphasigen Umgebung existieren demnach zwei unterschiedliche Bereiche. Im Grenzfall schwacher Kühlung dominiert Viskosität und erzeugt laminare Strömungen, welche zu Abweichungen in nicht-viskosen Skalierungsrelationen führen, die Gesamthelligkeit jedoch weitgehend unverändert lassen. Im Grenzfall starker Kühlung dominieren Strahlungsverluste über viskose Effekte, sodass klassische Zusammenhänge zwischen Turbulenz und Kühlungn erhalten bleiben. Diese Ergebnisse haben wichtige Auswirkungen auf die Interpretation von Beobachtungen und die Verfeinerung von Subgrid-Physik in kosmologischen Simulationen.

Alle in idealisierten Szenarien gewonnenen Erkenntnisse werden in Kapitel 6 auf realistischere kosmologische Simulationen von Galaxienhaufen angewendet. Mit OPENGADGET3 führen wir kosmologische Simulationen für drei massereiche Haufen durch ($M_{\rm vir} > 10^{15}\,{\rm M}_{\odot}$) und quantifizieren, wie sich unterschiedliche Viskositätsniveaus auf die Morphologie, Temperatur und Dichteschwankungen der Haufen auswirken. Viskosität unterdrückt insbesondere Instabilitäten auf kleinen Skalen, wodurch filamentäre und kleinräumige Strukturen durch reduzierte Mischung verstärkt werden. Sie erhöht auch die Virialtemperaturen um etwa 5–10%, während dichte Regionen kühl bleiben. Die Amplitude der Dichte- und Geschwindigkeitsfluktuationen steigt mit zunehmender Viskosität. Vergleiche mit Röntgenbeobachtungen zeigen jedoch konsistente Ergebnisse im Rahmen der Messungenaugigkeiten, unabhängig von der Viskosität. Dies erschwert die Eingrenzung der Viskosität durch Dichtefluktuationen. Das Verhältnis von Dichte- zu Geschwindigkeitsfluktuationen bleibt robust bei etwa Eins, was mit theoretischen Erwartungen übereinstimmt. Dies stellt die erste detaillierte kosmologische Untersuchung viskoser Effekte im ICM dar.

In Kapitel 7 erweitern wir die vorherigen Ergebnisse, indem wir analysieren, wie stark die Turbulenz in Galaxienhaufen in Abhängigkeit von der Viskosität unterdrückt wird. Es zeigt sich, dass die Viskosität mit zunehmender Entfernung vom Zentrum des Haufens effektiver wird. Gleichzeitig wird bei geringerer Turbulenz die Selbstverstärkung von Magnetfeldern beeinträchtigt, was in den äußeren Bereichen von Galaxienhaufen zu schwächeren Magnetfeldern führt.

Die in den vorherigen Kapiteln vorgestellten Analysen wurden mit einer isotropen Spitzer-Viskosität durchgeführt. In Kapitel 8 präsentieren wir jedoch die ersten Ergebnisse unserer neuen Implementierung einer anisotropen Braginskii-Viskosität in OPENGADGET3. Die ersten Tests zeigen vielversprechende Resultate und erfassen realistischere, richtungsabhängige Transportprozesse in magnetisierten Plasmen.

Abschließend stellen wir in Kapitel 9 unsere Schlussfolgerungen vor und in Kapitel 10 die zukünftigen Schritte im Anschluss an diese Arbeit. Diese beinhalten die Erweiterung kosmologischer Simulationen von Galaxienhaufen durch ein realistischeres anisotropes Viskositätsmodell sowie die Untersuchung isolierter Systeme, in denen viskose Effekte eine bedeutende Rolle spielen könnten, etwa bei „Jellyfish“-Galaxien.

Insgesamt untersucht diese Arbeit die Rolle der Viskosität über verschiedene Skalen hinweg – von fundamentalen Fluidinstabilitäten bis hin zu realistischen Galaxienhaufenumgebungen. Durch die Verknüpfung detaillierter mikrophysikalischer Erkenntnisse mit beobachtbaren Größen verbessert diese Arbeit unser Verständnis der Plasmadynamik in Galaxienhaufen erheblich und liefert wertvolle Beiträge zur Weiterentwicklung theoretischer Modelle und zur Interpretation zukünftiger hochauflösender astrophysikalischer Beobachtungen.

Abstract

Galaxy clusters are the largest gravitationally bound and virialized structures in the Universe, and due to their extreme conditions, they serve as essential laboratories for exploring cosmological processes and plasma physics. Processes like mergers or Active Galactic Nucleus (AGN) activity, inject energy at large scales, which decays towards smaller scales in a turbulent cascade, generating turbulence within the Intracluster Medium (ICM). However, recent observational results by Hitomi and XRISM find unexpectedly low turbulence levels, suggesting that there is a suppression of turbulence. In this thesis, we investigate the role of viscosity in regulating mixing and transport processes within galaxy clusters and multiphase astrophysical gas, as a key mechanism for suppressing turbulence. Our work aims to constrain the magnitude and influence of viscosity by employing advanced numerical simulations and theoretical analysis.

The work is structured as follows:

In Chapter 1, we introduce the fundamental physical processes governing the dynamics and evolution of galaxy clusters, emphasizing the lower-than-expected observational turbulence levels. Subsequently, in Chapter 2 we explore viscosity in detail, considering both isotropic (Spitzer) and anisotropic (Braginskii) descriptions, highlighting their applicable regimes.

Once we have presented the physics describing the dynamical evolution of galaxy clusters, in Chapter 3 we introduce the different codes we use to run our simulations: OpenGadget3, a Smoothed Particle Hydrodynamics (SPH) code that incorporates sophisticated models for gravity, hydrodynamics, Magnetohydrodynamics (MHD), and physical viscosity; Athena, an Eulerian mesh-based code designed to capture detailed fluid dynamics; and the postprocessing tool vortex-p, used to analyze velocity fields and isolate turbulent structures.

After having introduced the theory and numerics used in this work, in Chapter 4 we explore how physical viscosity modifies the dynamics of plasma by suppressing shear-driven instabilities and damping turbulence in an idealized setup. Using the SPH code OpenGadget3, we analyze the linear evolution of the Kelvin-Helmholtz instability (KHI) under different viscosity scenarios. The simulations confirm that viscosity significantly suppresses the growth of KHI, establishing a critical threshold at approximately 0.1% of the classical Spitzer viscosity for our initial conditions (ICs), beyond which the instability is fully damped. The numerical viscosity intrinsic to the SPH implementation is found to be significantly lower, confirming that modern SPH methods reliably capture these physical processes.

In Chapter 5, we expand the analysis made in Chapter 4 by analyzing the dependence of the critical viscosity on the overdensity and Mach number using the code Athena. We additionally explore the non-linear regime of a multiphase gas environment, and investigate how viscosity

affects turbulence and radiative cooling efficiency. In a multiphase environment, two distinct regimes emerge: a weak cooling regime, where viscosity dominates and produces laminar flows disrupting inviscid scaling relations, yet leaving total luminosity relatively unchanged; and a strong cooling regime, where radiative losses overpower viscous effects, thus preserving classical turbulence-cooling relationships. These findings have critical implications for interpreting observations and refining subgrid physics in cosmological simulations.

All these results found in idealized setups are applied to more realistic cosmological simulations of galaxy clusters in Chapter 6. Using OpenGadget3, we run cosmological simulations for three massive clusters ($M_{\rm vir} > 10^{15}$ $M_\odot$), and we quantify how varying viscosity levels impact cluster morphology, temperature, and density fluctuations. Viscosity notably suppresses small-scale instabilities, enhancing filamentary and small-scale structures due to reduced mixing. It also increases virial temperatures by approximately 5%-10% while keeping dense regions cool. The amplitude of density and velocity fluctuations increases with viscosity, yet comparison with X-ray observations reveals consistent results regardless of viscosity within error margins of measurements. This complicates direct observational constraints of viscosity from density fluctuations. The ratio of density to velocity fluctuations remains robustly around unity, aligning with theoretical expectations. This represents the first detailed cosmological exploration of viscous effects in the ICM.

In Chapter 7 we expand the previous results by analyzing the level of turbulence in galaxy clusters depending on the amount of viscosity, finding that viscosity becomes more effective further from the cluster center. This reduction of turbulence leads to a suppression of magnetic field amplification, producing weaker magnetic fields in the outskirts of galaxy clusters, the more viscous the ICM is.

All the analysis presented in the previous chapters was done using an isotropic Spitzer viscosity. However, in Chapter 8 we present the first results of our new implementation of an anisotropic Braginskii viscosity in OpenGadget3. The preliminary tests indicate promising results, capturing more realistic, direction-dependent transport processes in magnetized plasmas.

Finally, in Chapter 9, we present our final conclusions, and in Chapter 10 the future steps following this thesis. These future steps include extending cosmological simulations of galaxy clusters to incorporate a more realistic anisotropic viscosity model, as well as investigating isolated systems where viscous effects may be significant, such as jellyfish galaxies.

Overall, this thesis explores the role of viscosity across different scales, from fundamental fluid instabilities to realistic galaxy cluster environments. By linking detailed microphysical insights to observational constraints, this work significantly enhances our understanding of plasma dynamics in galaxy clusters, informing both theoretical models and observational interpretations. Ultimately, these results contribute critically to refining the physical models underlying cosmological simulations and interpreting future high-resolution astrophysical observations.

Contents

List of Acronyms

AC artificial conductivity

AV artificial viscosity

AGN Active Galactic Nucleus

AMR Adaptive Mesh Refinement

CDM Cold Dark Matter

CIC Cloud-In-Cell

CGM Circumgalactic Medium

CMB Cosmic Microwave Background

DM dark matter

DNS Direct Numerical Simulations

ICM Intracluster Medium

ICs initial conditions

ISM Interstellar Medium

KHI Kelvin-Helmholtz instability

ΛCDM Lambda Cold Dark Matter

MFM Meshless Finite Mass

MFV Meshless Finite Volume

MHD Magnetohydrodynamics

RM Faraday rotation measurements

RT Rayleigh–Taylor instability

SPH Smoothed Particle Hydrodynamics

SPMHD Smoothed Particle Magneto-Hydrodynamics

SZ Sunyaev-Zeldovich

SMBHs supermassive black holes

TRMLs turbulent radiative mixing layers

1 | Introduction

1.1 The Cosmology of our Universe

Our understanding of the Universe on its largest scales is founded on the Cosmological Principle, which asserts that the Universe appears homogeneous and isotropic when averaged over scales of hundreds of megaparsecs (Peebles, 1993). Early hints of this large-scale uniformity emerged from galaxy counts, but it was the discovery of the Cosmic Microwave Background (CMB) in 1965, which showed a near perfect blackbody spectrum and temperature fluctuations of only $\delta T/T \approx 10^{-5}$ in the large-scales of the Universe, confirming isotropy (Penzias & Wilson, 1965; Planck Collaboration et al., 2020). This foundational assumption enables the use of a single metric to describe spacetime, rather than having to account for every local inhomogeneity.

A crucial measurement to understand the behavior of our Universe was done in 1929 by Edwin Hubble, who quantified the recession of galaxies by measuring their redshifts and distances, finding a linear relation now known as Hubble's law (Hubble, 1929):

$$v \equiv cz = H_0 r\,, \tag{1.1}$$

where v is the recessional velocity, z is the observed redshift, c is the speed of light, r is the distance, and H_0 is the Hubble constant, the value of the present-day Hubble parameter, which shows the rate of expansion. Modern observations have measured $H_0 = 67.55 \pm 0.42$ km s^{-1} Mpc^{-1} from Planck CMB data (Planck Collaboration et al., 2020), and $H_0 = 73.04 \pm 1.04$ km s^{-1} Mpc^{-1} from Cepheids observations (Riess et al., 2022). Hubble's law implies that space itself is expanding: comoving observers see all distant galaxies receding, with velocities proportional to their separation. This global expansion stretches photon wavelengths, producing the cosmological redshift. This cosmological redshift (z) is defined by the ratio of observed to emitted wavelengths:

$$1 + z = \frac{\lambda_{\rm obs}}{\lambda_{\rm em}} = \frac{a_0}{a(t)}, \tag{1.2}$$

where $a(t)$ is the scale factor, and a_0 its value today. Thus, measuring z tells us when we are observing, with larger z corresponding to earlier times, when the scale factor was smaller than 1 (Peebles, 1993). $a(t)$ describes the separation between two points in space due to the expansion of the Universe: $r(t) = a(t)x$, where x is the comoving separation, which remains fixed for objects moving with the Hubble flow. This distinction simplifies the treatment of structure growth, as comoving scales factor out the overall expansion and allow direct comparison of length scales at

different epochs (Peacock, 1999). By convention, we set $a_0 = 1$ at the present cosmic time t_0, so that lengths measured today match comoving lengths directly. The expansion rate of the Universe at any point in time can be quantified by the Hubble parameter as:

$$H(t) \equiv \frac{\dot{a}(t)}{a(t)}\,, \tag{1.3}$$

which measures how fast distances between comoving observers grow with time. At $z = 0$ (present cosmic time), the Hubble parameter (presented in equation (1.1)) is given by

$$H_0 = 100\,h\ \mathrm{km\,s^{-1}\,Mpc^{-1}}\,, \tag{1.4}$$

where the dimensionless number h absorbs the uncertainty in its precise measurement (currently $h \simeq 0.67$-0.72).

Assuming homogeneity and isotropy, the geometry of spacetime (in spherical coordinates) is described by the Friedmann–Lemaître–Robertson–Walker (FLRW) metric (Friedmann, 1922, 1924; Lemaître, 1931, 1933; Robertson, 1935, 1936b,a; Walker, 1937):

$$\mathrm{d}s^2 = -c^2\,\mathrm{d}t^2 + a^2(t)\left[\frac{\mathrm{d}r^2}{1-kr^2} + r^2\left(\mathrm{d}\theta^2 + \sin^2\theta\,\mathrm{d}\phi^2\right)\right]\,, \tag{1.5}$$

where k denotes spatial curvature ($k = 0$ flat, $k > 0$ closed, $k < 0$ open; Ryden, 2003).

The time evolution of $a(t)$ is derived from Einstein's field equations (Einstein, 1916), leading to the Friedmann equations (Friedmann, 1922). The first equation defines the expansion rate of the Universe:

$$\left(\frac{\dot{a}}{a}\right)^2 = \frac{8\pi G}{3}\rho - \frac{kc^2}{a^2} + \frac{\Lambda}{3}\,, \tag{1.6}$$

where ρ is the total energy density (radiation, matter, and dark energy), G the gravitational constant, and Λ the cosmological constant (Peebles, 1993). The second is the acceleration equation:

$$\frac{\ddot{a}}{a} = -\frac{4\pi G}{3}\left(\rho + \frac{3p}{c^2}\right) + \frac{\Lambda}{3}, \tag{1.7}$$

revealing how pressure p and Λ control whether expansion accelerates or decelerates. During the radiation-dominated era ($p > 0$) and the matter-dominated era ($p \approx 0$), gravity decelerated the expansion. In the current dark energy-dominated epoch ($p < 0$), the Universe expands at an accelerated rate (Ryden, 2003). As the Universe evolves, $H(t)$ changes according to the balance of energy components—matter, radiation, curvature, and dark energy—via the Friedmann equations (Dodelson, 2003).

It is useful to compare each component's density to the critical density, the energy density required for a spatially flat geometry (Mukhanov, 2005). This critical value separates open and closed cosmologies. If the actual density equals this value, the Universe is exactly flat. It is defined by:

$$\rho_{\mathrm{crit}}(t) = \frac{3H^2(t)}{8\pi G}\,. \tag{1.8}$$

Comparing the density of each component ρ_i to $\rho_{\rm crit}$ defines the dimensionless density parameters:

$$\Omega_i(t) = \frac{\rho_i(t)}{\rho_{\rm crit}(t)}, \tag{1.9}$$

for radiation (Ω_r), matter (Ω_m), curvature (Ω_k), and dark energy (Ω_Λ). Summing over all yields

$$\Omega_r + \Omega_m + \Omega_k + \Omega_\Lambda = 1\,. \tag{1.10}$$

Current observations constrain these values at $z = 0$ to be approximately $\Omega_m = 0.3111 \pm 0.0056$, $\Omega_\Lambda = 0.6889 \pm 0.0056$, $\Omega_r \sim 10^{-4}$. This implies that $\Omega_k \approx 0$, indicating a spatially flat, dark energy-dominated Universe today (Planck Collaboration et al., 2020).

In the early development of structure formation theory, Press & Schechter (1974) introduced a simple yet powerful analytic expression for the abundance of collapsed haloes. Their formalism, now known as the Press–Schechter model, assumed an Einstein-de Sitter Universe: a flat-matter only model with $\Omega_m = 1$ and $\Omega_\Lambda = 0$ (Einstein & de Sitter, 1932). The predicted mass function is

$$M\frac{{\rm d}n}{{\rm d}M} = \frac{1}{\sqrt{\pi}}\,\frac{\bar{\rho}}{M}\left(\frac{M}{M^*}\right)^{1/2}\exp\left[-\frac{M}{M^*}\right]. \tag{1.11}$$

Here, $\bar{\rho}$ is the mean matter density of the Universe, and M^* is the characteristic mass scale. For masses well below M^*, the abundance of collapsed halos rises, while for $M \gtrsim M^*$ the exponential term enforces a rapid cutoff, reflecting the rarity of high–mass peaks in the Gaussian initial field. The prefactor $1/\sqrt{\pi}$ corrects for the fraction of underdense regions in the original derivation, and ensures that integrating $M\,{\rm d}n/{\rm d}M$ over all masses recovers the total mass density $\bar{\rho}$ (Press & Schechter, 1974).

Subsequent observations, particularly in the 1990s, showed that the Einstein-de Sitter model could not simultaneously account for the expansion rate, structure growth, and geometry of the Universe (Efstathiou et al., 1992; Riess et al., 1998). This led to the formulation of the Lambda Cold Dark Matter (ΛCDM) model as the standard cosmological paradigm (Ostriker & Steinhardt, 1995; Turok, 1997). In this picture, the total energy density today is partitioned into pressureless Cold Dark Matter (CDM) and a cosmological constant Λ (dark energy), with negligible curvature and radiation. The expansion history follows

$$\frac{H^2(z)}{H_0^2} = \Omega_{0,m}\,(1+z)^3 + \Omega_{0,\Lambda}\,, \tag{1.12}$$

where $\Omega_{0,m}$ and $\Omega_{0,\Lambda}$ are the present–day density parameters.

The linear growth factor, which describes how density perturbations grow over time, depends on the expansion rate $H(z)$ and the density parameters (Ω_i). Thus, comparisons between the predicted Press–Schechter mass function and observations provide tight constraints on Ω_m and σ_8, the present-day fluctuation amplitude at 8 h^{-1} Mpc (Press & Schechter, 1974; Planck Collaboration et al., 2020).

Galaxy clusters thus stand as the link between theory and observations. Their massive scales make them rare peaks in the density field, so small variations in cosmological parameters lead

to measurable differences in their abundance and distribution. By combining cluster counts, scaling relations (such as mass–observable correlations), and spatial clustering with other probes like the CMB and Type Ia supernovae, we can break degeneracies among parameters. This sets constraints on the matter density (Ω_m), the dark energy equation of state, and the amplitude of matter fluctuations (σ_8). In this way, galaxy clusters are characterized by the interplay between gravity, dark matter, and dark energy, offering one of the most powerful laboratories for understanding the fundamental constituents and fate of our Universe.

1.2 Galaxy Clusters

Galaxy clusters represent the largest gravitationally bound structures in the Universe, providing unique laboratories for studying cosmological and astrophysical processes. These massive systems span several Mpc and typically contain total masses of up to 10^{15} $M_\odot$, dominated by dark matter (DM), with baryons making up only $\sim$ 10% of the total mass (see review by Caprioli et al., 2019). At the heart of these clusters lies a hot, diffuse gas known as the Intracluster Medium (ICM), which is primarily composed of ionized hydrogen and helium with temperatures typically of $10^6 - 10^8$ K, corresponding to energies of approximately 1 – 10 keV, and densities of $10^{-4} - 10^{-1}$ cm^{-3} (Markevitch & Vikhlinin, 2007; ZuHone & Roediger, 2016).

Galaxy clusters were first recognized through systematic catalogs of nebulae created by Charles Messier and William Herschel. In the 1920s, Edwin Hubble established that these nebulae were indeed external galaxies, emphasizing the immense scale of galaxy clusters (Hubble, 1925, 1926). Soon after, measurements of galaxy velocities and the assumption of a virialized equilibrium were used to quantify the total mass of Coma (Zwicky, 1933) and Virgo (Smith, 1936). These mass measurements exceeded the total mass accounted for stars in the cluster, indicating for the first time the existence of DM. X-ray observations further confirmed this DM through the detection of the hot ICM emitting via thermal bremsstrahlung (Cavaliere et al., 1971; Gursky et al., 1971; Forman et al., 1972), requiring significant additional gravitational mass beyond visible matter (see review by Kravtsov & Borgani, 2012).

Galaxy clusters form and evolve through hierarchical collapse driven by gravitational instability, where initial density fluctuations in the early Universe grow via gravitational accretion and mergers (e.g. Hoffman & Shaham, 1985; Syer & White, 1998). Cosmological simulations and theoretical models consistently show that mergers significantly influence cluster structures, triggering turbulence, shocks, and particle acceleration processes (see reviews by Markevitch & Vikhlinin, 2007 and Caprioli et al., 2019).

Clusters consist predominantly of DM, galaxies, and the ICM (see Fig. 1.1, taken from Markevitch & Vikhlinin, 2007). The ICM, which is observed primarily in X-rays and through the Sunyaev-Zeldovich (SZ) effect, provides essential diagnostics on gas density, temperature, and chemical composition (Kravtsov & Borgani, 2012). Gravitational lensing measurements offer complementary information on cluster mass distributions, serving as critical tools for testing cosmological models (see reviews by Allen et al., 2011 and Pratt et al., 2019).

Galaxy clusters serve as fundamental probes of cosmological parameters since their mass distribution and growth history sensitively depend on the cosmological model. They also provide

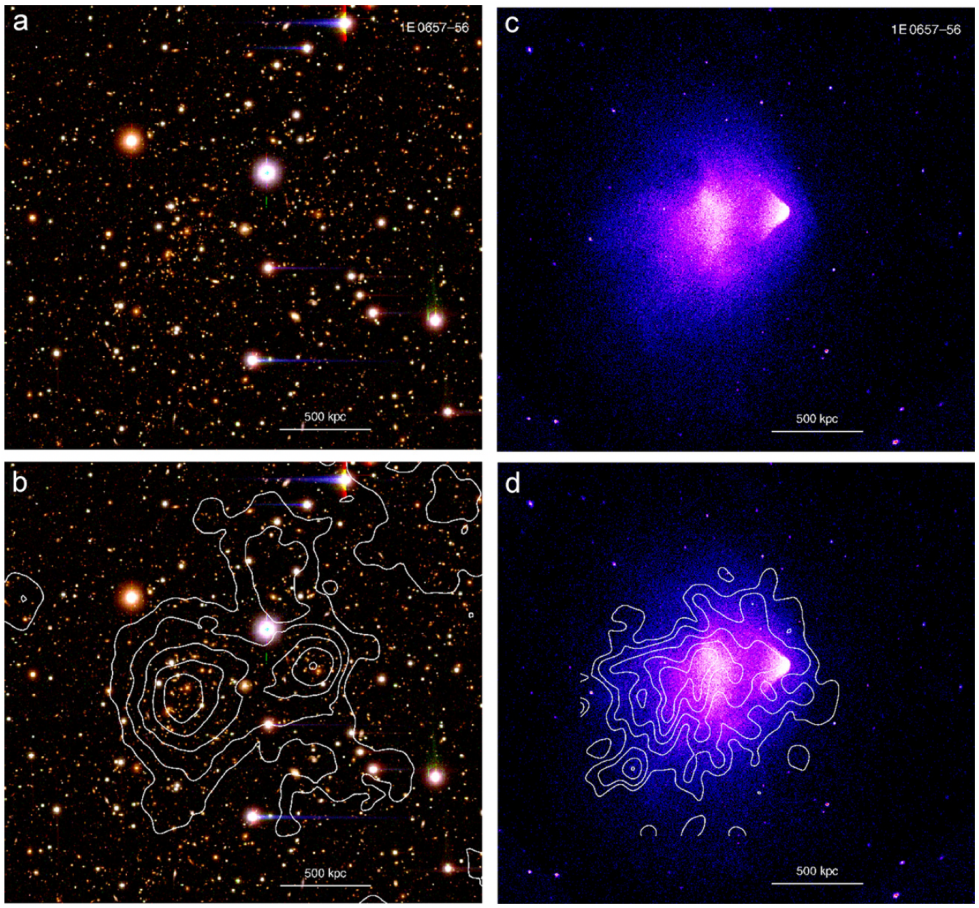

Figure 1.1: Bullet cluster observations in different wavelengths. *a)* Optical image, where faint red galaxies can be seen in two concentrations (Clowe et al., 2006). *b)* Same image as in *a)*, but the contours show the projected total mass derived from gravitational lensing (Clowe et al., 2006). The total mass is dominated by DM, and the two peaks of mass concentration correlate with the two areas where galaxies are concentrated. *c)* Image taken with Chandra, where the X-ray emission due to the hot diffuse ICM can be seen. *d)* Same image as in *c)*, but the contours show the surface brightness of the diffuse radio emission due to synchrotron emission of ultrarelativistic electrons in the magnetic field (Liang et al., 2000). Figure taken from Markevitch & Vikhlinin (2007).

unique conditions for studying plasma physics, which cannot be reproduced in laboratories on Earth, such as collisionless shocks, transport processes, or plasma microinstabilities (see reviews by Bykov et al., 2019 and Kunz et al., 2022). Furthermore, clusters offer critical environments for investigating galaxy evolution mechanisms, including ram-pressure stripping, galaxy mergers, and feedback processes like Active Galactic Nucleus (AGN) (see review by Simionescu et al., 2019).

The understanding of the gas properties of galaxy clusters has significantly benefited from observatories such as Chandra (Weisskopf et al., 2000), XMM-Newton (Jansen et al., 2001), and the LOFAR telescope (van Haarlem et al., 2013), which allow the study of the cluster dynamics and structure. More recently, the detections from the high-resolution spectrometer of XRISM facilitate the direct measurement of turbulent velocities, shedding light on energy transport mechanisms (XRISM Science Team, 2020; XRISM, 2025). Future telescopes like Athena (Barret et al., 2013) or the Square Kilometer Array (SKA; Lazio, 2009), aim to map the distribution and behavior of hot gas and magnetic fields in unprecedented detail, as well as enabling detailed studies of synchrotron emissions and magnetic field structures across a vast range of cluster environments.

1.2.1 Formation and Evolution of Galaxy Clusters

According to the ΛCDM cosmological model, galaxy clusters form through hierarchical structure formation. Initially, small primordial matter density field fluctuations, seeded during cosmic inflation, provide the initial seeds from which galaxy clusters grow (Hoffman & Shaham, 1985). They originate as quantum perturbations in the scalar field driving cosmic inflation, which then become classical perturbations that can be observed in the CMB (see reviews by Mukhanov et al., 1992 and Mo et al., 2010). The statistical nature of these fluctuations is described by their power spectrum, which is typically assumed to follow a nearly scale-invariant Harrison-Zeldovich spectrum (Harrison, 1970; Zeldovich, 1972). Observations from the Planck satellite have precisely measured these fluctuations (see Fig. 1.2, obtained from Planck Collaboration et al., 2014), allowing detailed predictions of structure formation patterns and aiding in cosmological parameter estimation (Mo et al., 2010; Planck Collaboration et al., 2020).

Initially, the density fluctuations are very small and evolve due to gravitational force according to linear perturbation theory. These initial density fluctuations are characterized by the overdensity:

$$\delta(\mathbf{x}) = \frac{(\rho(\mathbf{x}) - \bar{\rho})}{\bar{\rho}}\,, \tag{1.13}$$

where $\mathbf{x}$ is the position, and $\bar{\rho}$ is the mean density of the Universe. Assuming a simple Einstein-de Sitter Universe (flat-matter only), the mean density of the Universe evolves as

$$\bar{\rho} = \frac{1}{6\pi G t^2}\,. \tag{1.14}$$

During this initial phase, fluctuations grow proportionally to the cosmological scale factor in an expanding Universe. The linear growth is governed by the Jeans instability criterion, which

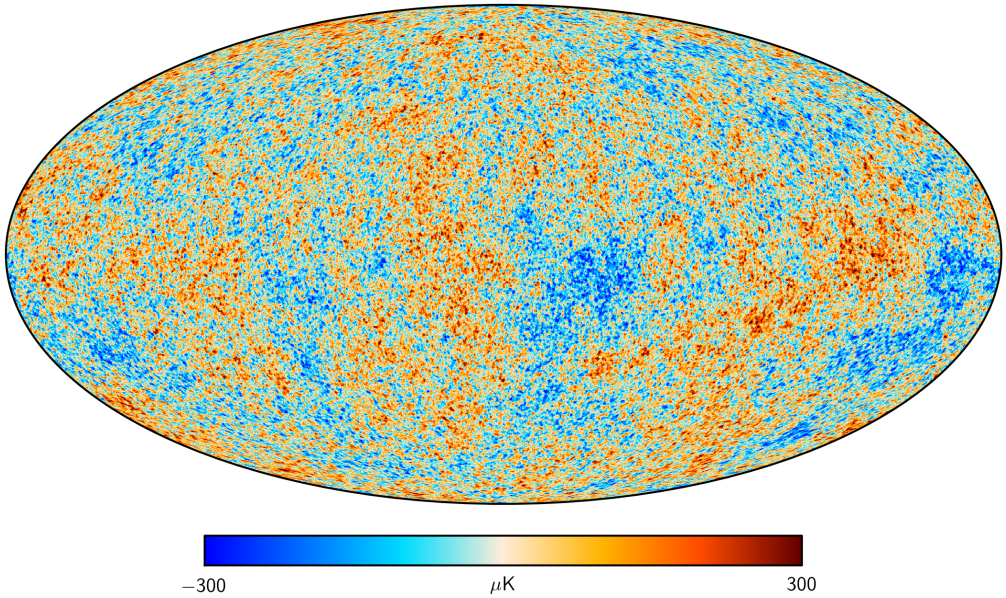

Figure 1.2: Primordial temperature fluctuations of the CMB measured by Planck Collaboration et al. (2014). Note that 3% of the sky was replaced by a constrained Gaussian realization to fill the Galactic mask. Figure taken from Planck Collaboration et al. (2014).

determines the minimum scale of fluctuations that can collapse gravitationally (Jeans, 1902; Mo et al., 2010):

$$\lambda_{\mathrm{J}} = c_s \sqrt{\frac{\pi}{G\bar{\rho}}}\,, \tag{1.15}$$

with c_s the soundspeed. As fluctuations grow larger and the overdensity becomes $\delta \sim 1$, they enter a quasi-linear regime where perturbation amplitudes become significant, and non-linear effects start to become important (Mo et al., 2010).

A description of how small matter density fluctuations can result in large-scale structures is given by the Zeldovich approximation (Zel'dovich, 1970)[1]. These initial fluctuations grow through gravitational instability while gradually decoupling from the Hubble flow, with overdense regions becoming increasingly dense over time. Once the amplitude of the perturbations becomes non-linear, gravitational collapse results in the formation of virialized dark matter halos. Baryonic matter subsequently falls into these potential wells, forming galaxies and galaxy clusters. On large scales, the initial density fluctuations lead to the formation of coherent structures like sheets and filaments. This bottom-up scenario is usually referred to as hierarchical clustering, and describes how galaxy clusters are built through the sequential merging and accretion of smaller structures like galaxies, galaxy groups, and dark matter halos in the ΛCDM model. Clusters thus emerge from overdense regions in the primordial matter density field, subsequently amplified

[1]The Zeldovich approximation is a first-order Lagrangian perturbative solution which does not describe the fully non-linear collapse. To describe non-linear collapse, one needs to use more complex descriptions like the spherical collapse.

through gravitational attraction and mergers (Springel et al., 2005; Kravtsov & Borgani, 2012). Galaxy cluster formation fundamentally involves gravitational collapse governed by Newtonian dynamics, well described by the Poisson equation in comoving coordinates:

$$\nabla^2\Phi = 4\pi G a^2 \bar{\rho}\,\delta\,, \tag{1.16}$$

where Φ denotes the gravitational potential perturbation. This equation states that the gravitational potential Φ is sourced by the density contrast δ. In a perfectly homogeneous Universe ($\delta = 0$), $\nabla^2\Phi = 0$ (see equation (1.13)). However, in overdense regions ($\delta > 0$), the RHS of equation (1.16) is positive. Given the boundary condition $\Phi \to 0$ at infinity, the Green-function solution results in $\Phi < 0$, creating attractive potential wells that draw in surrounding matter (Mo et al., 2010). These wells grow deeper over time as matter accumulates, enhancing gravitational collapse and leading to non-linear structure formation.

Gravitational growth is initially linear, but as the density contrast between the cluster and the background increases, it transitions into a highly non-linear regime, ultimately resulting in virialized structures. During virialization, kinetic and potential energies equilibrate, and a quasi-steady state, known as virial equilibrium, is satisfied:

$$2\langle E_{\rm kin}\rangle = -\langle E_{\rm pot}\rangle\,, \tag{1.17}$$

where $\langle E_{\rm kin}\rangle$ and $\langle E_{\rm pot}\rangle$ are the time-averaged kinetic and potential energy, respectively. However, processes like accretion or major mergers inject kinetic energy into the system, thus breaking the virial equilibrium until the galaxy clusters are thermalised.

The simplest model of non-linear collapse assumes a spherical model (see Kravtsov & Borgani, 2012 for a more detailed derivation). Initially, the overdense region expands along with the Universe, while slowing down under its own gravity. When the radial velocity cancels exactly the local Hubble flow, the overdense region reaches the turnaround point (at time $t = t_{\rm ta}$), and it stops expanding, with a radius $R_{\rm ta}$. After reaching turnaround, it collapses under gravity and virializes, reaching a final radius $R_{\rm coll} = R_{\rm ta}/2$, set by the virial theorem, at $t = t_{\rm coll}$. The interval between the collapse and the turnaround time ($t_{\rm coll} - t_{\rm ta} = t_{\rm ta}$) must be equal to the free-fall time of a sphere with density $\rho_{\rm ta}$:

$$t_{\rm ff} = \sqrt{\frac{3\pi}{32\,G\rho_{\rm ta}}}\,, \tag{1.18}$$

leading to a density at turnaround of

$$\rho_{\rm ta} = \frac{3\pi}{32\,G\,t_{\rm ta}^2}\,. \tag{1.19}$$

Since the radius after collapse is $R_{\rm coll} = R_{\rm ta}/2$, this leads to a collapse density of

$$\rho_{\rm coll} = 8\rho_{\rm ta} = \frac{3\pi}{G\,t_{\rm coll}^2}\,. \tag{1.20}$$

Thus, once the cluster is virialized, the overdensity in an Einstein-de Sitter Universe (flat-matter only) can be defined as

$$\Delta_{\rm Vir} = \frac{\rho_{\rm coll}}{\bar{\rho}} = 18\pi^2 = 177.653\,. \tag{1.21}$$

In the case of a ΛCDM with $\Omega_m = 0.27$ and $\Omega_\Lambda = 0.73$, $\Delta_{Vir} \approx 358$ at $z = 0$ (Komatsu et al., 2011). This allows us to define the virial radius (R_{Vir}), the radius at which the density contrast is Δ_{Vir}. The mass inside this radius is the virial mass (M_{Vir}) and the temperature predicted from the virial theorem, the virial temperature (T_{Vir}). Another common definition is to consider the distance for which the density is 200 times the critical density of the Universe (ρ_{Crit}, equation (1.8)) R_{200}, and in the case of central regions of the cluster, R_{2500}, the distance at which the overdensity is 2500 times the critical density of the Universe.

Once the galaxy cluster has collapsed, the DM radial profile follows (approximately) a NFW profile (Navarro et al., 1996):

$$\rho_{NFW}(r) = \frac{4\rho_s}{\frac{r}{r_s}\left(1 + \frac{r}{r_s}\right)^2}, \tag{1.22}$$

where r_s is the distance at which the logarithmic slope of the profile is equal to -2, and ρ_s is the value of the density at $r = r_s$. This quasi-universal profile emerges from the hierarchical assembly of structures in a cosmological context, shaped by the anisotropic collapse of matter along the large-scale features (Navarro et al., 1997).

Cosmological simulations predict the formation of a complex large-scale structure called the "cosmic web", consisting of voids, sheets, filaments, and nodes (see Fig. 1.3, obtained from Springel et al., 2005). Galaxy clusters are located at the nodes — the intersections of filaments —representing the densest regions in this cosmic structure. Matter streams along filaments, continuously feeding the gravitational growth of clusters through smooth accretion and discrete merging events (see reviews by Bond & Myers, 1996 and Overzier, 2016). The baryonic matter in galaxy clusters is heated primarily through these gravitational processes, including shock heating during mergers and adiabatic compression during collapse. The high-density core of the ICM cools radiatively, predominantly emitting X-rays through thermal bremsstrahlung. This cooling can initiate star formation and feed central supermassive black holes (SMBHs). Feedback mechanisms, particularly from AGN jets and supernova-driven winds, significantly impact cluster evolution (see review by Fabian, 2012). They inject substantial energy into the ICM, balancing cooling flows and influencing the observed thermal structure, metallicity distribution, and entropy profiles of clusters (see reviews by McNamara & Nulsen, 2007 and Simionescu et al., 2019).

Galaxy clusters are fundamental cosmological probes providing essential information about dark matter, dark energy, and the large-scale structure of the Universe. Their mass function, spatial clustering, and evolution serve as precise tests of cosmological models (Vikhlinin et al., 2009). Moreover, detailed studies of the ICM, via X-ray spectroscopy and SZ effect measurements, offer fundamental information into baryonic physics, feedback processes, and plasma dynamics (Mantz et al., 2010; Böhringer & Werner, 2010). Clusters also act as natural gravitational lenses, magnifying distant galaxies and enabling detailed studies of early galaxy formation (see review by Kneib & Natarajan, 2011). Hence, understanding galaxy clusters significantly advances our comprehension of cosmological evolution, galaxy formation processes, and the fundamental components of the Universe (Allen et al., 2011; Kravtsov & Borgani, 2012).

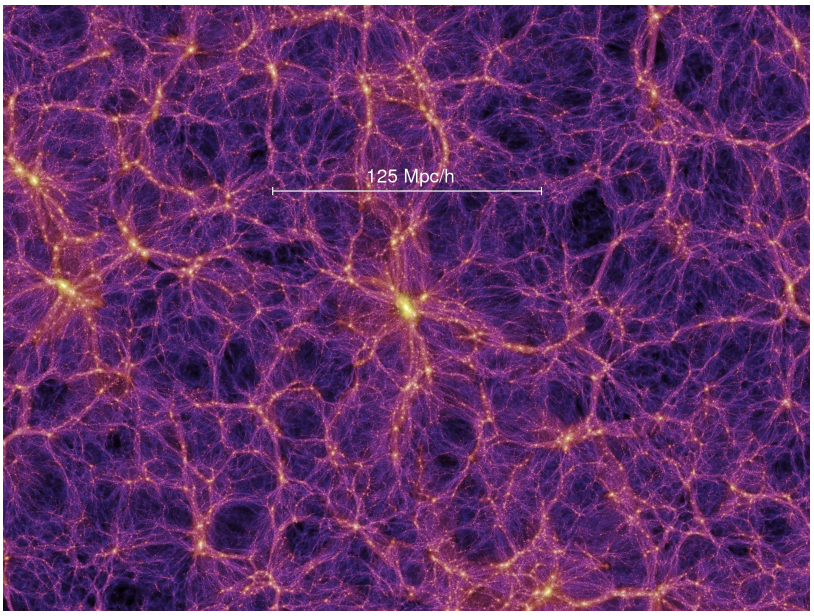

Figure 1.3: Dark matter density field of the large-scale cosmic web obtained from the Millennium Simulation (Springel et al., 2005), color-coded by density and local dark matter velocity dispersion. Figure taken from Springel et al. (2005).

1.3 The Cosmic Baryon Cycle

Galaxy clusters contain hundreds to thousands of galaxies bound within deep gravitational potential wells filled with the hot, X-ray emitting ICM. However, the evolution of these clusters, and of the galaxies they host, is governed not only by dark matter and gravity, but also by complex interactions between various baryonic components: the Interstellar Medium (ISM) within galaxies, where stars form; the Circumgalactic Medium (CGM), which surrounds galaxies within their dark matter halos; and the ICM, which spans the space between galaxies within clusters. Each of these media represents a different thermodynamic phase of baryonic matter, characterized by its temperature, density, pressure, and dynamical history. Yet they are fundamentally interconnected through a multiscale, multiphase baryon cycle that regulates gas accretion, star formation, feedback, chemical enrichment, and environmental quenching.

The ISM

The ISM is the gas and dust that resides within galaxies and directly participates in star formation. It is highly inhomogeneous and multiphase, existing in approximate pressure equilibrium. The classic three-phase model includes the cold neutral medium, with temperatures $T < 100$ K and densities $n > 100$ cm^{-3}; the warm media, which is partially ionized and has temperatures of $T \sim 10^4$ K and densities of $n \sim 0.1 - 1$ cm^{-3}; and the hot ionized medium, with $T > 10^5$ K and $n \sim 10^{-3}$ cm^{-3}, which is heated by supernova explosions (McKee & Ostriker, 1977; Cox, 2005). On large scales, the ISM exhibits turbulence, magnetization, and thermal instabilities that regulate

its fragmentation and phase structure (see review by Elmegreen & Scalo, 2004). Feedback from massive stars and supernovae drives material from the ISM into the CGM via winds and fountains (Chevalier & Clegg, 1985). This gas carries metals and energy out of galaxies, enriching and heating the CGM (see review by Tumlinson et al., 2017). Thus, the ISM acts both as the engine of baryon condensation and as a source of galactic feedback.

The CGM

The CGM is the gaseous halo surrounding galaxies, extending out to the virial radius ($\sim 10^2$ kpc for Milky Way-like galaxies), and the total gas and metal mass can exceed the mass of the galaxy. It is the interface between the ISM and the ICM, playing a central role in both gas accretion and feedback regulation, mediating in the interaction between the two environments (see review by Faucher-Giguère & Oh, 2023). Observations provide clear evidence of multiphase gas in the CGM. For instance, hot gas ($T \gtrsim 10^6$ K) in halos around galaxies has been detected in X-rays (e.g. Anderson & Bregman, 2010; Bregman et al., 2018). Meanwhile, cool gas ($T \sim 10^4$ K) has been detected through Lyα emission (e.g. Steidel et al., 2010; Wisotzki et al., 2018; Arrigoni Battaia et al., 2023), as well as absorption lines in the spectra of background quasars (e.g. Tripp et al., 1998; Péroux et al., 2019). Its multiphase structure arises from the interplay of turbulent mixing layers, thermal instability, conduction, and magnetic fields (Gronke et al., 2021; Fielding & Bryan, 2022).

Gas flows in the CGM are shaped by accretion from the cosmic web, satellite stripping, and feedback from star formation and AGN (Tumlinson et al., 2017). These complex processes lead to a messy structure on a big range of scales, from the galactic halo (~ 100 kpc) to turbulent mixing layers (< 1 pc) (Faucher-Giguère & Oh, 2023). The CGM also hosts recycled outflows: material is ejected from the ISM as galactic winds, cools, and re-accretes onto the galaxy (Oppenheimer et al., 2010). The CGM acts as a reservoir for galaxy evolution, balancing inflow and feedback to regulate the galaxy's gas budget available for star formation (Tumlinson et al., 2017).

The ICM

The ICM fills the deep gravitational potentials of galaxy clusters, extending over Mpc scales and containing the majority of baryonic mass. Despite its relatively homogeneous appearance, the ICM contains complex structures including cold fronts, shock fronts, sloshing gas, and metal-enriched bubbles from AGN feedback (Markevitch & Vikhlinin, 2007). In cluster centers, cooling times can be lower than 1 Gyr, potentially forming cooling flows of gas condensing onto the central galaxy, unless regulated by mechanical heating from AGN jets (Fabian, 1994; McNamara & Nulsen, 2007). The ICM also interacts with infalling galaxies, stripping their ISM and CGM via ram-pressure, therefore suppressing star formation and reshaping galaxy morphologies in clusters (Gunn & Gott, 1972; Boselli et al., 2022).

While the ISM and CGM are shaped by internal galactic processes, the ICM is dominated by gravity and fluid dynamics. It stores a fossil record of galaxy evolution and cluster assembly, evident in its temperature, entropy, and metallicity distributions.

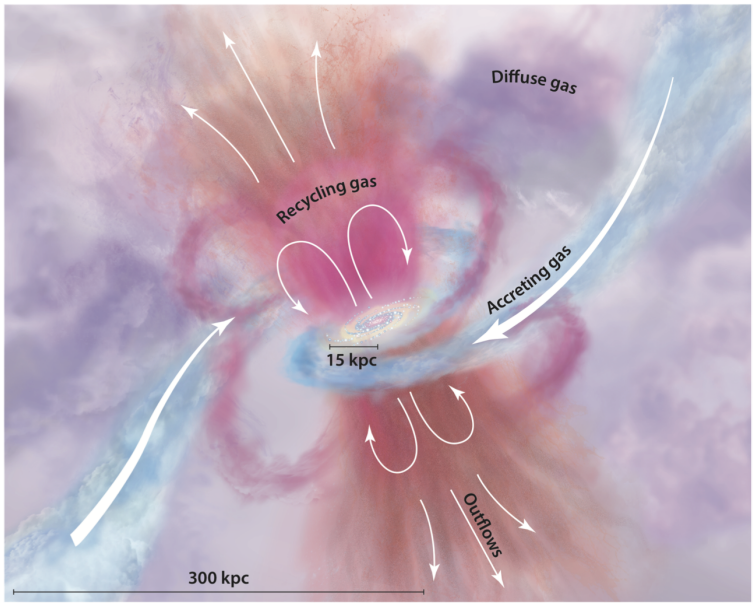

Figure 1.4: Schematic picture of the cosmic baryon cycle between the ICM accreted onto the CGM, galactic outflows emitting the gas from the ISM to the CGM and recycled gas infalling again to the ISM. Figure taken from Tumlinson et al. (2017).

Although the ISM, CGM, and ICM are often studied independently, they are deeply interconnected through the cosmic baryon cycle (see schematic picture of the interaction between ICM, CGM and ISM in Fig. 1.4, taken from Tumlinson et al., 2017). Material condenses from the ICM into the CGM, cools and accretes onto the ISM, and forms stars. Stellar and AGN feedback eject mass, metals, and energy back into the CGM, and eventually into the ICM. Metals observed in the CGM and ICM trace this cumulative enrichment history (Peeples et al., 2014; Tumlinson et al., 2017). Ultimately, these media define a continuum from dense, star-forming regions to the vast hot diffuse gas of galaxy clusters. Their interplay governs the life cycle of baryons and supports galaxy formation across cosmic time.

A crucial component of this interplay is the process of gas mixing, which mediates the transfer of mass, momentum, energy, and metals across these environments. Mixing occurs across a wide range of spatial and temporal scales, driven by a complex combination of hydrodynamic instabilities, turbulence, conduction, and magnetic fields. At the interfaces between cold and hot gas phases—such as outflows from the ISM into the CGM, or ram-pressure stripped material in the ICM—shear and density contrasts give rise to instabilities like the Kelvin-Helmholtz and Rayleigh-Taylor instabilities (Marin-Gilabert et al., 2022). These generate multiphase-turbulent mixing layers that broaden over time and foster the creation of intermediate-temperature gas (Fielding et al., 2020; Mandelker et al., 2020).

Such layers are not only sites of energy dissipation, but also regulate the survival of cool gas clouds as they traverse the hot halos (Gronke & Oh, 2018). In the CGM, mixing can enhance radiative cooling, enabling gas to condense and rain back onto the galaxy. In the ICM, infalling galaxies exhibit complex multiphase tails, showing that stripped ISM material survives and mixes

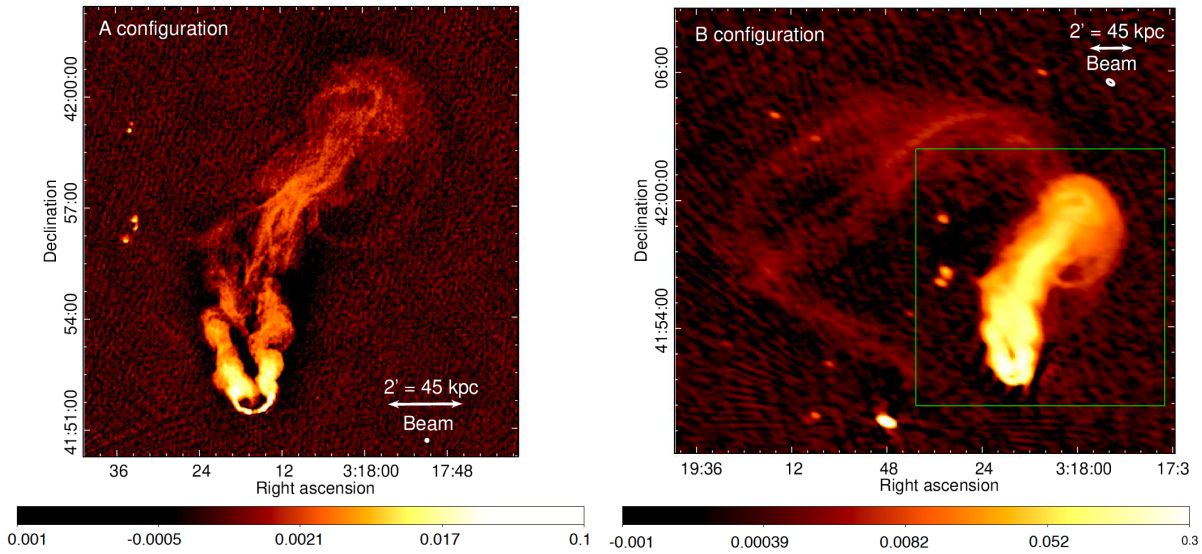

Figure 1.5: AGN jets in galaxy NGC 1265 mixing with the ICM due to the growth of instabilities as a consequence of ram-pressure stripping. Each picture shows a different configuration of the observations. Color scale units are Jy beam^{-1}. Figure taken from Gendron-Marsolais et al. (2020).

over significant distances (Tonnesen et al., 2011; Poggianti et al., 2019). Thermal conduction and magnetic fields modulate this process: conduction smooths temperature gradients, while magnetic tension can either suppress or guide turbulent eddies, depending on the field geometry (Armillotta et al., 2016; Ji et al., 2019).

On cluster-wide scales, mixing contributes to the distribution of heavy elements. Metals produced by stars and expelled via feedback are found dispersed across large volumes of the CGM and ICM, often showing remarkably uniform radial profiles (Werner et al., 2013; Simionescu et al., 2015). This implies either very early enrichment or long-term, large-scale mixing mechanisms, including turbulence driven by AGN feedback and mergers. AGN jets inflate cavities in the hot ICM, driving shocks and stirring motions that entrain ambient gas (see in Fig. 1.5 the filamentary AGN in galaxy NGC 1265 mixing with the hot ICM, triggered by the growth of instabilities. Figure taken from Gendron-Marsolais et al., 2020). Observations of metal-enriched, uplifted gas around cluster centers, along with simulations, support the view that AGN-driven turbulence plays a vital role in mixing and regulating cooling (McNamara & Nulsen, 2007; Gaspari et al., 2011; Bourne & Sijacki, 2017; Voit et al., 2017).

Despite significant progress in understanding these multiphase interactions, many uncertainties remain in the modeling of turbulent transport and mixing in astrophysical plasmas. The efficiency of these processes depends not only on the large-scale driving mechanisms, such as AGN feedback or galactic outflows, but also on the microphysical properties of the medium itself. The behavior of the plasma—whether it readily develops instabilities or sustains coherent structures—depends sensitively on how it responds to shear, compression, and anisotropic stress. For instance, observations of buoyant bubbles inflated by AGN jets in the ICM show

that they often remain coherent over tens to hundreds of kiloparsecs, persisting far longer than expected from simple hydrodynamic predictions (e.g. Fabian et al., 2003; Forman et al., 2007; Bîrzan et al., 2020). This apparent stability suggests that additional physical processes may be suppressing disruptive instabilities and damping turbulent mixing. Understanding how the internal properties of the plasma influence such behavior is therefore essential for building a complete picture of gas dynamics in galaxy clusters.

1.4 Plasma Physics of the ICM[2]

The high temperature and low density of the ICM ensure that it is a fully ionized plasma, which is characterized by electromagnetic interactions among electrons and ions. Due to its low density, the ICM is a good example of a weakly collisional plasma, where particle-particle collisions are infrequent compared to the dynamical timescales of the system (Schekochihin et al., 2005; Schekochihin & Cowley, 2006).

To properly describe the plasma physics of the ICM, we must first define its characteristic scales. The typical macroscopic scales of galaxy clusters range from tens to hundreds of kpc, representing the scales of density, temperature, and magnetic field gradients. Within these large-scale structures, an ion can travel freely between Coulomb collisions a distance known as the mean free path, defined as:

$$\lambda_i = \frac{3^{3/2}(k_B T_i)^2}{4\pi^{1/2} n_i e^4 \ln\Lambda} \approx \frac{v_{\mathrm{th},i}}{\nu_{ii}}\,, \tag{1.23}$$

where $v_{\mathrm{th},i} = \sqrt{2k_\mathrm{B}T_i/m_i}$ is the ion thermal velocity, and ν_{ii} is the ion collision frequency, given by:

$$\nu_{ii} = \frac{4\pi\, n_i e^4 \ln\Lambda}{m_i^{1/2} T_i^{3/2}}\,, \tag{1.24}$$

with n_i is the number density, with values of $n \sim 10^{-2} - 10^{-3}$ cm^{-3} in the cores of clusters, and $\ln\Lambda = 37.8$ is the Coulomb logarithm. ν_{ii} describes the number of Coulomb deflections an ion experiences each second, and $v_{\mathrm{th},i}$ as the distance it would cover in a second if it flew straight ahead. Therefore, $\lambda_i \approx v_{\mathrm{th},i}/\nu_{ii}$ represents the distance an ion can travel before experiencing a collision. A hotter plasma (larger $v_{\mathrm{th},i}$), or a more diffused plasma (smaller ν_{ii}) increase the mean free path (Sarazin, 1986; Kulsrud, 2004).

The mean free path in galaxy clusters is typically of the order of $1 - 10$ kpc. Such a long mean free path has significant consequences for the dynamics and transport properties of the ICM. Since λ_i can approach or even exceed the characteristic scales of temperature and pressure gradients, the plasma behaves as weakly collisional, and the assumptions underlying classical fluid descriptions begin to fail (Schekochihin et al., 2005; Kunz et al., 2012). In this regime, transport processes such as heat conduction and momentum exchange become non-local, with particles

[2]Parts of this section was published in MNRAS by Marin-Gilabert et al. (2022) and in ApJ by Marin-Gilabert et al. (2024).

carrying energy and momentum over macroscopic distances before interacting (Braginskii, 1965). As a result, classical diffusion approximations become inadequate, and kinetic descriptions are required to accurately capture the physics. A long mean free path also implies that the plasma can develop large-scale anisotropies in pressure and temperature, potentially triggering kinetic instabilities (see review by Kunz et al., 2014). These instabilities act to scatter particles and can effectively reduce the mean free path, providing a form of self-regulation for transport processes. To put this into perspective, a mean free path of ∼10 kpc is comparable to the size of a dwarf galaxy and constitutes a substantial fraction of a cluster core, highlighting the need to consider kinetic effects in models of the ICM. In this regime, magnetic fields play a crucial role in shaping these transport processes; therefore, understanding their strength and geometry is key for understanding the plasma physics in the ICM.

1.4.1 Magnetic Fields in the ICM

The ICM plasma is magnetized, although the origin of these magnetic fields in the early Universe is still unclear (see review by Subramanian et al., 2006, and references therein). Magnetic fields significantly influence the structure, dynamics, and observational properties of galaxy clusters, acting alongside relativistic particles as a crucial non-thermal component (Feretti et al., 2012). The presence of these magnetic fields is inferred primarily from observational signatures such as synchrotron emission, Faraday rotation measurements (RM), and inverse-Compton scattering measurements (Govoni & Feretti, 2004). Synchrotron radiation from relativistic electrons spiraling around magnetic fields produces diffuse radio halos and relics, which directly indicate the existence of magnetic fields within clusters (Feretti et al., 2012). Additionally, RM provide independent evidence of magnetic fields by detecting the rotation of polarized radio waves passing through magnetized plasma (Clarke et al., 2001). Current observational estimates indicate that magnetic fields in clusters typically range from 0.1 to 10 μG, significantly affecting cluster thermal dynamics by modulating transport processes, gas dynamics, and providing additional non-thermal pressure components (Subramanian et al., 2006).

The strength of magnetic fields within magnetized fluids, such as the ICM, is usually characterized by the plasma beta parameter, defined as the ratio of thermal to magnetic pressure, $\beta = P_{\rm th}/P_{\rm mag}$. In many astrophysical systems, including the ICM, the medium is typically weakly magnetized ($\beta \gg 1$). This is analyzed in more detail in section 2.6.

Magnetic fields strongly influence the dynamics of charged particles within the ICM. Specifically, the ions gyrate around the magnetic field lines in a circular motion of radius given by the gyroradius (or Larmor radius):

$$r_i = \frac{v_{{\rm th},i}}{\Omega_i}\,, \tag{1.25}$$

where $\Omega_i = eB/m_i c$ is the ion cyclotron frequency, m_i is the ion mass, B is the magnetic field strength, e is the electron charge, $k_{\rm B}$ the Bolztmann constant and c the speed of light (Schekochihin et al., 2005; Kunz et al., 2022). In typical ICM conditions, $\lambda_i \gg r_i$, which means that collisions are largely infrequent on the gyration scale and the ions undergo many rotations around the magnetic field lines before a collision (Schekochihin & Cowley, 2006). This condition implies that the plasma is collisionless at the gyration scale, thus ions maintain adiabatic invariants and the plasma

exhibits anisotropic pressure. Such anisotropy significantly affects plasma stability, making it susceptible to various instabilities, notably firehose and mirror instabilities (Schekochihin et al., 2005). The presence of these instabilities has important consequences, such as altering thermal conduction and viscosity, modifying turbulence properties, and potentially regulating the effective transport processes within the ICM (Kunz et al., 2014).

The origin of ICM magnetic fields remains a highly active research area, generally divided into primordial and astrophysical scenarios. Primordial magnetic fields may originate from early Universe processes, including inflationary mechanisms, phase transitions, or cosmic strings (see review by Grasso & Rubinstein, 2001). These fields can imprint detectable signatures in cosmic voids—regions largely untouched by astrophysical processes, thus retaining primordial magnetic information (Neronov & Vovk, 2010). Cosmic voids provide an ideal environment for detecting weak primordial fields (of the order of 10^{-18} G) via observations of gamma-ray blazars. By measuring the secondary emission from blazar-induced electromagnetic cascades, upper limits on magnetic fields in voids can be established, helping to constrain primordial field models (Neronov & Semikoz, 2009; Tavecchio et al., 2010). Astrophysical mechanisms, however, remain prominent candidates for generating and amplifying magnetic fields within clusters. Stellar winds and AGN jets inject magnetic energy directly into the ICM, although these processes alone typically produce fields around 0.1 μG or lower (see review by Brandenburg & Lazarian, 2013). Therefore, additional mechanisms must amplify these initial seed fields to observed levels.

The amplification and evolution of magnetic fields are deeply linked with turbulence resulting from hierarchical cluster formation and mergers of clusters (Schekochihin et al., 2005; Subramanian et al., 2006). Turbulent motions amplify magnetic fields primarily through a dynamo process, where turbulent flows stretch and fold magnetic field lines, exponentially increasing their strength. This fluctuation dynamo can effectively amplify initially weak fields to observed microgauss strengths within typical cluster evolution timescales ($\sim$ 5 Gyr) (Brandenburg & Lazarian, 2013).

Turbulence is a fundamental process influencing the magnetic field scale. Initially, magnetic fields generated on smaller scales ($\sim$10–20kpc) through galaxy wakes and interactions evolve into coherent structures across larger scales (hundreds of kiloparsecs) through turbulent cascading (Dimopoulos & Davis, 1997; Subramanian et al., 2006). The existence and effectiveness of such turbulent dynamos have been demonstrated through extensive numerical simulations and analytical theory (see Porter et al., 2015 and review by Brandenburg & Subramanian, 2005). Once the magnetic fields are amplified, they become crucial for the transport properties of the plasma and its overall dynamical behavior (Squire et al., 2017, 2023).

1.4.2 Turbulence

Turbulence in the ICM plays a critical role in the formation and evolution of galaxy clusters. It has an important effect on heat and mass transport, magnetic field amplification, cosmic-ray re-acceleration, and the thermodynamic properties of the cluster gas (Schekochihin et al., 2005; Brunetti & Lazarian, 2007; Brunetti & Jones, 2014). Understanding the nature of turbulence, driving mechanisms, and dissipation processes is essential for understanding the gas properties

of the ICM.

The ICM gas is continually perturbed by galaxy motions (e.g. Faltenbacher et al., 2005), mergers (e.g. ZuHone, 2011; Iapichino et al., 2017), AGN outflows (e.g. O'Neill et al., 2009; Gaspari, 2015) and accretion of gas along filaments (e.g. Kravtsov & Borgani, 2012; Vallés-Pérez et al., 2021a). These processes inject energy at large scales (low wavenumber k), which decays towards higher k modes in a Kolmogorov-like cascade, introducing turbulence on a wide range of scales (e.g. Kolmogorov, 1941, 1962). The energy is dissipated into heat at the Kolmogorov scale ($\eta_{\rm L}$, Kolmogorov, 1941), affecting small-scale processes such as cosmic ray re-acceleration (e.g. Fujita et al., 2003; Brunetti & Lazarian, 2007), star formation (e.g. Federrath, 2016) or magnetic field amplification (e.g. Kazantsev, 1968; Kulsrud & Anderson, 1992). These complex mechanisms over cosmological periods of time produce very complicated scenarios in which the transport properties of the gas are fundamental.

Turbulence is a time-dependent, stochastic flow characterized by a chaotic behavior (Beresnyak, 2019). It can be described by the Reynolds number (Re), defined as:

$$\mathrm{Re} = \frac{vL}{\nu} = \frac{\rho v L}{\eta}\,, \tag{1.26}$$

where v is the characteristic turbulent velocity, L is the driving scale of turbulence, ν is the kinematic viscosity, and η is the dynamic viscosity. In galaxy clusters, the Reynolds number is estimated to be in the range $\mathrm{Re} \sim 10^2 - 10^3$ (Schekochihin et al., 2005; Schekochihin & Cowley, 2006; Roediger et al., 2013b). These moderate Reynolds numbers indicate that, while turbulence can be sustained, it is not fully developed in the classical hydrodynamic sense due to the complex microphysics of the ICM. Transport processes like viscosity or conduction significantly alter the turbulent cascade and dissipation mechanisms, leading to moderate low Reynolds numbers. For comparison, fully developed turbulence has typically $\mathrm{Re} \gg 10^4$, where the dissipation scale is orders of magnitude smaller than the driving scale ($\eta_{\rm L} \lesssim 10^{-3} L$), leading to a highly chaotic environment where coherent structures do not survive (Landau & Lifshitz, 1987; Pope, 2000). In contrast, at $\mathrm{Re} \sim 10^2 - 10^3$, the dissipation scale is $\eta_{\rm L} \sim 0.01 L$, producing that microphysics play an important role. This leads to a chaotic environment, but where we can find coherent structures, like cold fronts (ZuHone & Roediger, 2016).

The energy injection at large scales is dominated by major and minor mergers (Vallés-Pérez et al., 2021a), which inject energy at scales of $L \sim 1$ Mpc with velocities of $v \sim 10^2 - 10^3$ km/s (Schekochihin et al., 2005). These mergers stir the ICM, generating bulk flows that fragment into smaller-scale eddies, where solenoidal turbulence dominates the dissipation of turbulent motions in the center, while compressive modes dominate at large radii (Vazza et al., 2016). AGN feedback also contributes to the energy injection, although at smaller scales, typically $L \sim 10 - 100$ kpc (Gaspari, 2015; Lau et al., 2017). Buoyant expanding bubbles trigger shocks and stir the local gas, leading to turbulence near the galaxy cluster center (at distances of $\sim 10 - 100$ kpc, Lau et al., 2017).

This energy injected at large scales decays in a turbulent cascade until it reaches the dissipation scale (Kolmogorov scale), where viscosity dissipates the kinetic energy into heat. The viscous scale of turbulence in galaxy clusters is typically of the order of $\eta_{\rm L} \sim 0.1 - 100$ kpc (Schekochihin & Cowley, 2006; Ruszkowski & Oh, 2010). For incompressible, isotropic

turbulence, Kolmogorov's dimensional analysis predicts the energy spectrum (Kolmogorov, 1941, 1962):

$$E(k) \propto k^{-5/3}\,, \tag{1.27}$$

where k is the wavenumber.

In a magnetized plasma like the ICM, the presence of Alfven waves and magnetic tension leads to a more complex and anisotropic cascade. In the regime of incompressible Magnetohydrodynamics (MHD), the turbulent energy cascades primarily in directions perpendicular to the local magnetic field, resulting in anisotropic spectra. This turbulent cascade follows a Kolmogorov-like slope: $E(k_\perp) \propto k_\perp^{-5/3}$, while the parallel spectrum steepens due to anisotropic interactions: $E(k_\parallel) \propto k_\parallel^{-2}$ (Beresnyak, 2015; Goldreich & Sridhar, 1995). As energy cascades toward smaller scales, the eddies become more and more elongated in the direction of the magnetic field (Brandenburg & Lazarian, 2013).

In the case of compressible MHD turbulence, this anisotropic cascade reveals a mixture of Alfven, slow, and fast magnetosonic modes (Cho & Lazarian, 2003; Kowal et al., 2009). The slow modes behaves similar to the incompressible MHD, following a Kolmogorov-like cascade: $E(k_\perp) \propto k_\perp^{-5/3}$ and $E(k_\parallel) \propto k_\parallel^{-2}$; while the fast modes are nearly isotropic and follow: $E(k) \propto k^{-3/2}$ (Cho & Lazarian, 2003; Brunetti & Lazarian, 2007).

All these turbulent processes stretch, fold, and bend the magnetic field lines, amplifying the extremely weak primordial magnetic field of the order of 10^{-18} G in a process known as turbulent dynamo (see Fig. 1.6). During the kinematic (early) phase of the dynamo, the magnetic field grows exponentially:

$$\frac{\mathrm{d}E_{\mathrm{mag}}}{\mathrm{d}t} = 2\gamma E_{\mathrm{mag}}\,, \tag{1.28}$$

where γ is the growth rate of the dynamo, which is correlated with the smallest eddies' turnover time (Subramanian et al., 2006). Once the magnetic energy is equal to the kinetic energy of the smallest eddies, the magnetic field back-reacts, suppressing the turbulence at these small scales. Larger eddies, which are more energetic but have longer timescales, continue the dynamo effect until the magnetic field becomes strong enough to suppress those eddies too (Schekochihin et al., 2002). This process produces an *inverse turbulent cascade*, where the magnetic field is amplified from small towards large scales (Steinwandel et al., 2022). Once the magnetic energy becomes comparable to the turbulent kinetic energy, the growth stops, and the magnetic energy saturates. The magnetic and turbulent energy reach an (approximately) equipartition (see reviews by Brandenburg & Subramanian, 2005 and Donnert et al., 2018). In galaxy clusters, the magnetic field saturates at a strength of a few μG in the cluster center (Schekochihin et al., 2005; Ryu et al., 2008).

Understanding turbulence in the ICM is therefore essential not only to characterize how energy cascades across spatial scales, but also to constrain the efficiency of mixing, heat transport, and magnetic field evolution in galaxy clusters. Turbulent motions play a key role in driving the redistribution of metals and thermal energy, shaping the structure and composition of the ICM. However, the extent to which turbulence promotes or suppresses mixing depends critically on the plasma's internal transport properties. Small-scale processes governing how momentum and energy diffuse can regulate the cascade itself and determine how efficiently turbulence couples to

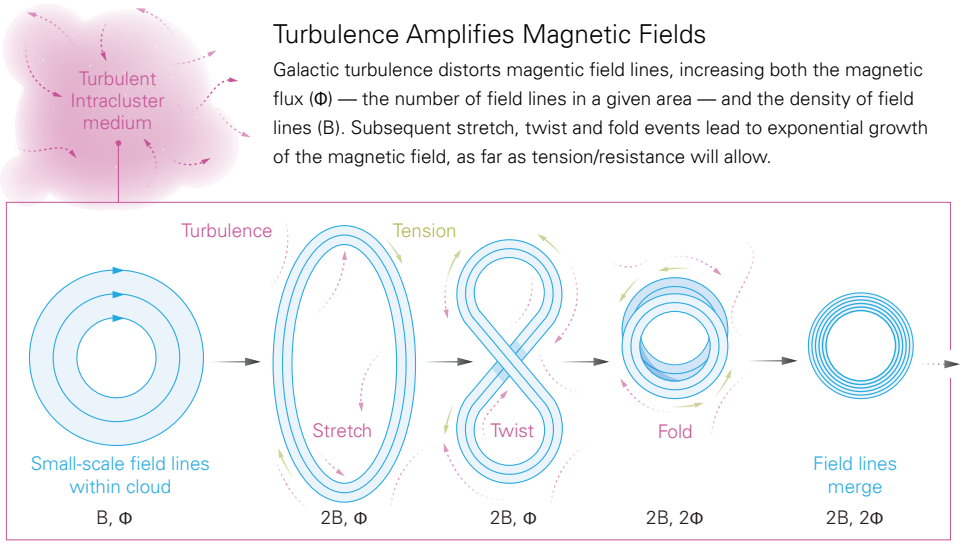

Figure 1.6: Sketch on how the small-scale dynamo amplifies the magnetic field with time. Figure taken from Steinwandel et al. (2024).

the surrounding gas. Subtle changes in these properties may have huge implications: altering how cold gas survives, how bubbles remain coherent, or how feedback redistributes mass and energy. This raises a fundamental question: how well do our current models capture the true behavior of turbulence and its impact on mixing in a medium as complex as the ICM? Understanding the role of these microphysical effects is essential for a complete picture of cluster thermodynamics.

1.4.3 Density Fluctuations as a Proxy for the Turbulent Velocity Field

Assuming subsonic gas motions within the galaxy cluster ($v \ll c_s$), small density perturbations are expected to be proportional to the one-component velocity at each scale $l = 1/k$; therefore, measuring density fluctuations can allow us to understand the turbulent velocity field.

On large scales, assuming local pressure balance ($\delta P/P \ll \delta\rho/\rho$) and an adiabatic equation of state $s = P/\rho^\gamma$, where s is the entropy and γ the adiabatic index, the small density perturbations can be written as

$$\left(\frac{\delta\rho}{\rho}\right)^2 = \left(\frac{1}{\gamma}\frac{\delta s}{s}\right)^2 , \tag{1.29}$$

where s is the specific entropy of the gas. The restoring buoyancy force over a gas element will create an oscillatory movement in the radial direction, dependent on the scale. Considering this, we can rewrite equation (1.29) as

$$\left(\frac{\delta\rho}{\rho}\right)^2 = \left(\frac{v_r}{\gamma\omega H_s}\right)^2 = \frac{H_p}{H_s}\frac{k^2}{k_\perp^2}\left(\frac{v_r}{c_s}\right)^2 , \tag{1.30}$$

where v_r is the radial velocity, ω is the oscillation frequency, k is the wavenumber of the oscillations, $k_\perp$ is its projection perpendicular to the radial direction, $H_p = (\mathrm{d}\ln P_0/\mathrm{d}r)^{-1}$ the

pressure scale height and $H_s = (\mathrm{d}\ln s_0/\mathrm{d}r)^{-1}$ is the entropy scale height (see Zhuravleva et al., 2014 for a detailed derivation). Assuming a stratified atmosphere, the motions are dominated by the perpendicular component of the velocity ($v_{1\mathrm{D}} \sim v_\perp \sim (k_r/k_\perp)v_r \gg v_r$) and we can write equation (1.30) as

$$\left(\frac{\delta\rho}{\rho}\right)^2_k = \eta_\rho^2 \left(\frac{v_{1\mathrm{D}}}{c_s}\right)^2_k = \eta_\rho^2 \mathcal{M}^2_{1\mathrm{D},k}\,, \tag{1.31}$$

where η_ρ is a scale-independent dimensional constant of the order of unity (Zhuravleva et al., 2014).

On small scales (i.e. smaller than the Ozmidov scale[3]), the turbulent cascade becomes isotropic ($k_r \sim k_\perp$ and $v_r \sim v_\perp$) and the density fluctuations become a passive scalar field. Thus, its variance is conserved and can be written as

$$\left(\frac{\delta\rho}{\rho}\right)^2_k \sim \frac{\varepsilon_\rho \tau_k}{c_s^2}\,, \tag{1.32}$$

which describes a flux ε_ρ over the cascade time τ_k at which $(\delta\rho/\rho)$ is mixed, normalized by the soundspeed. The turbulent motions decay at a speed

$$v_k^2 \sim \varepsilon_v \tau_k\,, \tag{1.33}$$

where ε_v is the kinetic flux. Plugging equation (1.33) into equation (1.32), the density fluctuations can be written as

$$\left(\frac{\delta\rho}{\rho}\right)^2_k \sim \frac{\varepsilon_\rho}{\varepsilon_v}\left(\frac{v}{c_s}\right)^2_k\,. \tag{1.34}$$

$\varepsilon_\rho/\varepsilon_v$ depends on how much variance of the scalar field reaches the inertial range from the larger scales, which must be equal to equation (1.31) at the Ozmidov scale ($\varepsilon_\rho/\varepsilon_v \sim \eta_\rho^2$). For a more detailed derivation of equations (1.31) and (1.34), see Zhuravleva et al. (2014).

Relation (1.31) has been tested in galaxy cluster simulations, where Zhuravleva et al. (2014) found a proportionality coefficient between density and velocity amplitude fluctuations of $\eta_\rho \approx 1.0 \pm 0.3$, as predicted theoretically, and Gaspari et al. (2014) a value of $\eta_\rho \approx 1.3$. Using cosmological simulations of galaxy cluster formation, Simonte et al. (2022) found that this relation depends on the dynamical state of the cluster, with $\eta_\rho \approx 1.15 \pm 0.06$ for relaxed clusters, but a flatter relation and a larger dispersion for unrelaxed clusters persists. The importance of the dynamical state was tested by Zhuravleva et al. (2023), showing that relaxed clusters tend to have a proportionality coefficient closer to 1 than unrelaxed clusters, where the coefficient tends to be larger. This is because in unrelaxed clusters, the assumption of a nearly hydrostatic atmosphere does not hold anymore, producing a larger scatter in the density-velocity fluctuations. Zhuravleva et al. (2023) also showed that accounting for halo ellipticity might be important, especially for the inner regions of relaxed clusters. The density-velocity fluctuations relation is not universal, but

[3]The Ozmidov scale (Ozmidov, 1992) is defined as the scale where the turbulent shear and the stratification terms are equal in magnitude.

depends on the level of stratification, characterized by the Richardson number Ri[4]. Mohapatra et al. (2020) found that η_ρ increases with Ri, ranging from $0.01 \lesssim \eta_\rho^2 \lesssim 1$ for Ri from 0 to 10.

It is important to note that the derivations above rely on the assumption that the ICM behaves as an ideal, adiabatic gas in local pressure equilibrium. In particular, equations (1.29) through (1.34) are based on linear perturbation theory applied to a stratified, subsonic, and nearly hydrostatic atmosphere, where thermodynamic variables are smoothly varying and fluid elements respond predictably to buoyant and turbulent forcing. However, the ICM is a weakly collisional plasma, and deviations from ideal behavior, such as anisotropic pressure, magnetic tension, or finite transport coefficients, may introduce corrections to this picture. In particular, any process that modifies the efficiency of momentum or entropy transport could alter both the amplitude and scale-dependence of density fluctuations. The proportionality coefficient η_ρ, while robust in idealized conditions, may become scale- or environment-dependent when additional microphysical processes are at play. Understanding the limits of this theory is therefore essential when applying it to real astrophysical systems, where non-ideal effects could significantly alter the observed relation between density and velocity fluctuations.

1.4.4 Radiative Cooling

Radiative cooling is a natural process in astrophysical fluids that influences the gas properties, therefore affecting the evolution of galaxies, galactic halos, and galaxy clusters. It takes place when a gas emits radiation, loses internal energy, and, therefore, cools down (Sarazin, 1986). These gas losses take place over a timescale defined as cooling time $t_{\rm cool}$. The particular process that leads to radiative cooling depends on the environmental conditions: temperature, densities, and metallicities (Binney & Tremaine, 2008).

The main radiative processes contributing to cooling are (Cimatti et al., 2019):

1. **Bremsstrahlung (free-free radiation):** This mechanism dominates at high temperatures, typically above 10^7 K. It occurs when free electrons pass close to ions and are accelerated by their Coulomb fields, emitting continuous X-ray radiation.

2. **Recombination (free-bound radiation):** Free electrons recombine with ions, emitting photons as they transition to lower energy bound states or form neutral atoms.

3. **Radiative de-excitation (bound-bound radiation):** Electrons bound to atoms or ions transition from higher to lower energy levels, emitting discrete spectral lines.

4. **Collisional ionization (bound-free):** Collisions of free electrons with bound electrons result in ionization.

5. **Collisional excitation (bound-bound):** Free electrons excite bound electrons to higher energy states, which subsequently emit photons upon de-excitation.

[4]On large scales, stratification is expected to be dominant over turbulence (Ri $>$ 1), while on small scales turbulence dominates (Ri $<$ 1) (Mohapatra et al., 2020).

In astrophysical fluids, it is often assumed that the gas is in a state of collisional ionization equilibrium. This means that the rates of collisional ionization and recombination are balanced perfectly, meaning there is no net change in the ionization state of the gas. This equilibrium condition neglects external photoionization processes and assumes that ions and neutral atoms predominantly remain in their ground states (Dopita & Sutherland, 2003; Draine, 2011). Despite being an idealized assumption, collisional ionization equilibrium provides valuable insights and enables detailed tabulations of cooling functions (e.g. Cox & Tucker, 1969; Raymond et al., 1976; Sutherland & Dopita, 1993).

We introduce the internal energy per unit volume of a gas as:

$$U = \frac{3}{2} n k_{\mathrm{B}} T \,, \tag{1.35}$$

where n is the total gas number density, k_{B} is Boltzmann's constant, and T is the gas temperature (Sutherland & Dopita, 1993; Cimatti et al., 2019).

Assuming an optically thin gas, the rate of change of internal energy due to radiative cooling under the assumption of collisional ionization equilibrium can be expressed as:

$$\frac{\mathrm{d}U}{\mathrm{d}t} = -n_{\mathrm{t}} n_{\mathrm{e}} \Lambda(T) \,, \tag{1.36}$$

where n_{t} is the total atomic number density (including ions and neutral atoms), n_{e} is the electron number density, and $\Lambda(T)$ is the cooling function (Sutherland & Dopita, 1993; Wiersma et al., 2009). The cooling function, $\Lambda(T)$, encapsulates the energy lost per unit time per unit volume due to radiative processes, and it depends uniquely on the temperature and metallicity. Fig. 1.7 shows the typical cooling curve assuming solar metallicity, where different elements contribute to the total cooling rates, depending on the temperature (figure taken from Wiersma et al., 2009). Each peak corresponds to a temperature at which particular ions of these elements are most abundant and therefore most effective at radiating energy.

The efficiency and timescale of radiative cooling are characterized by the cooling time, defined as:

$$t_{\mathrm{cool}} = \frac{U}{|\mathrm{d}U/\mathrm{d}t|} = \frac{3 n k_{\mathrm{B}} T}{2 n_{\mathrm{t}} n_{\mathrm{e}} \Lambda(T)} \,. \tag{1.37}$$

This equation represents the characteristic timescale over which the gas would lose its thermal energy completely, assuming the cooling rate remains constant (Binney & Tremaine, 2008).

Depending on the medium, the temperatures are different, and so are the mechanisms of radiation and cooling rates. The ICM is very hot, with temperatures above 10^7 K; therefore, the dominant radiative cooling mechanism is the Bremsstrahlung emission (Sarazin, 1986; Sutherland & Dopita, 1993). For temperatures lower than 10^7 K, line emission from electrons transitioning between energy levels becomes important. In contrast, in the CGM, where temperatures are typically lower than in the ICM (10^4 K $< T < 10^7$ K), the emission lines dominate radiative cooling, predominantly carbon, oxygen, neon and iron. Free electrons transfer energy via collisions to bound electrons, exciting them to higher energy levels. Different ions dominate at different temperatures, producing the peaks observed in Fig. 1.7.

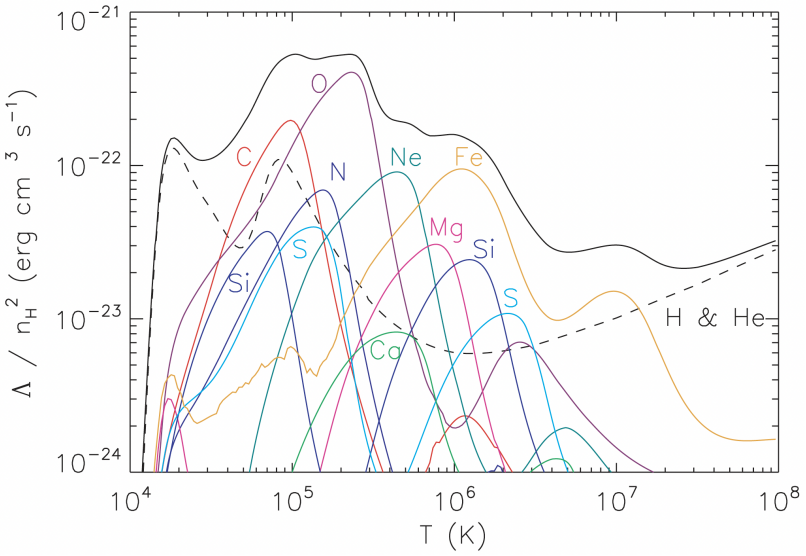

Figure 1.7: Cooling curve depending on the temperature, assuming solar metallicity, normalized to the number density. Figure taken from Wiersma et al. (2009).

The efficiency of radiative cooling is closely linked to how effectively gas phases interact and exchange energy across temperature regimes. In particular, mixing between hot and cold components of the plasma can generate intermediate-temperature gas that cools more rapidly due to enhanced line emission (Fielding et al., 2020). If mixing is suppressed, the amount of gas passing through these temperature ranges may be reduced, limiting the formation of rapidly cooling phases. This has direct implications for the cooling budget of galactic halos and the cores of galaxy clusters. The degree to which mixing occurs depends on the characteristics of turbulence and on the transport properties of the plasma itself. Even subtle differences in how momentum and thermal energy are redistributed across mixing layers can shift the balance between heating and cooling. Accurately describing this behavior is therefore essential for understanding how gas cools, condenses, and ultimately fuels star formation in large-scale structures.

1.4.5 Turbulent Radiative Mixing Layers

The dependence of cooling rates with temperature produces that mixing of hot and cold gas affects cooling strongly, where the cooling curve peaks at intermediate temperatures 10^4 K $< T < 10^6$ K (Begelman & Fabian, 1990; Fielding et al., 2020; Tan et al., 2021). As hot and cold gas mix, intermediate temperature gas is created, which can cool more efficiently than the two stable phases separately (Ji et al., 2019). This intermediate temperature gas is unstable and determines the amount of cold gas available for star formation; therefore, a proper understanding of turbulence and mixing is key in order to understand galaxy formation and evolution.

The mass transfer from the hot to the cold gas due to cooling has been extensively studied in the context of turbulent radiative mixing layers (TRMLs) (e.g. Begelman & Fabian, 1990; Slavin et al., 1993), which can be applied to several astrophysical systems, such as galactic outflows

(Brüggen & Scannapieco, 2016; Schneider & Robertson, 2017; Fielding & Bryan, 2022), or stellar wind bubbles (El-Badry et al., 2019; Lancaster et al., 2021a,b). These layers are formed at the interface of two gas phases: a hot, diffuse gas phase and a cold, dense gas phase. The relative motion of these two phases induces shear instabilities, mainly the Kelvin-Helmholtz instability (KHI), which drives turbulence and leads to the gas mixing between the phases (Tan et al., 2021). The structure and evolution of TRMLs can be understood using analogies taken from combustion theory. In turbulent combustion, the flame front is described by the mixing and reaction of fuel and oxidizer, producing products. Similarly, in radiative mixing layers, the hot gas acts as "fuel", cold gas as the "oxidizer", and the resultant cooled gas as the "combustion product" (Tan et al., 2021).

To describe the strength of radiative cooling, it is important to introduce the Damköhler number (Da, Damköhler, 1940), a dimensionless parameter taken from combustion theory, defined by the ratio of turbulent to cooling time:

$$\mathrm{Da} = \frac{t_{\mathrm{turb}}}{t_{\mathrm{cool}}(T)} \simeq \frac{\lambda}{u'\, t_{\mathrm{cool}}(T)}\,, \tag{1.38}$$

where $t_{\mathrm{turb}} \simeq \lambda/u'$ is the eddy turnover time, t_{cool} the cooling time, and u' the turbulent velocity.

When $t_{\mathrm{turb}} < t_{\mathrm{cool}}$ (Da < 1), the effect of cooling is weak compared to turbulence, and the gas entropy is dominated by mixing. This leads to a characteristic luminosity $\propto t_{\mathrm{cool}}^{-1/2}$ (Ji et al., 2019; Tan et al., 2021). However, when $t_{\mathrm{cool}} < t_{\mathrm{turb}}$ (Da > 1), cooling is stronger than turbulence and, as soon as the gas is mixed, it is cooled down, leading to a multiphase medium where the gas entropy is dominated by cooling (see e.g. Kuo & Acharya, 2012; Tan et al., 2021). Specifically, in this strong cooling regime, the total luminosity of the mixing layer scales as $\propto t_{\mathrm{cool}}^{-1/4}$ (Gronke & Oh, 2019; Fielding et al., 2020; Tan et al., 2021).

In radiative mixing layers, the net radiative losses due to cooling are balanced by the enthalpy flux, producing a mass flow from the hot to the cold medium. This means that the total luminosity is proportional to the mass transfer from the hot to the cold medium: $\dot{m} \propto L_{\mathrm{rad}}$ (Ji et al., 2019; Gronke et al., 2021). The total luminosity of a system depends on how much gas can be mixed to intermediate temperatures, therefore, the suppression of turbulence and mixing might lead to differences in luminosity.

The emission due to cooling follows a power-law relation, which depends on the cooling strength (Damköhler number). The surface brightness $Q = L_{\mathrm{rad}}/l^2$, where l^2 is the surface area, depends on Da as

$$Q \propto \begin{cases} u'^{1/2}\lambda^{1/2} \propto u'\mathrm{Da}^{1/2}, & \text{if Da} < 1 \text{ (Weak cooling)} \\ u'^{3/4}\lambda^{1/4} \propto u'\mathrm{Da}^{1/4}, & \text{if Da} > 1 \text{ (Strong cooling)}\,. \end{cases} \tag{1.39}$$

This relation has been tested numerically by Tan et al. (2021), where the change of slope can be seen at Da ≈ 1 (see Fig. 1.8, taken from Tan et al., 2021).

Another important dimensionless parameter in combustion theory is the Karlovitz number (Klimov, 1963; Williams, 1975), defined as the ratio of the Field length to the Kolmogorov scale squared: $\mathrm{Ka} = \delta_{\mathrm{L}}^2/\eta_{\mathrm{L}}^2$. The Kolmogorov scale ($\eta_{\mathrm{L}}$, Kolmogorov, 1941) is set by viscosity and marks the smallest scale of the turbulent cascade, where kinetic energy is dissipated into

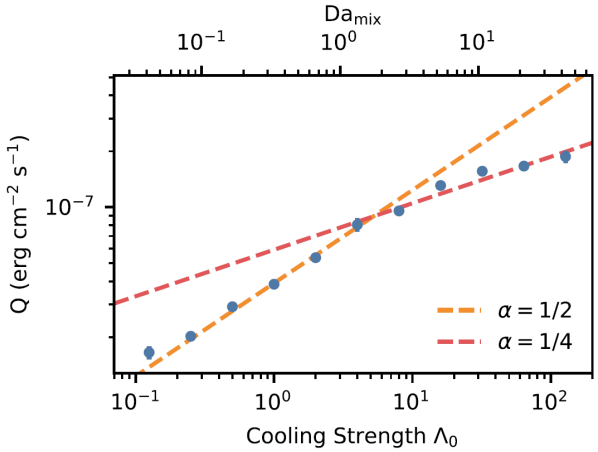

Figure 1.8: Surface brightness Q as a function of Da. The orange dashed line shows the best fit in the weak cooling regime (Da < 1) with a slope of $\alpha = 1/2$. The red dashed line shows the best fit in the strong cooling regime (Da > 1) with a slope of $\alpha = 1/4$. Figure taken from Tan et al. (2021).

heat; below this scale, hydrodynamic instabilities are suppressed. On the other hand, the Field length (δ_L, Field, 1965) is set by thermal conduction and represents the largest scale over which conduction can efficiently suppress thermal instability in the presence of radiative cooling (Begelman & McKee, 1990). The Karlovitz number thus captures the competition between turbulent and thermal stabilization mechanisms. If Ka < 1, the small-scale turbulence is not small enough to break up the flame, and the combustion happens in a laminar flow. If Ka > 1, the small-scale turbulence grows faster than it can locally burn through its thickness, leading to a turbulent flame front (Kuo & Acharya, 2012). Translated to TRMLs terminology, Ka < 1 describes a scenario in which cooling takes place in a laminar regime, whereas if Ka > 1, cooling happens in a turbulent regime. In the absence of explicit conduction and viscosity, the Kolmogorov scale and Field length are given numerically by a similar multiple of the resolution scale in both cases ($\eta_L \sim \delta_L \sim \Delta x$), therefore, Ka ~ 1 (Tan et al., 2021). By including explicit viscosity, the Kolmogorov scale becomes larger than the Field length set by resolution ($\eta_L > \delta_L$), therefore Ka < 1.

The dimensionless Damköhler and Karlovitz numbers are essential for distinguishing different regimes of turbulent mixing and radiative cooling, determining the efficiency of multiphase gas, and the associated observational signatures. Understanding these processes in detail is crucial for accurately interpreting astrophysical observations and improving subgrid physics models in large-scale cosmological simulations.

These relations, however, rely on the assumption that turbulence behaves according to ideal fluid dynamics, where eddy turnover times and turbulent velocities evolve predictably with scale. In realistic astrophysical plasmas, small-scale physical processes can modify both the efficiency of turbulent mixing and the spectral distribution of energy. Even modest changes in the turbulent velocity field or its characteristic timescale can alter the Damköhler number and shift the system between weak and strong cooling regimes. This has important implications for scaling relations

such as equation (1.39), potentially breaking their universality across different environments. The presence of additional transport effects could further suppress or enhance mixing, changing the fraction of gas able to reach intermediate temperatures and, consequently, the overall luminosity. Accurately capturing these effects is therefore essential to robustly link turbulence, cooling, and observable emission in galaxy halos and clusters.

1.5 Observations

The large variety of physical processes happening in galaxy clusters lead to very different emissions that can be measured across the electromagnetic spectrum. Multi-wavelength observations are fundamental for a comprehensive understanding of the ICM. Each wavelength of the electromagnetic spectrum reveals a unique process of the ICM, enabling us to study its thermal, non-thermal, magnetic, and dynamical properties. These observations are crucial for constructing a detailed picture of galaxy cluster physics, their evolution, and their role in large-scale structure formation (e.g. Sarazin, 1986).

X-ray observations are a cornerstone for studying the ICM, as this hot plasma mainly emits thermal bremsstrahlung radiation due to the presence of free electrons interacting with positively charged ions (see review by Walker et al., 2019). The intensity and spectral shape of this emission allow us to determine fundamental plasma properties such as temperature, electron density, and metallicity distributions within clusters (see review by Böhringer & Werner, 2010). These measurements are key for understanding the thermal structure, energy content, and gas distribution of galaxy clusters. X-ray observations show that the temperature of the ICM typically ranges from about 2 to 10 keV ($\approx 10^7 - 10^8$ K), requiring vast gravitational potential wells to contain the gas (Walker et al., 2019).

Together with X-ray, optical, and infrared observations also contribute to the understanding of the potential well via gravitational lensing. The gravitational lensing of background galaxies by galaxy clusters can determine the total mass distribution independently of the dynamical state of the cluster. These lensing measurements, when combined with X-ray observations, provide robust constraints on the mass profiles and hence the gravitational potential governing the ICM distribution (Umetsu et al., 2014; Walker et al., 2019).

Complementary radio observations reveal the presence and properties of magnetic fields and cosmic-ray particles within the ICM. Synchrotron radiation from relativistic electrons spiraling around magnetic field lines manifests in diffuse, extended radio sources such as radio halos and relics, typically associated with merging and dynamically active galaxy clusters (van Weeren et al., 2021). These features indicate large-scale acceleration mechanisms, such as shocks or turbulence induced by cluster mergers, thus providing valuable diagnostics on the magnetic field strength. The observed magnetic fields in clusters typically range from a fraction of a microgauss up to several microgauss, depending on the cluster dynamical state and region considered (Feretti et al., 2012).

RM offers another observational technique, sensitive to the line-of-sight component of magnetic fields weighted by the electron density. Polarized radio signals from background sources passing through the cluster medium experience rotation due to these magnetic fields,

allowing us to infer their strength and spatial structure. Studies show differences between relaxed and dynamically disturbed clusters. Disturbed systems typically exhibit higher RM dispersions, suggesting enhanced magnetic fields and increased coherence lengths. In contrast, relaxed clusters show smaller coherence lengths and intrinsic depolarization effects (Bonafede et al., 2013; Stasyszyn & de los Rios, 2019).

Additionally, observations using the SZ effect provide information about the ICM pressure distribution. The SZ effect occurs when the hot ICM electrons inverse-Compton scatter CMB photons, causing characteristic distortions of the CMB spectrum observable at millimeter and sub-millimeter wavelengths (Walker et al., 2019). SZ measurements, in combination with X-ray data, are particularly powerful for determining the thermal pressure profile and total mass of clusters (see reviews by Birkinshaw, 1999 and Carlstrom et al., 2002).

1.5.1 Observations of Turbulence in the ICM

Understanding the velocity structure of the hot, diffuse ICM is essential to constrain the microphysical properties of this plasma and to quantify the non-thermal processes that can influence cluster thermodynamics. Direct measurements of the turbulent velocities can be done via high-resolution spectroscopy of emission lines, with missions like Hitomi (Hitomi et al., 2016) or XRISM (XRISM Science Team, 2020). This can be done by measuring the broadening of X-ray emission lines. By modeling the thermal and instrumental contributions to line widths, one can isolate the line-of-sight velocity dispersion associated with turbulence, allowing direct measurements of gas motions and the corresponding non-thermal pressure support in galaxy clusters.

Direct Measurements

Hitomi was able to measure the turbulent velocities of the core of the Perseus cluster using a Soft X-ray Spectrometer (SXS). The velocity dispersion measured was of $\sigma_v = 163 \pm 10$ km s^{-1}, corresponding to a three-dimensional Mach number of approximately $\mathcal{M}_{3D} \simeq 0.30 - 0.45$. The turbulent pressure support measured was of $\sim 2 - 7\%$, indicating that the core of Perseus is relaxed (Hitomi et al., 2018).

More recently, XRISM observations of the relaxed, hot galaxy cluster Abell 2029 revealed a similarly low velocity dispersion of $\sigma_v = 169 \pm 10$ km s^{-1}, despite the higher ICM temperature (~ 7 keV). This translates to a Mach number of approximately $\mathcal{M}_{3D} \simeq 0.22$ and a turbulent pressure support of only $2.6 \pm 0.3\%$, one of the lowest levels yet measured (XRISM, 2025). In observations of Centaurus, the velocity dispersion found is $\sigma_v \leq 120$ km s^{-1}, the 3D Mach number $\mathcal{M}_{3D} \leq 0.25$ for $T \sim 2.5$ keV and the turbulent pressure support is $\sim 3\%$ (Audard et al., 2025). In the case of Coma (XRISM et al., 2025), the velocity dispersion is $\sigma_v = 208 \pm 12$ km s^{-1}, with $\mathcal{M}_{3D} = 0.24 \pm 0.015$ and a turbulent pressure support of only $3.1 \pm 0.4\%$ (see Fig. 1.9, where the measurements of line of sight velocities relative to the mean velocity of the cluster (left panel) and the line of sight velocity dispersion (right panel) measured by XRISM, are overplotted with an image taken by XMM-Newton. Figure taken from XRISM et al., 2025). These measurements are still consistent with the predictions, but they are at the lower end expected in galaxy clusters.

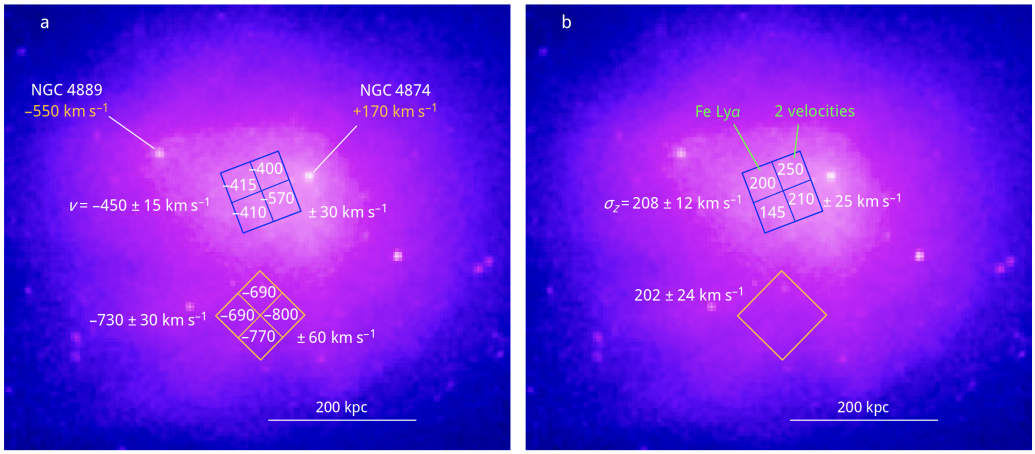

Figure 1.9: XRISM measurements overplotted on a Coma image taken by XMM-Newton. *Left panel*: Measurements of line-of-sight velocities relative to the mean velocity of the cluster. *Right panel*: Measurements of line-of-sight velocity dispersion. Image taken from XRISM et al. (2025).

They suggest that the turbulent velocity in galaxy clusters might be lower than expected, therefore, a suppression mechanism (such as viscosity) could be reducing the motions of the gas.

Indirect Measurements

Nevertheless, direct observations of turbulent velocity via spectroscopy are still scarce. Therefore, indirect methods such as measurements of density fluctuations (see §1.4.3) are needed to measure turbulent velocities and constrain the microphysical properties of the ICM. Using X-ray telescopes like Chandra (Weisskopf et al., 2000) and XMM-Newton (Jansen et al., 2001), fluctuations of the X-ray surface brightness can be used as a proxy for the turbulent velocity field (Zhuravleva et al., 2014).

Using high-resolution Chandra observations of 80 nearby galaxy clusters, Heinrich et al. (2024) inferred the turbulent velocities across the ICM, excluding the cool-core regions to avoid contamination from AGN feedback. They found characteristic one-dimensional turbulent velocities of approximately 150 km s^{-1} in relaxed clusters and up to 200–250 km s^{-1} in intermediate and unrelaxed clusters, respectively. These values correspond to a $\mathcal{M}_{3D} = 0.31 \pm 0.09$ on average. The inferred non-thermal pressure support was found to be modest, with turbulent to total pressure ratios of about 6% in relaxed clusters, 4% in intermediate, and up to 7% in unrelaxed clusters. Table 1.1 summarizes key turbulence measurements from various clusters and instruments.

The consistently low levels of turbulent velocity and pressure support observed across a range of galaxy clusters raise a critical question: what physical processes could be acting to suppress turbulence in the ICM? One plausible candidate is the action of transport processes, particularly viscosity, which governs the rate at which momentum is redistributed throughout the plasma. In a highly ionized, weakly collisional medium like the ICM, viscosity can have a big influence on the evolution of turbulent flows. Even when large-scale stirring mechanisms such as mergers or

Table 1.1: Observational measurements of turbulence in galaxy clusters. The first column shows the cluster observed and the reference; the second column shows the instrument used for the measurement; the third whether they use a direct or indirect method to calculate the turbulent velocities; the fourth column is the value of velocity dispersion; fifth the 3D Mach number; and sixth the turbulent pressure support.

Cluster	**Instrument**	**Method**	σ_v **[km s^{-1}]**	$\mathcal{M}_{\mathbf{3D}}$	$P_{\mathbf{NT}}/P_{\mathbf{th}}$
Perseus Hitomi et al. (2018)	Hitomi	Direct	163 ± 10	0.30 – 0.45	2 – 7%
Abell 2029 XRISM (2025)	XRISM	Direct	169 ± 10	0.22	2.6 ± 0.3%
Centaurus Audard et al. (2025)	XRISM	Direct	≤ 120	≤ 0.25	∼ 3%
Coma XRISM et al. (2025)	XRISM	Direct	208 ± 12	0.24 ± 0.015	3.1 ± 0.4%
80 clusters Heinrich et al. (2024)	Chandra	Indirect	- Relaxed: ∼ 150 - Intermediate: ∼ 200 - Unrelaxed: ∼ 250	0.31 ± 0.09	6 ± 2% 4 ± 2% 7 ± 4%

AGN feedback are active, viscous dissipation can act efficiently to damp turbulent eddies and suppress the energy cascade at smaller scales. This not only affects the amplitude and spectrum of turbulent motions but also alters the way energy is redistributed within the cluster, with potential implications for mixing, thermal conduction, and gas dynamics. The fact that turbulence appears lower than expected suggests that viscosity—and more broadly, transport processes—may play a far more significant role than currently appreciated. Understanding the extent to which these processes operate in the ICM is therefore essential to constructing a self-consistent picture of cluster thermodynamics.

2 | Viscosity in the ICM

The ICM is a hot, diffuse plasma with temperatures reaching $T \sim 10^7 - 10^8$ K and densities of $n \sim 10^{-3}$ cm^{-3}, where thermal particle velocities are high and Coulomb collisions are infrequent. In such a weakly collisional environment, the particle mean free path becomes comparable to—or even exceeds—typical macroscopic length scales such as pressure or temperature gradients (Sarazin, 1986). Under these conditions, individual particles can carry momentum over large distances, making collisional transport processes, like viscosity, effective even in a plasma that is not strongly collisional in the classical sense. Viscosity arises from the momentum exchange between particles moving along different velocity gradients (Schekochihin et al., 2005; Kunz et al., 2012). In the ICM, where the ion mean free path can be on the order of several kiloparsecs, ions from one fluid element can traverse significant distances before scattering. This means that even weak velocity gradients can lead to substantial momentum flux, resulting in a non-negligible viscous stress tensor.

The dynamic viscosity coefficient η reflects this transport, and for a fully ionized plasma it scales approximately as $\eta \sim n\, m_i\, v_{\mathrm{th},i}\, \lambda_i$ (Spitzer, 1962; Sarazin, 1986), where $v_{\mathrm{th},i} \propto \sqrt{T}$ and $\lambda_i \propto T^2$ (see §1.4). This leads to a temperature dependence of $\eta \propto T^{5/2}$, increasing rapidly with temperature. Consequently, with the hot temperatures of the ICM, viscosity can become large enough to suppress velocity perturbations on scales of tens to hundreds of kiloparsecs. This sets a viscous cutoff scale above which turbulent motions may develop, therefore suppressing significantly the development of the turbulence (Sijacki & Springel, 2006; Kunz, 2011).

This is a potential explanation of the recent high-resolution X-ray spectroscopic measurements from XRISM and Hitomi, which reveal unexpectedly low levels of turbulent pressure support in cluster cores: values as low as 2–3% of the total pressure in systems like Perseus, Abell 2029, and Coma (Hitomi et al., 2018; XRISM, 2025; XRISM et al., 2025; Audard et al., 2025, see §1.5.1). These results challenge expectations from cosmological simulations, which typically predict non-thermal pressure fractions of 5–15% even in relaxed clusters (Nelson et al., 2014; Vazza et al., 2018; Sayers et al., 2021). Viscous stresses can naturally provide such damping, and may also regulate mixing, modify shock structures, and influence the propagation of sound waves and weak shocks generated by AGN feedback (Fabian et al., 2005). Taken together, these clues point to viscosity as a potentially crucial but under-constrained transport process in the ICM.

To evaluate whether viscosity can indeed play this regulatory role in the ICM, we must first understand its theoretical foundations. The classical description for describing viscosity in a fully ionized plasma is given by the formulation developed by Spitzer (Spitzer, 1962), which applies in the limit where Coulomb collisions dominate particle interactions. This collisional regime

provides a useful starting point for quantifying momentum transport.

2.1 Spitzer Viscosity

Spitzer viscosity describes momentum transport in plasmas dominated by Coulomb collisions, where the plasma can be considered collisional. In this regime, the particle mean free path is shorter than the gyro-radius ($\lambda_i \ll r_i$, see §1.4.1), and frequent collisions rapidly isotropize particle velocities, making the viscosity isotropic. This scenario is typical in high-temperature plasmas of astrophysical objects, where the influence of collisions surpasses that of magnetic fields. Under these conditions, the isotropic components of viscosity dominate the transport properties, simplifying the understanding of plasma behavior on large scales. Thus, isotropic viscosity is generally appropriate for weakly magnetized or unmagnetized plasmas, where particle trajectories are less restricted by magnetic fields, allowing momentum transport to be directionally uniform.

The behavior of a viscous plasma is determined by the viscous stress tensor, which in the case of an isotropic viscosity is given by:

$$\mathbf{\Pi}_{\rm Iso} = \eta\,\boldsymbol{\sigma} = \eta\left(\nabla\mathbf{v} + \nabla\mathbf{v}^{\rm T} - \frac{2}{3}(\nabla\cdot\mathbf{v})\mathbf{I}\right), \tag{2.1}$$

where we have dropped the bulk viscosity term, since it is related to the degrees of freedom of molecular rotations, being zero for monoatomic gases (Zeldovich & Raizer, 1967; Pitaevskii & Lifshitz, 1981). The viscous stress tensor is equal to the rate of strain tensor ($\boldsymbol{\sigma}$) multiplied by the shear viscosity coefficient η (also referred to as dynamic viscosity), defined as

$$\eta = 0.960\frac{n_i k_{\rm B} T_i}{\nu_{ii}} = 0.406\frac{m_i^{1/2}(k_B T_i)^{5/2}}{(Z\,e)^4\ln\Lambda}, \tag{2.2}$$

where n_i is the number density, ν_{ii} is the collision frequency (see §1.4), m_i is the mass of the proton, and T_i is the temperature of the plasma. The numerical prefactor and scaling follow from solving the linearized Boltzmann equation with a Fokker–Planck collision operator under the assumption of a small departure from a Maxwellian distribution (Spitzer, 1962; Braginskii, 1965).

2.2 Viscous Diffusivity

Viscosity fundamentally describes how plasma responds to shear motions and how momentum is diffused. Two forms of viscosity are typically considered in fluid dynamics: dynamic viscosity and kinematic viscosity. Although they are closely related, these two forms of viscosity quantify different physical aspects of the viscous behavior in fluids, including astrophysical plasmas.

The dynamic viscosity (η, equation (2.2)) describes the resistance of the fluid to be deformed under a shear stress, and it is independent of the density. It measures the internal friction between

layers of the plasma, i.e. how hard it is for the plasma layers to slide past each other. This parameter is the shear viscosity coefficient that appears in the viscous stress tensor (2.1) and it has units of $\mathrm{g} \cdot \mathrm{cm}^{-1}\mathrm{s}^{-1}$.

On the other hand, the kinematic viscosity (ν) is defined as the ratio between the dynamic viscosity and the density:

$$\nu = \frac{\eta}{\rho} \,. \tag{2.3}$$

The kinematic viscosity has units of $\mathrm{cm}^2 \cdot \mathrm{s}^{-1}$ and describes how momentum-diffusive a medium is, i.e., how fast the velocity gradient is smoothed out. Therefore, when considering multiphase systems with large density contrasts – typical in astrophysical contexts such as CGM or ICM – it becomes essential to distinguish between these two viscosity parameters (Landau & Lifshitz, 1987). When there is a shear movement between two fluids, assuming symmetry – i.e., a planar slab (or sheet) setup –, the shear velocity gradient is smoothed out following:

$$v_{\mathrm{Shear}}(y) = |v_{\mathrm{Shear}_0}| \, \mathrm{erf}\left(\frac{y}{2\sqrt{\nu t}}\right) , \tag{2.4}$$

where v_{Shear_0} is the initial shear velocity, y is the direction perpendicular to the interface, t is the time and ν is the kinematic viscosity. This formula arises from solving the Rayleigh problem (also known as Stokes' first problem; Stokes, 1851; Rayleigh, 1911) for a viscous fluid where there are two flat plates located at the boundaries. These plates suddenly accelerate to some fixed constant velocities in opposite directions, leading to the velocity profile shown in equation (2.4) (e.g. Drazin & Riley, 2006).

In a scenario with constant dynamic viscosity, the diffusivity of momentum in each fluid differs primarily due to their respective densities. This difference in momentum diffusivity increases the larger the density contrast is. Specifically, since kinematic viscosity depends inversely on density, the hot, less dense medium will possess a higher diffusivity compared to the cold, denser medium. As a consequence, in systems exhibiting a high density contrast, the hot medium typically dominates momentum diffusion processes, setting the characteristic diffusivity scale for the entire system. On top of that, since the dynamic viscosity depends strongly on temperature, it is negligible in the cold medium compared to the hot medium. Thus, from a practical point of view, viscous diffusion becomes predominantly controlled by the hot medium, making the viscous effects in the cold phase negligible.

It is important to note that, although the hot medium dominates momentum diffusion, the cold medium carries almost all the momentum of the system. This implies that a denser cold medium will have a larger effect on momentum diffusion than a lighter cold medium. The momentum diffused by viscosity in the hot medium is determined by the cold medium. These two processes work together, and are key in understanding the growth or suppression of instabilities (this is studied in detail in §5.2.4).

2.3 Consequences of a Viscous ICM

The effect of viscosity primarily manifests through the smoothing of velocity gradients, reducing differences in velocity across adjacent fluid layers. By redistributing momentum, viscosity acts to dampen small-scale motions, effectively limiting the growth of fluid instabilities that rely on sharp shear flows. Examples of such instabilities are the KHI or the Rayleigh–Taylor instability (RT), which arise at the interface of two fluids with different shear velocities. The growth of KHI depends critically on the steepness of the velocity gradient, with a more pronounced gradient facilitating greater instability growth (Chandrasekhar, 1961). High viscosity counteracts this process by significantly reducing velocity gradients, thereby suppressing instability growth (this is studied in detail in §4.4.2).

This might be particularly relevant in several astrophysical processes in galaxy clusters, particularly involving sharp velocity gradients that trigger the growth of instabilities. A prime example is ram-pressure stripping of galaxies, where the hot ICM interacts dynamically with the cooler CGM surrounding infalling galaxies. In such interactions, the high viscosity of the ICM might effectively suppress KHI at the CGM-ICM interface, resulting in smoother, elongated gaseous tails that exhibit reduced small-scale turbulence (Roediger et al., 2015; Kraft et al., 2017; Ignesti et al., 2024). Consequently, stripped tails remain coherent over larger spatial scales, significantly altering their observational signatures.

Another critical phenomenon impacted by viscosity-induced instability suppression involves cold fronts observed in clusters. These sharp discontinuities in temperature and density typically result from sloshing motions within the ICM, generating shear interfaces prone to instability-driven disruption (Markevitch & Vikhlinin, 2007; ZuHone et al., 2015). When instabilities such as the KHI grow, they induce the characteristic creation of ‘bays’ along cold front interfaces, effectively disrupting their coherent structure (Walker et al., 2017; Ge et al., 2020; Breuer et al., 2020). Conversely, in a viscous ICM, the potential suppression of these instabilities stabilizes the cold fronts, preserving their sharp boundaries and coherent structures over extended periods (Roediger et al., 2013a; ZuHone et al., 2015).

The suppression of fluid instabilities by viscosity extends its influence to turbulence dynamics within the ICM. Turbulence significantly impacts energy transport, metal mixing, and entropy redistribution in galaxy clusters. Viscosity primarily damps turbulent eddies at smaller scales, reducing the effective Reynolds number and thus diminishing turbulent mixing and diffusion (Gaspari et al., 2014; Zhuravleva et al., 2019). This decrease in turbulence might lead to less efficient mixing between the ISM of galaxies and the surrounding ICM, resulting in distinct and potentially steeper metallicity gradients observed in cluster cores (Rebusco et al., 2005; Werner et al., 2013; Simionescu et al., 2019). Such gradients reflect inhibited metal transport, which can alter local cooling and star formation rates by limiting the availability of enriched gas (Müller et al., 2021).

Radiative cooling in the dense central regions of clusters can lead to the formation of cold gas and subsequent star formation, unless counteracted by heating mechanisms such as thermal conduction, AGN feedback, or mixing with high-entropy gas. When viscosity suppresses turbulent mixing, it effectively isolates the cooling gas from its surroundings, making it harder

for heat to be transported into the core of the cluster. This can exacerbate the development of cooling flows and lead to the formation of dense, cold gas reservoirs. Moreover, reduced turbulent mixing has significant consequences for radiative cooling processes in galaxy clusters. Dense cluster cores are prone to cooling instabilities, which can form cold gas reservoirs and stimulate star formation unless balanced by energy injection processes such as thermal conduction, AGN feedback, or turbulent mixing (see reviews by McNamara & Nulsen, 2012 and Fabian, 2012). In a viscous environment, suppressed turbulence isolates cool gas regions by limiting energy and entropy transport from hotter, outer regions. Consequently, viscosity enhances the conditions necessary for the development of cooling flows, potentially increasing the mass of cold gas reservoirs and intensifying star formation episodes within cluster cores (Ruszkowski et al., 2011; Voit et al., 2017).

In summary, viscosity might profoundly affect galaxy cluster evolution by modulating instability growth, turbulent dynamics, metal transport, and cooling processes. All these viscous effects leave distinct observational signatures, such as smoother and extended ram-pressure stripped tails, stable and sharp cold front boundaries, reduced turbulence-induced mixing, and distinct metal abundance gradients. Current and future observational facilities are capable of detecting these signatures, thereby providing crucial constraints on the magnitude and physical characteristics of viscosity within the ICM.

2.4 Constraints of Viscosity from Observations

To determine how viscous the ICM actually is, we can rely on observational diagnostics by comparing observed signatures with predictions from theoretical models and numerical simulations. Structures such as the coherence and smoothness of ram-pressure stripped galaxy tails, the sharpness and stability of cold fronts, and the spectrum of density and pressure fluctuations are all influenced by viscosity. By analyzing these features in high-resolution X-ray and radio observations, and matching them with simulations that incorporate different levels of viscosity, we can place meaningful constraints on the effective viscosity of the ICM. This method provides a link between theoretical predictions and empirical data, enabling a more quantitative understanding of plasma microphysics in galaxy clusters.

Ram-Pressure Stripped Galaxies

Observations of ram-pressure stripped galaxies, such as NGC 4552 observed with Chandra (Roediger et al., 2015; Kraft et al., 2017) and the jellyfish galaxies from the GASP survey (Ignesti et al., 2024), provide valuable constraints on ICM viscosity. In NGC 4552, the observed morphology of the stripped gas tail indicates efficient turbulent mixing of the ICM and stripped gas, matching inviscid hydrodynamical simulations rather than viscous models (see Fig. 2.1 comparing observations with simulations with different levels of viscosity. Figure taken from Roediger et al., 2015). The comparison shows that only the inviscid case reproduces key morphological features: the irregular flaring of the tail, small-scale turbulence, and efficient downstream mixing of the ISM with the ambient ICM. Simulations with even a modest viscosity

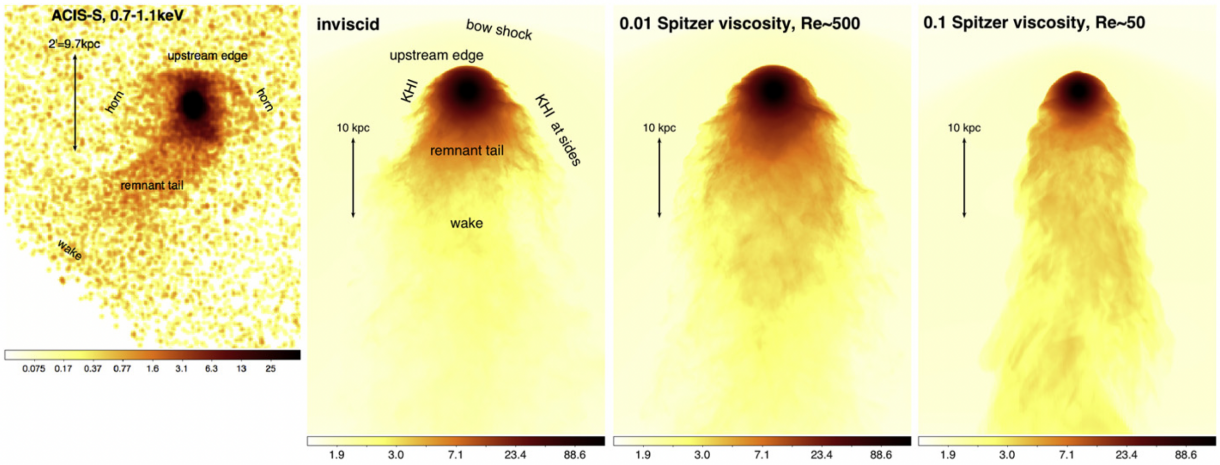

Figure 2.1: Comparison of the tail morphology in galaxy NGC 4552 with numerical simulations with different levels of viscosity. *From left to right*: Merged Chandra ACIS-S image, inviscid fluid simulation, 0.01 of Spitzer value, 0.1 of Spitzer value. Figure taken from Roediger et al. (2015).

(~10% of Spitzer's value) suppress the development of the KHI, resulting in smooth, laminar tails that are inconsistent with the observed filamentary and diffuse morphology.

Deep Chandra observations showed that the turbulent wake behind this galaxy is well-mixed, which requires a high Reynolds number flow, implying a strongly suppressed viscosity. The lack of coherent vortices or layered structure in the wake suggests that the characteristic damping scale of turbulence lies well below the observed spatial resolution (Kraft et al., 2017).

Similarly, velocity structure function (VSF) analysis, derived from MUSE integral-field spectroscopy, exhibits complex and chaotic motions, probing that the turbulent cascade extends down to scales of a few kpc, substantially smaller than expected if classical Coulomb collisions determined the plasma viscosity (Ignesti et al., 2024). This implies that energy is cascading to small scales with minimal damping, inconsistent with a high-viscosity ICM. Comparisons with synthetic VSFs from high-resolution hydrodynamical simulations, including both viscous and inviscid ICM models, demonstrate that only scenarios with effective viscosities in the range of 0.3% to 25% of the Spitzer value are compatible with the data (Ignesti et al., 2024). The best-fitting models are found around ~1–5% of Spitzer, consistent with previous findings for individual galaxies such as ESO137-001 (Li et al., 2023) and with constraints derived from the wake of NGC 4552.

Cold Fronts Stability

Cold fronts are sharp contact discontinuities characterized by density and temperature jumps, common in both merging clusters and relaxed, cool-core systems undergoing gas sloshing. These structures are prone to the growth of the KHI due to shear flows across the interface (Breuer et al., 2020). The presence, morphology, and suppression of these instabilities are sensitive to the microphysical properties of the ICM, particularly viscosity.

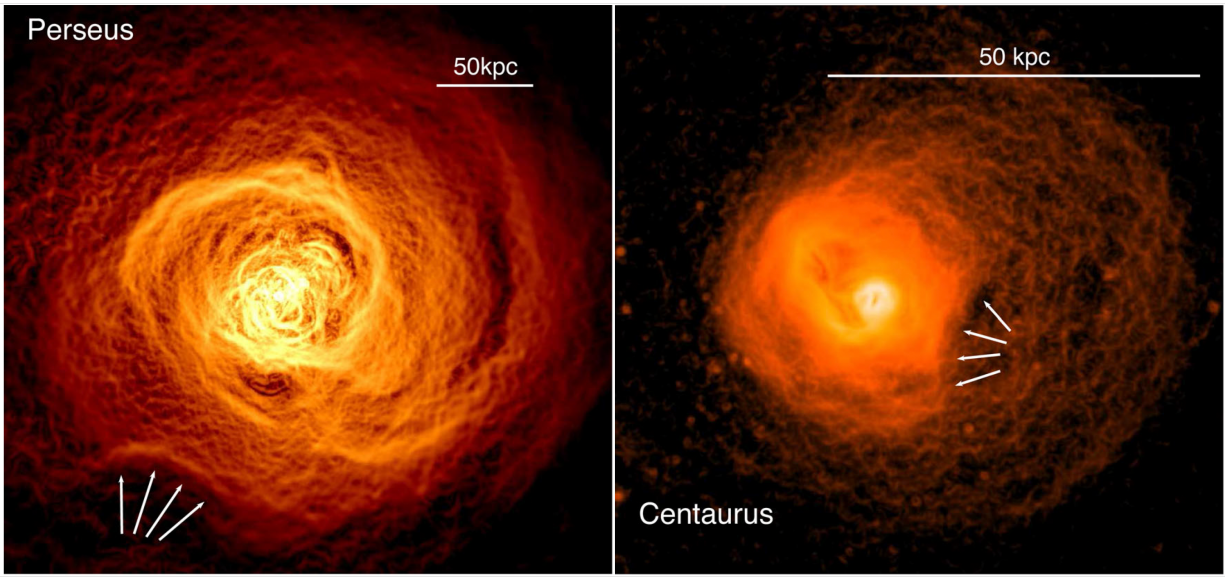

Figure 2.2: Observations of cold fronts show well-developed KHI eddies that lead to the partial disruption of the structure. *Left panel*: Chandra observation of Perseus, with a 'bay' along the cold front interface indicated by the arrows. *Right panel*: Chandra observation of Centaurus, with a 'bay' along the cold front interface. Both images were filtered with the GGM filter. Figure taken from Walker et al. (2017).

Detailed observational analysis show well-developed KHI eddies at cold front interfaces (see Chandra images of Perseus (left panel) and Centaurus (right panel) of Fig. 2.2, highlighting the 'bays' along the interface of the cold fronts due to the growth of KHI. Figure taken from Walker et al., 2017). These features offer a direct way to probe the transport properties of the ICM, since the growth of the KHI should be strongly damped by viscosity. Comparisons of these structures with numerical simulations allow constraints on viscosity (ZuHone et al., 2015). Specifically, the morphology and development of these instabilities suggest that an effective viscosity of 10% of the isotropic Spitzer viscosity is in qualitative agreement with observations. This suggests that the effective viscosity of the ICM must be reduced by at least an order of magnitude (ZuHone et al., 2015). Moreover, simulations of the Virgo cluster by Roediger et al. (2013a) agree on this level of suppression, indicating that observed cold fronts imply suppression factors around 10% of the isotropic Spitzer viscosity, pointing again toward reduced ICM viscosity.

Additional analysis has been done by Wang & Markevitch (2018) of Chandra observations of the merging galaxy cluster A2142. By comparing the wavelength and amplitude of well-developed KHI in the southern cold front of the cluster with hydrodynamic simulations, they estimated the effective viscosity to be at most 20% of the Spitzer value. This limit is consistent with other observationally inferred values and further supports a model in which the plasma viscosity is significantly reduced.

Density Fluctuations

The amount of viscosity can be constrained at large scales by analyzing the amplitude of density fluctuations and their corresponding power spectra. Zhuravleva et al. (2019) performed a detailed analysis using deep Chandra observations of the Coma cluster, computing the gas density fluctuations down to spatial scales where transport processes should manifest. To calculate the density fluctuations, they first divided the observed X-ray surface brightness image by the best-fitting β-model of the unperturbed cluster emission to isolate small-scale perturbations. They then applied the Δ-variance method to this residual image to derive the two-dimensional power spectrum of surface brightness fluctuations (see Arévalo et al., 2012 for details). This 2D spectrum was deprojected into a 3D power spectrum of gas density fluctuations, assuming isotropy and using the known emissivity distribution along the line of sight (Churazov et al., 2012; Zhuravleva et al., 2014). Finally, the 3D fluctuations amplitude as a function of the scale can be computed as

$$\left(\frac{\delta\rho}{\rho}\right)_k = \sqrt{4\pi P(k)k^3}\,, \tag{2.5}$$

where $P(k)$ is the power spectrum, and $k = 1/l$ the wavenumber.

Assuming that the gas motions are subsonic and isotropic, they used the density fluctuations as a proxy for velocity fluctuations (see §1.4.3). This way, the 3D amplitude fluctuations power spectrum derived from observations can be directly compared with Direct Numerical Simulations (DNS) results, where the simulations explicitly modeled turbulent motions and viscous dissipation. In these simulations, varying the level of viscosity modifies the slope and shape of the power spectrum. Higher viscosity increases the dissipation scale, producing a cutoff of the power spectrum at larger scales, thus steepening significantly the power spectrum at small scales. By comparing the slope of the density fluctuations power spectrum with the DNS results, they were able to constrain the amount of viscosity in Coma (Zhuravleva et al., 2019; Kunz et al., 2022).

Observational data from the Coma Cluster revealed no such steepening in the measured power spectrum, indicating that the effective isotropic viscosity in the ICM must be suppressed by at least an order of magnitude compared to predictions from purely hydrodynamic models dominated by Coulomb collisions (see Fig. 2.3 comparing the power spectrum obtained from observations of Coma, with DNS simulations with different levels of viscosity. Figure taken from Caprioli et al., 2019). Quantitatively, their results suggested that the effective viscosity is smaller by factors ranging from approximately 5 to 1000, depending on the thermal Prandtl number (the ratio of kinematic viscosity to thermal conductivity).

Similarly, Heinrich et al. (2024) used a dataset of 80 galaxy cluster observations by Chandra, where they extracted the density fluctuations and computed the power spectrum. By fitting the slopes with DNS simulations, they obtained that the effective viscosity in galaxy clusters is suppressed by at least a factor of 8 compared to the Spitzer value.

In summary, by calculating the amplitude of density fluctuations from high-resolution X-ray observations and comparing these to DNS simulations with varying viscosity levels, these studies robustly concluded that the effective viscosity in the ICM is substantially suppressed. The observed power spectra do not exhibit the exponential cutoff predicted by high-viscosity

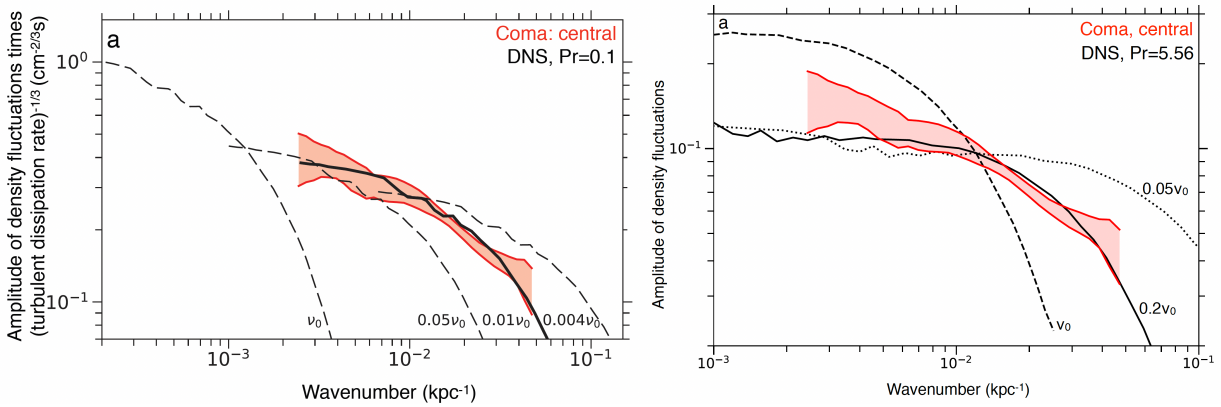

Figure 2.3: Comparison of density fluctuations power spectrum obtained from Chandra observations of Coma (red regions), with DNS simulations with different levels of viscosity (dashed lines). By fitting the slope of observations with simulations, one can constrain the amount of viscosity. *Left panel*: Prandl number of 0.1, where the value of viscosity obtained is 1% the Spitzer value. *Right panel*: Prandl number of 5.56, where the value of viscosity obtained is 20% the Spitzer value. Figure taken from Zhuravleva et al. (2019).

models, indicating a low-viscosity regime. These combined observational, numerical, and theoretical results highlight the complex and highly suppressed nature of viscosity within the ICM.

Collectively, these observational approaches strongly support a scenario where the effective viscosity of the ICM is significantly suppressed compared to the classical isotropic Spitzer model. Although the plasma is characterized by low densities and large Coulomb mean free paths, the presence of magnetic fields and plasma microinstabilities effectively reduces the mean free path of particles, thereby limiting the role of classical isotropic viscosity. Instead, transport processes in the ICM are governed by anisotropic mechanisms, for which the Braginskii viscosity model offers a more accurate theoretical framework (Schekochihin et al., 2005; Kunz, 2011).

2.5 Braginskii Viscosity

In contrast to the collisional approximation, when considering a weakly collisional plasma where the gyro-radius is smaller than the mean free path ($\lambda_i \gg r_i$, see §1.4.1), anisotropic viscosity becomes relevant. Magnetic fields impose a directional preference within a plasma, leading to an anisotropic behavior that significantly impacts the plasma's physical properties (see Fig. 2.4 for a sketch of a magnetized plasma, where the magnetic field lines result in a preferred direction of plasma). This anisotropy affects different transport properties of the plasma, like thermal conductivity and viscosity. This anisotropy due to the change of magnetic fields can be written as:

$$\frac{1}{B}\frac{\mathrm{d}B}{\mathrm{d}t} = \hat{b}\hat{b} : \nabla\mathbf{v} - \nabla\cdot\mathbf{v}\,, \tag{2.6}$$

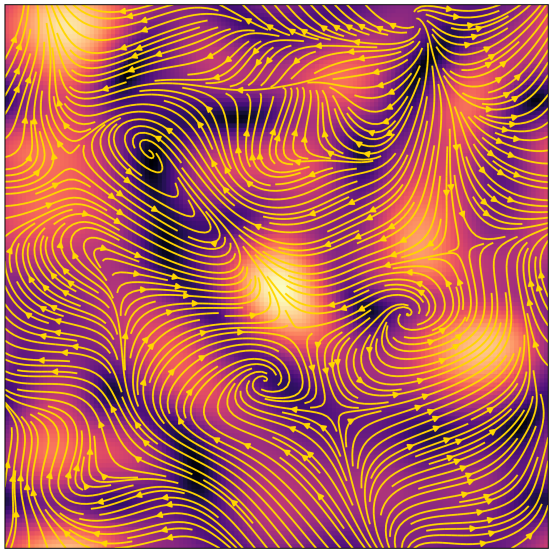

Figure 2.4: Sketch of a magnetized medium, showing how magnetic fields produce a preferred direction of the plasma, resulting in pressure anisotropies.

where $\hat{b} = \mathbf{B}/B$. The notation ":" denotes the Frobenius inner product and is defined as the sum of the products of their components: $\hat{b}\hat{b} : \nabla\mathbf{v} = \Sigma_i \Sigma_j b_i b_j \partial_i v_j$.

The constrained motion of particles in directions perpendicular to the magnetic field leads to a difference in pressure parallel ($p_\parallel$) and perpendicular ($p_\perp$) to the magnetic field, resulting in pressure anisotropy. This anisotropy can affect the stability of the plasma, leading to various instabilities such as the firehose and mirror instabilities (see §2.5.1, Kunz et al., 2014), which further influence the dynamics and evolution of the plasma. The total thermal pressure can be split into its parallel and perpendicular components:

$$P_{\rm th} = \frac{2}{3} p_\perp + \frac{1}{3} p_\parallel \,. \tag{2.7}$$

The anisotropy in pressure arises naturally due to the conservation of the first adiabatic invariant, $\mu = m_i v_\perp^2/(2B)$, where m_i is the ion mass and $v_\perp$ is the particle velocity perpendicular to the magnetic field[1]. In the regime where $\lambda_i \gg r_i$, the conservation is only weakly broken by collisions. This conservation produces that any change in $\mathbf{B}$ leads to a change in $p_\perp$ (Schekochihin et al., 2005).

The Braginskii viscosity (Braginskii, 1965; Squire et al., 2023) accounts for these anisotropies. The plasma moves according to the pressure anisotropy, leading to a viscous pressure anisotropy, where viscosity behaves as the isotropic case only when the velocity gradient is parallel to the magnetic field lines. When collisions dominate the pressure anisotropy ($|\nabla\mathbf{v}| \ll \nu_{ii}$) and $\beta \gtrsim 1$

[1]The first adiabatic invariant μ corresponds to the magnetic momentum of a gyrating particle.

(Chew et al., 1956; Squire et al., 2017), the pressure anisotropy can be written as:

$$\Delta p = p_\perp - p_\parallel = \eta \left(3\hat{b}\hat{b} : \nabla \mathbf{v} - \nabla \cdot \mathbf{v}\right) \simeq \frac{3p}{\nu_{\text{eff}}} \frac{\mathrm{d} \ln B}{\mathrm{d}t}, \tag{2.8}$$

where ν_{eff} is the effective collision frequency, which is equal to the plasma collision frequency (equation (1.24)) plus the collision rate due to scatter ($\nu_{\text{eff}} = \nu_{ii} + \nu_{\text{scatt}}$).

This expression describes the creation of pressure anisotropy due to motions of the plasma: through the parallel rate of strain ($\hat{b}\hat{b} : \nabla \mathbf{v}$) and through the compression of the fluid ($\nabla \cdot \mathbf{v}$). Positive Δp is created in regions of increasing field strength, while negative Δp in regions of decreasing field strength (Schekochihin et al., 2005; Squire et al., 2023). The shear viscosity coefficient (η) is the same as the isotropic case (equation (2.2)).

This anisotropy strongly affects viscous transport. Parallel to magnetic fields, the plasma can move freely along the magnetic field lines, and viscosity behaves similarly to the isotropic Spitzer viscosity. However, perpendicular to the magnetic field lines, the movement is restricted and viscosity becomes significantly suppressed due to the smaller gyroradius (r_i) compared to λ_i. Assuming a strongly magnetized plasma, the effective parallel and perpendicular components of the shear viscosity coefficient are given by (Braginskii, 1965):

$$\eta_\parallel \approx \eta_{\text{Iso}}, \qquad \eta_\perp \approx \eta_{\text{Iso}} \left(\frac{r_i}{\lambda_i}\right)^2. \tag{2.9}$$

Fig. 2.5 shows how, when the magnetic field is aligned with the velocity gradient (red arrow), the parallel rate of strain ($\hat{b}\hat{b} : \nabla \mathbf{v}$) becomes maximum (right panel), while if they are perpendicular, the rate of strain becomes zero.

The anisotropic viscous stress tensor accounts for the pressure anisotropy and can be written as:

$$\mathbf{\Pi}_{\text{Aniso}} = \Delta p \left(\hat{b}\hat{b} - \frac{1}{3}\mathbf{I}\right). \tag{2.10}$$

2.5.1 Plasma Microinstabilities

When $\beta \gg 1$, weakly collisional plasmas might become unstable against plasma microinstabilities, such as firehose and mirror instabilities. They arise from pressure anisotropies and are crucial for understanding plasma dynamics in a magnetized medium. These instabilities manifest when the differences between each pressure direction reach thresholds that destabilize the magnetic field structure, keeping pressure anisotropy at marginally stable levels, and significantly affecting the plasma's macroscopic behavior and transport properties (Schekochihin & Cowley, 2006; Kunz et al., 2014). The plasma microinstabilities grow, and when they reach a critical value, they feed back on the plasma (Rappaz & Schober, 2024). In the regime where the gyro-radius is much smaller than the mean free path, this feedback takes place effectively instantaneously (Squire et al., 2023).

The firehose instability occurs when the parallel pressure component significantly exceeds the perpendicular component ($\Delta p < 0$, see equation (2.8)). The magnetic field lines are stretched

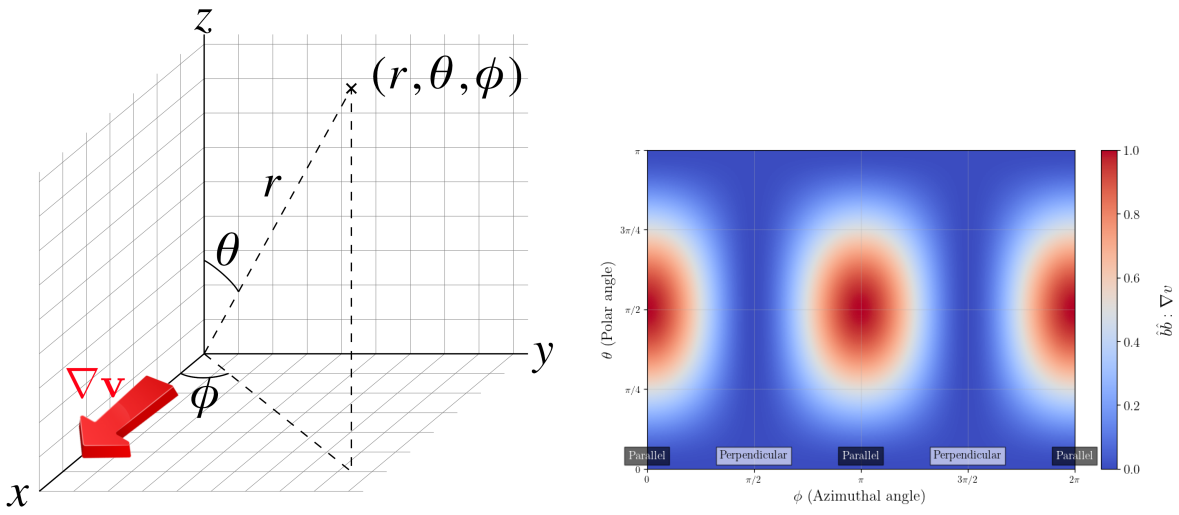

Figure 2.5: *Left panel*: Spherical coordinates showing the direction of the magnetic field and the red arrow indicating the direction of the velocity gradient. *Right panel*: Normalized value of the parallel rate of strain ($\hat{b}\hat{b} : \nabla\mathbf{v}$) depending on the direction of the magnetic field, with the velocity gradient in the x-direction. $\hat{b}\hat{b} : \nabla\mathbf{v}$ becomes one when they are parallel, and zero when they are perpendicular.

by the parallel pressure component, reducing magnetic tension and leading to the growth of Alfvénic, oblique perturbations. These perturbations scatter plasma, increasing the effective collision frequency ($\nu_{\rm eff} = \nu_{ii} + \nu_{\rm scatt}$) by $\nu_{\rm scatt} \sim (|\delta B|/B_0)\, k_\parallel v_{{\rm th},i}$, reducing the Coulomb mean free path (equation (1.23)), decreasing the system's viscosity (equation (2.2)), and maintaining the pressure anisotropy at marginally stable levels (equation (2.8)) (Kunz et al., 2014; Arzamasskiy et al., 2023):

$$p_\parallel > p_\perp \tag{2.11}$$

$$\Delta p = p_\perp - p_\parallel < -\frac{B^2}{4\pi}\,. \tag{2.12}$$

In contrast, the mirror instability arises from perpendicular pressure anisotropy being larger than the parallel component ($\Delta p > 0$, see equation (2.8)), bending the magnetic field lines and creating zones of weaker magnetic field strength (Rincon et al., 2014). This generates magnetic field structures (mirrors) that trap and scatter particles, increasing the collision frequency by $\nu_{\rm scatt} \sim (|\delta B|/B_0)\, k_\parallel v_{{\rm th},i}$,[2] reducing the system's viscosity, and keeping the pressure anisotropy near marginal stability (Kunz et al., 2014; Arzamasskiy et al., 2023):

$$p_\perp > p_\parallel \tag{2.13}$$

$$\Delta p = p_\perp - p_\parallel > \frac{B^2}{8\pi}\,. \tag{2.14}$$

[2]Note that $k_\parallel \ll k_\perp$ for mirror modes. However, the mirror instability saturates at values of $|\delta B|/B_0 \sim 0.1 - 1$, while the firehose instability at values of $|\delta B|/B_0 \sim \beta^{-1/2}$ (Rincon et al., 2014; Squire et al., 2017). Thus, $\nu_{\rm scatt} \sim (|\delta B|/B_0)\, k_\parallel v_{{\rm th},i}$ of both instabilities is comparable in magnitude.

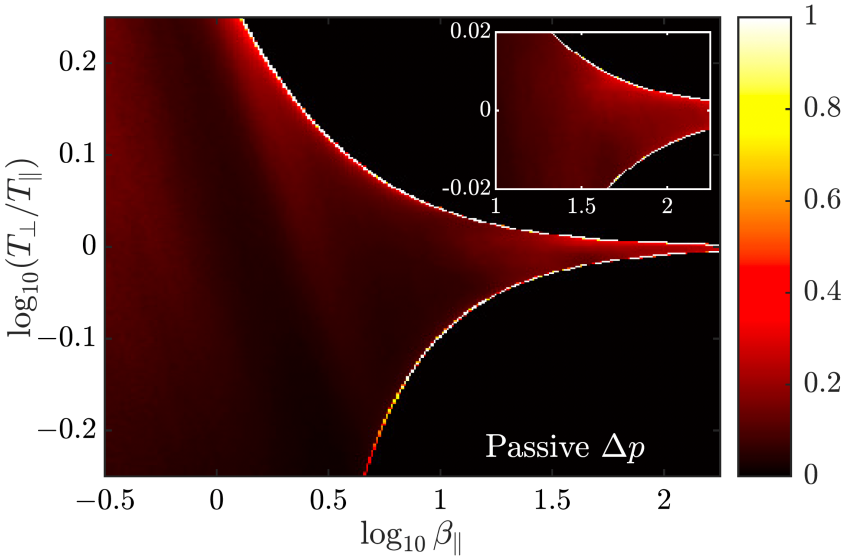

Figure 2.6: 'Brazil plot': histogram of the pressure anisotropy (expressed as $T_\perp/T_\parallel$) as a function of β, color-coded by the normalized probability. The Δp distribution is dominated by the values of the firehose and mirror instabilities. Figure taken from Squire et al. (2023).

The pressure anisotropy is stable within the firehose and mirror instability limits, therefore, we can write the stability criterion as (Kunz et al., 2012, 2014):

$$-\frac{B^2}{4\pi} < \Delta p < \frac{B^2}{8\pi}\,. \tag{2.15}$$

This means that the stability of Δp depends on the magnetic field strength. In high-β plasmas (weak magnetic fields), the thermal pressure dominates over magnetic pressure, and the magnetic field is more susceptible to distortion, thus triggering the instabilities more easily. The threshold for triggering plasma microinstabilities is reduced, limiting the pressure anisotropy and suppressing the effect of viscosity. On the other hand, in low-β plasmas (strong magnetic fields), magnetic tension stabilizes the field lines against perturbations and the plasma microinstabilities are not triggered so easily. Therefore, the plasma can sustain larger pressure anisotropies, leading to larger viscosity.

Both instabilities play a key role in the energy distribution and stability of high-beta plasmas, influencing large-scale plasma behavior. They act as self-regulating mechanisms to maintain the anisotropy within marginally stable limits, thereby fundamentally affecting the evolution and transport properties of magnetized astrophysical plasmas. This behavior can be observed in the so-called 'Brazil plots', 2D-histograms where the pressure anisotropy is plotted versus the local β (see Fig. 2.6 taken from Squire et al., 2023).

2.6 Equations of Magnetohydrodynamics

The large difference in magnitude between the gyroradius and the viscous scale allows treating the ICM as a compressible magnetized plasma, where the dynamic interactions significantly impact the evolution of magnetic fields. The magnetic field applies forces to the plasma, while plasma motions bend, fold, and stretch the magnetic field lines in return, leading to the amplification of the magnetic field itself. These complex interactions are captured by the equations of MHD, which describe the large-scale evolution of a conducting fluid coupled to electromagnetic fields. This framework is particularly well-suited for describing the behavior of the ICM, where magnetic fields, though dynamically subdominant to thermal pressure in high-β regions, still regulate plasma dynamics through both large-scale forces and the mediation of microscale instabilities.

In the Lagrangian form, the MHD equations (conservation of mass, momentum, energy, and magnetic field) can be written as:

$$\frac{\mathrm{d}\rho}{\mathrm{d}t} + \rho\nabla\cdot\mathbf{v} = 0, \tag{2.16}$$

$$\rho\frac{\mathrm{d}\mathbf{v}}{\mathrm{d}t} + \nabla P = -\rho\nabla\Phi - \nabla\cdot\mathbf{\Pi} + \frac{(\nabla\times\mathbf{B})\times\mathbf{B}}{4\pi}\,, \tag{2.17}$$

$$\frac{\mathrm{d}E}{\mathrm{d}t} + \mathbf{v}\cdot\nabla P + (E+P)\nabla\cdot\mathbf{v} - \nabla\cdot\frac{\mathbf{B}(\mathbf{v}\cdot\mathbf{B})}{4\pi} = -\rho\mathbf{v}\cdot\nabla\Phi - \nabla\cdot\mathbf{Q} - \nabla\cdot(\mathbf{\Pi}\cdot\mathbf{v})\,, \tag{2.18}$$

$$\frac{\partial\mathbf{B}}{\partial t} = \nabla\times(\mathbf{v}\times\mathbf{B})\,, \tag{2.19}$$

where

$$\frac{\mathrm{d}}{\mathrm{d}t} = \frac{\partial}{\partial t} + (\mathbf{v}\cdot\nabla) \tag{2.20}$$

is the Lagrangian derivative. ρ is the gas density, $\mathbf{v}$ the velocity of the fluid, $\mathbf{Q}$ is the heat flux, $\mathbf{\Pi}$ is the viscous stress tensor and Φ is the gravitational potential. E is the energy per unit volume (kinetic + thermal + magnetic)

$$E = \frac{\rho v^2}{2} + \rho u + \frac{B^2}{8\pi}\,. \tag{2.21}$$

The total pressure P is equal to the thermal pressure $P_{\mathrm{th}} = (\gamma-1)\rho u$ plus the magnetic pressure $P_{\mathrm{mag}} = B^2/8\pi$

$$P = P_{\mathrm{th}} + P_{\mathrm{mag}} = (\gamma-1)\rho u + \frac{B^2}{8\pi}\,, \tag{2.22}$$

with an adiabatic index of $\gamma = 5/3$ for monoatomic gases.

The ratio of thermal to magnetic pressure is given by

$$\beta = \frac{P_{\mathrm{th}}}{P_{\mathrm{mag}}} = \frac{8\pi P_{\mathrm{th}}}{B^2} = \frac{8\pi(\gamma-1)\rho u}{B^2} \tag{2.23}$$

and gives an estimate of the magnetic field strength in a magnetized fluid. In many astrophysical systems, such as the ICM, the medium is weakly magnetized ($\beta \gg 1$).

2.6.1 Thermal Conduction

The second term of the RHS of equation (2.18) describes the thermal conduction, the transport of heat through the scattering of electrons. In the isotropic approximation, the heat flux is given by:

$$\mathbf{Q}_{\rm Iso} = -\kappa \nabla T \,, \tag{2.24}$$

where κ is the thermal conductivity and ∇T the temperature gradient. In plasma physics, the value of κ is defined as (Spitzer, 1962):

$$\kappa = 20 \left(\frac{2}{\pi}\right)^{3/2} \frac{(k_B T_e)^{5/2}}{(Z\,e)^4\, m_e^{1/2} \ln \Lambda} \,, \tag{2.25}$$

where m_e is the electron mass. Unlike viscosity, where the momentum transfer is dominated by protons, the heat transfer is dominated by electrons. When the temperature gradient and the mean free path of the electrons are of the same order of magnitude, the energy transfer due to conduction is limited by the low number of interactions within the plasma (Cowie & McKee, 1977). In this case, the value of thermal conductivity saturates as (Sarazin, 1986):

$$\kappa_{\rm Sat} = \frac{\kappa}{1 + 4.2 \frac{\lambda_e}{l_T}} \,, \tag{2.26}$$

where $l_T = T/\nabla T$ is the length scale associated with the temperature gradient, and λ_e is the mean free path of electrons, which is the same as the ion's mean free path (equation (1.23)) (Sarazin, 1986).

In the same way as viscosity, when considering a weakly collisional plasma, the motions across the magnetic field lines are suppressed, leading to an anisotropic heat flux dependent on the magnetic field direction:

$$\mathbf{Q}_{\rm Aniso} = -\kappa_{\parallel} \left(\hat{b} \cdot \nabla T\right) \hat{b} - \kappa_{\perp} \left[\nabla T - \left(\hat{b} \cdot \nabla T\right) \hat{b}\right] \,. \tag{2.27}$$

Conduction sets the Field length ($\delta_{\rm L}$, Field, 1965), the maximum scale over which conductive energy transport is effective in the presence of radiative cooling (see §1.4.5 Begelman & McKee, 1990).

3 | Numerical Methods

Numerical simulations represent an essential tool for studying the formation and evolution of astrophysical systems, such as galaxy clusters, allowing detailed investigation of processes including gravitational collapse, turbulence, cooling, or transport processes. Simulations help in interpreting observational data, testing theoretical predictions, and guiding future observational strategies.

Different numerical methods have been introduced to perform astrophysical hydrodynamical simulations, which can be mainly divided into two types: Eulerian mesh-based methods (e.g. Evans & Hawley, 1988; Stone & Norman, 1992), with and without Adaptive Mesh Refinement (AMR) (Berger & Colella, 1989) and Lagrangian Smoothed Particle Hydrodynamics (SPH) (Lucy, 1977; Gingold & Monaghan, 1977). In grid-based codes (e.g. Zeus, Stone & Norman, 1992; Ramses, Teyssier, 2002; Athena, Stone et al., 2008; Enzo Bryan et al., 2014; or Athena++ Stone et al., 2020), the volume of the whole domain is discretised into cells, and a Riemann problem is solved between the two states that meet at each plane separating adjacent zones (Springel, 2014). Conversely, in SPH codes (e.g. Gasoline, Wadsley et al., 2004; Gadget, Springel, 2005; OpenGadget3, Beck et al., 2016; or Phantom, Price et al., 2018), the fluid is discretised in comoving mass elements, leading to Galilean-invariance and exact momentum, energy, angular momentum, and entropy conservation. Due to the conservation of entropy, no energy dissipation occurs, which might be an advantage over grid codes. However, this becomes a problem in treating discontinuities and mixing processes properly as a consequence of spurious surface tension at the interface between the two fluids (Agertz et al., 2007).

An alternative to overcome the shortcomings of pure Eulerian or pure Lagrangian approaches is offered by methods combining their advantages. Such hybrid methods include moving mesh techniques, where the computational mesh is allowed to deform and move with the fluid, adapting dynamically to fluid flows, thereby retaining high accuracy and resolving structures more efficiently (e.g. Springel, 2010). Another class of hybrid methods comprises the Meshless Finite Volume (MFV) and Meshless Finite Mass (MFM) approaches (Hopkins, 2015; Groth et al., 2023). MFV discretizes fluid properties into volumes surrounding each particle but solves the hydrodynamic equations similarly to traditional finite-volume schemes. This preserves excellent shock-capturing capabilities and reduces numerical diffusion. In contrast, MFM, similarly to SPH, uses mass-defined particles without explicitly requiring a fixed volume partitioning, combining the benefits of particle-based methods, such as intrinsic Galilean invariance and conservation properties, with improved treatment of discontinuities and reduced artificial surface tension. These hybrid methods can effectively capture the strengths of both Eulerian and Lagrangian

schemes.

Within Lagrangian codes, OpenGadget3 is particularly optimized for large-scale cosmological simulations due to its efficient parallel performance and adaptive resolution. In contrast, Athena is a grid-based, Eulerian code designed to solve the equations of MHD using higher-order Godunov schemes. While it lacks self-gravity and cosmological capabilities, its accuracy and robustness make it ideal for high-resolution simulations of fluid dynamics.

3.1 OpenGadget3[1]

OpenGadget3 is a simulation code optimized for cosmological N-body and hydrodynamic simulations. It is an improved version of Gadget2 (Springel, 2005), including a modern SPH implementation (Beck et al., 2016). OpenGadget3 employs a TreePM algorithm to compute the gravitational forces across vast dynamic ranges typical in astrophysical phenomena. For solving the equations of hydrodynamics, OpenGadget3 uses an improved implementation of SPH, including a Wendland kernel function, as well as the implementation of artificial conductivity (AC) and artificial viscosity (AV). These improvements allow an accurate modeling of shocks and subsonic turbulence, as well as proper treatment of mixing and the development of hydro-instabilities. We will discuss the individual methods in detail in the following sections.

3.1.1 Gravity Solver - TreePM

Gravity is the fundamental force driving structure formation in the Universe on large scales. To accurately simulate the gravitational interactions in cosmological volumes, numerical methods must efficiently handle the vast range of scales and particle numbers involved. To solve this issue, OpenGadget3 uses a TreePM (Tree Particle Mesh) algorithm (Xu, 1995; Bode et al., 2000), described in detail in Springel (2005).

The TreePM method is a hybrid scheme designed to combine the advantages of both tree and particle-mesh (PM) approaches. PM methods are highly efficient at computing gravitational interactions on large scales using Fast Fourier Transforms (FFTs) but lack sufficient resolution for small-scale dynamics. On the other hand, tree algorithms offer high spatial adaptivity and accuracy at short distances but become computationally expensive on large scales (Springel, 2014).

In the TreePM method, the gravitational potential is explicitly split into two components: a long-range part, which is computed with a PM method; and a short-range part, calculated with a tree algorithm. This decomposition is conducted in Fourier space as

$$\Phi_k = \Phi_k^{\text{long}} + \Phi_k^{\text{short}}\,, \tag{3.1}$$

where the long-range potential is defined by

$$\Phi_k^{\text{long}} = \Phi_k \, \exp(-k^2 r_s^2)\,. \tag{3.2}$$

[1]Parts of this section were published in MNRAS by Marin-Gilabert et al. (2022) and in ApJ by Marin-Gilabert et al. (2024).

Here, r_s is the spatial scale parameter that separates the long and short-range components of the force (Springel, 2005).

Long-Range forces - PM algorithm

The long-range component of the gravitational potential (Φ_k^{long}) is computed using a PM algorithm. First, a mass density field is built by assigning the particle masses to a grid using the Cloud-In-Cell (CIC) interpolation method (Hockney & Eastwood, 1981). This mass density field, defined on a regular mesh, is then transformed into Fourier space, where the Poisson equation is solved:

$$-k^2\Phi_k = 4\pi G\rho_k \,, \tag{3.3}$$

with corrections for small-scale truncation and periodic boundary conditions. Then, the gravitational potential in real space is obtained via an inverse Fourier transform.

Forces are derived by finite differencing the potential using the four-point differencing rule. This leads to an accuracy of order $O(\Delta x^4)$, where Δx is the mesh spacing (Springel, 2005). Finally, these forces are interpolated back to particle positions using the CIC scheme, ensuring consistency in mass and force assignment.

Short-Range Forces - Tree algorithm

The short-range gravitational potential (Φ_k^{short}) is calculated in real space using a hierarchical multipole expansion, known as the tree algorithm (Barnes & Hut, 1986). Particles are grouped into hierarchical structures (nodes) based on their spatial locations. For each particle, the gravitational influence of distant nodes is approximated by their multipole expansions (OpenGadget3 uses monopole contributions only), while nearby nodes are individually considered. This approach reduces the computational complexity dramatically from $O(N^2)$ for direct summation to approximately $O(N \log N)$ (Springel, 2014).

In the TreePM approach, the short-range gravitational potential ($r_s \ll L$) for a particle located at position $\mathbf{x}$ is given by:

$$\Phi^{\text{short}}(\mathbf{x}) = -G \sum_i \frac{m_i}{r_i} \operatorname{erfc}\left(\frac{r_i}{2r_s}\right) , \tag{3.4}$$

where r_i is the distance from particle i to the target particle at position $\mathbf{x}$, and erfc is the complementary error function. This function ensures a rapid decrease of the short-range forces beyond a certain scale ($\sim 4.5r_s$ for a drop to about 1% in force), effectively restricting the computational domain of the tree algorithm to only local neighborhoods (Springel, 2005).

The accuracy of the tree algorithm critically depends on the opening criterion (Barnes & Hut, 1986), which determines whether a node's multipole expansion is sufficiently precise for approximating the gravitational influence on a given particle, or if the node needs to be further subdivided (Springel et al., 2001). The opening criterion is commonly defined as:

$$\frac{GM}{r^2}\left(\frac{l}{r}\right)^2 \leq \alpha|a| \,, \tag{3.5}$$

where M is the node mass, l is the node size, r is the distance to the particle, $|a|$ is the magnitude of the total acceleration at the last time-step, and the tolerance parameter $\alpha = 0.005$ controls the error magnitude. Additionally, a spatial criterion is employed to prevent errors when particles are close to or within nodes:

$$|\mathbf{r} - \mathbf{c}| \leq 0.6l, \tag{3.6}$$

where $\mathbf{c}$ is the geometric center of the node (Springel, 2005). A node that meets this condition is not subdivided further and contributes as a single multipole expansion. The choice of the opening criterion is vital because it directly influences both the computational speed and the accuracy of the gravitational forces calculated. If the criterion is too relaxed, force errors can grow significantly, compromising the physical reliability of the simulation. Conversely, overly conservative criteria drastically increases computational costs (Springel, 2005).

Advantages of the TreePM Method

The TreePM method decreases the computational costs of gravitational force interaction while keeping a high spatial force accuracy. It effectively mitigates the anisotropies inherent in pure PM schemes by introducing an exponential truncation at small scales, thus delivering isotropic and highly accurate long-range forces. Additionally, it resolves efficiently short-range interactions with arbitrary precision controlled by the opening criterion (Springel, 2014). This combination makes this algorithm perfect for large cosmological simulations, where a high gravitational force accuracy is needed across all scales of cosmological interest.

3.1.2 Hydrodynamics Solver - SPH

OpenGadget3 is a Lagrangian - SPH code. This means that, instead of discretizing the volume of the domain like AMR codes, or moving mesh codes, the fluid is discretized in comoving mass elements, leading to Galilean-invariance and exact momentum, energy, angular momentum, and entropy conservation.

SPH works by interpolating physical quantities among the closer neighbor particles (N_{ngb}) using a Gaussian-like smoothing kernel with compact support, which means that the kernel is truncated at a finite radius to reduce the total number of computations. This kernel assigns more weight to nearby particles and less to those further away, enabling a smooth interpolation that avoids the issues of fixed-grid approaches. Using this kernel, the density is computed as

$$\rho_i = \sum_{j=1}^{N_{\mathrm{ngb}}} m_j W(|r_i - r_j|, h_i)\,, \tag{3.7}$$

where m_j is the particle's mass. The kernel W depends on the distance between particles and the smoothing length h_i, which scales with local density as

$$h = \eta \left(\frac{m}{\rho}\right)^{1/d}, \tag{3.8}$$

where η specifies the smoothing length in units of the average particle spacing and d is the spatial dimension of the system. The dependence of h on ρ ensures a roughly constant number of neighbors.

The kernel must satisfy the normalization condition

$$\int W(|r_i - r_j|, h_i)\, \mathrm{d}V = 1\,, \tag{3.9}$$

and it must be symmetric with respect to $(r_i - r_j)$, positive, monotonically decreasing, and have smooth derivatives (Price, 2012). Furthermore, it should flatten near the center to avoid overweighting close neighbors. Wendland functions fulfill all these requirements (Wendland, 1995; Dehnen & Aly, 2012). In particular, we employ the Wendland C^6 kernel in 3D (Price et al., 2018), defined as

$$W_{ij}(r, h) = \frac{C_{\mathrm{norm}}}{h^3} f(q)\,, \tag{3.10}$$

with normalization constant $C_{\mathrm{norm}} = 1365/512\pi$, and

$$f(q) = \begin{cases} (1 - \frac{q}{2})^8 (4q^3 + \frac{25q^2}{4} + 4q + 1), & q < 2; \\ 0, & q \geq 2\,, \end{cases} \tag{3.11}$$

with $q = |r_i - r_j|/h$.

The Wendland functions preserve the smooth, positive, and compact characteristics of a Gaussian-like kernel with a compact support of $R = 2h$, but with the crucial advantage of having a non-negative Fourier transform, making them stable even for high N_{ngb}.

In cases of an irregular particle distribution, the so-called 'E_0 error' (e.g. Read et al., 2010; Hu et al., 2014) may arise, caused by particles not being perfectly arranged according to an ordered pattern. This error is the attempt of SPH to restore the particle order, and it can produce spurious results in fluid mixing (e.g. Hopkins, 2013; Beck et al., 2016; Wadsley et al., 2017). The 'E_0 error' can be reduced by increasing N_{ngb}. However, a high N_{ngb} leads to the 'pairing instability' (e.g. Schuessler & Schmitt, 1981; Price, 2012). The 'pairing instability' arises from kernels whose Fourier transform is not non-negative and becomes dominant for large numbers of neighbors. It causes particles to attract each other at very small separations, forming artificial "pairs" that collapse to the same location, thus degrading the accuracy of the simulation. Therefore, the higher N_{ngb} allowed by the Wendland kernels provides a big advantage against other Gaussian-like kernels.

The derivatives can be expressed as derivatives of the kernel. In the case of ρ, the derivative with respect to time can be written as

$$\frac{\mathrm{d}\rho}{\mathrm{d}t} = \frac{1}{\Omega_i} \sum_{j=1}^{N_{\mathrm{ngb}}} m_j\, (\vec{v}_i - \vec{v}_j)\, \nabla W_{ij}(r, h_i)\,, \tag{3.12}$$

where $\vec{v}_{i,j}$ is the velocity of each particle. Ω_i is a term that depends on the derivative of the kernel with respect to the smoothing length, which reads as

$$\Omega_i = \left[1 - \frac{\partial h_i}{\partial \rho_i} \sum_{j=1}^{N_{\mathrm{ngb}}} m_j \frac{\partial W_{ij}(r, h_i)}{\partial h_i} \right]. \tag{3.13}$$

The density gradient is given by

$$\nabla\rho = \frac{\partial\rho_i}{\partial r_k} = \frac{1}{\Omega_i}\sum_{j=1}^{N_{\rm ngb}} m_j\,\nabla_k W_{ij}(r,h_i)(\delta_{ik}-\delta_{jk})\,. \tag{3.14}$$

The dynamics of the system are derived from the discretization of the fluid Lagrangian and result in motion equations that naturally conserve mass, momentum, and energy. The acceleration of a particle is given by

$$\frac{\mathrm{d}\vec{v}_i}{\mathrm{d}t} = -\sum_{j=1}^{N_{\rm ngb}} m_j\left[\frac{P_i}{\Omega_i\rho_i^2}\nabla_i W_{ij}(r,h_i)+\frac{P_j}{\Omega_j\rho_j^2}\nabla_i W_{ij}(r,h_j)\right], \tag{3.15}$$

and the internal energy evolves as

$$\frac{\mathrm{d}u_i}{\mathrm{d}t} = \frac{P_i}{\Omega_i\rho_i^2}\sum_{j=1}^{N_{\rm ngb}} m_j\,(\vec{v}_i-\vec{v}_j)\,\nabla W_{ij}(r,h_i)\,, \tag{3.16}$$

where $P_{i,j}$ is the pressure of each particle.

Optionally, one can evolve the entropic function $A = P/\rho^\gamma$ (this is the choice in OpenGadget3), where γ is the adiabatic index. The entropic function A is constant in the absence of dissipation:

$$u = \frac{\rho^{\gamma-1}}{\gamma-1}A\,. \tag{3.17}$$

Evolving A is advantageous because it decouples the evolution from numerical integration schemes in non-dissipative flows (Price, 2012).

However, SPH in its ideal form cannot properly capture discontinuities such as shocks and contact interfaces. To mitigate this, artificial diffusion is introduced. AV is used to resolve shock fronts and prevent post-shock oscillations and noise, by introducing momentum dissipation; while AC introduces thermal energy diffusion across contact discontinuities, addressing issues with energy discontinuities at interfaces.

3.1.3 Artificial Conductivity

The AC (Price, 2008) is introduced in OpenGadget3 to treat discontinuities in the internal energy and capture mixing processes properly (we follow the notation introduced by Beck et al., 2016). The AC implemented is time and space dependent, where the variation of internal energy due to AC reads:

$$\left.\frac{\mathrm{d}u_i}{\mathrm{d}t}\right|_{\rm cond} = \sum_{j=1}^{N_{\rm ngb}}\frac{m_j}{\rho_{ij}}(u_j-u_i)\,\alpha_{ij}^c v_{ij}^{{\rm sig},c}\overline{F}_{ij}\,. \tag{3.18}$$

Here, $v_{ij}^{{\rm sig},c}$ is the signal velocity, $\overline{F}_{ij} = (F_{ij}(h_i)+F_{ij}(h_j))/2$ is the symmetrised scalar part of the kernel gradient terms $\nabla_i W_{ij}(h_i) = F_{ij}\,\hat{r}_{ij}$, $\rho_{ij} = (\rho_i+\rho_j)/2$ is the symmetrised density and

$\alpha^c_{ij} = (\alpha^c_i + \alpha^c_j)/2$ is the symmetrised conduction coefficient. The signal velocity depends on the pressure gradient (see Price, 2008):

$$v^{\mathrm{sig},c}_{ij} = \sqrt{\frac{|P_i - P_j|}{\rho_{ij}}} \,. \tag{3.19}$$

The AC coefficient is defined as

$$\alpha^c_i = \frac{h_i}{2} \frac{|\nabla u|_i}{|u_i|} \,, \tag{3.20}$$

where the time dependence stems from the dependence on the internal energy and on its gradient, which is computed using

$$(\nabla u)_i = \frac{1}{\rho_i} \sum_{j=1}^{N_{\mathrm{ngb}}} m_j \, (u_j - u_i) \nabla_i W_{ij} \,. \tag{3.21}$$

When α^c_i is larger than a threshold value (in our case $\alpha_{\max} = 1.0$), we set $\alpha^c_i = \alpha_{\max}$.

3.1.4 Artificial Viscosity

OpenGadget3 includes AV to damp post-shock oscillations and reduce kernel distribution noise. Since in ideal fluids AV is not needed away from shocks, a switch triggers viscosity in shocks but keeps it inactive otherwise. Our implementation of an adaptive AV reads (Monaghan & Gingold, 1983; Monaghan, 1992):

$$\left.\frac{\mathrm{d}\mathbf{v_i}}{\mathrm{d}t}\right|_{\mathrm{visc}} = \frac{1}{2} \sum_{j=1}^{N_{\mathrm{ngb}}} \frac{m_j}{\rho_{ij}} \, (\mathbf{v_j} - \mathbf{v_i}) \, \alpha^v_{ij} \, f^{\mathrm{shear}}_{ij} \, v^{\mathrm{sig,v}}_{ij} \overline{F}_{ij} \,. \tag{3.22}$$

An additional term accounting for the variation of internal energy due to AV offsets the work done against the viscous force in the thermal reservoir. It reads:

$$\left.\frac{\mathrm{d}u_i}{\mathrm{d}t}\right|_{\mathrm{visc}} = -\frac{1}{2} \sum_{j=1}^{N_{\mathrm{ngb}}} \frac{m_j}{\rho_{ij}} \, (\mathbf{v_j} - \mathbf{v_i})^2 \, \alpha^v_{ij} \, f^{\mathrm{shear}}_{ij} \, v^{\mathrm{sig,v}}_{ij} \overline{F}_{ij} \,. \tag{3.23}$$

Here, $\alpha^v_{ij} = (\alpha^v_i + \alpha^v_j)/2$ is the symmetrised viscosity coefficient, $f^{\mathrm{shear}}_{ij} = (f^{\mathrm{shear}}_i + f^{\mathrm{shear}}_j)/2$ the symmetrised shear flow limiter and $v^{\mathrm{sig,v}}_{ij}$ the pairwise signal velocity.

The signal velocity[2] (Monaghan, 1997) aids in switching on or off the AV, depending on whether two particles are approaching ($\mathbf{v_{ij}} \cdot \hat{r}_{ij} \leq 0$) or moving away ($\mathbf{v_{ij}} \cdot \hat{r}_{ij} > 0$), respectively. It also determines the strength of the AV and measures the particle disorder:

$$v^{\mathrm{sig,v}}_{ij} = \begin{cases} c_{\mathrm{s},i} + c_{\mathrm{s},j} - \beta \, \mathbf{v_{ij}} \cdot \hat{r}_{ij} \,, & \mathbf{v_{ij}} \cdot \hat{r}_{ij} \leq 0; \\ 0 \,, & \mathbf{v_{ij}} \cdot \hat{r}_{ij} > 0 \,, \end{cases} \tag{3.24}$$

[2]Note that this signal velocity is not the same as for the AC ((3.19)).

where c_s is the sound speed of the particle and $\beta = 3$ (see Beck et al., 2016).

To avoid a shear viscosity that could lead to sub-optimum behavior in simulations of shear flows, Balsara (1995) suggested the shear flow limiter:

$$f_i^{\rm shear} = \frac{|\nabla \cdot \mathbf{v}|_i}{|\nabla \cdot \mathbf{v}|_i + |\nabla \times \mathbf{v}|_i + \sigma_i}\,, \tag{3.25}$$

with $\sigma_i = 0.0001 c_{s,i}/h_i$ for numerical stability reasons. When there is a shock, the limiter is dominated by $|\nabla \cdot \mathbf{v}|_i$ and thus, $f_i^{\rm shear} \simeq 1$, while if there is a shearing flow, the limiter is dominated by $|\nabla \times \mathbf{v}|_i$ and $f_i^{\rm shear} \simeq 0$.

The viscosity coefficient α_i^v is computed following Cullen & Dehnen (2010), which use the shock indicator

$$R_i = \frac{1}{\rho_i} \sum_{j=1}^{N_{\rm ngb}} {\rm sign}(\nabla \cdot \mathbf{v})_j m_j W_{ij}\,, \tag{3.26}$$

where ${\rm sign}(\nabla \cdot \mathbf{v})_j$ is negative and, therefore, $R_i \simeq -1$ when there is a shock. Nevertheless, R_i cannot distinguish between pre- and post-shock regions. To determine the direction of the shock, an additional factor, A_i, exploits the time derivative of the velocity divergence:

$$A_i = \xi_i \max(0, -(\dot{\nabla} \cdot \mathbf{v})_i)\,, \tag{3.27}$$

where $(\dot{\nabla} \cdot \mathbf{v})_i < 0$ indicates a pre-shock region and $(\dot{\nabla} \cdot \mathbf{v})_i > 0$ a post-shock region. ξ_i indicates the ratio of the strength of the shock and reads:

$$\xi_i = \frac{\left|2(1-R_i)^4 (\nabla \cdot \mathbf{v})_i\right|^2}{\left|2(1-R_i)^4 (\nabla \cdot \mathbf{v})_i\right|^2 + |\nabla \times \mathbf{v}|_i^2}\,. \tag{3.28}$$

The target value $\alpha_i^{{\rm loc},v}$ of AV is therefore:

$$\alpha_i^{{\rm loc},v} = \alpha_{\rm max} \frac{h_i^2 A_i}{h_i^2 A_i + (v_i^{\rm sig})^2}\,. \tag{3.29}$$

When $\alpha_i^{{\rm loc},v} < \alpha_i^v$, the latter is set to $\alpha_i^{{\rm loc},v}$. If $\alpha_i^{{\rm loc},v} > \alpha_i^v$, α_i^v decays with time, and the value is calculated by integrating:

$$\dot{\alpha_i^v} = \left(\alpha_i^{{\rm loc},v} - \alpha_i^v\right) \frac{v_i^{\rm sig}}{l h_i}\,, \tag{3.30}$$

where we set $l = 4.0$ (Beck et al., 2016), which specifies the decay length of the AV. We set an initial value $\alpha_i^v = 0.02$ in all our simulations.

3.1.5 Magnetohydrodynamics Solver - SPMHD

The evolution of magnetic fields is governed by the MHD equations, which can be solved in OpenGadget3 (see Dolag & Stasyszyn, 2009; Bonafede et al., 2011; Stasyszyn et al., 2013 for

a detailed description). In ideal MHD, the magnetic field evolves according to the induction equation (Dolag & Stasyszyn, 2009):

$$\frac{\mathrm{d}\mathbf{B}}{\mathrm{d}t} = (\mathbf{B}\cdot\nabla)\,\mathbf{v} - \mathbf{B}\,(\nabla\cdot\mathbf{v})\ , \tag{3.31}$$

assuming a perfectly conducting plasma without dissipative terms. The discretization implemented in OpenGadget3 reads

$$\frac{\mathrm{d}\mathbf{B}_i}{\mathrm{d}t} = \frac{1}{Ha^2}\frac{f_i^{\mathrm{co}}}{\rho_i}\sum_{j=1}^{N_{\mathrm{ngb}}} m_j\left[\mathbf{B}_i(\mathbf{v}_{ij}\cdot\nabla_i W_i) - \mathbf{v}_{ij}(\mathbf{B}_i\cdot\nabla_i W_i)\right] - 2\,\mathbf{B}_i\,, \tag{3.32}$$

where H is the Hubble parameter, a is the scale factor and

$$f_i^{\mathrm{co}} = \left(1 + \frac{h_i}{3\rho_i}\frac{\partial\rho_i}{\partial h_i}\right)^{-1}\ , \tag{3.33}$$

accounts for correction terms arising from varying the smoothing length. The Lorenz factor is included via the magnetic stress tensor (Phillips & Monaghan, 1985)

$$M_i^{kl} = B_i^k B_i^l - \frac{1}{2}|B_i|^2\delta^{kl}\,, \tag{3.34}$$

producing an acceleration

$$\left(\frac{\mathrm{d}\mathbf{v}_i}{\mathrm{d}t}\right)^{(\mathrm{mag})} = \frac{a^{3\gamma}}{\mu_0}\sum_{j=1}^{N_{\mathrm{ngb}}} m_j\left(f_i^{\mathrm{co}}\frac{M_i}{\rho_i^2}\nabla_i W_i + f_j^{\mathrm{co}}\frac{M_j}{\rho_j^2}\nabla_j W_j\right)\,, \tag{3.35}$$

with μ_0 the vacuum permeability.

The magnetic divergence must be generally zero, therefore, for a correct integration, numerical schemes keep the magnetic divergence $\nabla\cdot\mathbf{B}$ to a minimum. For this reason, a divergence cleaning is implemented in OpenGadget3, following Dedner et al. (2002). An additional term dependent on a scalar potential (ψ) is added to the induction equation (Stasyszyn et al., 2013). This scalar potential represents the non-vanishing $\nabla\cdot\mathbf{B}$, and propagates the numerical errors outwards the simulation, while damping them. This term is implemented in OpenGadget3 as

$$\left.\frac{\mathrm{d}\mathbf{B}}{\mathrm{d}t}\right|_i^{\mathrm{Ded}} = -(\nabla\psi)_i\,. \tag{3.36}$$

Although, to be energy conserving, the internal energy needs to be modified as

$$\mu_0\left.\frac{\mathrm{d}u}{\mathrm{d}t}\right|_i^{\mathrm{Ded}} = -\mathbf{B}_i\cdot(\nabla\psi)_i\,. \tag{3.37}$$

The most efficient solution to construct and evolve ψ is to use a hyperbolic/parabolic cleaning, where the evolution of ψ is given by

$$\frac{\mathrm{d}\psi_i}{\mathrm{d}t} = -\left[(c_{\mathrm{h}})_i^2(\nabla\cdot\mathbf{B})_i - \frac{\psi_i}{\tau_i}\right]\,. \tag{3.38}$$

Now ψ satisfies a wave equation propagating the errors outwards the source at a speed c_h, and decaying on a time-scale τ (Stasyszyn et al., 2013).

In non-ideal MHD, the induction equation (3.31) includes the magnetic diffusivity term $\eta_m \nabla^2 \mathbf{B}$, which modifies the magnetic field evolution by including an extra term (Bonafede et al., 2011)

$$\left.\frac{\partial \mathbf{B}_i}{\partial t}\right|_{\mathrm{res}} = \frac{\eta_m \rho_i}{Ha^2} \sum_{j=1}^{N_{\mathrm{ngb}}} \frac{m_j}{\rho_{i,j}^2} \left(\mathbf{B}_i - \mathbf{B}_j\right) \frac{\mathbf{r}_{i,j}}{|\mathbf{r}_{i,j}|} \cdot \nabla_i W_i \,, \tag{3.39}$$

with the corresponding energy evolution term

$$\left.\frac{du_i}{dt}\right|_{\mathrm{res}} = -\frac{1}{2\mu_0} \sum_{j=1}^{N_{\mathrm{ngb}}} \frac{m_j}{\rho_{i,j}^2} \left(\mathbf{B}_i - \mathbf{B}_j\right)^2 \frac{r_{i,j}}{|r_{i,j}|} \cdot \nabla_i \overline{W}_{i,j} \,, \tag{3.40}$$

with $\overline{W}_{i,j}$ being the mean between the two kernels W_i and W_j. However, in our simulations, we will solve ideal MHD only.

3.1.6 Spitzer Viscosity Implementation

While AV is necessary for the correct behavior of SPH in treating shocks with ideal fluids, the physical viscosity rules viscous fluids according to the Navier-Stokes equation.

The isotropic physical viscosity implemented in OpenGadget3 follows Sijacki & Springel (2006). Taking into account the summation notation for repeated Greek indices, the viscous stress tensor (equation (2.1)) is discretised as:

$$\Pi_{\mathrm{Iso},\,\alpha\beta}\Big|_i = \eta\, \sigma_{\alpha\beta}\Big|_i = \eta \left(\left.\frac{\partial v_\alpha}{\partial x_\beta}\right|_i + \left.\frac{\partial v_\beta}{\partial x_\alpha}\right|_i - \frac{2}{3}\delta_{\alpha\beta} \left.\frac{\partial v_\gamma}{\partial x_\gamma}\right|_i \right) . \tag{3.41}$$

This stress tensor enters the hydrodynamic equations by modifying the momentum evolution. Specifically, the acceleration of a particle i due to shear viscosity is given by:

$$\left.\frac{\mathrm{d}v_\alpha}{\mathrm{d}t}\right|_{i,\,\mathrm{shear}} = \sum_{j=1}^{N_{\mathrm{ngb}}} m_j \left[\frac{\boldsymbol{\Pi}_{\mathrm{Iso},\,\alpha\beta}\big|_i}{\rho_i^2} \left(\nabla_i W_{ij}(r, h_i)\right)\Big|_\beta + \frac{\boldsymbol{\Pi}_{\mathrm{Iso},\,\alpha\beta}\big|_j}{\rho_j^2} \left(\nabla_i W_{ij}(r, h_j)\right)\Big|_\beta \right] . \tag{3.42}$$

In addition to affecting momentum, the friction due to viscosity causes an increase in the entropy, which is computed using the entropic function A_i (see Sijacki & Springel (2006) for details) as:

$$\left.\frac{\mathrm{d}A_i}{\mathrm{d}t}\right|_{\mathrm{shear}} = \frac{1}{2} \frac{\gamma - 1}{\rho_i^{\gamma-1}} \frac{\eta_i}{\rho_i} \boldsymbol{\sigma}_i^2 \,. \tag{3.43}$$

Finally, the additional variation to the internal energy reads:

$$\left.\frac{\mathrm{d}u_i}{\mathrm{d}t}\right|_{\mathrm{shear}} = \frac{1}{2} \frac{\eta_i}{\rho_i} \boldsymbol{\sigma}_i^2 \,. \tag{3.44}$$

3.1.7 Viscosity Saturation

A proper treatment of viscosity in cosmological simulations requires the implementation of a viscosity saturation to avoid unphysical results. The viscous stress saturates when the scale over which the velocity varies becomes smaller than the ion mean free path. This means that the viscous momentum transfer propagates faster than the mean soundspeed of the medium, overestimating this momentum transfer (Sarazin, 1986).

To avoid this, we need to introduce a viscosity saturation that limits the momentum propagation and ensures a smooth transition from the non-saturated to the saturated state. We do this in such a way that the momentum transfer of the saturated viscosity propagates at a velocity comparable to the soundspeed of the medium. We define the velocity length scale as $l_v = 2\,c_s/|\boldsymbol{\sigma}|$, where

$$|\boldsymbol{\sigma}| = \sqrt{\mathrm{tr}(\boldsymbol{\sigma}^2)} = \sqrt{\mathrm{tr}(\boldsymbol{\sigma}\cdot\boldsymbol{\sigma})} = \sqrt{\mathrm{tr}(\sigma_{xx}^2 + \sigma_{yy}^2 + \sigma_{zz}^2 + 2\sigma_{xy}^2 + 2\sigma_{xz}^2 + 2\sigma_{yz}^2)} \tag{3.45}$$

is the strength of the rate of strain tensor. We introduce the viscosity saturation as analogous to the thermal conduction saturation (see §2.6.1; Cowie & McKee, 1977), following the implementation of Su et al. (2017):

$$\eta_{\mathrm{Sat}} = \frac{\eta}{1 + 4.2\frac{\lambda_i}{l_v}}\,. \tag{3.46}$$

This way we make sure that when $l_v < \lambda_i$, the shear viscosity coefficient saturates, avoiding unphysical large values of the viscous stress tensor $\boldsymbol{\Pi}$ and numerical issues like extremely small timesteps.

3.1.8 Braginskii Viscosity Implementation

In addition to the isotropic implementation, to capture the directional momentum transfer in weakly magnetized plasmas, an anisotropic viscosity formulation is currently under testing in OpenGadget3. In this case, the pressure anisotropy (equation (2.8)) is discretised as:

$$\Delta p\Big|_i = \eta\left(3\hat{b}_\alpha\hat{b}_\beta\frac{\partial v_\alpha}{\partial x_\beta}\Big|_i - \delta_{\alpha\beta}\frac{\partial v_\gamma}{\partial x_\gamma}\Big|_i\right)\,, \tag{3.47}$$

where $\hat{b} = \mathbf{B}/|\mathbf{B}|$ is the magnetic unit vector. And the anisotropic viscous stress tensor (equation (2.10)):

$$\boldsymbol{\Pi}_{\mathrm{Aniso},\,\alpha\beta}\Big|_i = -\Delta p\Big|_i\left(\hat{b}_\alpha\hat{b}_\beta\Big|_i - \frac{1}{3}\delta_{\alpha\beta}\right)\,. \tag{3.48}$$

Similarly to the isotropic case, the change in velocity and entropy are described as:

$$\frac{\mathrm{d}v_\alpha}{\mathrm{d}t}\Big|_{i,\,\mathrm{shear}} = \sum_{j=1}^{N_{\mathrm{ngb}}} m_j\left[\frac{\boldsymbol{\Pi}_{\mathrm{Aniso},\,\alpha\beta}\big|_i}{\rho_i^2}\left(\nabla_i W_{ij}(r,h_i)\right)\Big|_\beta + \frac{\boldsymbol{\Pi}_{\mathrm{Aniso},\,\alpha\beta}\big|_j}{\rho_j^2}\left(\nabla_i W_{ij}(r,h_j)\right)\Big|_\beta\right]\,, \tag{3.49}$$

and:

$$\frac{\mathrm{d}A_i}{\mathrm{d}t}\Big|_{\mathrm{shear}} = \frac{1}{2}\frac{\gamma-1}{\rho_i^{\gamma-1}}\frac{\Delta p_i^2}{3\rho_i\eta_i}\,. \tag{3.50}$$

3.2 Athena

Athena is a computational hydrodynamics code designed specifically for astrophysical hydrodynamics (Stone et al., 2008). It solves numerically the hydrodynamic equations using finite-volume methods, where the fluid domain is discretised into cells, forming either a fixed mesh or using an AMR. Within each cell, the physical quantities are represented by average values. These quantities can be expressed using vectors of the conserved (**U**) and primitive (**W**) variables:

$$\mathbf{U} = \begin{pmatrix} \rho \\ M_x \\ M_y \\ M_z \\ E \end{pmatrix}, \qquad \mathbf{W} = \begin{pmatrix} \rho \\ v_x \\ v_y \\ v_z \\ P \end{pmatrix}, \tag{3.51}$$

where $\mathbf{M} = \rho\mathbf{v}$ is the momentum density. The conserved variables are quantities directly related to the fundamental conservation laws of physics—mass, momentum, and energy. They represent quantities that, in the absence of sources or sinks, remain constant within a closed system. In contrast, primitive variables are quantities that have a direct physical interpretation and are often more intuitive to understand. Although primitive variables are easier to interpret physically, the hydrodynamic equations are formulated and solved in terms of conserved variables to ensure numerical conservation and stability.

The conservation laws in Cartesian coordinates can be written in a compact way as

$$\frac{\partial \mathbf{U}}{\partial t} + \frac{\partial \mathbf{F}}{\partial t} + \frac{\partial \mathbf{G}}{\partial t} + \frac{\partial \mathbf{H}}{\partial t} = 0\,, \tag{3.52}$$

where $\mathbf{F}, \mathbf{G}, \mathbf{H}$ are the vectors of the fluxes in the x, y and z directions respectively. They can be expressed as:

$$\mathbf{F} = \begin{pmatrix} \rho v_x \\ \rho v_x^2 + P \\ \rho v_x v_y \\ \rho v_x v_z \\ (E + P) v_x \end{pmatrix}, \tag{3.53}$$

$$\mathbf{G} = \begin{pmatrix} \rho v_y \\ \rho v_y v_x \\ \rho v_y^2 + P \\ \rho v_y v_z \\ (E + P) v_y \end{pmatrix}, \tag{3.54}$$

$$\mathbf{H} = \begin{pmatrix} \rho v_z \\ \rho v_z v_x \\ \rho v_z v_y \\ \rho v_z^2 + P \\ (E + P) v_z \end{pmatrix}. \tag{3.55}$$

Equation (3.52) is integrated over the volume of a grid cell, and over a discrete interval of time δt. After applying the divergence theorem, the integration of the discretised equations reads:

$$\mathbf{U}^{n+1}_{i,j,k} = \mathbf{U}^{n}_{i,j,k} - \frac{\delta t}{\delta x}\left(\mathbf{F}^{n+1/2}_{i+1/2,j,k} - \mathbf{F}^{n+1/2}_{i-1/2,j,k}\right) - \frac{\delta t}{\delta y}\left(\mathbf{G}^{n+1/2}_{i,j+1/2,k} - \mathbf{G}^{n+1/2}_{i,j-1/2,k}\right) - \frac{\delta t}{\delta z}\left(\mathbf{H}^{n+1/2}_{i,j,k+1/2} - \mathbf{H}^{n+1/2}_{i,j,k-1/2}\right), \tag{3.56}$$

where

$$\mathbf{U}^{n}_{i,j,k} = \frac{1}{\delta x\,\delta y\,\delta z}\int_{z_{k-1/2}}^{z_{k+1/2}}\int_{y_{j-1/2}}^{y_{j+1/2}}\int_{x_{i-1/2}}^{x_{i+1/2}} \mathbf{U}(x,y,z,t^n)\,dx\,dy\,dz \tag{3.57}$$

is the vector of volume-averaged variables, while

$$\mathbf{F}^{n+1/2}_{i-1/2,j,k} = \frac{1}{\delta y\,\delta z\,\delta t}\int_{t^n}^{t^{n+1}}\int_{z_{k-1/2}}^{z_{k+1/2}}\int_{y_{j-1/2}}^{y_{j+1/2}} \mathbf{F}(x_{i-1/2},y,z,t)\,dy\,dz\,dt \tag{3.58}$$

$$\mathbf{G}^{n+1/2}_{i,j-1/2,k} = \frac{1}{\delta x\,\delta z\,\delta t}\int_{t^n}^{t^{n+1}}\int_{z_{k-1/2}}^{z_{k+1/2}}\int_{x_{i-1/2}}^{x_{i+1/2}} \mathbf{G}(x,y_{j-1/2},z,t)\,dx\,dz\,dt \tag{3.59}$$

$$\mathbf{H}^{n+1/2}_{i,j,k-1/2} = \frac{1}{\delta x\,\delta y\,\delta t}\int_{t^n}^{t^{n+1}}\int_{y_{j-1/2}}^{y_{j+1/2}}\int_{x_{i-1/2}}^{x_{i+1/2}} \mathbf{H}(x,y,z_{k-1/2},t)\,dx\,dy\,dt \tag{3.60}$$

are the vectors of the time and area-averaged fluxes. Half-integer subscripts indicate the edges of the cells, while integers indicate the center of the cell.

At each cell boundary, ATHENA utilizes Riemann solvers, which determine the fluxes by solving local Riemann problems that describe how discontinuities propagate in the fluid. The code also incorporates reconstruction methods to estimate variable states at cell interfaces, enhancing accuracy. The computations in ATHENA proceed in discrete time steps. During each step, fluxes are computed based on the current cell states, and these fluxes are used to update the cell-averaged quantities.

Solving a Riemann problem produces entropy implicitly when fluxes from different thermodynamic states mix in one single cell: as a consequence, there is no need to add numerical dissipation artificially. However, some finite volume schemes introduce AV to stabilize the solver, which is the case of the early version of ZEUS (Stone & Norman, 1992). Nevertheless, mesh-based methods are not strictly Galilean-invariant; therefore, difficulties can arise when, e.g., simulating galaxies in high-velocity orbits, where galaxy velocity is larger than the sound speed of the medium (Springel, 2010). In addition, dissipation terms are purely numerical and sensitive to the absolute velocity of the flow, which means that the mixing occurs even when no physical motivation exists (Wadsley et al., 2008).

3.3 VORTEX-P

VORTEX-P (Vallés-Pérez et al., 2021b,a, 2024) is a postprocessing tool designed to perform a numerical Helmholtz-Hodge decomposition and an optional Reynolds decomposition of the velocity field. Although to achieve this numerically an AMR is needed, it can also be used

in particle-based simulations, such as SPH or moving-mesh, by mapping the particle data onto an AMR hierarchy and then solving elliptic equations using a hybrid of Fourier and iterative solvers. The approach ensures accuracy across a wide range of spatial resolutions and preserves the physical separation of turbulent components relevant to cosmological and astrophysical fluid dynamics.

3.3.1 Helmholtz-Hodge Decomposition

Any vector field $\mathbf{v}$ can be decomposed in:

$$\mathbf{v} = \mathbf{v}_{\rm comp} + \mathbf{v}_{\rm sol} + \mathbf{v}_{\rm harm}\,, \tag{3.61}$$

where $\mathbf{v}_{\rm comp}$ is the compressive (irrotational, $\nabla \times \mathbf{v}_{\rm comp} = 0$) component, $\mathbf{v}_{\rm sol}$ is the solenoidal (divergence-free, $\nabla\cdot\mathbf{v}_{\rm sol} = 0$) component, and $\mathbf{v}_{\rm harm}$ is the harmonic part. Under periodic boundary conditions, the harmonic term vanishes, and the compressive and solenoidal components are derived as:

$$\begin{cases} \mathbf{v}_{\rm comp} = -\nabla\phi, & \text{with } \nabla^2\phi = -\nabla\cdot\mathbf{v}, \\ \mathbf{v}_{\rm sol} = \nabla\times\mathbf{A}, & \text{with } \nabla^2\mathbf{A} = -\nabla\times\mathbf{v}\,. \end{cases} \tag{3.62}$$

The scalar potential ϕ and the vector potential $\mathbf{A}$ are obtained by solving these Poisson equations on the AMR grid. For the base grid, VORTEX-P uses Fourier transforms under the assumption of periodicity, which reduces the equations to multiplications by the Green's function in Fourier space. At finer AMR levels, boundary conditions are interpolated from coarser grids, and the equations are solved iteratively using a Successive Over-Relaxation method. Once the potentials ϕ and $\mathbf{A}$ have been obtained, $\mathbf{v}_{\rm comp}$ and $\mathbf{v}_{\rm sol}$ can be calculated by differentiating ϕ and $\mathbf{A}$.

3.3.2 Reynolds Decomposition

To isolate turbulent velocities, VORTEX-P implements a multi-scale filter based on the iterative algorithm of Vazza et al. (2012, 2016), adapted to AMR. This method separates the bulk ($\mathbf{v}(\mathbf{x})$) and turbulent motions $\delta\mathbf{v}(\mathbf{x})$ of the velocity field by constraining the injection scale of turbulence $L(\mathbf{x})$ without explicitly fixing a filter length (Vallés-Pérez et al., 2021a):

$$\delta\mathbf{v}(\mathbf{x}) = \mathbf{v}(\mathbf{x}) - \langle\mathbf{v}\rangle_L(\mathbf{x})\,. \tag{3.63}$$

The injection scale $L(\mathbf{x})$ is initialized to $L_{n=0} = 3\Delta x_l$, where Δx_l is the cell size at the refinement level l and n is the algorithm iteration. Then, $L(\mathbf{x})$ grows iteratively until the turbulent field converges or until a shock is encountered, as identified by either Mach numbers or thresholds in AV and velocity divergence.

3.3.3 Astrophysical Applications

The Helmholtz-Hodge decomposition enables the direct analysis of the physical role of different turbulent modes in structure formation. Solenoidal motions, linked to vorticity and magnetic

field amplification, can be distinguished from compressive flows, which are more directly associated with shock heating and entropy generation. Furthermore, the Reynolds decomposition isolates turbulent component contributions that may bias hydrostatic mass estimates in galaxy clusters without imposing a fixed filtering scale. This flexibility is crucial in the inherently multi-scale environment of cosmological simulations, where characteristic turbulence scales vary dramatically across environments such as the ICM, cosmic filaments, and galactic halos.

4 | The Role of Physical Viscosity in Hydrodynamical Instabilities[1]

Understanding the role of viscosity in the ICM is crucial, as it can significantly modify the dynamics of the plasma by damping turbulence and suppressing the development of fluid instabilities. Among these, the suppression of shear-driven modes like the KHI is one of the most important signatures of viscous effects. By analyzing the linear evolution of the KHI, we aim to quantify the accuracy of OpenGadget3 in reproducing its linear growth under different physical setups. In particular, we consider a physically motivated Spitzer viscosity, quantify its effect on the growth of the instability, and study the overall contribution of numerical viscosity.

As expected, our simulations recover the suppression of the KHI in the presence of physical viscosity and allow us to determine the threshold level required to fully damp the instability. For conditions typical of the ICM in clusters with a virial temperature of 3×10^7 K, this threshold corresponds to a suppression factor of $\approx 10^{-3}$ relative to the classical Spitzer value. The intrinsic numerical viscosity of our SPH implementation is inferred to be at least an order of magnitude smaller (i.e. $\approx 10^{-4}$), re-ensuring that modern SPH methods are suitable to study the effect of physical viscosity in galaxy clusters.

4.1 Kelvin-Helmholtz Instability

Despite Moore (1979) proposed an approximation to the exact evolution equation for incompressible fluids, no analytic solution for the non-linear KHI has been achieved yet in the case of compressible fluids. However, the growth of the instability in the linear regime, including viscosity, can be described using 2D analysis (Chandrasekhar, 1961). From linear perturbation theory, the y-velocity of the instability can be found to grow exponentially $\sim \exp[i \cdot n \cdot t]$ (see Junk et al., 2010, for a detailed derivation). n is the mode of the perturbation:

$$n = \left[k^2 v_x^2(\alpha_2 - \alpha_1)\right] + i\left[\frac{\nu k^2}{2} \pm \sqrt{\frac{\nu^2 k^4}{4} + 4k^2 v_x^2 \alpha_1 \alpha_2}\right], \tag{4.1}$$

[1]This Chapter was published in MNRAS by Marin-Gilabert et al. (2022).

where k is the wavenumber of the perturbation, v_x is the velocity of one of the fluids (in the laboratory frame of reference), and ν is the kinematic viscosity. α_1 and α_2 are defined as

$$\alpha_1 = \frac{\rho_1}{\rho_1 + \rho_2}, \qquad \alpha_2 = \frac{\rho_2}{\rho_1 + \rho_2}. \tag{4.2}$$

The real part of equation (4.1) deals with the oscillatory behavior of the KHI and is not of interest here. The imaginary part determines whether the KHI decays (positive solution of the square root) or grows exponentially (negative solution), damped by ν.

In the ideal case where $\nu = 0$, equation (4.1) becomes:

$$n = \left[k^2 v_x^2 (\alpha_2 - \alpha_1)\right] + i\left[\pm 2 k v_x (\alpha_1 \alpha_2)^{1/2}\right]. \tag{4.3}$$

Expressing the exponential growth of the perturbation as $\sim \exp[i\omega t]$, one can write the growth time of the KHI as

$$\tau_{\mathrm{KH}} = \frac{2\pi}{\mathrm{Im}(\omega)} = \frac{2\pi}{2 k v_x (\alpha_1 \alpha_2)^{1/2}} = \frac{\lambda}{\Delta v_x} \frac{(\rho_1 + \rho_2)}{(\rho_1\, \rho_2)^{1/2}}, \tag{4.4}$$

where Δv_x is the velocity difference between the two fluids ($\Delta v_x = 2 v_x$) and $\lambda = \frac{2\pi}{k}$ the wavelength of the perturbation.

4.2 Setup

To describe the growth of the KHI, we set up the initial conditions (ICs) following Murante et al. (2011). We create a 3D box (see Fig. 4.1) with 774144 particles of equal mass ($m = 3.13 \cdot 10^{-8}$), using a cubic lattice with periodic boundary conditions. The size of the box in internal units[2] is $\Delta x = 256$, $\Delta y = 256$, and $\Delta z = 8$. The domain satisfies:

$$\rho, T, v_x = \begin{cases} \rho_1, T_1, v_1 & |y| < 64 \\ \rho_2, T_2, v_2 & |y| > 64 \end{cases}. \tag{4.5}$$

Densities, temperatures, and x-velocities are: $\rho_1 = 6.26 \cdot 10^{-8}$, $\rho_2 = 3.13 \cdot 10^{-8}$; $T_1 = 2.5 \cdot 10^6$, $T_2 = 5 \cdot 10^6$; $v_1 = -40$ and $v_2 = 40$, respectively. The density and temperature ratio is constant, i.e. $R_\rho = \rho_1/\rho_2 = T_2/T_1 = 2$, ensuring a pressure equilibrium in the system. With these ICs, the Mach number corresponds to $\mathcal{M}_1 = v_1/c_1 \approx 0.23$ for the first fluid and $\mathcal{M}_2 = -v_2/c_2 \approx 0.17$ for the second one. The initial properties of both fluids can be seen in Fig. 4.1.

We introduce a small perturbation in the y-velocity at $y_{\mathrm{Int}} = \pm 64$ (equation (4.6)) to trigger the instability. This is similar to Read et al. (2010), but values have been adapted to our ICs:

$$v_y = -\delta v_y \left[\sin\left(\frac{2\pi(x + \lambda/2)}{\lambda}\right) \exp\left(-\left(\frac{y - y_{\mathrm{Int}}}{\sigma}\right)^2\right) + \sin\left(\frac{2\pi x}{\lambda}\right) \exp\left(-\left(\frac{y + y_{\mathrm{Int}}}{\sigma}\right)^2\right)\right]. \tag{4.6}$$

Here, $\lambda = 128$ is the wavelength of the perturbation, $\delta v_y = |v_x|/10 = 4$ is the amplitude, and $\sigma = 0.2\lambda$ is a scaling parameter to control the width of the perturbation layer.

[2]The internal units correspond to the basic Gadget units, where mass is given in 10^{10} $\mathrm{M}_\odot$, length in kpc, and velocity in km/s. We use a mean molecular weight of ≈ 0.588. In this Chapter, we will always refer to internal units.

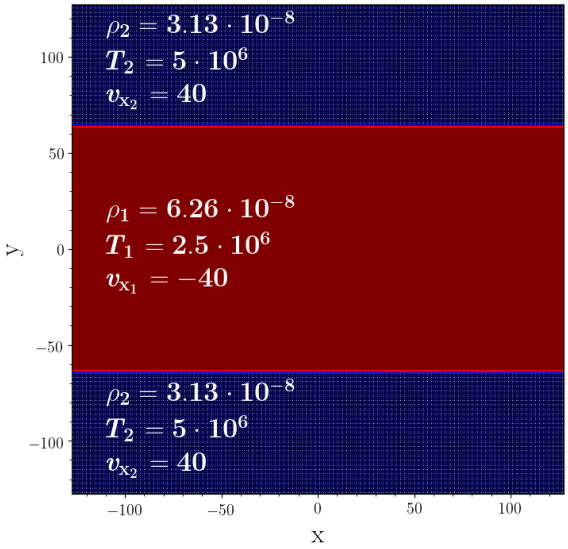

Figure 4.1: Graphical description of the ICs set in our simulations.

4.3 Effect of Physical Viscosity

The viscosity of a fluid can determine its properties and behavior, so in order to study this effect, we introduce viscosity in the system to quantify how the results change when the assumption of an inviscid fluid does not hold. For this purpose, we use OpenGadget3 with $N_{\text{ngb}} = 295$ to study the behavior of the system depending on the amount of viscosity implemented.

To study the effect that physical viscosity has on our results, we run 11 different simulations with 11 different fractions of Spitzer viscosity[3]. Table 4.1 shows the 11 different fractions with the corresponding value of the dynamic viscosity (η) in internal units, as well as the corresponding value of kinematic viscosity (ν). Taking fractions of η mimics the effect that the magnetic field has on viscosity, which is suppressed in the direction perpendicular to the magnetic field (see §2.5).

Note that the kinematic viscosity (defined by equation (2.3)) depends on the density of the fluid. Since we have two different fluids but the dynamic viscosity is the same for both of them, in our analysis we have computed the kinematic viscosity using the mean value of the kinematic viscosities of each fluid[4].

As a first qualitative result, Fig. 4.2 shows the mass-weighted projected density for three different viscosities, $10^{-2}\,\eta$ (top), $10^{-3}\,\eta$ (center) and $10^{-4}\,\eta$ (bottom), where η is the value of Spitzer viscosity at $T = 3 \cdot 10^7$ K. With a large amount of viscosity, the instability is fully suppressed and the roll is no longer developed, but as soon as we decrease the amount of viscosity, the instability appears and grows with higher amplitude. In the particular case with a viscosity of $10^{-4}\,\eta$, the shape of the roll happens to be similar to the ones expected for the ideal case.

[3] As mentioned before, for the viscosity we will assume a constant temperature of the fluids of $3 \cdot 10^7$ K to match the typical conditions within the ICM.

[4] For a detailed discussion on how to average the kinematic viscosities of two fluids, see §5.2.1.

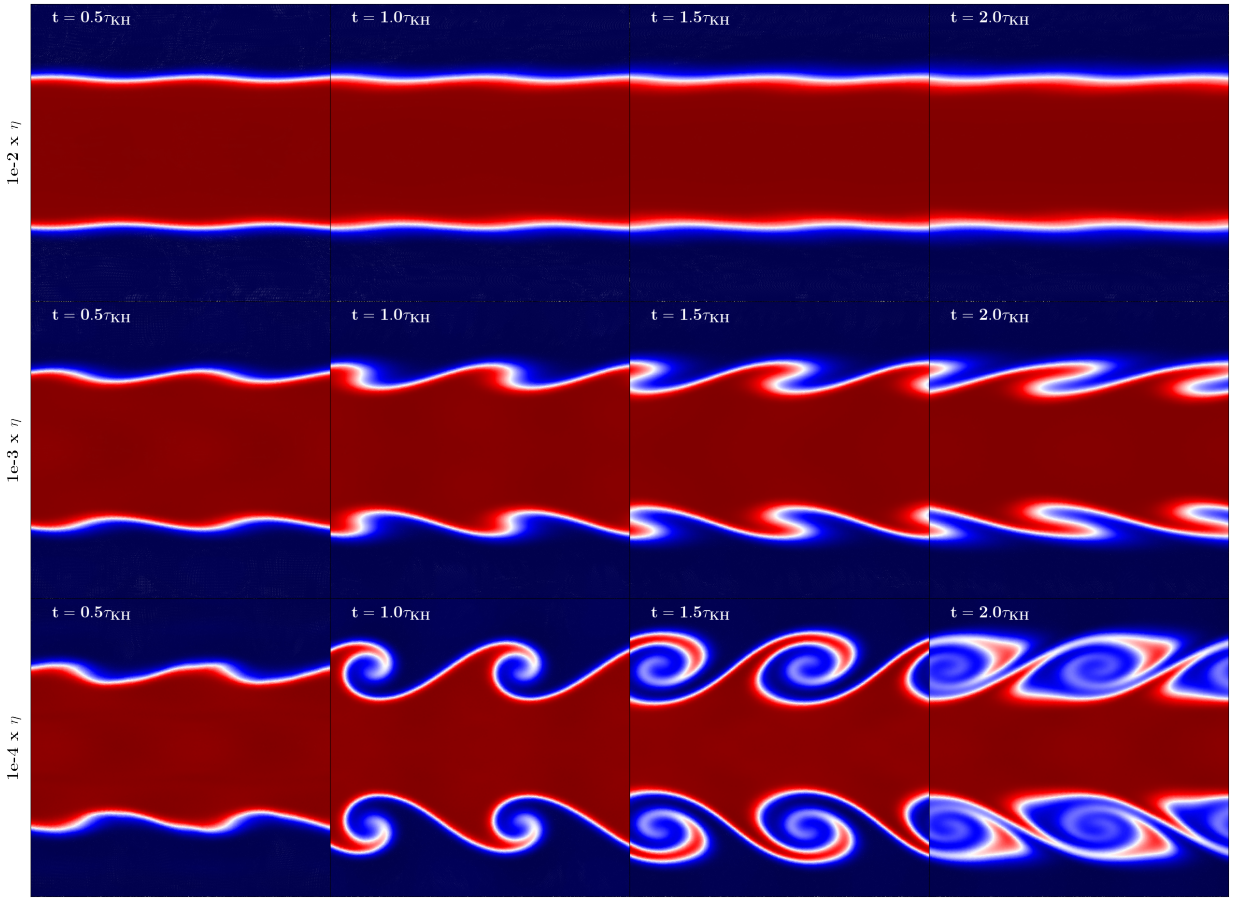

Figure 4.2: Projection of the mass-weighted density. *Left to right*: Different times. *Top to bottom*: Three different values of the physical viscosity from higher viscosity to lower. The run with the highest viscosity $10^{-2}\,\eta$ (top row) suppresses completely the growth of the KHI. In the case of $10^{-3}\,\eta$ (middle row), the instability is partially suppressed, but there is still some growth of the perturbation. With a low viscosity $10^{-4}\,\eta$ (bottom row), the instability can grow properly, showing similar results to the ideal case.

Table 4.1: Different amounts of viscosity employed in our simulations with the actual viscosity computed for both $N_{\mathrm{ngb}} = 150$ and $N_{\mathrm{ngb}} = 295$ and their deviation with respect to the theoretical value.

Fraction (η)	$\hat{\eta}$	ν	Actual ν ($N_{\mathrm{ngb}} = 150$)	Deviation ($N_{\mathrm{ngb}} = 150$)	Actual ν ($N_{\mathrm{ngb}} = 295$)	Deviation ($N_{\mathrm{ngb}} = 295$)
10^{-4}	$1.379 \cdot 10^{-7}$	3.305	9.57 ± 0.15	6.26 (189.53%)	5.69 ± 0.31	2.38 (72.15%)
$2.5 \cdot 10^{-4}$	$3.449 \cdot 10^{-7}$	8.263	14.68 ± 0.38	6.42 (77.65%)	10.15 ± 0.21	1.89 (22.83%)
$5 \cdot 10^{-4}$	$6.897 \cdot 10^{-7}$	16.527	23.41 ± 0.65	6.88 (41.65%)	18.20 ± 0.32	1.67 (10.13%)
$7.5 \cdot 10^{-4}$	$1.035 \cdot 10^{-6}$	24.790	31.46 ± 0.97	6.67 (26.91%)	26.32 ± 0.34	1.53 (6.17%)
10^{-3}	$1.379 \cdot 10^{-6}$	33.053	39.25 ± 0.80	6.20 (18.75%)	34.37 ± 0.36	1.25 (3.77%)
$1.5 \cdot 10^{-3}$	$2.069 \cdot 10^{-6}$	49.580	55.27 ± 0.76	5.69 (11.48%)	50.10 ± 0.55	0.52 (1.05%)
$2 \cdot 10^{-3}$	$2.759 \cdot 10^{-6}$	66.106	70.66 ± 1.64	4.55 (6.89%)	66.50 ± 0.56	0.39 (0.60%)
$2.5 \cdot 10^{-3}$	$3.449 \cdot 10^{-6}$	82.633	87.34 ± 1.28	4.71 (5.70%)	83.08 ± 1.47	0.45 (0.54%)
$5 \cdot 10^{-3}$	$6.897 \cdot 10^{-6}$	165.265	169.3 ± 2.9	4.07 (2.46%)	168.0 ± 4.1	2.76 (1.67%)
$7.5 \cdot 10^{-3}$	$1.035 \cdot 10^{-5}$	247.898	249.9 ± 9.2	2.00 (0.81%)	247.2 ± 9.0	−0.70 (0.28%)
10^{-2}	$1.379 \cdot 10^{-5}$	330.530	326.9 ± 3.6	−3.64 (1.10%)	334.0 ± 5.5	3.48 (1.05%)

4.4 Growth of the KHI

4.4.1 Amplitude Analysis

Theory predicts that, in an inviscid fluid, the initial perturbation triggers the instability and its amplitude starts to increase approximately linearly until it saturates with a height of $\sim \lambda/2$ (see e.g. Roediger et al., 2013b). The amplitude is expected to decrease afterwards, as each billow pairs with the adjacent ones (e.g. Rahmani et al., 2014). The height of the roll is a good indicator of the level of viscosity, which suppresses the instability and prevents its growth.

By measuring the height of the rolls, we are able to study the level of suppression that the KHI suffers depending on how viscous the system is. The top panel of Fig. 4.3 shows that the amplitude is reduced when the fluids are more viscous due to the fact that the friction between particles reduces the kinetic energy, causing the KHI not to develop. This means that the instability is fully suppressed for the simulations with the highest viscosities, and as soon as the fluids are less viscous, the instability is able to develop with larger amplitudes. At early times, we can see some increase in the amplitude due to the mixing of the fluids triggered by the thermal conduction. However, after this, the amplitude does not grow anymore. Despite the case with $10^{-4}\,\eta$ (orange line) reaches an amplitude of almost $\lambda/2$, we can observe a difference compared to the non-viscous case ($0\,\eta$, dark blue line), where the maximum height reached is larger than the $10^{-4}\,\eta$ case.

4.4.2 Velocity Analysis

In the non-viscous case, the y-velocity is expected to grow exponentially until $t = \tau_{\mathrm{KH}}$ (see §4.1). To measure the growth rate of the instability, depending on N_{ngb}, we calculate how the y-velocity

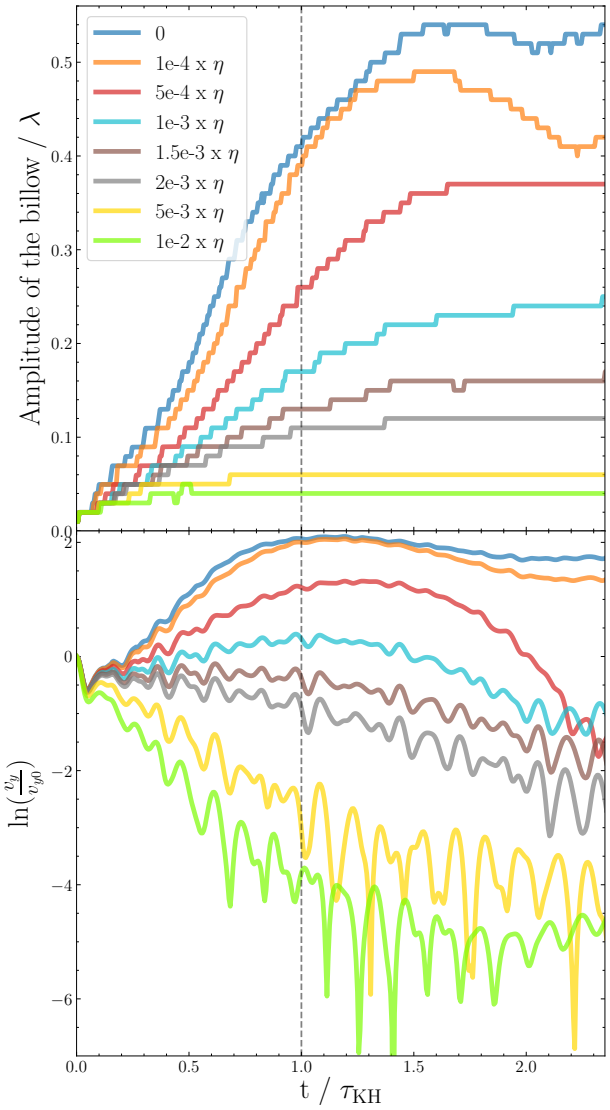

Figure 4.3: *Top panel*: Height of the rolls depending on how viscous the fluids are. For the most viscous case ($10^{-2}\,\eta$), the amplitude barely increases, but as soon as we decrease the viscosity of the system, the rolls reach a higher amplitude until we have $10^{-4}\eta$, where the rolls reach an amplitude close to $\lambda/2$. However, this height is smaller than the one reached in the ideal case. *Bottom panel*: Evolution of the y-velocity depending on the amount of viscosity of the system. In a very viscous system ($10^{-2}\,\eta$), the KHI decays exponentially, while the case with the lowest amount of viscosity ($10^{-4}\,\eta$) follows a similar path to the ideal case. The amount of viscosity that produces no growth of the y-velocity (slope zero) characterizes a viscosity threshold above which the KHI is fully suppressed. This threshold can be determined numerically and compared to a theoretical estimate.

of the particles changes with time. This tells us the level of suppression of the KHI. To compute the amplitude of the y-velocity, we use a discrete convolution of the sinusoidal perturbation (see appendix B for a detailed description of the method; Sijacki & Springel, 2006; Obergaulinger & Aloy, 2020). The results are shown in the bottom panel of Fig. 4.3. Due to friction, the more viscous the system is, the slower the KHI grows. For higher viscosities, the growth rate of the y-velocity up to $t = \tau_{\rm KH}$ progressively decreases. Beyond a critical viscosity, the velocity no longer grows exponentially (positive slope) but instead decays exponentially (negative slope). We consider the amount of viscosity where the slope changes as the major indication for full suppression. For viscosities higher than this threshold, the instability decays, i.e., it is fully suppressed.

By fitting a linear function to our data we can estimate when the slope changes its sign, and therefore, the viscosity threshold[5]. We obtain that the viscosity threshold computed numerically is between $1.5 \cdot 10^{-3}\,\eta$ and $2 \cdot 10^{-3}\,\eta$. This translates to a kinematic viscosity threshold in the range of $\nu = [49.580 - 66.106]$ (see Table 4.1).

For a validation of our numerical result, we estimate this viscosity threshold theoretically using three different approaches suggested by Roediger et al. (2013b).

The growth of a viscous KHI described in §4.1 is only true for a steady background flow ($\partial v_x/\partial t = 0$), which is strictly speaking only true for low values of viscosity. For higher values of viscosity, we cannot assume a steady background flow anymore ($\partial v_x/\partial t \neq 0$) due to the fact that viscosity smooths out the x-velocity gradient (see appendix C). Therefore, we cannot get an analytical solution, and we need to make different assumptions to estimate this viscosity threshold.

For the first estimate, we use the fact that the physical viscosity smooths out the velocity gradient over a length $\pm d$ above and below the interface. As demonstrated by Chandrasekhar (1961), the KHI is suppressed for wavelengths smaller than $\sim 10d$. Now, we make use of the diffusion length $l_D = \pm 2\sqrt{\nu t}$, which measures how much the interface gets widened by diffusion at time t. If we take into account that in the inviscid case it takes $t = \tau_{\rm KH}$ for the instability to grow, we can calculate the width of the interface at that time and see whether the instability is able to grow or not. If $\lambda < 10 l_D(t = \tau_{\rm KH})$, the KHI will be suppressed, and otherwise it will grow. So using the inviscid definition of $\tau_{\rm KH}$ (equation (4.4)), we obtain

$$\lambda < 10 l_D(\tau_{\rm KH}) = 20\sqrt{\nu \tau_{\rm KH}} \tag{4.7}$$

$$\frac{\lambda^2}{400} < \nu \frac{\lambda}{\Delta v_x} \frac{(\rho_1 + \rho_2)}{(\rho_1\,\rho_2)^{1/2}} \tag{4.8}$$

$$\nu > \nu_{\rm Crit} = \frac{\lambda\,\Delta v_x}{400} \frac{(\rho_1\,\rho_2)^{1/2}}{(\rho_1 + \rho_2)}\,. \tag{4.9}$$

Using our values inferred from our initial setup, we get a critical viscosity of $\nu_{\rm Crit} = 12.07$, which is below what we calculated numerically. However, as Roediger et al. (2013b) states, the interface

[5]For this fit we used the time interval of $[0.05\tau_{\rm KH}, \tau_{\rm KH}]$ to avoid the initial decay of the velocity at early times due to the loss of kinetic energy of the particles by moving along the y axis through a fluid streaming in the opposite direction (Junk et al., 2010).

is being smoothed out continuously, and therefore comparing the wavelength of the perturbation with the diffusion length at $t = \tau_{\mathrm{KH}}$ is somewhat arbitrary.

For the second estimate, we assume that the effect of viscosity dominates when the viscous dissipation time-scale, which is given by $\tau_\nu = d^2/\nu$, is shorter than the KHI time-scale τ_{KH}. As mentioned before, the KHI is suppressed if $\lambda < 10d$, so we can write d as $d = \lambda/10$. Now, if we compare both time-scales, we get

$$\tau_{\mathrm{KH}} > \tau_\nu \tag{4.10}$$

$$\frac{\lambda}{\Delta v_x}\frac{(\rho_1+\rho_2)}{(\rho_1\,\rho_2)^{1/2}} > \frac{\lambda^2}{100\nu} \tag{4.11}$$

$$\nu > \nu_{\mathrm{Crit}} = \frac{\lambda\,\Delta v_x}{100}\frac{(\rho_1\,\rho_2)^{1/2}}{(\rho_1+\rho_2)}\,. \tag{4.12}$$

Under these assumptions, the critical value of viscosity is four times bigger than before, leading to $\nu_{\mathrm{Crit}} = 48.27$. This threshold correlates much better with our results and is in the range of values we measured.

Finally, we made a third estimate assuming that the instability is suppressed when it reaches its maximum height and the width of the x-velocity gradient is bigger than the height of the roll. The roll usually reaches a height of $\lambda/2$ at $t = \tau_{\mathrm{KH}}$, so this means that at $t = \tau_{\mathrm{KH}}$ the width of the x-velocity gradient must be larger than $\lambda/2$

$$\frac{\lambda}{2} < l_D(\tau_{\mathrm{KH}}) = 2\sqrt{\nu\tau_{\mathrm{KH}}} \tag{4.13}$$

$$\frac{\lambda^2}{16} < \nu\,\frac{\lambda}{\Delta v_x}\frac{(\rho_1+\rho_2)}{(\rho_1\,\rho_2)^{1/2}} \tag{4.14}$$

$$\nu > \nu_{\mathrm{Crit}} = \frac{\lambda\,\Delta v_x}{16}\frac{(\rho_1\,\rho_2)^{1/2}}{(\rho_1+\rho_2)}\,. \tag{4.15}$$

This gives us a value of $\nu_{\mathrm{Crit}} = 301.70$, which is too large for our simulations. This can be due to the fact that we assumed that the maximum height is reached at $t = \tau_{\mathrm{KH}}$. However, by considering the ideal case on the top panel of Fig. 4.3 (dark blue line), one can see that the maximum is reached at later times. If, for example, instead of considering that the maximum height is reached at $t = \tau_{\mathrm{KH}}$, we consider that it is reached at $t = 2\tau_{\mathrm{KH}}$, the value for the critical viscosity is reduced by half.

Additionally, we do an extra estimate depending on the exact smoothing of the x-velocity gradient. As explained in appendix 2.2, the x-velocity gradient is smoothed out following equation (2.4). In our case, we do not have fixed plates moving at constant velocities, which means that the particles at the boundaries will progressively slow down, and the theoretical result will not be valid anymore.

The more viscous the system is, the faster the system will move away from the initial state of the Rayleigh problem. Assuming that the instability is not suppressed if at $t = \tau_{\mathrm{KH}}$ the system still follows equation (2.4), i.e., the particles at the boundaries still move at their initial v_x, one can estimate the maximum viscosity that allows this behavior.

We also assume that our boundaries correspond to the particles at $d = \pm\lambda/2$, which is the height that the rolls are expected to reach. Only at $t = 0$ the particles move exactly at the initial x-velocity, so in order to do this calculation, we consider three different cases: we consider that the particles still move at their initial v_x when they move 10% slower than the initial v_x, when they move 1% slower and 0.1% slower. After this computation, we got

1. 10% slower $\rightarrow$ $\nu_{\text{Crit}} = 66.02$
2. 1% slower $\rightarrow$ $\nu_{\text{Crit}} = 45.00$
3. 0.1% slower $\rightarrow$ $\nu_{\text{Crit}} = 33.97$.

Given the values obtained by these estimates, we can see that the results we obtained for the viscosity threshold are in agreement with what we have estimated. These estimates were made using very general and ideal assumptions, and we cannot rely much on the exact value we got. However, we can observe that our results are in keeping with theoretical expectations.

4.5 Energy Conservation

As the simulation runs, the friction between particles produces a loss of kinetic energy, turning it into internal energy, and since the domain is a closed system with periodic boundary conditions, the total energy has to be conserved as a function of time. To test how well the code conserves energy, we compute the mass-weighted mean of kinetic energy per unit mass of the whole simulation domain and the internal energy per unit mass of the system.

In Fig. 4.4 we show the variation of the internal (top panel) and kinetic energy (bottom panel) of the system normalized to the initial total energy for each run. For higher values of viscosity, there is more friction between particles, and more kinetic energy is turned into internal energy. The symmetry between the two panels shows the conversion of kinetic into internal energy and the conservation of energy of the system. By summing up the two values to compute the total energy, we find that the runs with physical viscosity conserve 99.992% of the total energy and the run without physical viscosity the 99.986%. We note that, while energy is largely conserved in both cases, the performance of the runs with viscosity in terms of energy conservation is slightly improved.

4.6 Total Viscosity

Finally, we measure the actual viscosity of the system and compare it to the theoretical input viscosity. For the computation of the effective viscosity, we follow the method explained in appendix C. After computing the total viscosity of our simulations and calculating the average value for different times, we find small standard deviation errors ($\sim$ 1%, with the highest error being 5.45% in the least viscous case[6]), meaning that the results are consistent in time. These results can be seen in Table 4.1.

[6]The relative errors are calculated dividing the standard deviation by the value and multiplying by 100.

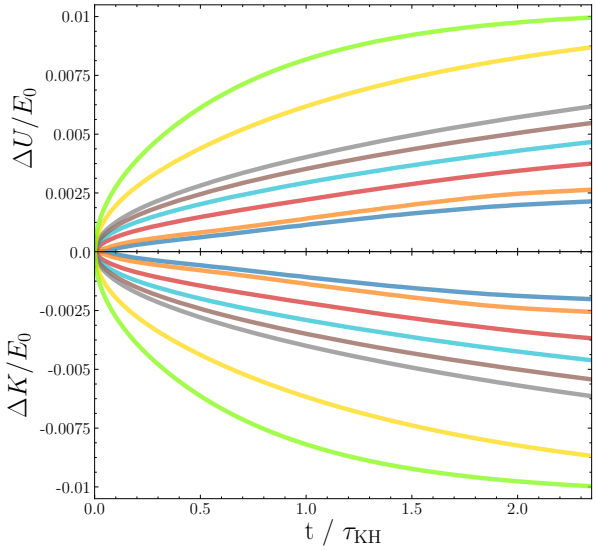

Figure 4.4: *Top panel*: Variation of the mean internal energy per unit mass normalized to the initial total energy. *Bottom panel*: Variation of the mean kinetic energy per unit mass normalized to the initial total energy. The runs with a higher viscosity transform more kinetic energy into internal energy, and the symmetry of the two plots demonstrates the conservation of energy in all the runs. We use the same color code as the previous plot (Fig. 4.3).

To see the correlation between the theoretical (input) value and the actual (from the fit) value of viscosity for the different runs, we plot the viscosity we obtained numerically versus the theoretical one in Fig. 4.5. For comparison, we show the cases with $N_{\rm ngb} = 150$ and $N_{\rm ngb} = 295$. Since they are expected to be the same, we would expect a relation with a slope of 1 and the intercept at $y = 0$ (black dashed line). Hence, we fit our points to a linear function. In the case of $N_{\rm ngb} = 295$, the data follows a linear trend with a slope of 1.001631 ± 0.000013, which is what we could expect, but an intercept of 1.3 ± 0.3, meaning that the actual viscosity of the system is slightly higher than the theoretical one. This deviation becomes more relevant in the case of $N_{\rm ngb} = 150$, where the slope is 0.973146 ± 0.000009, also close to one, but the intercept is higher than in the previous case. In this case, the intercept is 7.04 ± 0.17, showing a systematic shift upwards. This systematic increase is likely due to the intrinsic numerical viscosity of the code, which is acting alongside the physical, Spitzer-type viscosity that we implemented in the code. This would explain the effective larger viscosity for $N_{\rm ngb} = 150$ vs $N_{\rm ngb} = 295$, indicating that $N_{\rm ngb} = 150$ introduces more numerical viscosity in the system than $N_{\rm ngb} = 295$[7]. This result indicates that, when the physical viscosity is low enough ($\lesssim 2.5 \cdot 10^{-4}$ in the case of $N_{\rm ngb} = 150$ and $\lesssim 10^{-4}$ in the case of $N_{\rm ngb} = 295$, see Table 4.1), the system will be governed by the intrinsic viscosity of the code over the physical viscosity implemented.

[7]Note that the recommended amount of $N_{\rm ngb}$ for a Wendland C^6 kernel is $N_{\rm ngb} = 295$ (Dehnen & Aly, 2012; Price et al., 2018).

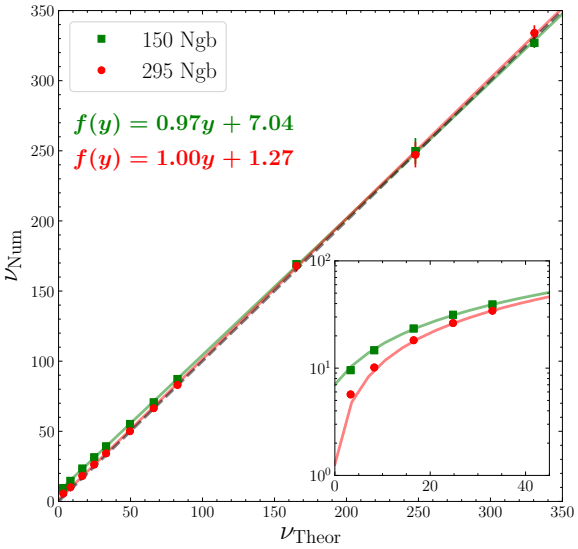

Figure 4.5: Numerical computation of the total viscosity of the system against the theoretical viscosity we implement. One would expect a one-to-one relation (black dashed line). In the run with $N_{\mathrm{ngb}} = 295$, the data follows a linear function with a slope of 1.001631 ± 0.000013, but an intercept of 1.3 ± 0.3, which is slightly higher than the one expected. In the case of $N_{\mathrm{ngb}} = 150$, the slope is 0.973146 ± 0.000009 and the intercept 7.04 ± 0.17, which corresponds to a shift upwards of the data.

4.7 Conclusions

In this Chapter, we carried out a detailed investigation on how physical viscosity affects the behavior of the KHI in the linear regime. The results found can translate into a significant impact in the non-linear regime, and as a consequence, the development of turbulence and mixing in the ICM.

To study the role of the physical viscosity, we computed the amplitude of the KHI billows, showing that the instability cannot grow in a highly viscous fluid, but the height of the rolls increases when the amount of viscosity decreases. By measuring the evolution of the y-velocity, we found a viscosity threshold ($\approx 10^{-3}\,\eta$) where, for viscosities higher than this threshold, the KHI is fully suppressed and for smaller amounts of viscosity the instability is able to grow exponentially. We computed the threshold numerically and compared it with three different theoretical estimates and one numerical estimate, concluding that the threshold computed from our simulations is in agreement with these estimates. In terms of energy conservation, the higher the viscosity in the simulations is, the more kinetic energy is turned into internal energy. In this process, the code is always conserving more than 99.99% of the total energy.

Additionally, we measured the actual viscosity of the system and compared it to the theoretical viscosity we had implemented, observing that the effective viscosity of the system tends to be higher than the one we implemented. This effect could be explained if the intrinsic viscosity of the code is taken into account, meaning that the total viscosity of the system we simulate is not

only the physical viscosity we implement, but the intrinsic viscosity of the code contributes as well. This contribution is also dependent on $N_{\rm ngb}$, where the case with $N_{\rm ngb} = 150$ shows a larger contribution compared to the run with $N_{\rm ngb} = 295$.

In summary, OpenGadget3 successfully reproduces the expected reduction of the growth rate of the KHI in the presence of physical viscosity and recovers very well the threshold level of physical viscosity needed to fully suppress the instability. In the case of galaxy clusters with a virial temperature of 3×10^7 K, this level corresponds to a suppression factor of $\approx 10^{-3}$ of the classical Spitzer value for instabilities with $\lambda = 128$ kpc wavelength. The intrinsic, numerical viscosity of our SPH implementation corresponds to a value smaller by an order of magnitude (i.e. $\approx 10^{-4}\,\eta$) within an ICM environment. All the tests presented are re-ensuring that modern SPH methods are suitable to study the effect of physical viscosity in galaxy clusters.

Appendix A: Amplitude of the Rolls

The method employed to compute the height of the rolls is similar to the one described in Roediger et al. (2013b). We focus only on the upper half of the domain (since the domain is symmetric, we choose only the upper half, and therefore, the total number of particles is reduced by half). Then we mark every particle depending on whether they are "red" (denser fluid) or "blue" (lighter fluid) at $t = 0$ so we can trace them later. Once we have marked every particle, we divide the half domain into 100 bins along the y direction and calculate the number of "red" and "blue" particles in every bin for every snapshot. The top of the billow will correspond to the lowest bin, where at least 95% of the particles are "blue", while the bottom will be the highest bin with at least 95% of "red" particles. Finally, we compute the amplitude of the roll by calculating the distance between the top and the bottom of the billow for every snapshot.

Appendix B: Growth of the Velocity

We use the discrete convolution suggested by McNally et al. (2012) to compute the amplitude M of the initially excited mode. We have adapted the formula to our ICs, leading to

$$s_i = v_y h_i^3 \sin\left(\frac{2\pi\left(x + \frac{\lambda}{2}\right)}{\lambda}\right) \exp\left(-\frac{2\pi}{\lambda}\,|64 - y|\right) \tag{B1}$$

$$c_i = v_y h_i^3 \cos\left(\frac{2\pi\left(x + \frac{\lambda}{2}\right)}{\lambda}\right) \exp\left(-\frac{2\pi}{\lambda}\,|64 - y|\right) \tag{B2}$$

$$d_i = h_i^3 \exp\left(-\frac{2\pi}{\lambda}\,|64 - y|\right) \tag{B3}$$

$$M = 2\sqrt{\left(\frac{\sum_{i=1}^{N} s_i}{\sum_{i=1}^{N} d_i}\right)^2 + \left(\frac{\sum_{i=1}^{N} c_i}{\sum_{i=1}^{N} d_i}\right)^2}\,, \tag{B4}$$

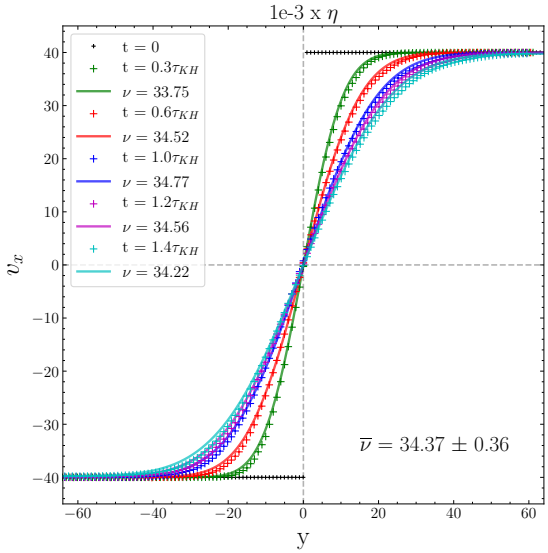

Figure C1: Fit of the analytic formula (2.4) to our data for the computation of the kinematic viscosity for the different simulations. It starts from a discontinuity in the x-velocity profile at $t = 0$ and, as time passes, the x-velocity gradient is smoothed out by viscosity. The crosses represent our data, and the solid lines the fit of the analytic function, coded by different colors for different times.

where h_i is the smoothing length, λ the wavelength of the perturbation and N is the total number of particles in the domain. For the computation of M, we used only one quarter of the full domain in order to take only one perturbation for the calculation.

Appendix C: Total Viscosity of the System

The effect of viscosity is to smooth out the velocity gradient between the two fluids by momentum diffusion, and therefore, the more viscosity a system has, the more the gradient is smoothed out and the more difficult it is to develop the instability (see §2.2). The x-velocity profile is smoothed out following equation (2.4) (see Fig. C1, which shows the velocity gradient at different times). In order to calculate the intrinsic viscosity of the system, we simulate our two fluids without any initial perturbation and we fit the analytical function (2.4) to our data at different times with the kinematic viscosity as a free parameter. To do so, we use only the top half of the full domain and we displace it to set the interface at $y = 0$. We then divide the half domain into 127 bins and compute the mean x-velocity of each bin at five different times. Finally, we calculate the average value of the five fits in order to get a value for the total viscosity of the system.

5 | The (Limited) Effect of Viscosity in Multiphase Turbulent Mixing[1]

In Chapter 4 we quantified how physical viscosity can suppress the growth of instabilities in idealized shear layers, identifying a critical threshold beyond which the KHI is fully suppressed. The results found indicated a potential impact on the non-linear evolution of the instability, and therefore the development of turbulence, although it was not studied in detail. In this Chapter, we study the effects of viscosity in turbulence and mixing, also introducing radiative cooling. By exploring how viscosity modulates both the development of turbulence and radiative losses, we aim to determine under which conditions multiphase structure is maintained or disrupted, and how these processes shape the thermodynamic evolution of gas in the CGM and ISM.

Multiphase gas can be found in many astrophysical environments, such as galactic outflows, stellar wind bubbles, and the CGM, where the interplay between turbulence, cooling, and viscosity can significantly influence gas dynamics and star formation processes. In this Chapter, we aim to determine how different amounts of viscosity affect the KHI, turbulence evolution, and the efficiency of gas mixing and cooling. Using idealized 2D numerical setups, we compute the critical viscosity required to suppress the KHI in shear flows characterized by different density contrasts and Mach numbers. These results are then used in a 3D shear layer setup to explore the impact of viscosity on cooling efficiency and turbulence across different cooling regimes. We find that the critical viscosity follows the expected dependence on overdensity and Mach number. Our viscous TRMLs simulations show different behaviors in the weak and strong cooling regimes. In the weak cooling regime, viscosity has a strong impact, resulting in laminar flows and breaking previously established inviscid relations between cooling and turbulence (albeit leaving the total luminosity unaffected). However, in the strong cooling regime, when cooling timescales are shorter than viscous timescales, key scaling relations in TRMLs remain largely intact. In this regime – which must hold for gas to remain multiphase – radiative losses dominate, and the system effectively behaves as non-viscous regardless of the actual level of viscosity. Our findings have direct implications for both the interpretation of observational diagnostics and the development of subgrid models in large-scale simulations.

[1]This Chapter was submitted for publication to A&A (Marin-Gilabert et al., 2025).

5.1 Numerical setup

In this Chapter, we perform our simulations using the code Athena (Stone et al., 2008), which is well suited for hydrodynamics simulations (see §3.2). We use the HLLC Riemann solver, a second-order reconstruction with slope limiters in the primitive variables, the van Leer unsplit integrator (Gardiner & Stone, 2008), a Cartesian geometry, and an adiabatic EOS with $\gamma = 5/3$. In all our simulations, we keep the shear viscosity coefficient (η) constant, to simplify the analysis and understand the effect of viscosity in the most simple way[2].

5.1.1 Adiabatic 2D simulations

To better understand fluid dynamics and the effects of viscosity while reducing computational costs, two different 2D setups are used without cooling. These provide a more controlled environment compared to a chaotic 3D system, while allowing us to study the KHI in detail. The first setups explore how critical viscosity depends on overdensity and Mach number by varying viscosity across different overdensity and Mach number values.

We describe each 2D setup in detail below.

The planar slab

To understand how the critical viscosity at which the KHI is suppressed changes as a function of the overdensity, we use a modified version of the numerical setup suggested by Lecoanet et al. (2015), which provides a benchmark for the growth of the KHI in grid codes. We create a 2D domain with a resolution of 320×320 in the $\hat{x}$ and $\hat{y}$ directions, respectively, with periodic boundary conditions with dimensions $L_x = 256$ and $L_y = 256$. The density and velocity profiles satisfy:

$$\rho = \rho_{\rm hot} + \frac{\rho_{\rm cold} - \rho_{\rm hot}}{2}\left[\tanh\left(\frac{y + y_{\rm Int}}{a}\right) - \tanh\left(\frac{y - y_{\rm Int}}{a}\right)\right], \tag{5.1}$$

$$v_x = -v_{\rm shear} \times \left[\tanh\left(\frac{y + y_{\rm Int}}{a}\right) - \tanh\left(\frac{y - y_{\rm Int}}{a}\right) - 1\right]. \tag{5.2}$$

$\rho_{\rm hot}$ is a fixed value for all our simulations, and we modify $\rho_{\rm cold}$ as we change the value of overdensity. $y_{\rm Int} = 64$ indicates the position of the interface between the two fluids, and $v_{\rm shear}$ is the shear velocity of each fluid, i.e., the relative motion can be expressed as $\mathcal{M}_{\rm h} \equiv 2v_{\rm shear}/c_{\rm c,hot}$.

In this setup we keep $\mathcal{M}_{\rm h} = 0.34$ constant, as well as $T_{\rm cold} = 10^4$ K, while $T_{\rm hot}$ will be given by the overdensity to ensure pressure equilibrium in the whole domain. The value of $a = \lambda/10$ ensures smooth initial conditions, fundamental for the growth of the desired instability mode without spurious secondary instabilities in grid codes. $\lambda = 128$ indicates the wavelength of the perturbation used to trigger the instability. We use the initial perturbation described in equation (4.6).

To study how the critical viscosity changes with the overdensity of the system, we use different values of $\chi \equiv \rho_{\rm cold}/\rho_{\rm hot}$ from 1 to 100, and we test different values of viscosity for each

[2]For a discussion on the effect of temperature-dependent viscosities, see §5.2.4.

overdensity. For reference, the Spitzer viscosity value of a fluid with $T = 10^6$ K is $\eta_{\rm Sp} \simeq 0.11 \mathrm{g(cm\ s)^{-1}}$, which corresponds to $\eta_{\rm Sp} \simeq 1809.28$ in our unit system.

The planar sheet

When increasing the Mach number, body modes caused by pressure waves moving across the domain between the stream boundaries appear in the planar slab setup (Mandelker et al., 2019). To avoid this, we modify our initial conditions to study the dependence of the critical viscosity as a function of the Mach number. We use a similar setup as before, but with just one interface between the two fluids at $y_{\rm Int} = 0$. The density and velocity profiles read:

$$\rho = \frac{1}{2} \times \left[\rho_{\rm cold} \left(1 - \tanh\left(\frac{y}{a}\right)\right) + \rho_{\rm hot} \left(1 + \tanh\left(\frac{y}{a}\right)\right)\right] , \tag{5.3}$$

$$v_x = v_{\rm shear} \times \tanh\left(\frac{y}{a}\right) , \tag{5.4}$$

and the initial perturbation:

$$v_y = -\delta v_y \sin\left(\frac{2\pi(x + \lambda/2)}{\lambda}\right) \exp\left(-\left(\frac{y}{\sigma}\right)^2\right) . \tag{5.5}$$

With this setup, we want to study the dependence of the critical viscosity on the Mach number. Therefore, we keep constant $\chi = 10$ and we modify $v_{\rm shear}$ in order to have values of Mach number ranging from 0.01 to 1.8. As with the previous setup, we test different values of viscosity for each Mach number to identify the critical viscosity in each case.

5.1.2 3D simulations: Turbulent Radiative Mixing Layers

Once we have obtained the value for the critical viscosity in a system with an overdensity of 100, we make use of this value to study how different values of viscosity affect a TRMLs system. For a proper development of turbulence, a 3D setup is needed, therefore, we use a modified version of the setup suggested in Ji et al. (2019), where the density profile is the same as in equation (5.3), but the velocity profile is:

$$v_x = \frac{v_{\rm shear}}{2} \times \left[1 - \tanh\left(-\frac{y}{a}\right)\right] , \tag{5.6}$$

and the initial perturbation:

$$v_y = \delta v_y \sin\left(\frac{2\pi x}{\lambda}\right) \sin\left(\frac{2\pi z}{\lambda}\right) \exp\left(-\left(\frac{y}{a}\right)^2\right) . \tag{5.7}$$

In this case, $v_{\rm shear}$ corresponds to the velocity difference between the media, where the lower (colder) medium is stationary and the upper one moves at $v_{\rm shear}$. We use a Mach number of $\mathcal{M}_{\rm h} = 0.5$ and $\delta v_y = v_{\rm shear}/100$. In this case, our domain is ten times larger in the $\hat{y}$ direction, whereas in the $\hat{x}$ and $\hat{z}$ directions it is equal to the wavelength of the perturbation $L_y = 10L_x = 10L_z = 10\lambda$. We keep the hot gas density and the cold gas temperature constant,

$\rho_{\rm hot}$ and $T_{\rm cold} = 10^4$ K, respectively. In this setup, we use a fixed overdensity $\chi = 100$ (i.e., $T_{\rm hot} = 10^6$ K). The resolution is the same as in Das & Gronke (2023), consisting of $64 \times 640 \times 64$ in the $\hat{x}$, $\hat{y}$ and $\hat{z}$ directions respectively, with outflow boundaries in the $\hat{y}$ direction and periodic boundaries in $\hat{x}$ and $\hat{z}$.

We use the Townsend radiative cooling algorithm (Townsend, 2009) (as, e.g., in Gronke et al., 2021), with a solar metallicity cooling curve (Sutherland & Dopita, 1993, Fig. 1.7) and a $T_{\rm floor} = 10^4$ K. Unlike Tan et al. (2021), we do not modify the cooling strength. Instead, we modify the wavelength to have different values of Damköhler number (see §1.4.5). Since ${\rm Da} = t_{\rm turb}/t_{\rm cool}$, and $t_{\rm turb} \propto \lambda$ (see equation (1.38)), by varying the wavelength (and also the size of the box) we get different values of Da. We run a total 12 simulations with different Da for each amount of viscosity, from ${\rm Da}_{\rm mix} \simeq 2.3 \times 10^{-3}$ to ${\rm Da}_{\rm mix} \simeq 1.1 \times 10^3$, where the temperature of the intermediate mixed gas chosen to compute the cooling time is $T_{\rm mix} = 2 \times 10^5$ K (to be consistent with Tan et al., 2021). The values of Da are calculated assuming that $t_{\rm turb} \sim \tau_{\rm KH}$. In the presence of cooling, the box is filled with cold gas, causing the mixing layer to leave the domain, especially in the strong cooling regime. To prevent this, we calculate the velocity at which the box is being filled with cold gas and add a velocity in the opposite direction to the whole box, following Das & Gronke (2023).

5.2 Results

5.2.1 Critical Viscosity vs Overdensity

We provide an analytical estimate for the critical viscosity in a KHI setup in §4.4.2 (in this Chapter we only use the second estimate described in §4.4.2, equation (4.12)), based on the growth time of the KHI and the viscous time. Numerically, this critical viscosity is computed by measuring the growth or decay of the instability within $1\tau_{\rm KH}$ (see appendix B for details).

The analytical estimate presented in §4.4.2 sets a criterion for the kinematic viscosity (ν). However, in our simulations, we use a constant dynamic viscosity (η) for both fluids. In a multi-fluid system with different densities but the same η, each fluid will exhibit its own ν. Therefore, to be able to compute the critical η for our setup, it is necessary to define an appropriate average of these ν to find a general $\bar{\nu}$ of the whole system. Thus, for a system characterized by a single dynamic viscosity (η), two densities ($\rho_{\rm h}$ and $\rho_{\rm c}$), and consequently two different kinematic viscosities ($\nu_{\rm h}$ and $\nu_{\rm c}$), we define an averaged kinematic viscosity using the harmonic mean:

$$\nu_{\rm h} = \frac{\eta}{\rho_{\rm h}}\,, \qquad \nu_{\rm c} = \frac{\eta}{\rho_{\rm c}}\,, \tag{5.8}$$

$$\bar{\nu} = \frac{\sum_i \eta_i}{\sum_i \rho_i} = \frac{2\eta}{\rho_{\rm h} + \rho_{\rm c}} = \frac{2\eta}{\frac{\eta}{\nu_{\rm h}} + \frac{\eta}{\nu_{\rm c}}} = \frac{2}{\frac{1}{\nu_{\rm h}} + \frac{1}{\nu_{\rm c}}}\,, \tag{5.9}$$

which is equivalent to a density-weighted mean:

$$\bar{\nu} = \frac{\nu_{\rm h}\rho_{\rm h} + \nu_{\rm c}\rho_{\rm c}}{\rho_{\rm h} + \rho_{\rm c}} = \frac{2\eta}{\rho_{\rm h} + \rho_{\rm c}}\,. \tag{5.10}$$

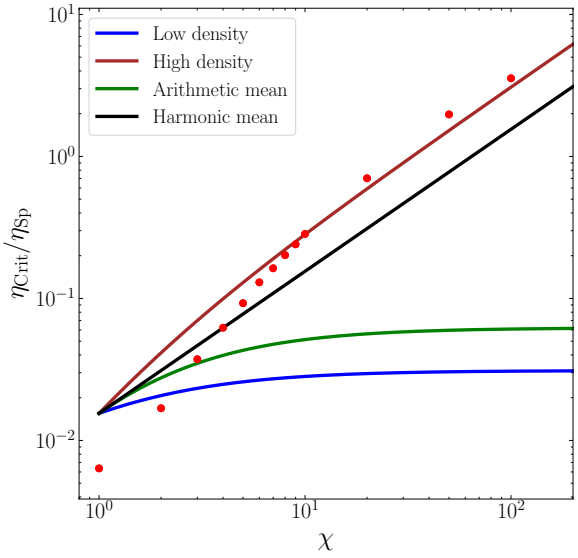

Figure 5.1: Dependence of $\eta_{\rm Crit}$ on the overdensity χ. The red dots show the numerical results; the blue line shows the theoretical expectation assuming that only the low density is relevant for kinematic viscosity; red line that only the high density is relevant; green line assuming an arithmetic mean of kinematic viscosity between the fluids; and black line a harmonic (weighted) mean. Note that we normalized the values of viscosity to the Spitzer value at 10^6 K.

With the harmonic mean, we can express the value of critical dynamic viscosity using expression (4.12) as

$$\eta_{\rm Crit} = \frac{\lambda\, \rho_{\rm h}\, \mathcal{M}_{\rm h} c_{\rm s,cold}\, \chi}{200}\,, \tag{5.11}$$

where the wavelength (λ), the density and Mach number of the hot gas ($\rho_{\rm h}$, $\mathcal{M}_{\rm h}$) and the soundspeed of the cold gas ($c_{\rm s,cold}$) are kept constant.

Previous studies have tested the critical viscosity estimate for different overdensities, but the results deviated from the predictions at high overdensities since they did not consider the difference in momentum (e.g. Esch, 1957; Roediger et al., 2013b). For high overdensities, each fluid carries a very different momentum (inertia) that viscosity needs to compensate for. By using a harmonic (weighted) mean, we are taking this effect into account.

To test the dependence of a critical viscosity on the overdensity χ, we run different simulations changing the value of χ and measure the critical viscosity in each case, using the planar slab setup described in §5.1.1. Since we use a unique dynamic viscosity in our setup, we quantify the critical dynamic viscosity (equation (5.11)). Fig. 5.1 shows the numerical results (red dots) normalized to the Spitzer value of viscosity at $T = 10^6$ K, together with different methods to average the kinematic viscosity besides the harmonic mean (black line): considering only the low density fluid $\bar{\nu} = \eta/\rho_{\rm h}$ (blue line); considering only the high density fluid $\bar{\nu} = \eta/\rho_{\rm c}$ (red line); and doing an arithmetic mean $\bar{\nu} = (\nu_{\rm h} + \nu_{\rm c})/2$ (green line).

The cold medium becomes denser when the density contrast increases. This has two effects: *(i)* the cold medium has a much lower kinematic viscosity $\nu_{\rm c} = \eta/\rho_{\rm c}$. *(ii)* The cold medium

carries much more momentum than the hot medium. For the high overdensity flows $\chi \gg 1$ we consider, it is a good approximation that the viscosity of the cold gas is negligible (as we show explicitly in §5.2.4, the hot gas viscosity is what matters), but that it contains almost all the momentum. Thus, the critical viscosity increases with overdensity, $\eta_{\rm crit} \propto \chi$ (equation (5.11) and Fig. 5.1), because the total momentum in the flow is higher and stronger friction is required to have an effect[3].

From the values of critical viscosity obtained and using the harmonic mean, we can compute their corresponding Reynolds number as

$$\mathrm{Re}_{\rm Crit} = \frac{\lambda\, v_{\rm shear}}{\bar{\nu}_{\rm Crit}} = \frac{\lambda\, v_{\rm shear}(\rho_{\rm h}+\rho_{\rm c})}{2\eta_{\rm Crit}} = 100\frac{1+\chi}{\chi^{1/2}}, \tag{5.12}$$

i.e., $\mathrm{Re}_{\rm Crit} \approx 100\chi^{1/2}$ for large χ.

5.2.2 Critical Viscosity vs Mach Number

According to our analytical estimate, the critical viscosity depends linearly on the Mach number for a given overdensity (see equation (5.11)). To test this relation, we run different simulations varying $\mathcal{M}_{\rm h}$ while keeping $\chi = 10$ fixed, and we measure the critical viscosity in each case, using the planar sheet setup described in §5.1.1. However, the theoretical analysis was made assuming incompressible fluids, which is a good approximation for low Mach number, but breaks down at high Mach numbers, where compressibility effects become significant.

When compressibility is taken into account, the classical dispersion relation of the KHI derived from linear analysis is not valid anymore (Landau, 1944; Landau & Lifshitz, 1987). Instead, the dispersion relation for compressive fluids in a planar sheet is

$$\left[\chi(\varpi-1)^2-\varpi^2\right]\cdot\left[\chi(\varpi-1)^2(\mathcal{M}_{\rm h}^2\varpi^2-1)-\varpi^2\right]=0\,, \tag{5.13}$$

where $\varpi \equiv \omega/k\Delta v_{\rm shear}$ (see Mandelker et al., 2016 for details).

The two roots of the quadratic part of the equation are always real, therefore, they do not describe the growth of the KHI. Two of the four roots in the quartic factor are also real, while two are complex conjugates. We take the imaginary part of both complex conjugates, which describe an exponential growth (positive sign) or decay (negative sign) of the instability. The positive imaginary numerical solutions of equation (5.13) for $\chi = 5, 10, 100$ are shown in Fig. 5.2.

In the case of $\chi = 10$, the instability grows (positive $\mathrm{Im}(\varpi)$) for $\mathcal{M}_{\rm h} \lesssim 1.77$. Above this critical value of Mach number ($\mathcal{M}_{\rm Crit}$), the solution becomes real and the KHI is stable (vertical dashed lines in Fig. 5.2). The general solution for $\mathcal{M}_{\rm Crit}$ is given by (Mandelker et al., 2016)

$$\mathcal{M}_{\rm Crit} = \left(1+\chi^{-1/3}\right)^{3/2}. \tag{5.14}$$

The value of $\mathcal{M}_{\rm Crit}$ for $\chi = 10$ is computed numerically in Fig. 5.3 for non-viscous fluids using the method described in appendix B[4], finding a $\mathcal{M}_{\rm Crit} = 1.65 \pm 0.5$.

[3]Note that in §4.3 we averaged by doing an arithmetic mean. However, at low overdensities ($\chi = 2$), the differences with a harmonic mean are small.

[4]The method in grid codes is slightly different than SPH codes. See McNally et al. (2012) for details.

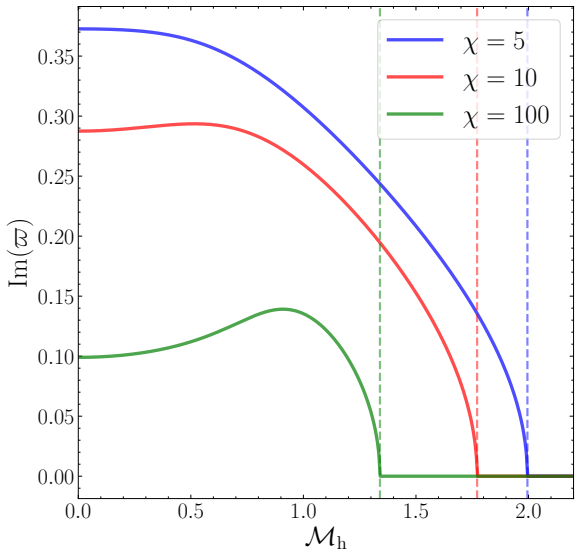

Figure 5.2: Numerical solution for the values of $\mathrm{Im}(\varpi)$ of equation (5.13) as a function of $\mathcal{M}_\mathrm{h}$ for $\chi = 5, 10, 100$. The dashed lines show the $\mathcal{M}_\mathrm{h}$ above which the KHI is stable.

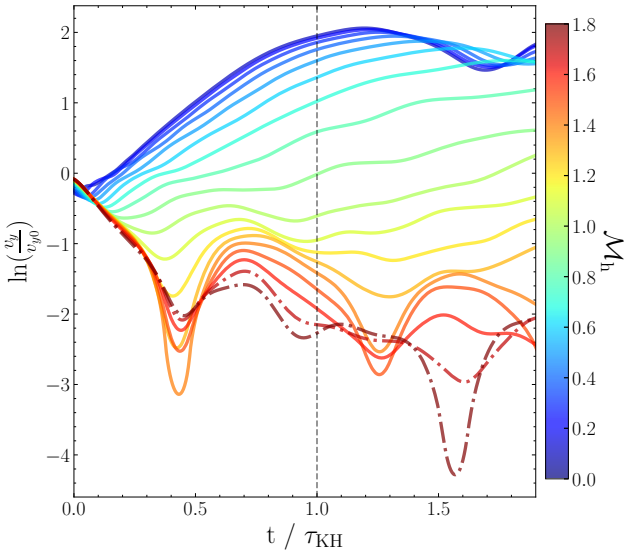

Figure 5.3: Growth of the KHI with time for $\chi = 10$, color-coded by $\mathcal{M}_\mathrm{h}$. The solid lines indicate the simulations in which the KHI is still unstable and the dash-dotted lines where the instability is suppressed (values above $\mathcal{M}_\mathrm{Crit}$), finding a $\mathcal{M}_\mathrm{Crit} = 1.65 \pm 0.5$.

For $\mathcal{M}_h > \mathcal{M}_{Crit}$, the instability is suppressed and the growth rate decays. An intuitive explanation for this is that when the instability starts growing, areas of high and low pressure are formed around the perturbation at a rate of approximately the sound-crossing time. These areas feed the instability, leading to its growth. At large Mach number, the shear motion of the fluids is faster than the soundspeed, preventing these areas of high and low pressure from forming and leading to the flattening and stabilization of the wave.

For $\mathcal{M}_h > \mathcal{M}_{Crit}$, the instability is fully suppressed by the compressive nature of the fluids, and the viscosity needed to keep the system stable is zero. Therefore, there is a transition from the incompressible limit where the suppression is dominated by viscosity to the compressible limit set by $\mathcal{M}_{Crit}$. An analytical solution for η_{Crit} as a function of $\mathcal{M}_h$ can be estimated in a similar way as in §4.4.2, but for compressible fluids.

In the incompressible limit ($\mathcal{M}_h \to 0$), the positive imaginary solution of equation (5.13) yields

$$\mathrm{Im}(\varpi) = \frac{\sqrt{\chi}}{(\chi+1)}, \qquad \mathrm{Im}(\omega) = k\Delta v \, \frac{\sqrt{\chi}}{(\chi+1)}, \tag{5.15}$$

recovering the KHI time scale (equation (4.4)), which in its general form is defined as

$$\tau_{KH} = \frac{2\pi}{\mathrm{Im}(\omega)} = \frac{2\pi}{k\Delta v_{shear}\,\mathrm{Im}(\varpi)}. \tag{5.16}$$

By using the numerical solution for $\mathrm{Im}(\varpi)$ (shown in Fig. 5.2) and evaluating $\tau_{KH} > \tau_\nu$ (i.e., the same analysis as in §4.4.2 for the incompressible case), we obtain an analytical solution for a critical viscosity in the compressible case:

$$\eta_{Crit} = \frac{\lambda\,\rho_h\,\mathcal{M}_h c_{s,cold}\sqrt{\chi}\,(\chi+1)\,\mathrm{Im}(\varpi)}{200}. \tag{5.17}$$

Fig. 5.4 shows the analytical estimate of η_{Crit}, normalized to the Spitzer value at $T = 10^6$ K, as a function of $\mathcal{M}_h$ for incompressible fluids (black dashed line) and for compressible fluids (blue dashed line). The red data points are the numerical values of η_{Crit} obtained from the simulations. Although the fit is not perfect due to the large assumptions made in the estimate, the initial growth at low $\mathcal{M}_h$ and the decay when $\mathcal{M}_h \sim \mathcal{M}_{Crit}$ match the theoretical estimate. However, there is a drop at $\mathcal{M}_h \sim 1$, indicating that the KHI becomes stable at transonic speeds. Although the origin of this drop is not clear, one possibility is that higher order modes of the KHI have different values of η_{Crit}. We will explore this purely adiabatic suppression in future work.

5.2.3 Turbulent Radiative Mixing Layers

To study how viscosity affects the TRMLs, we make use the value of critical viscosity and Reynolds number obtained in §5.2.1 for $\chi = 100$: $\eta_{Crit} = 6425 \pm 25$ and $\mathrm{Re}_{Crit} = 248.6 \pm 2.4$ respectively. In terms of Spitzer viscosity, the critical viscosity measured corresponds to $\eta_{Crit} \simeq 3.55\eta_{Sp}$ at a temperature of $T = 10^6$ K. We express the amount of viscosity in our setup as a function of the critical viscosity needed to suppress the instability. Using the 3D setup described in §5.1.2, we run a simulation with no viscosity for each Damköhler number Da (labeled as "No

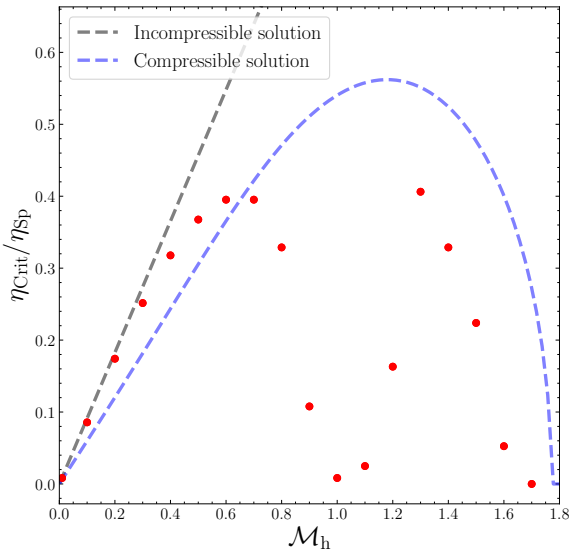

Figure 5.4: Dependence of $\eta_{\rm Crit}$ with the Mach number $\mathcal{M}_{\rm h}$. The numerical results (red dots) deviate from the analytical incompressible $\eta_{\rm Crit}(\mathcal{M}_{\rm h})$ (equation (5.11), black dashed line). However, this is corrected by taking into account the suppression due to high $\mathcal{M}_{\rm h}$ (equation (5.17), dashed blue line). Note that we normalized the viscosities to the Spitzer value at 10^6 K.

Table 5.1: Simulations of viscous, radiative mixing layers.

Label	Fraction of $\eta_{\rm Crit}$	Re	Spitzer Fraction
No visc	-	-	-
$0.05\eta_{\rm Crit}$	5% of $\eta_{\rm Crit}$	4972 ± 48	$0.18\eta_{\rm Sp}$
$0.1\eta_{\rm Crit}$	10% of $\eta_{\rm Crit}$	2486 ± 24	$0.36\eta_{\rm Sp}$
$0.5\eta_{\rm Crit}$	50% of $\eta_{\rm Crit}$	497.2 ± 4.8	$1.78\eta_{\rm Sp}$

visc"), with 5% of the critical viscosity ("$0.05\eta_{\rm Crit}$"), 10% of critical viscosity ("$0.1\eta_{\rm Crit}$") and 50% of critical viscosity ("$0.5\eta_{\rm Crit}$"). Although the definition of critical viscosity considers only the growth of the KHI within $1\tau_{KH}$, in this section we run the simulations for longer times for the proper development of turbulence. The set of simulations with different viscosities, as well as the value of the Reynolds number in each case, are shown in Table 5.1.

It is important to note that in the *No visc* run, although we do not include any explicit physical viscosity, there is still numerical viscosity given by resolution. Since our resolution consists of 64×64 in the $\hat{x}\hat{z}$ plane and the length of the box is $L_x = L_z = \lambda$, the cell length is $\Delta x = \lambda/64$, which sets the Kolmogorov scale of our *No visc* runs. The runs with explicit viscosity set the Kolmogorov scale at larger values, given by the percentage of critical viscosity taken in each case. Since we have not included explicit thermal conduction, the Field length of thermal conduction is given by $\delta = \Delta x = \lambda/64$. This allows us to explore the Karlovitz number (cf. §1.4.5) parameter space from Ka = 1 (*No visc* run) towards smaller values of Ka.

Front Morphology

Fig. 5.5 shows how viscosity affects mixing in the different runs for $\mathrm{Da}_{\mathrm{mix}} \ll 1$ (weak cooling, top panels) and $\mathrm{Da}_{\mathrm{mix}} \gg 1$ (strong cooling, bottom panels). Each panel shows a temperature slice through the box, centered at the interface between the two fluids at $t = 2.5\tau_{\mathrm{KH}}$. In the weak cooling regime (low Da, top panels), turbulence has developed in the run without explicit viscosity, whereas it is more suppressed the more viscous the mediums are (left to right).

It is important to note that the computation of critical viscosity is done during $t < \tau_{\mathrm{KH}}$, but naturally, viscosity is affecting the fluid movement for the entire simulation. This implies that, although during $t < \tau_{\mathrm{KH}}$ the instability can grow ($\eta < \eta_{\mathrm{Crit}}$), it might eventually lead to a quasi-laminar flow. This can be seen in the top right panel of Fig. 5.5, where a laminar regime has already been reached.

In the strong cooling regime (high Da, bottom panels), the results look similar regardless of the amount of viscosity. In all cases, the hot and cold media are clearly separated, and the front consists of (approximately) one cell only. Surprisingly, unlike in the weak cooling regime, the simulations show some movement in the interface independently of the amount of viscosity. This will be analyzed in §5.2.3.

Effect of Viscosity on Cooling Efficiency

The luminosity of turbulent radiative mixing layers is predominantly due to enthalpy flux (i.e., mass conversion from hot to cold medium) and not due to dissipation of kinetic energy (cf. Ji et al., 2019; Tan et al., 2021). We checked that this is also true in the case with viscosity (cf. appendix D), specifically also that viscous heating plays a negligible role.[5]

To study quantitatively the difference in results with and without viscosity, we measure the surface brightness Q in each case for each $\mathrm{Da}_{\mathrm{mix}}$. This surface brightness is calculated by measuring the total luminosity of the box L_{rad}, and dividing it by the area of the interface ($Q = L_{\mathrm{rad}}/\lambda^2$).

Fig. 5.6 shows the effect of viscosity for the simulations with the weakest cooling (left panel) and the simulations with the strongest cooling (right panel) considered. Note that the dark blue lines correspond to the *No visc* run, considering the estimated numerical viscosity. Although visually viscosity suppresses the development of turbulence in the weakest regime (see top panel of Fig. 5.5), the surface brightness obtained after several τ_{KH} is very similar in all cases.

In the case of strong cooling (right panel of Fig. 5.6)[6] the differences become larger, with an increase of Q with viscosity. This might be counter-intuitive if one thinks of viscosity suppressing the turbulent movement and, therefore, the cooling process. This will be analyzed in more detail in §5.2.3.

Fig. 5.7 shows the relation between surface brightness and Da (equation (1.39)). Our simulations without viscosity reproduce the expected broken powerlaw behavior (cf.

[5] We checked that viscous dissipation (RHS of equation (2.18)) contributes negligibly to Q by switching off the relevant terms explicitly and found no differences in the overall cooling.

[6] Since for $\mathrm{Da}_{\mathrm{mix}} > 1$, $t_{\mathrm{cool}} < \tau_{\mathrm{KH}}$, we run the simulations for less Kelvin-Helmholtz times.

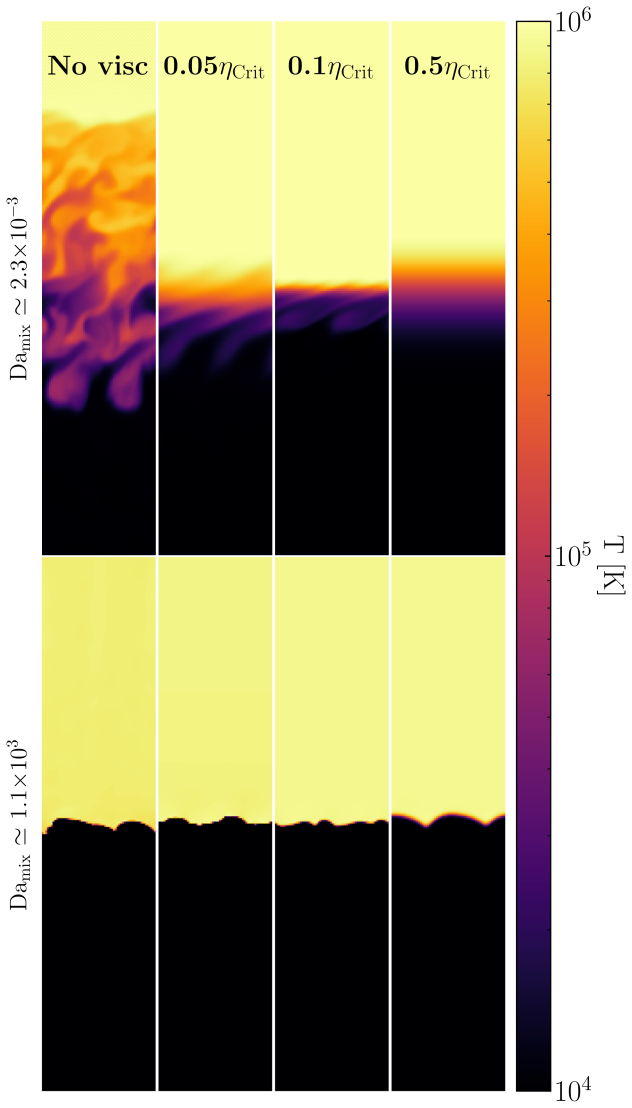

Figure 5.5: Temperature slices for the different TRMLs simulations. *From left to right*: Non-viscous case, 5% of critical viscosity, 10% of critical viscosity and 50% of critical viscosity. *Top row*: very weak cooling with $\mathrm{Da_{mix}} \simeq 2.3 \times 10^{-3}$. *Bottom row*: very strong cooling with $\mathrm{Da_{mix}} \simeq 1.1 \times 10^{3}$.

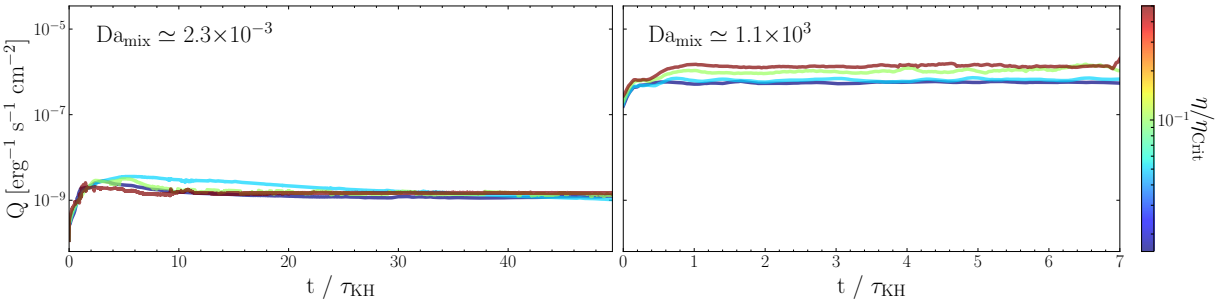

Figure 5.6: Evolution of the surface brightness due to cooling in the mixing layers. *Left panel*: Evolution of Q color-coded by viscosity in a very weak cooling regime with $\mathrm{Da_{mix}} \simeq 2.3 \times 10^{-3}$. *Right panel*: Evolution of Q for different viscosities in a very strong cooling regime with $\mathrm{Da_{mix}} \simeq 1.1 \times 10^{3}$.

equation (1.39)) with the change of regime from weak to strong cooling occurring at $\mathrm{Da_{mix}} \simeq 1$[7]. Although in the weak cooling regime the differences are small, in the strong cooling regime, viscosity leads to larger values of Q. This implies that the transition from weak to strong cooling regime is shifted towards larger values of $\mathrm{Da_{mix}}$ when increasing the amount of viscosity.

In summary, both Figs. 5.6 and 5.7 reveal two counter-intuitive behaviors: while we expect viscosity to suppress the mixing process and, thus, the amount of intermediate temperature gas available for cooling, we find *(i)* for the weak cooling regime a mass transfer rate between the phases independent of viscosity, and *(ii)* for the strong cooling regime even an *increased* $\dot{m}$ with larger values of viscosity. This implies that either the naive expectation of how viscosity affects turbulence is wrong, or the u'-Q relation is changed due to viscosity. We will explore this by analyzing the turbulence inside the mixing layer in the next sections.

Effect of Viscosity on Turbulence

From visual inspection of Fig. 5.5, viscosity seems to suppress turbulence in the weak cooling regime, but not in the strong cooling regime. To test this in a quantitative way, we compute the turbulent velocity in our domain following Tan et al. (2021), i.e., to avoid the effect of bulk motions, we measure the velocity dispersion in the $\hat{z}$ direction, by taking the maximum of v_z profile for each snapshot and then averaging over several τ_{KH}[8].

Fig. 5.8 shows relation (1.39), between Q and the turbulent velocity normalized to the cold gas sound speed, color-coded by $\mathrm{Da_{mix}}$. To get rid of the $\mathrm{Da_{mix}}$ dependence, we normalize the value of Q to the value of $\widetilde{Da}^{\alpha}$, as done in Das & Gronke (2023). $\widetilde{Da}$ is calculated from equation (1.38), using the turbulent velocity measured from the simulations and α corresponds to the index from equation (1.39). By doing this normalization, $Q/\widetilde{Da}^{\alpha} \propto u'$. This relation is satisfied in the strong cooling regime ($\mathrm{Da_{mix}} > 1$), regardless of the amount of viscosity. However, in the weak cooling

[7]The values for very weak cooling lie under the fitted line. This was also found in Das & Gronke (2023). For this reason, for the fit we take the values of $\mathrm{Da_{mix}} > 5 \times 10^{-2}$.

[8]In this process, we also check the velocity dispersion in the $\hat{x}$ and $\hat{y}$ direction after subtracting the bulk motions, making sure that turbulence is isotropic.

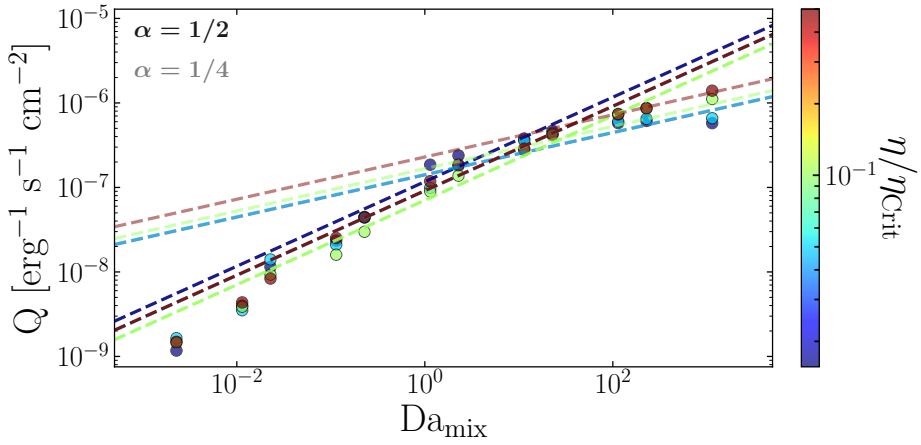

Figure 5.7: Surface brightness Q as a function of $\mathrm{Da}_{\mathrm{mix}}$ color-coded by viscosity. The darker dashed line shows the best fit in each case in the weak cooling regime (Da < 1) with a slope of $\alpha = 1/2$. The lighter dashed line shows the best fit in each case in the strong cooling regime (Da > 1) with a slope of $\alpha = 1/4$.

regime ($\mathrm{Da}_{\mathrm{mix}} < 1$), the relation is satisfied for the *No visc* (circles) and $0.05\eta_{\mathrm{Crit}}$ (triangles) cases. The turbulent velocity of the runs with $0.1\eta_{\mathrm{Crit}}$ (squares) is one order of magnitude lower than expected, and the runs with $0.5\eta_{\mathrm{Crit}}$ (crosses), more than two orders of magnitude lower.

This result indicates that, as previously noticed by visual inspection in Fig. 5.5, viscosity suppresses turbulence but does not reduce surface brightness. However, the suppression occurs in the weak cooling regime, whereas in the strong cooling regime, the relation between Q and u' is not modified. This is surprising, due to the weak dependence of u' with Da ($u' \propto \mathrm{Da}^{1/10}$, see Tan et al., 2021).

We also tested this weak dependence of the cooling on turbulence explicitly and show the results in Fig. 5.9. The simulations without viscosity fall on the $u' \propto \mathrm{Da}^{1/10}$ relation found in Tan et al. (2021). In the weak cooling regime ($\mathrm{Da}_{\mathrm{mix}} < 1$), the relation is not satisfied in the viscous runs. The turbulent velocities drop until they reach the u' in adiabatic simulations, saturating at this value (blue-dashed lines). The adiabatic system sets the floor for turbulent velocities depending on viscosity.

In this weak cooling regime, the simulations show the expected behavior: the more viscous the system is, the less turbulent it becomes. However, for larger values of $\mathrm{Da}_{\mathrm{mix}} > 1$, all the runs tend to follow the $u' \propto \mathrm{Da}^{1/10}$, i.e., the runs mostly exhibit a level of turbulence *(a)* much higher than expected and *(b)* fairly independent of viscosity.

Furthermore, Fig. 5.9 also shows that the characteristic Damköhler number at which the simulations follow the expected $u' \propto \mathrm{Da}^{1/10}$ relation increases with increasing viscosity, i.e. the runs with lower viscosity start following the relation at a lower $\mathrm{Da}_{\mathrm{mix}}$, while the more viscous runs at a higher $\mathrm{Da}_{\mathrm{mix}}$. In the strong cooling regime, all the simulations follow the $u' \propto \mathrm{Da}^{1/10}$ relation, suggesting that the effect of viscosity is reduced due to cooling.

Viscosity acts as a friction, reducing the velocity of the gas, therefore, it is expected to produce lower values of turbulent velocity. However, two questions arise:

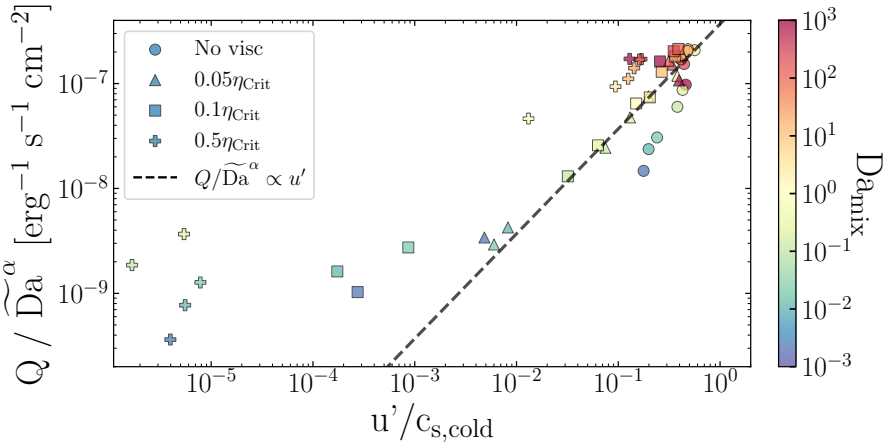

Figure 5.8: Relation between Q normalized by the numerically measured Damköhler number $\widetilde{Da}$ in each regime, and the turbulent velocity for different viscosities and color-coded by $\mathrm{Da_{mix}}$. The dashed line shows the relation $Q/\widetilde{Da}^{\alpha} \propto u'$ expected.

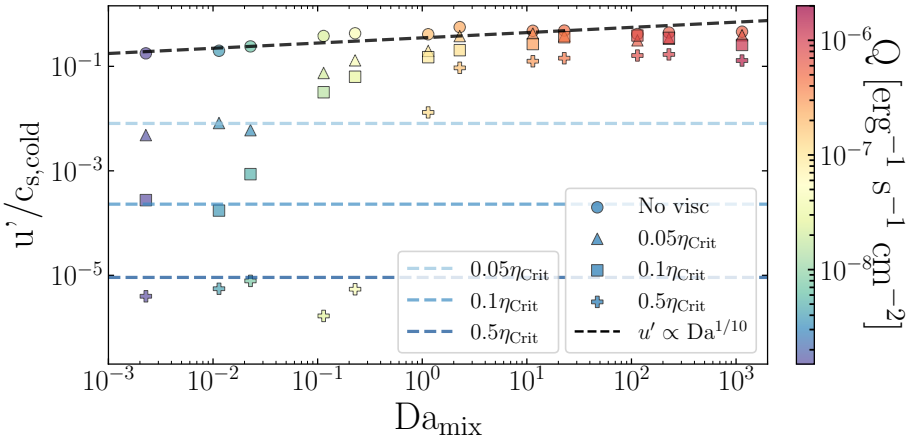

Figure 5.9: Dependence of the turbulent velocity with $\mathrm{Da_{mix}}$ for different amounts of viscosity and color-coded by the surface brightness. The black-dashed line indicates the dependency of $u' \propto \mathrm{Da_{mix}}^{1/10}$. The blue-dashed lines show the turbulent velocity values of the adiabatic system with different viscosities.

1. Viscosity suppresses turbulence in the weak cooling regime (Da $<$ 1) – as expected. However, why is the amount of cooling only weakly affected (cf. Fig. 5.7), and therefore effectively breaking the universal $u' - Q$ relation (cf. Fig. 5.8)?

2. On the other hand, viscosity has a weak effect on both the level of turbulence as well as the amount of cooling in the strong cooling regime (cf. Figs. 5.8 and 5.9). This is particularly puzzling, since turbulence only depends very weakly on cooling (cf. Fig. 5.9); thus, even with very strong cooling, turbulence should not directly 'overpower' the effect of viscosity.

In the following two sections, we will discuss the two questions raised above subsequently.

Weak Cooling Regime

To address the first question, i.e., why for Da $<$ 1 the cooling rate is not affected by viscosity (but u' is), we need to understand the behavior of a viscous gas in the weak cooling regime. Due to the long cooling time, the gas behaves similarly to an adiabatic gas, which has been previously studied in detail (e.g. Roediger et al., 2013b; Marin-Gilabert et al., 2022). Viscosity smooths out the shear velocity gradient and suppresses the growth of instabilities, leading to a reduced turbulent velocity (see the top panel of Fig. F1, and Chapter 4). However, if turbulence is not the driver for mixing, why is Q of the same order of magnitude regardless of the amount of viscosity?

When viscosity is strong enough, the instabilities are suppressed, leading to a laminar flow, rather than a turbulent flow. The theoretical relation in Fig. 5.8 assumes turbulent mixing (e.g. Damköhler, 1940; Shchelkin, 1943), therefore it is not surprising that for high viscosities the simulations do not follow the expected relation. Viscous diffusion dominates over convection and cooling, increasing the thickness of the interphase, producing that the theoretical analysis fails (e.g. Klimov, 1963; Libby & Williams, 1982). Although the viscous runs present a laminar flow, the amount of gas at intermediate temperatures where the cooling curve peaks is similar among the viscous cases (see top row of Fig. E1 in appendix E). The non-viscous case leads to a higher amount of intermediate temperature gas due to turbulent mixing. However, the long cooling time in the weak cooling regime produces a bottleneck effect, which explains the constant Q obtained, despite the different diffusion mechanisms. Note that our criterion for critical viscosity is defined within $1\tau_{\rm KH}$, but our simulations in the week cooling regime are run until $50\tau_{\rm KH}$. This means that, although within $1\tau_{\rm KH}$ the instability might grow, the system might become laminar after several $\tau_{\rm KH}$.

Strong Cooling Regime

To answer the second question, i.e., why neither u' nor the cooling is strongly affected by viscosity for Da $>$ 1, we need to study in detail the strong cooling regime. Viscosity is expected to reduce turbulence, although in the strong cooling regime, the $Q - u'$ relation follows the analytical expectations from turbulent theory. So if viscosity is expected to suppress turbulence, why is u' similar in all cases regardless of the amount of viscosity?

In the strong cooling regime, cooling acts much faster than turbulent mixing, cooling quickly all the intermediate gas and producing a front where cooling occurs that is $\sim$ 1 cell thick. As

a consequence, cooling tends to keep the temperature profile sharp and, if the system is in pressure equilibrium, also the momentum and shear velocity profiles. This is the opposite effect to viscosity, which tends to smooth out the shear velocity gradient. This produces that, in the strong cooling regime, cooling dominates over viscosity, keeping the shear velocity profile sharp and, as a consequence, being able to induce turbulence in a similar way as the non-viscous case and reducing the effect of viscosity (see Fig. F1 in appendix F).

Keeping the shear profile sharp leads to continuous Kelvin-Helmholtz instabilities forming (see Chapter 4), and hence to turbulence, as we can see in the top panel of Fig. 5.10, where we show the dependence of turbulence with the scale d at which the shear velocity profile is smoothed after $t = 1.25\tau_{\rm KH}$ (see appendix G for details). For *No visc* and $0.05\eta_{\rm Crit}$, d is always small, producing larger values of u' (i.e. turbulence). For the cases of $0.1\eta_{\rm Crit}$ and $0.5\eta_{\rm Crit}$, the weak cooling regime results show the effect of viscosity in smoothing out the gradient (large values of d), leading to a low u'. However, in the strong cooling regime, the shear velocity gradient becomes sharp (low values of d), inducing turbulence. In summary, while cooling does not (strongly) affect the turbulence directly, it sharpens the density gradient required to seed KHI, and hence combats the smoothing effect of viscosity.

In other words, a sharp velocity gradient induces turbulence and, therefore, leads to larger surface brightness. This can be seen in the bottom panel of Fig. 5.10, where larger values of $\rm Da_{mix}$ lead to sharper gradient (lower d) and, therefore, larger Q.

To test our assumption that the system follows the expected $u' \propto \rm Da^{1/10}$ when cooling dominates over viscosity, we estimate analytically at which value of $\rm Da_{mix}$ this should happen. Cooling dominates over viscosity when $t_{\rm cool} < \tau_\nu$, where $t_{\rm cool}$ is measured at $T_{\rm mix} = 2 \times 10^5$ K and τ_ν corresponds to the time that a given viscosity takes to smooth out the velocity gradient a distance $d = \lambda/10$ (see §4.4.2).

In our case, we express the different amounts of viscosity as a function of the critical viscosity as $\eta = \zeta\, \eta_{\rm Crit}$, where ζ is the fraction of the critical viscosity used. Using the equation for critical viscosity (equation (4.12)), KH time (equation (4.4)) and $\nu = \eta/\rho$, we can express η as

$$\eta = \zeta\, \eta_{\rm Crit} = \zeta \frac{\lambda^2 \rho}{100 \tau_{\rm KH}}\,. \tag{5.18}$$

We can also express $t_{\rm cool}$ as

$$t_{\rm cool} = \frac{\tau_{\rm KH}}{\rm Da}\,, \tag{5.19}$$

where $t_{\rm turb} = \lambda/u' \sim \tau_{\rm KH}$ and the viscous time scale as

$$\tau_\nu = \frac{d^2}{\nu} = \frac{d^2 \rho}{\eta} = \frac{\lambda^2 \rho}{100\, \eta} = \frac{\tau_{\rm KH}}{\zeta}\,. \tag{5.20}$$

Therefore, cooling will dominate over viscosity when

$$\rm Da > \zeta\,. \tag{5.21}$$

We tested this estimate with our simulations by checking the critical value of $\rm Da_{mix}$ (which we denote as $\rm Da^*$), when the simulations start to follow the $u' \propto \rm Da^{1/10}$ relation for the different

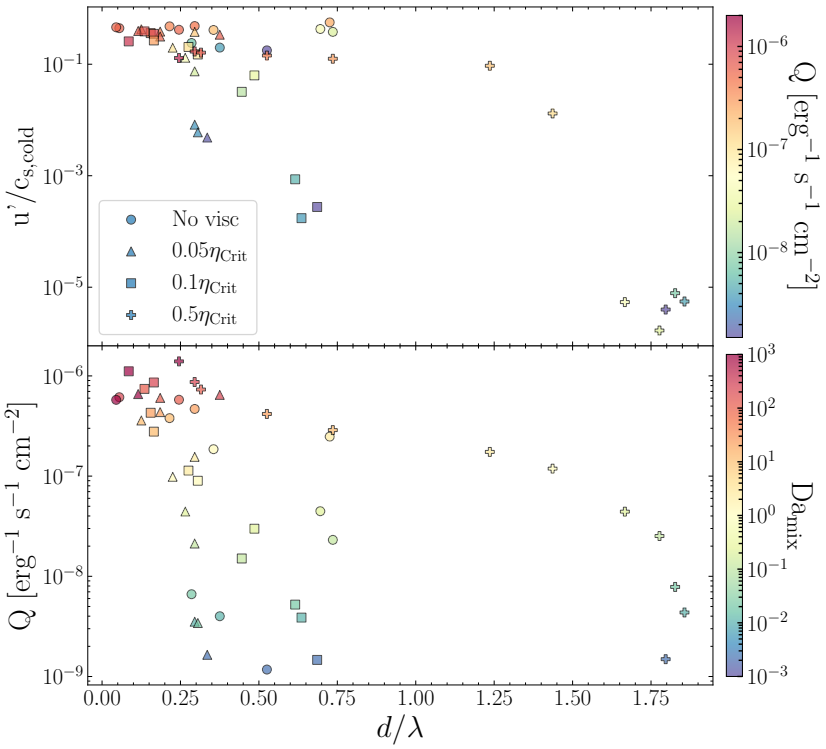

Figure 5.10: *Top panel*: Turbulent velocity as a function of the velocity gradient width, color-coded by the surface brightness. *Bottom panel*: Surface brightness as a function of the velocity gradient width, color-coded by $\mathrm{Da}_{\mathrm{mix}}$.

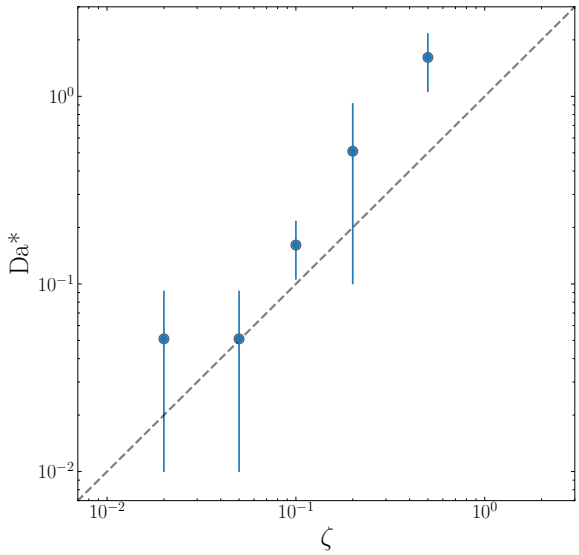

Figure 5.11: Measured critical Da (Da*) vs fraction of critical viscosity (ζ) for different sets of simulations. We included two more sets for completeness that are not shown in the previous plots. The dashed line indicates the expected one-to-one relation.

amounts of viscosity (cf. Fig. 5.9 in which one can read off Da* directly). We included two more sets of simulations for completeness, and we plot the computed values of Da* as a function of ζ in Fig. 5.11.

Although the theoretical estimate was based on broad assumptions, the computed values of Da* from our simulations fit the theoretical estimate. This agrees with our previous assumption that cooling effectively reduces the effect of viscosity by keeping the temperature gradient sharp.

To understand why cooling is increased (by a factor of ~ 2) for the more viscous runs at Da $>$ Da*, recall that while cooling reduces the effect of viscosity, the viscous runs still lead to a broader front (see bottom row of Fig. 5.5). As a consequence, the amount of gas with an intermediate temperature is larger with viscosity (see bottom row of Fig. E1 in appendix E). This produces that the overall amount of cooling is larger with viscosity than without viscosity, leading to a slightly higher Q in the strong cooling regime in the cases with higher viscosity.[5] This can also be seen in the bottom panel of Fig. 5.10 where, despite d becomes small in the strong cooling regime regardless of the amount of viscosity, d is still larger in the most viscous runs, leading also to a larger Q for a given $\mathrm{Da}_{\mathrm{mix}}$.

To study how u' depends on viscosity in more detail, Fig. 5.12 shows how turbulent velocities change with viscosity. In the non-viscous case, the data points cluster together, corresponding to the weak dependence of u' with Da. For higher viscosities, the two regimes defined by Da*(η) can be identified in each case: the data points group separately in the viscous-dominated regime ($\mathrm{Da}_{\mathrm{mix}} < \zeta$) and in the cooling-dominated regime ($\mathrm{Da}_{\mathrm{mix}} > \zeta$).

Assuming that u' depends on viscosity by a power law $u' \propto \eta^{\alpha}$, we can fit the slopes for individual $\mathrm{Da}_{\mathrm{mix}}$ in Fig. 5.12 and check the two different regimes. Fig. 5.13 shows the different values of α depending on $\mathrm{Da}_{\mathrm{mix}}$, reflecting the change of regime from viscous-dominated to

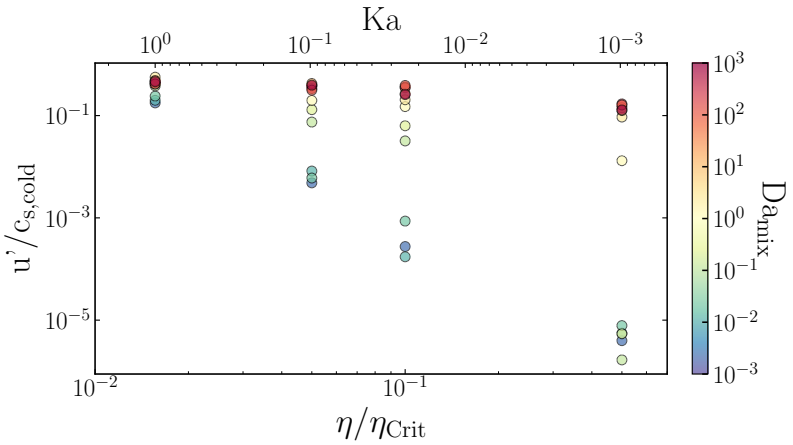

Figure 5.12: Turbulent velocity as a function of the amount of viscosity of the medium (Karlovitz number), color-coded by $\mathrm{Da_{mix}}$.

cooling-dominated at $\mathrm{Da_{mix}} \sim 0.5$. In the viscous-dominated regime (low $\mathrm{Da_{mix}}$) the turbulent velocity decays with viscosity as $u' \propto \eta^{-3}$, while in the cooling-dominated regime (high $\mathrm{Da_{mix}}$) the exponent is close to zero, indicating that the system behaves similarly regardless of the amount of viscosity[9].

5.2.4 Temperature Dependent Viscosity

Considering a more realistic Spitzer viscosity dependent on the temperature of the gas, each fluid will have a viscosity η. In the case of the cold fluid: $\eta_{\mathrm{Cold}} \propto T_{\mathrm{Cold}}^{5/2}$; while in the hot medium: $\eta_{\mathrm{Hot}} \propto T_{\mathrm{Hot}}^{5/2}$. Therefore, by comparing both viscosities, we have:

$$\eta_{\mathrm{Hot}} = \eta_{\mathrm{Cold}} \left(\frac{T_{\mathrm{Hot}}}{T_{\mathrm{Cold}}} \right)^{5/2} = \eta_{\mathrm{Cold}}\, \chi^{5/2} \,. \tag{5.22}$$

In the case of an overdensity of $\chi = 100$: $\eta_{\mathrm{Hot}} = 10^5\, \eta_{\mathrm{Cold}}$, rendering the viscosity of the cold medium negligible.

Additionally, the diffusivity of a system depends on the diffusion coefficient, which in the viscous case is set by the kinematic viscosity (ν, see §2.2). For a system with a constant dynamic viscosity (η, as in our setup) but two different densities, each fluid will have a different diffusivity (see equation (2.3)). Since the kinematic viscosity depends on the inverse of the density, for a given dynamic viscosity, the cold medium will have a lower diffusivity compared to the hot medium. As a consequence, for systems with a high density contrast, the diffusivity of the system is set by the hot gas.

Taking into account that: with a more realistic temperature-dependent Spitzer viscosity, the dynamic viscosity of the cold medium is negligible and that the viscous diffusion is set by the hot

[9]Since the change of regime depends on the value of viscosity, the "transition zone" produces big errors in the fit, where low viscosity runs behave already as non-viscous, but high viscosity runs are still viscous-dominated.

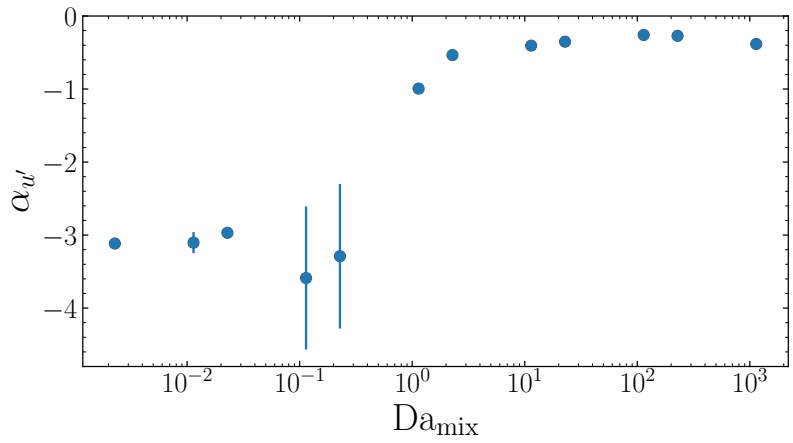

Figure 5.13: Exponent of the dependence of the turbulent velocity with the amount of viscosity (Karlovitz number) calculated from Fig. 5.12 as a function of $\mathrm{Da}_{\mathrm{mix}}$.

gas, a viscous cold medium should have a small impact compared to a viscous hot medium. We tested this using 1D simulations, with the following setup:

$$(\rho,\, T,\, v,\, \eta) = \begin{cases} (\rho_{\mathrm{Cold}},\, T_{\mathrm{Cold}},\, -v_x,\, \eta_{\mathrm{Cold}}) & \text{for } y < 0 \\ (\rho_{\mathrm{Hot}},\, T_{\mathrm{Hot}},\, v_x,\, \eta_{\mathrm{Hot}}) & \text{for } y > 0\,, \end{cases} \tag{5.23}$$

where $\Delta v_x/c_s = 0.24$, we keep T_{Hot} and ρ_{Hot} constant and change density (and temperature) of the cold medium as $T_{\mathrm{Hot}}/T_{\mathrm{Cold}} = \rho_{\mathrm{Cold}}/\rho_{\mathrm{Hot}} = 2, 5, 10, 100, 1000$. To analyze the diffusivity depending on the medium, we set a constant viscosity of $\eta = 25$ (in internal units) first in the cold medium and then in the hot medium. Fig. 5.14 shows the v_x profile after $\Delta v_x t/L = 2.50$ for the two cases: the viscous cold medium on the top panel and the viscous hot medium on the bottom panel.

When the cold medium is viscous (top panel in Fig. 5.14), diffusivity is decreased as the cold medium becomes denser. Thus, if the initial (i.e., lowest overdensity) value of viscosity is too low to have a discernible effect, it becomes increasingly negligible at higher overdensity. When the hot medium is viscous (bottom panel in Fig. 5.14), diffusivity remains constant, since the density of the hot medium is kept constant. However, the velocity profile becomes smoother as the cold medium becomes denser, despite the cold medium not being viscous. This happens because, although the cold medium is not viscous, it carries a lot more momentum than the hot (and viscous) medium. Therefore, when the cold medium transfers momentum to the hot medium, viscosity changes the momentum of the hot medium very effectively, smoothing the velocity gradient. The denser the cold medium is, the more momentum is transferred to the hot medium, leading to a smoother velocity profile. These results corroborate the assertion in §5.2.1, that the hot phase dominates viscosity and the cold phase dominates momentum. Note that this leads to the interesting effect that higher overdensities imply a larger degree of smoothing of the velocity profile, however, as η_{crit} also rises (cf. equation (5.11); Fig. 5.1), a higher viscosity is required to suppress the KHI.

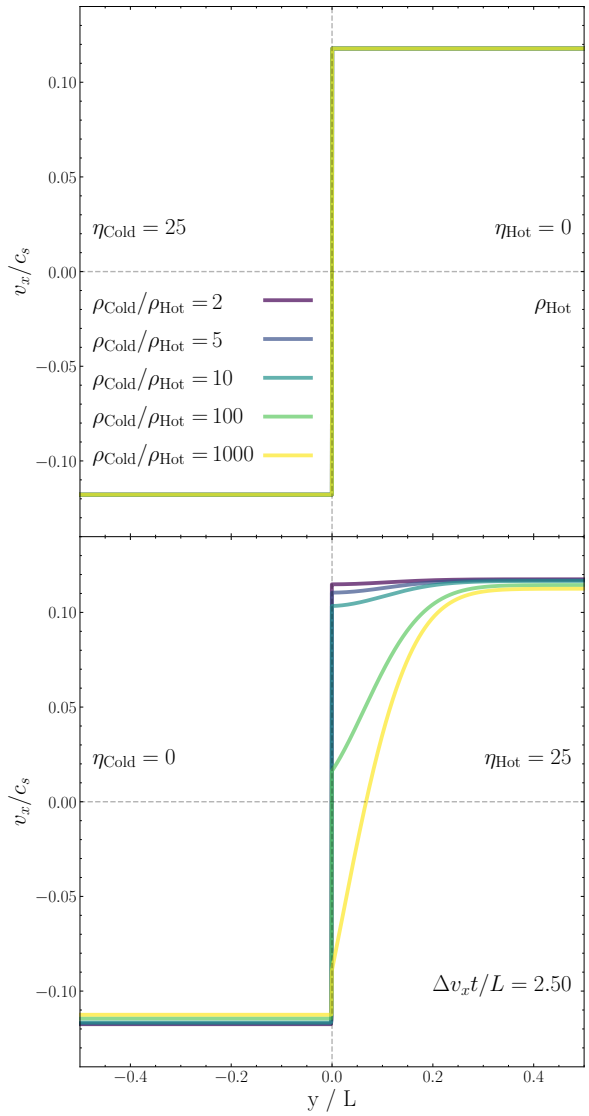

Figure 5.14: Velocity profile of 1D simulations. *Top panel*: Only the cold gas ($y < 0$) is viscous. *Bottom panel*: Only the hot gas ($y > 0$) is viscous.

Considering a constant η for the whole system leads to a diminishing momentum diffusion in the cold medium, similar to a realistic temperature-dependent Spitzer viscosity. Therefore, a constant η would lead to more realistic results than considering a constant ν, where both media would be equally diffusive.

In this Chapter, we have focused on the sub-critical viscosity regime, where all the cases studied have a viscosity smaller than the critical viscosity. The instability is able to grow within one KH time, being enhanced by strong cooling and allowing to keep the turbulence (see §5.2.3). In the temperature domain that we consider in this Chapter, where the cooling function peaks (10^4 K $< T < 10^6$ K), the Spitzer value for the $2\eta_{\rm Crit}$ is $2\eta_{\rm Crit} \simeq 7.10\eta_{\rm Sp}$ (cf. §5.2.3, Table 5.1), which is not realistic in plasma physics (Kunz et al., 2022). Therefore, an astrophysical scenario with such a high level of viscosity is very unlikely.

5.3 Applications

Viscosity becomes relevant in very hot and ionized media, with temperatures typically above 10^6 K. On the other hand, cooling efficiency peaks between $10^4 - 10^6$ K. This means that both cooling and viscosity will act together in astrophysical scenarios where very hot and cold mediums co-exist and mix, which is the case for the ICM, ISM, and CGM (see §1.3) – but also in other multiphase systems such as galactic winds or coronal rain. This interaction might happen in different astrophysical processes, where the Reynolds number is comparable to the ones used in this Chapter (see Table 5.1). Similarly, mixing and radiative cooling are physical processes that occur frequently in these multiphase systems. In fact, viscosity, mixing, and cooling are commonly thought of as being crucial in determining their long-term evolution.

Examples of such multiphase systems include:

- Galaxies moving through the ICM experience a ram pressure that strips the cold ISM (e.g. Gisler, 1976; Nulsen, 1982). The growth of instabilities in the tails mixes the hot ICM with the cold ISM (e.g. Iapichino et al., 2008; Ghosh et al., 2024). As a consequence, the hot ICM cools down, providing new gas and enhancing star formation (Müller et al., 2021). Viscosity not only affects the morphology and mixing of the tail with the medium (e.g. Kraft et al., 2017; Marin-Gilabert et al., 2024), but also the cooling efficiency and, therefore, it might change the star formation rate.

- The existence of multiphase gas within galactic winds is commonly often attributed to the effects of continuous cooling (see reviews by Veilleux et al., 2020; Thompson & Heckman, 2024). Similarly, cold clouds infalling through the CGM is another example where the hot gas of the CGM mixes with the cold gas of the cloud being disrupted (Gronke & Oh, 2018; Gronke et al., 2021). When the CGM is hot enough ($T > 10^6$ K), transport processes become relevant and shape the morphology of the tails of the cloud (Brüggen et al., 2023). Viscosity affects the cloud dynamics, as well as the evolution and evaporation of the tail (Jennings & Li, 2021). It will affect, therefore, the amount of cold gas and the mixing efficiency of the cloud and the CGM. The mixing between the cold stripped gas and the medium can be observed and studied using different ion lines (e.g. Kwak & Shelton, 2010).

- 'Cold streams' in hot galactic halos are likely crucial in order to understand galaxy fueling and growth (Dekel et al., 2009). As those are another classical example of multiphase gas interactions, mixing, cooling, as well as the effect of viscosity, have been discussed in the context of cold streams (Brüggen & Ruszkowski, 2005; Mandelker et al., 2020).

In each of these systems, turbulence, mixing, and cooling are key to understanding the dynamics and ultimate fate of the gas. As a result, key findings from studies of turbulent radiative mixing layers (e.g. Ji et al., 2019; Fielding et al., 2020; Tan et al., 2021) are commonly invoked to interpret a wide range of observational diagnostics (e.g. Qu et al., 2022; Lin et al., 2025). However, most previous work has neglected the role of viscosity, meaning that such interpretations could be significantly biased. Particularly if viscosity were to strongly suppress turbulent mixing and, consequently, cooling, as might be naively expected.

In this study, however, we show that—contrary to expectations—viscosity has only a modest impact on the dynamics of turbulent mixing layers. In particular, for systems in the 'fast cooling' regime (Da $>$ 1), which includes most of the astrophysical environments described above, not only does the u'–Q relation remain unchanged, but also the amount of turbulence expected from KHI. This allows one to continue using established theoretical predictions to relate, for instance, line widths to expected emissivities.

Another important application of our work relates to the growing number of multiphase subgrid models, which aim to address the long-standing resolution problem in large-scale (e.g., cosmological) simulations. Such simulations are unable to fully resolve multiphase structures—like those discussed above—and therefore rely on subgrid prescriptions to approximate their behavior (Huang et al., 2020; Smith et al., 2023; Butsky et al., 2024; Das et al., 2024). These models commonly adopt a numerical multi-fluid framework (e.g. Weinberger & Hernquist, 2022), with source and sink terms for each fluid component informed by small-scale simulations of TRMLs (e.g. Tan et al., 2021).

However, to date, none of these models account for the combined effects of radiative cooling and viscosity. Instead, they implicitly assume – or hope – that the omitted effect (e.g., viscosity) has a negligible influence on the relevant dynamics. In this work, we provide a robust physical foundation for current and future implementations of multiphase subgrid models by explicitly testing this assumption. In particular, we show how mass transfer rates between phases are (largely) unaffected by viscosity, thus justifying the use of existing cooling-based prescriptions in multi-fluid models.

Taken together, our results show that viscosity, while potentially important in shaping large-scale morphology, does not significantly alter the fundamental scaling relations governing turbulent mixing and radiative cooling. Although one might naively expect viscosity to suppress mixing and thereby invalidate commonly used theoretical predictions, we find – perhaps surprisingly – that this is not the case. This lends confidence to both the interpretation of observational diagnostics and the construction of multiphase subgrid models, which often rely on idealized, inviscid small-scale simulations. By clarifying the limited role of viscosity, our work helps bridge the gap between detailed local physics and the broader astrophysical systems

in which these processes operate.

5.4 Conclusions

The role of viscosity in turbulent radiative mixing layers is key for understanding the suppression of hydrodynamical instabilities and their effect on multiphase gas evolution in astrophysical environments. In this Chapter, we investigated the impact of viscosity on the KHI and its implications for mixing and cooling processes. Using numerical simulations, we systematically varied viscosity, overdensity, and Mach number to study the transition from turbulent to laminar regimes and characterized the interplay between viscosity and radiative cooling.

We confirm previous results (e.g. Roediger et al., 2013b; Marin-Gilabert et al., 2022, see Chapter 4) that in adiabatic setups, the KHI is suppressed when the dynamical viscosity exceeds a critical threshold. We derived an analytical solution based on the comparison between the viscous time scale and the instability growth time, and confirmed numerically that the critical viscosity depends linearly on overdensity.

At high Mach numbers in compressive-adiabatic setups, the KHI transitions from a viscosity-dominated suppression to a compressibility-induced stabilization. We verified numerically that the instability is fully suppressed above a critical Mach number, in agreement with previous analytical work (Mandelker et al., 2016).

In a multiphase system, viscosity alters the turbulent cascade, modifying the mixing layer properties. In the weak cooling regime, viscosity suppresses turbulence, transitioning the mixing layer into a laminar state dominated by diffusion rather than convection (leading to an altered $u' - Q$ relation). Nevertheless, because here cooling is the bottleneck, the overall luminosity is unchanged.

Perhaps surprisingly, in the strong cooling regime, we find that all the TRMLs simulations have the same surface brightness and net cooling rates as inviscid simulations, regardless of the amount of viscosity. This counter-intuitive behavior arises from cooling, sharpening the temperature profile, thus, directly compensating the smoothing effect of viscosity, allowing for KHI to develop and keeping the scaling relations in TRMLs intact. We derived an analytical estimate for when viscosity does not affect cooling rates based on the relative time scales of turbulence, viscosity, and cooling. Our numerical results match this theoretical prediction, confirming that cooling can compensate for the viscous suppression in sufficiently strong cooling conditions.

The suppression of turbulence only mildly affects the energy dissipation in TRMLs. In the weak cooling regime, viscosity reduces turbulent velocities but has a weak effect on surface brightness. In the strong cooling regime, the surface brightness increases up to a factor ~ 2 with viscosity, suggesting that the smoother temperature gradient leads to a larger amount of intermediate temperature gas, enhancing cooling efficiency.

These results quantify the impact of viscosity in astrophysical TRMLs and have important implications for the dynamics of ram-pressure stripping galaxies, galaxy halos, as well as the CGM and ICM.

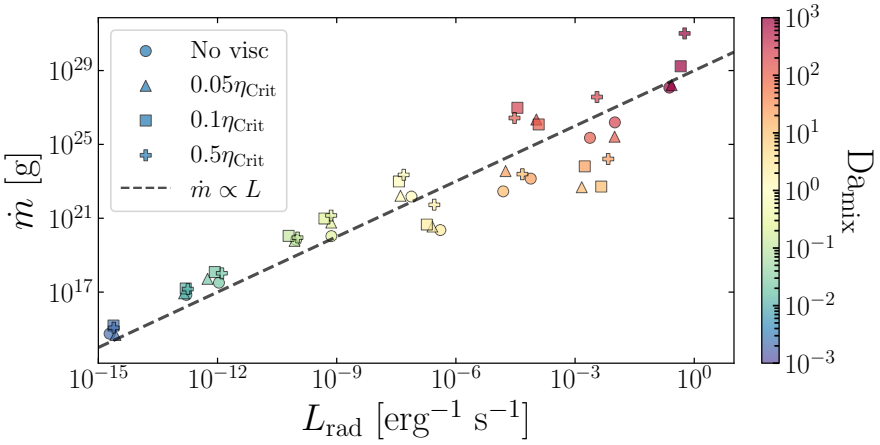

Figure D1: Mass conversion from hot to cold gas as a function of the total luminosity, color-coded by $\mathrm{Da}_{\mathrm{mix}}$. The mass transfer is proportional to the total luminosity, indicating that the luminosity is due to enthalpy flux.

Appendix D: Mass Conversion and Luminosity

In radiative mixing layers, the net radiative losses due to cooling are balanced by the enthalpy flux, producing a mass flow from the hot to the cold medium. This means that the total luminosity is proportional to the mass transfer from the hot to the cold medium: $\dot{m} \propto L_{\mathrm{rad}}$ (Ji et al., 2019; Gronke et al., 2021). We checked that the total luminosity measured in our system was due to enthalpy flux and not to dissipation of kinetic energy by measuring the mass transfer from hot to cold gas and the total luminosity (see Fig. D1). The linear dependence (black dashed line) shows that the luminosity in our system is due to enthalpy flux (mass transfer from hot to cold gas), and not due to dissipation of kinetic energy or viscous heating, regardless of the amount of viscosity and the Da.

Appendix E: Intermediate Temperature Histogram

The cooling curve reaches the highest values at intermediate temperatures (see Fig. 1.7), making cooling more effective in this range. This means that the amount of Q for a given Da depends on the amount of gas with an intermediate temperature. Quantifying the amount of intermediate gas gives us a hint at what Q looks like for different simulations.

Fig. E1 shows the histogram of intermediate temperature gas for different $\mathrm{Da}_{\mathrm{mix}}$ (top to bottom: $\mathrm{Da}_{\mathrm{mix}} \simeq 2.3 \times 10^{-3}$, $\mathrm{Da}_{\mathrm{mix}} \simeq 2.3$ and $\mathrm{Da}_{\mathrm{mix}} \simeq 1.1 \times 10^{3}$) and different times (left to right: $t = 2.5\tau_{\mathrm{KH}}$, $t = 5\tau_{\mathrm{KH}}$ and $t = 6.25\tau_{\mathrm{KH}}$).

In the weak cooling regime (top row), the *No visc* mixes the gas more effectively, leading to a larger amount of intermediate temperature gas. However, since cooling is the bottleneck in this case, this does not make a big impact on Q (see Fig. 5.8). In the viscous runs, the amount of intermediate temperature gas is very similar. This is due to the smooth momentum profile as a

consequence of viscosity. Due to pressure equilibrium, this smoother momentum is translated into a smoother temperature profile, leading to more intermediate temperature gas. Note the flat histogram in the case of $0.5\eta_{\rm Crit}$ due to its laminar flow, where the temperatures are distributed approximately equally along the y-axis.

For $\mathrm{Da}_{\rm mix} \simeq 2.3$ (middle row), the histograms look very similar, since at this value of $\mathrm{Da}_{\rm mix}$ all the simulations are already cooling-dominated, although at later times the *No visc* seems to produce more intermediate temperature gas.

In the strong cooling regime (bottom row), viscosity leads to a slightly broader temperature profile, and therefore, more intermediate temperature gas. Although the effect is only a factor of ~ 2, the strong cooling produces that this effect can be visible when Q is calculated (see right panel of Fig. 5.6).

Appendix F: Shear Velocity Profiles

In a planar slab (or sheet) setup, the effect of viscosity in the velocity gradient is obtained by equation (2.4). The more viscous the medium is, the faster the velocity gradient is smoothed out. This can be seen in the top panel of Fig. F1, where in the weak cooling regime, a higher viscosity leads to a smoother velocity profile within the same amount of time. The effect of turbulence can be seen in the *No visc* case, where the profile is not completely smooth. However, in the strong cooling regime (bottom panel), all the profiles remain sharp after the same amount of time due to the effect of cooling.

Appendix G: Measurement of Smoothing Distance d

To quantify the distance d at which the velocity gradient has been smoothed due to the effect of viscosity, we focus on the hot medium ($y > 0$, see Fig. G1). The reason for this is that, in a system with a constant dynamic viscosity (η), the high density of the cold medium leads to a lower diffusion coefficient (ν), therefore the overall diffusion of the system is dominated by the hot gas (see §5.2.4). The effect of viscosity is given by equation (2.4), which tells us how much the velocity gradient has been smoothed after a time t for a given viscosity. By fitting this equation to our data (thick dashed lines), we have a smooth function for our system, avoiding spurious artifacts that can affect the results. Once we have fitted the function, we calculate the distance d from the center to the point where the velocity gradient has been smoothed 5% with respect to the initial value (vertical dashed lines).

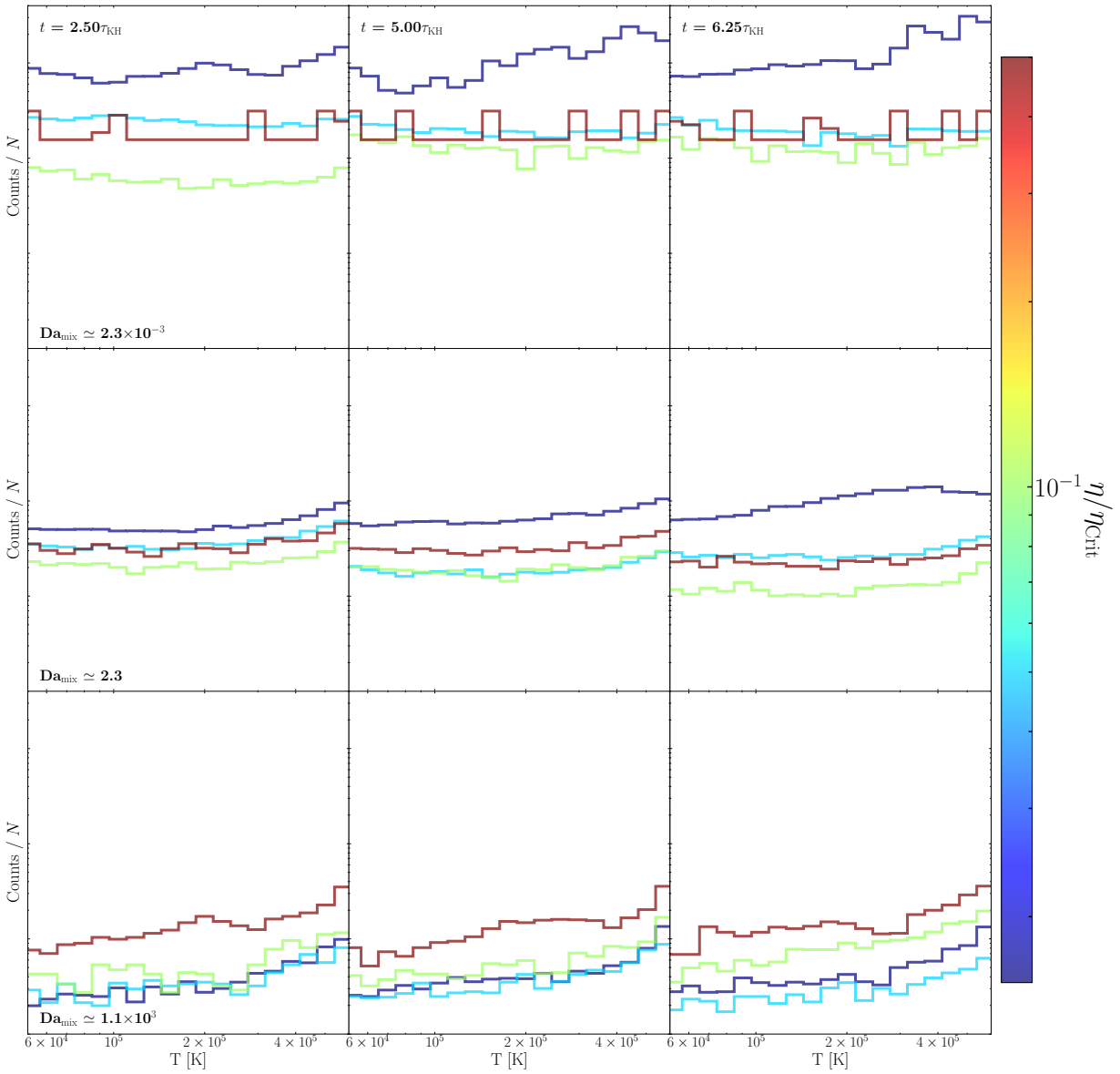

Figure E1: Intermediate temperature histograms color-coded by viscosity. *From top to bottom*: weak cooling ($Da_{mix} \simeq 2.3 \times 10^{-3}$), intermediate cooling ($Da_{mix} \simeq 2.3$) and strong cooling ($Da_{mix} \simeq 1.1 \times 10^3$). *From left to right:* Histogram measured at $t = 2.5\tau_{KH}$, $t = 5\tau_{KH}$ and $t = 6.25\tau_{KH}$.

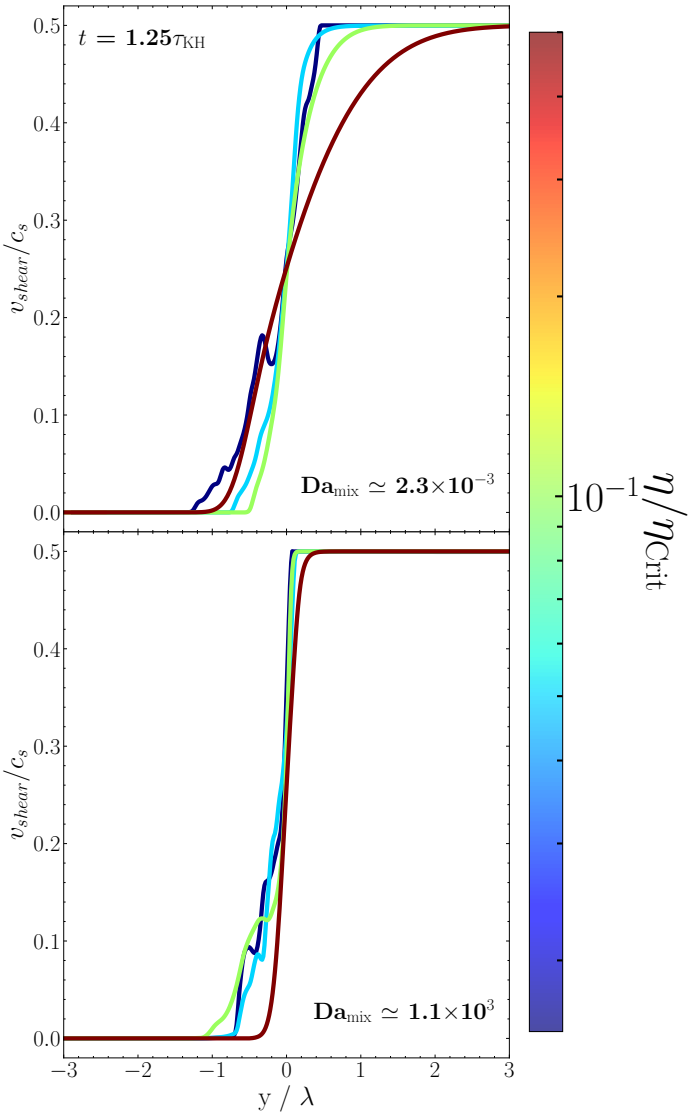

Figure F1: $v_{\rm shear}$ profiles after $t = 1.25\tau_{\rm KH}$ color-coded by viscosity. *Top panel:* Results for $\mathrm{Da_{mix}} \simeq 2.3 \times 10^{-3}$, where the velocity gradient is smoothed depending on the amount of viscosity. *Bottom panel:* Results for $\mathrm{Da_{mix}} \simeq 1.1 \times 10^{3}$, where cooling dominates over viscosity and keeps the profiles sharp.

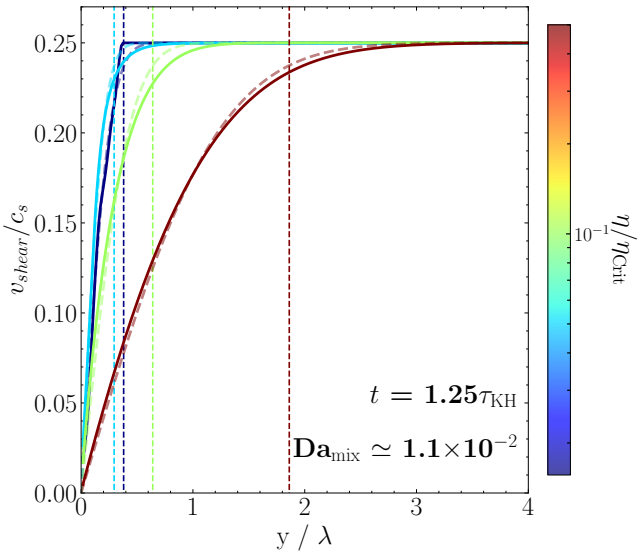

Figure G1: v_{shear} profiles at $\text{Da}_{\text{mix}} \simeq 2.3\times10^{-3}$ and $t = 1.25\tau_{\text{KH}}$ showing the fit of equation (2.4) for the different viscosities (thick dashed lines). The distance d at which the shear profile has been smoothed 5% with respect to the original value is given by the vertical dashed lines.

6 | An Attempt to Constrain Viscosity in the ICM with Cosmological Simulations[1]

In previous chapters, we studied in detail how viscosity affects the growth and development of instabilities, and consequently, the evolution of turbulence and mixing. We found that viscosity can significantly reduce, or even suppress completely, the growth of hydrodynamical instabilities. This leads to a notable reduction in the level of turbulence. However, these conclusions were drawn from idealized simulations with controlled initial conditions. To understand whether these microphysical results hold in the stratified, evolving, and highly non-linear environment of galaxy clusters, we now investigate the effect of viscosity in fully cosmological simulations. In this Chapter, we deliberately omit radiative cooling to isolate the specific impact of viscosity on the dynamics of the ICM.

The impact of viscosity in the ICM is still an open question in astrophysics. To address this problem, we have run a set of cosmological simulations of three galaxy clusters with a mass larger than $M_{\rm Vir} > 10^{15}{\rm M}_{\odot}$ at $z = 0$ using the Smoothed Particle Magneto-Hydrodynamics (SPMHD) code OpenGadget3. We aim to quantify the influence of viscosity and constrain its value in the ICM. Our results show significant morphological differences at small scales, temperature variations, and density fluctuations induced by viscosity. We observe a suppression of instabilities at small scales, resulting in a more filamentary structure and a larger number of small structures due to the lack of mixing with the medium. The conversion of kinetic to internal energy leads to an increase of the virial temperature of the cluster of ~5% - 10%, while the denser regions remain cold. The amplitude of density and velocity fluctuations is found to increase with viscosity. However, comparison with observational data indicates that the simulations, regardless of the viscosity, match the observed slope of the amplitude of density fluctuations, challenging the direct constraint of viscosity solely through density fluctuations. Furthermore, the ratio of density to velocity fluctuations remains close to 1 regardless of the amount of viscosity, in agreement with the theoretical expectations. Our results show, for the first time in a cosmological simulation of a galaxy cluster, the effect of viscosity in the ICM, a study that is currently missing in the literature.

[1]This Chapter was published in ApJ by Marin-Gilabert et al. (2024).

6.1 Simulation Setup

We perform cosmological, magneto-hydrodynamical simulations of galaxy clusters using the SPMHD code OpenGadget3 (Springel, 2005; Groth et al., 2023). Gravity is solved via the Tree-PM method, where the long-distance gravitational forces are computed on a PM mesh and the short-distance forces are computed on a gravity tree (see §3.1.1). For the hydro computation we used the modern SPH implementation (Beck et al., 2016, see §3.1.2), including artificial viscosity (Balsara, 1995; Cullen & Dehnen, 2010, see §3.1.4) and artificial conductivity (Price, 2008, see §3.1.3), with a Wendland C^6 kernel (Wendland, 1995; Dehnen & Aly, 2012) and 295 neighbors (see §3.1.2). This is necessary to avoid the 'pairing instability' (Price, 2012) and the 'E_0 error' (Read et al., 2010) and capture mixing properly (Tricco & Price, 2013; Hu et al., 2014).

We also include magnetic fields based on the implementation of Bonafede et al. (2011) and Stasyszyn et al. (2013) (see §3.1.5), with an initial seed of $B_{\rm seed} = 10^{-12}$ G (comoving) in the x-direction, which corresponds to an initial magnetic field of $B_{\rm ini,ph} = B_{\rm seed} \cdot (1 + z_{\rm ini})^2 = 1.98 \times 10^{-8}$ G in physical units. The choice of this initial magnetic field leads to a saturation of the dynamo at z∼1.5 at this resolution (Steinwandel et al., 2022, this will be discussed in detail in §7.2). Our simulations also include anisotropic thermal conductivity via a bi-conjugate gradient solver (Arth et al., 2017; Steinwandel et al., 2022).

To properly understand the effects of physical viscosity, we perform three different simulations for each cluster: one with no viscosity (labeled as "Ideal"), one with 1/3 of Spitzer viscosity (labeled as "$1/3\,\eta$") and one with full Spitzer viscosity (labeled as "η"). The implementation of viscosity in OpenGadget3 is described in §3.1.6. Now, we additionally include a viscous saturation (see §3.1.7 for details) to avoid unphysical results (Cowie & McKee, 1977; Sarazin, 1986; Su et al., 2017). On top of the physical viscosity, a higher-order shock capturing method (i.e., artificial viscosity) is necessary to properly capture shocks in SPH (Monaghan & Gingold, 1983; Monaghan, 1992) even when physical viscosity is implemented (Sijacki & Springel, 2006).

We want to focus on understanding the complex properties of gas in the ICM, in particular the effect of viscosity and its observational implications. For this reason, we run non-radiative simulations without the effects of subgrid models (e.g., star formation and feedback).

6.2 Initial Conditions

We ran a total of nine zoom-in simulations of three different galaxy clusters from the Dianoga suite (Bonafede et al., 2011; Ragone-Figueroa et al., 2013): the g5503149, g1657050, and g6348555 regions (labeled as g55, g16, and g63, respectively) at the 10x resolution level. These clusters were taken from a low-resolution N-body cosmological simulation of a periodic box of 1 h^{-1} Gpc comoving size. Each Lagrangian region was then re-simulated with a higher resolution using the *zoomed initial conditions technique* (Tormen et al., 1997).

We chose the g55, g16 and g63 clusters because they have a $M_{\rm Vir}{}^2 > 10^{15}$ M$_\odot$ at $z = 0$; g55

[2]The suffix *Vir* indicates the virialized gas, i.e. the gas within the galaxy cluster that satisfies the virial theorem (see §1.2.1).

Table 6.1: Properties of the three different clusters used in this work with three different amounts of viscosity. The first column shows the virial mass, the second column the virial temperature, the third column the R_{2500c}, and the fourth column shows R_{200c}, each at $z = 0$.

	M_{Vir} [10^{15} $M_\odot$]			T_{Vir} [10^7 K]			R_{2500c} [kpc]			R_{200c} [kpc]		
	Ideal	1/3 η	η	Ideal	1/3 η	η	Ideal	1/3 η	η	Ideal	1/3 η	η
g55	1.34	1.38	1.33	7.05	7.32	7.39	498.21	509.77	510.40	3000.96	3020.54	2995.14
g16	1.44	1.40	1.20	6.22	6.29	6.22	459.07	460.04	435.29	3232.38	3204.37	3086.66
g63	1.11	1.22	1.17	6.40	7.81	6.91	455.19	499.39	471.84	2939.73	3019.53	2976.75

and g16 are expected to be unrelaxed, while g63 is very relaxed. To classify the clusters as relaxed or unrelaxed, we used the centre-of-mass offset, where we measured the separation between the density peak position and the center of mass within R_{200c} (Power et al., 2012; Cui et al., 2016). The adopted cosmological parameters are $\Omega_0 = 0.24$, $\Omega_\Lambda = 0.76$, $\Omega_b = 0.04$, $h = 0.72$ and $\sigma_8 = 0.8$. The initial redshift for all the simulations is $z_{ini} = 140$ and the mass resolution is $m_{gas} = 1.56 \times 10^7$ $M_\odot$ in gas particles and $m_{dm} = 8.44 \times 10^7$ $M_\odot$ in dark matter. The choice of this particle resolution is due to the convergence in the magnetic field amplification shown in Steinwandel et al. (2022) against a lower particle resolution. The details of each cluster at $z = 0$ are shown in Table 6.1.

6.3 Morphology

Viscosity acts by transforming kinetic energy into internal energy, leading to a suppression of the growth of hydrodynamical instabilities and an increase of the gas temperature (Roediger et al., 2013b; Marin-Gilabert et al., 2022, see also §4.5). This is expected to produce a strong effect in the morphology of galaxy clusters at small scales (a few kpc), where the turbulent cascade is truncated due to the effect of viscosity. Fig. 6.1 shows the surface density for each of the three clusters and the three different configurations. The inner dotted circle corresponds to R_{2500c} and the outer dashed circle corresponds to R_{200c}[3].

By comparing each cluster independently, we can observe that there are no major changes at large scales (a few hundred kpc - Mpc), where the big structures remain in the same position in the three different cases and the overall gas distribution is very similar. However, the ICM is more homogeneous in the non-viscous case, whereas in the viscous cases we find sharper density discontinuities and more regions with very diffuse gas.

Although at a large scale the picture is similar, we find many differences at smaller scales. The lack of mixing due to viscosity leads to more small structures that have not been disrupted due to the growth of instabilities. The survival of the clump will depend on different parameters such as the size of the clump, its velocity, or the overdensity with respect to the medium (Klein et al., 1994; Pittard et al., 2005; Valentini & Brighenti, 2015), which is beyond the scope of this Chapter. The growth or suppression of instabilities will also depend on the amount of viscosity,

[3]In this Chapter, R_{2500c} (R_{200c}) is defined as the radius enclosing the region of the cluster with a mean density 2500 (200) times larger than the critical density of the Universe (see §1.2.1).

which depends on the temperature, generating a very complex system difficult to analyze in cosmological simulations. However, its effect can be seen in the amount of clumps observed in Fig. 6.1.

Another morphological difference observed in the cases with viscosity is the filamentary structure. This is produced by the infalling structures moving towards the center of the cluster, which experience a ram pressure stripping (e.g. Gisler, 1976; Nulsen, 1982; Randall et al., 2008). This stripped gas produces a tail with a density contact discontinuity with respect to the medium, resulting in the growth of instabilities. Viscosity slows down the growth process of these instabilities, leading to longer tails that last for longer periods of time (Roediger et al., 2015; Kraft et al., 2017). Although magnetic fields can also produce these filamentary structures (Das & Gronke, 2023), all our simulations include magnetic fields, excluding them as the origin of these differences.

Because of the strong dependence of viscosity on temperature, one might expect that the above-mentioned differences might correlate well with the temperature of the cluster. In Fig. 6.2 we show temperature colormaps of the nine different simulations. The cases with more viscosity lead to higher temperatures in the diffuse gas; however, the temperatures of the dense clumps are very similar in all three cases. Overall, the virial temperature at $z = 0$ is around 5% to 10% higher in the viscous cases compared to the ideal ones due to heat dissipation (see Table 6.1). We find again a more homogeneous temperature in the ideal runs, while more fluctuations are present in the viscous runs. Due to the dependence of viscosity on temperature, viscosity starts to become important at low redshift, when the virial temperature becomes larger than $\sim 10^7$ K. In this respect, the merger history of the cluster becomes very important, as mergers behave differently whether we have or do not have viscosity. The hotter medium leads to a larger viscosity, which heats up the medium, producing a larger viscosity, entering a runaway cycle which is prevented by the viscous saturation, avoiding unphysical temperatures (see §3.1.7).

6.4 Density and Velocity Fluctuations

6.4.1 Gas Distribution

Quantifying the density fluctuations observed in Fig. 6.1 is fundamental for understanding the small-scale processes which determine the ICM properties. Comparing with observations can help us to constrain the amount of viscosity in the ICM, as suggested by Zhuravleva et al. (2019) (see §2.4). To this end, we first remove the high-density clumps, leaving only the bulk gas (source of the X-ray emission in the ICM), and then compute the density and velocity fluctuations.

To remove the high-density regions, we follow the method introduced by Zhuravleva et al. (2012): we divide the galaxy cluster into spherical shells and compute the density PDF for each of the shells. We calculate the median value of each shell and, alongside it, a threshold value to separate the bulk gas from the high-density gas. A particle is considered to belong to the high-density gas if the following criterion is met:

$$\log_{10} n > \log_{10}\{n\} + f_{\rm cut}\sigma_{10}\,, \tag{6.1}$$

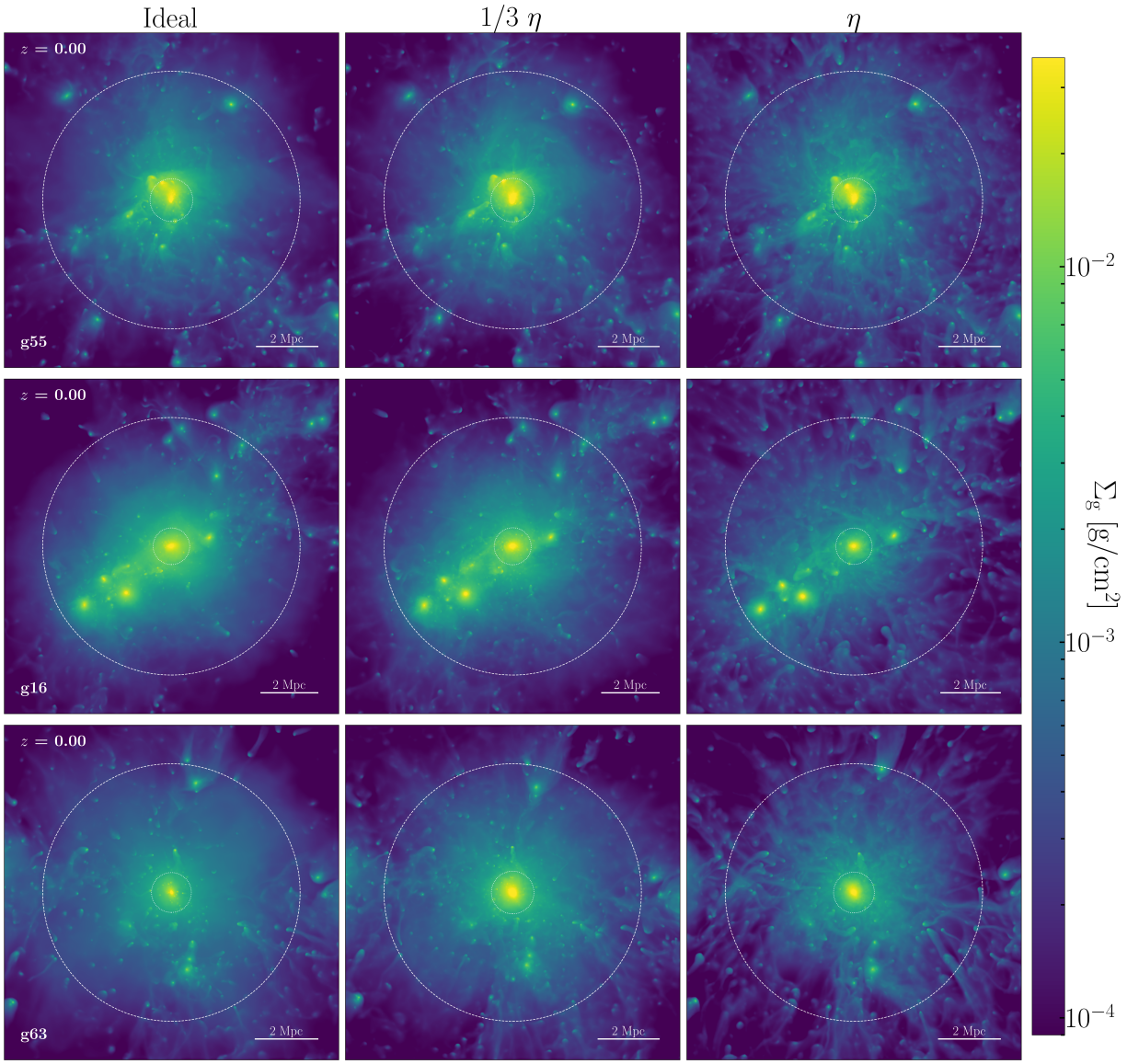

Figure 6.1: Density projections for all of our simulations listed in Table 6.1. *From left to right*: MHD only, MHD with $1/3$ of Spitzer viscosity, and full Spitzer viscosity at redshift zero. *From top to bottom*: the runs g55, g16 and g63.

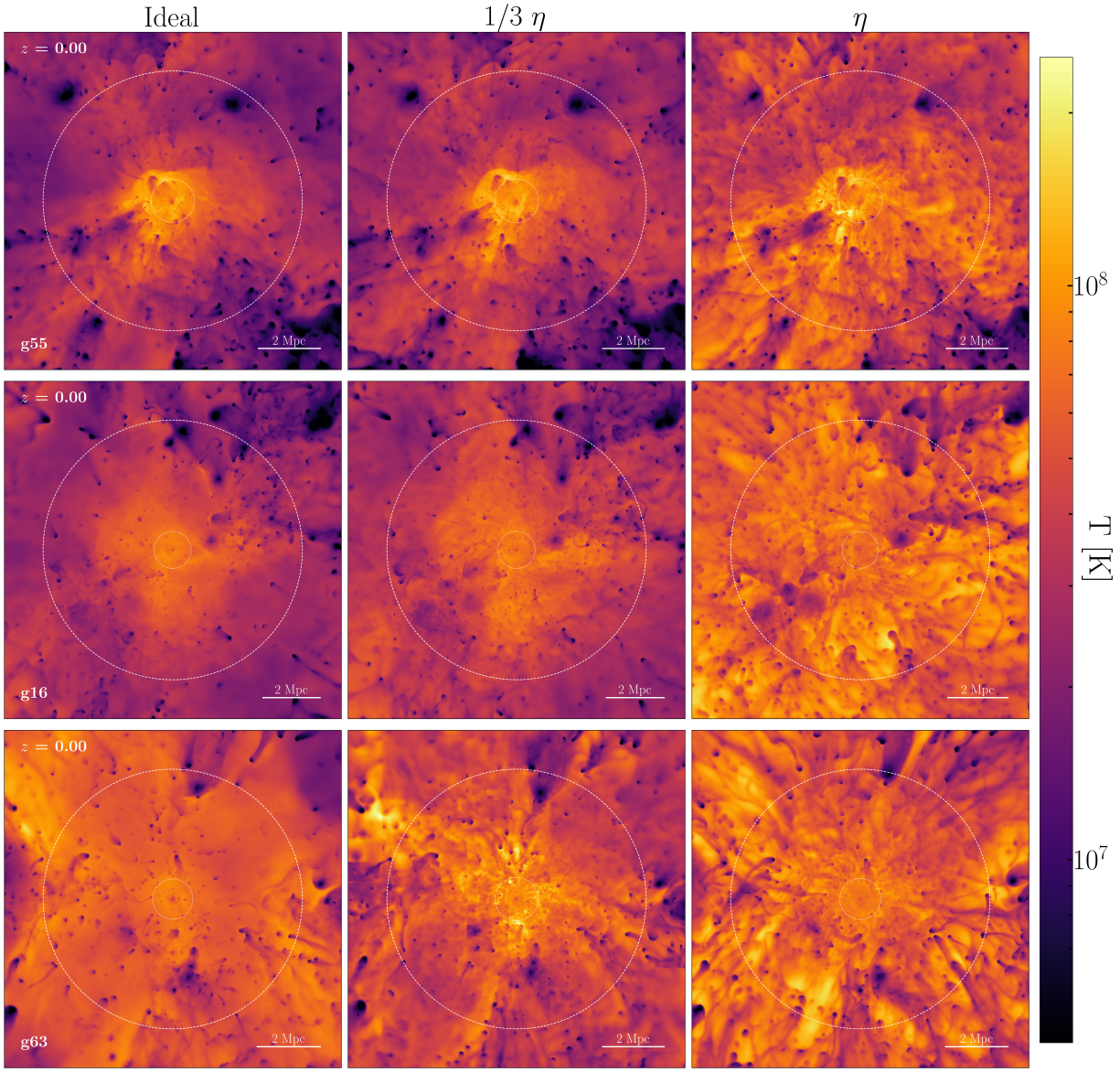

Figure 6.2: Temperature projections for all of our simulations listed in Table 6.1. *From left to right*: MHD only, MHD with $1/3$ of Spitzer viscosity, and full Spitzer viscosity at redshift zero. *From top to bottom*: the runs g55, g16 and g63.

where $\{n\}$ is the median value of the density in the shell, $f_{\rm cut}$ is a parameter tuned to select more or less gas as high-density and σ_{10} is the standard deviation ($\log_{10}$ based) assuming a log-normal distribution of the density PDF. σ_{10} can be expressed as

$$\sigma_{10} = \frac{W_{10}}{2\sqrt{2\ln 2}}\,, \tag{6.2}$$

with

$$W_{10}(n) = \log_{10}\frac{n_2}{n_1}\,. \tag{6.3}$$

W_{10} accounts for the logarithmic interval where 76% of the particles are contained, n_1 corresponds to the 12th percentile of density and n_2 to the 88th percentile. The value of $f_{\rm cut}$ is set to be between 2.5 and 4.5 (Zhuravleva et al., 2012). A lower value will displace the threshold towards lower densities, selecting a larger number of particles as high-density gas, while a higher value will displace it towards larger densities. We choose a value of $f_{\rm cut} = 2.5$ for our analysis. The reason for this choice can be seen in Fig. 6.3. This figure shows the effect of viscosity in the density distribution within a thin shell of 5 kpc around the virial radius of the cluster g55. The vertical dashed lines indicate the position of the density threshold to split the distribution into bulk and high-density gas. Once the gas has been separated, we fit the bulk gas to a log-normal distribution, indicated with the dash-dotted lines. Even though the mean value of the distribution does not change much, viscosity broadens the distribution. This result shows quantitatively what we observed in Fig. 6.1. Viscosity produces larger density fluctuations, where particles deviate more from the mean value of the density distribution than in the non-viscous case. As a consequence, choosing a larger value of $f_{\rm cut}$ would displace the threshold in the viscous case further towards larger densities, taking particles of the high-density tail as bulk gas. On the other hand, choosing a rather low value of $f_{\rm cut}$ means that we might be underestimating the threshold in the ideal case (see appendix H). For this reason, we take the lowest value suggested by Zhuravleva et al. (2012).

6.4.2 Density Fluctuations

Fig. 6.3, however, only shows a thin slice of cluster g55 to illustrate the effect of viscosity on the gas distribution and the method employed to separate the bulk gas from the high-density gas. To understand the overall effect of viscosity in the whole cluster, Fig. 6.4 shows the variation of the standard deviation (σ) of the log-normal fit as a function of the radius for the three different clusters. Assuming the bulk gas follows a log-normal distribution, the value of σ can be understood as a density fluctuation measurement (i.e., the width of the distribution), since

$$\frac{\delta\rho}{\rho} = \log_{10}\frac{\rho_2}{\rho_1} = \frac{2\sqrt{2\ln 2}}{\ln 10}\,\sigma \simeq 1.02\sigma\,, \tag{6.4}$$

where, as before, ρ_1 and ρ_2 correspond to the 12th and the 88th percentile of the density, respectively. Increasing the amount of viscosity produces broader distributions for all the shells along the radius, which translates into larger density fluctuations. Overall, with full Spitzer viscosity, we get the largest fluctuations. Comparing the case with $1/3\,\eta$ and the ideal case, we still see larger fluctuations in the runs with $1/3\,\eta$, although the differences are not large.

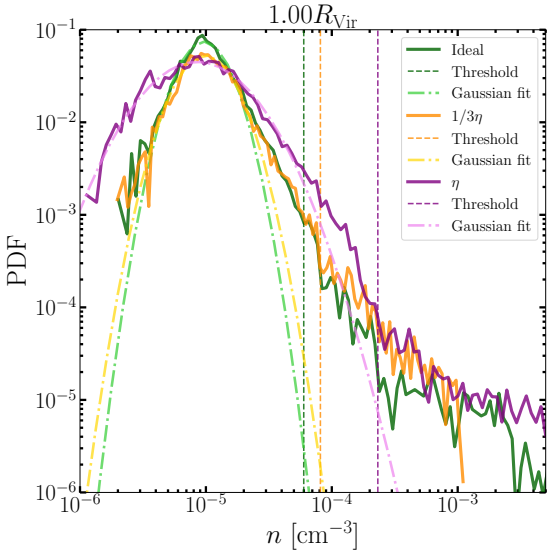

Figure 6.3: Density probability density function (PDF) of a thin shell of 5 kpc of the cluster g55 to show the effect of viscosity on the gas density distribution. The solid lines show the data; the vertical dashed lines indicate the values of the density thresholds separating bulk and high-density gas; and the dash-dotted lines indicate the log-normal distribution fit to the bulk density component of the gas.

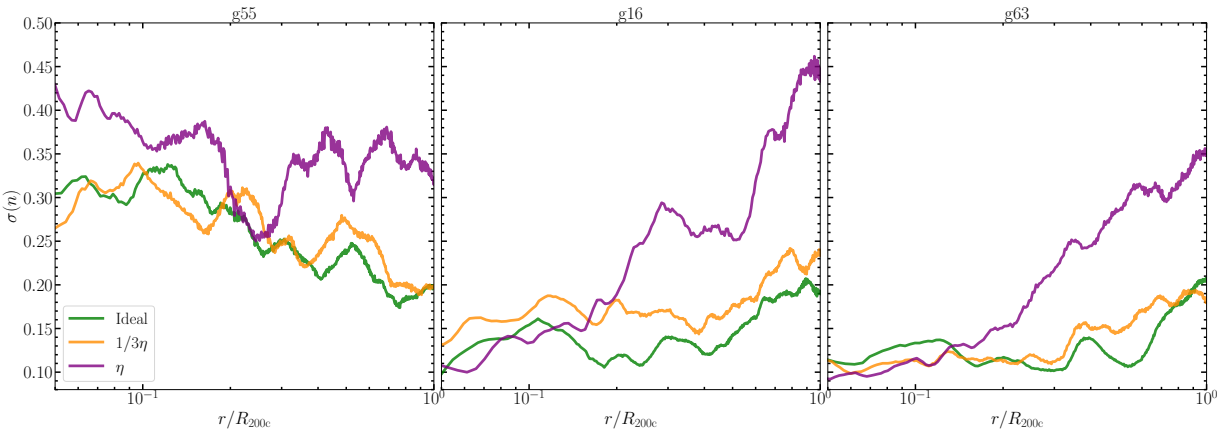

Figure 6.4: Radial profile of the standard deviation of the log-normal fit for each one of the spherical shells. *From left to right*: clusters g55, g16 and g63 for the different runs.

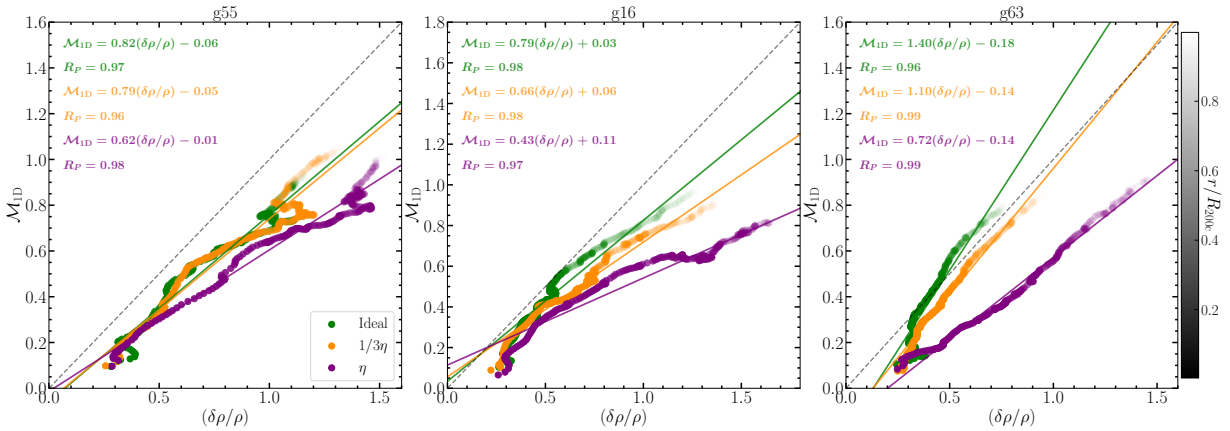

Figure 6.5: Velocity fluctuations against density fluctuations within R_{200c}. The transparency of the dots indicates the distance to the center of the cluster. The dots are calculated by averaging over 40 snapshots from redshift 0.4 to redshift 0 for each radial shell. For each of the runs, we do a linear fit, indicating the slope, intercept, and the Pearson's coefficient for each case. *From left to right*: clusters g55, g16 and g63 for each one of the configurations.

6.4.3 Density vs Velocity Fluctuations

As explained in §1.4.3, the density fluctuations are expected to scale linearly with velocity fluctuations. In the ICM, it has been found that the density fluctuations correlate with $\mathcal{M}_{1D}$ with a slope close to 1 (Zhuravleva et al., 2014; Gaspari et al., 2014). However, this might also depend on the dynamical state of the cluster, where unrelaxed clusters might deviate from that value (Simonte et al., 2022; Zhuravleva et al., 2023). We want to investigate how viscosity affects that relation. To do so, we first calculate the velocity fluctuations via the root mean square velocity (v_{rms}) as

$$\delta v = \sqrt{(v_x - \langle v_x \rangle)^2 + (v_y - \langle v_y \rangle)^2 + (v_z - \langle v_z \rangle)^2}\,, \tag{6.5}$$

where $\langle v_x \rangle$, $\langle v_y \rangle$ and $\langle v_z \rangle$ are the mean velocities in each shell. We then calculate the 1D mach number of each particle as $\mathcal{M}_{1D} = \delta v/(c_s\sqrt{3})$. We take the region within R_{200c} of the cluster, similar to the one taken in Zhuravleva et al. (2023). For better statistics, we take the last 40 snapshots from $z \sim 0.4$ to $z = 0$ and calculate the mean value of density and velocity fluctuations of each shell in each snapshot using equations (6.4) and (6.5) respectively. For each snapshot, we take the same radial bins normalized to R_{200c}. Finally, we take the mean value of the density and velocity fluctuations for each shell over the snapshots and plot $\mathcal{M}_{1D}$ against $\delta\rho/\rho$, as shown in Fig. 6.5. Since we have taken the average over a period of time, we cannot take into account the dynamical state of the clusters here.

There is a clear linear trend in all clusters, independently of the amount of viscosity, with a low scatter in all cases (the Pearson's correlation coefficient is close to 1, indicating a good correlation). Viscosity reduces the slopes of the linear fits[4]. We observe that density and

[4]Note that the slope is the inverse η_ρ.

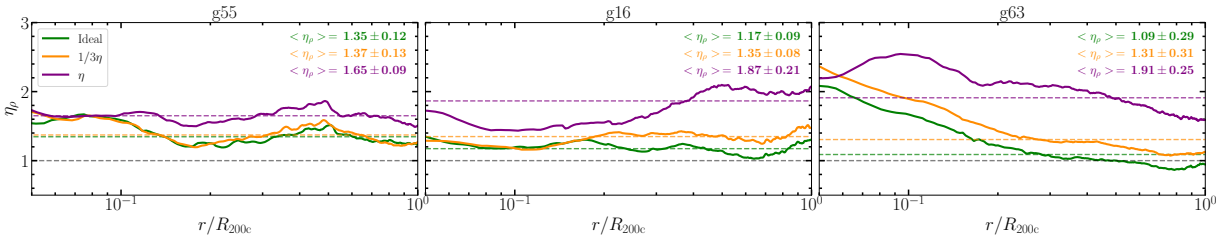

Figure 6.6: Ratio between density fluctuations and velocity fluctuations as a function of the radius within R_{200c} (same data as in Fig. 6.5). The solid lines indicate the data from the simulations, while the dashed lines indicate the mean value in each case within R_{200c}. The mean value and the standard deviation calculated over all the shells in each run are indicated in each panel. *From left to right*: clusters g55, g16 and g63 for each one of the configurations.

velocity fluctuations increase further from the center (lighter data points). This reflects the state of the ICM in clusters that keep growing by accretion (Zhuravleva et al., 2023). The values of $\mathcal{M}_{1D}$ are consistent with direct observations of Perseus (Hitomi et al., 2018), where they found $\mathcal{M}_{3D} = \sqrt{3}\mathcal{M}_{1D} \simeq 0.3 - 0.45$ within the central 100kpc of the cluster ($\sim 0.03R_{200c}$) and indirect measurements from observations (Lovisari et al., 2024; Dupourqué et al., 2024), with $\mathcal{M}_{3D} \simeq 0.36{-}0.41$ for relaxed clusters in the inner regions of the cluster (within $R_{500c} \sim 0.7R_{200c}$).

To study in more detail the ratio of density to velocity fluctuations, Fig. 6.6 shows the radial dependence of this ratio (η_ρ).

The cases with full viscosity consistently have a larger value of η_ρ, as a consequence of the shallower slope seen in Fig. 6.5. Cluster g63 shows a mean value closer to one (although with a large scatter) in the inviscid case compared to clusters g55 and g16, all in agreement with the results found previously by Simonte et al. (2022) and Zhuravleva et al. (2023). The values of η_ρ in the cases with $1/3\,\eta$ do not change significantly among the different clusters, whereas the runs with full viscosity have a larger value of η_ρ.

6.5 Comparison with Observations

We have discussed the effects that viscosity has in galaxy clusters, focusing so far on the comparison between viscous and inviscid simulations. However, for a comparison with observations, we need to calculate the 3D amplitude fluctuations as a function of the wavenumber $k = 1/l$ (where l is the length scale of the fluctuations). To do so, we first need to calculate the density fluctuations of our data elements and then compute the power spectrum (see §2.4). In particle-based simulations, the computation of the Fourier Transform to calculate the power spectrum is not possible, so we need to interpolate the particle properties onto a grid. By doing so, we also avoid spurious effects caused by the voids after removing the high-density regions (see §6.4.1). In grid simulations, the voids are replaced by the median value of the shell (e.g. Zhuravleva et al., 2023). In our case, the voids are automatically replaced by an average value over the particles of the region due to the interpolation method employed. This is done using the code VORTEX-P (Vallés-Pérez et al., 2021b,a, 2024), which creates an ad-hoc

AMR mesh hierarchy from the density and velocity fields with the ultimate goal of providing a multi-resolution Helmholtz-Hodge and Reynolds decomposition (see §3.3). In this Chapter, we use it exclusively to assign the density and velocity fields onto an AMR mesh, which is done using the same kernel configuration as for evolving the simulation. Once the particle data have been interpolated into the mesh, we calculate the density fluctuations. This is done by decomposing the density field into unperturbed and fluctuating components (Churazov et al., 2012):

$$\rho(x, y, z) = \rho_0(x, y, z)[1 + \delta(x, y, z)] \,, \tag{6.6}$$

where $\rho_0(x, y, z)$ is the unperturbed density distribution and

$$\delta(x, y, z) = \frac{\delta\rho}{\rho_0} = \frac{|\rho_i - \rho_0|}{\rho_0} = \frac{|\rho_i - \langle\rho\rangle|}{\langle\rho\rangle} \tag{6.7}$$

are the fluctuations. ρ_i is the density of each cell, and $\langle\rho\rangle$ is the value of the density profile at that distance from the center (see density profiles in appendix I). In our case, we evaluate the density profile at a given radius to estimate the unperturbed $\rho_0(x, y, z)$. For the power spectrum, we assume an isotropic fluctuation field that is a function of $k = \sqrt{k_x^2 + k_y^2 + k_z^2}$. The 3D amplitude fluctuations can be computed from the power spectrum as

$$\left(\frac{\delta\rho}{\rho}\right)_k = \sqrt{4\pi P(k) k^3} \,, \tag{6.8}$$

where $P(k)$ is the power spectrum.

These 3D amplitude density fluctuations can be observed from X-ray emission and can be used to constrain the amount of viscosity in the ICM (Zhuravleva et al., 2019, §2.4). Fig. 6.7 shows a comparison of density fluctuations of our sample of clusters for both unrelaxed (g55 and g16) and relaxed clusters (g63), with observations taken from Heinrich et al. (2024). The observational data is composed by 80 clusters (24 relaxed, 30 intermediate and 26 unrelaxed) of $M_{2500c} \in [8 \times 10^{13}, 10^{15}]$ $M_\odot$, comparable to our sample (our clusters have $M_{2500c} \sim 2.4 - 3.9 \times 10^{14} M_\odot$). For a better comparison with observations, we take the same region of the cluster as in Heinrich et al. (2024), i.e., the gas inside R_{2500c}. The gray region indicates the average at each scale of the density fluctuations for the relaxed (unrelaxed) subsample, plus/minus one standard deviation.

In all cases, viscosity leads to a larger amplitude of the fluctuations at all scales, leading to around two times larger amplitude in the cases with full viscosity. Furthermore, the case with $1/3\,\eta$ has similar results compared to the non-viscous case in g55 and g63, but it is $\sim$ 30% higher in g16. Although in cluster g55 the $1/3\,\eta$ and non-viscous runs are more consistent with observations, in clusters g16 and g63 the full viscosity case matches better the overall amplitude of observations. However, due to the small sample of simulations that we have, it is difficult to exclude any particular amount of viscosity by comparing our results with the overall amplitude of the observations.

To constrain the amount of viscosity in the ICM, Zhuravleva et al. (2019) suggested a criterion based on studying the slope of the density fluctuations spectrum. In the cases with higher viscosity, the turbulent cascade is stopped earlier, leading to a steeper power spectrum that translates into

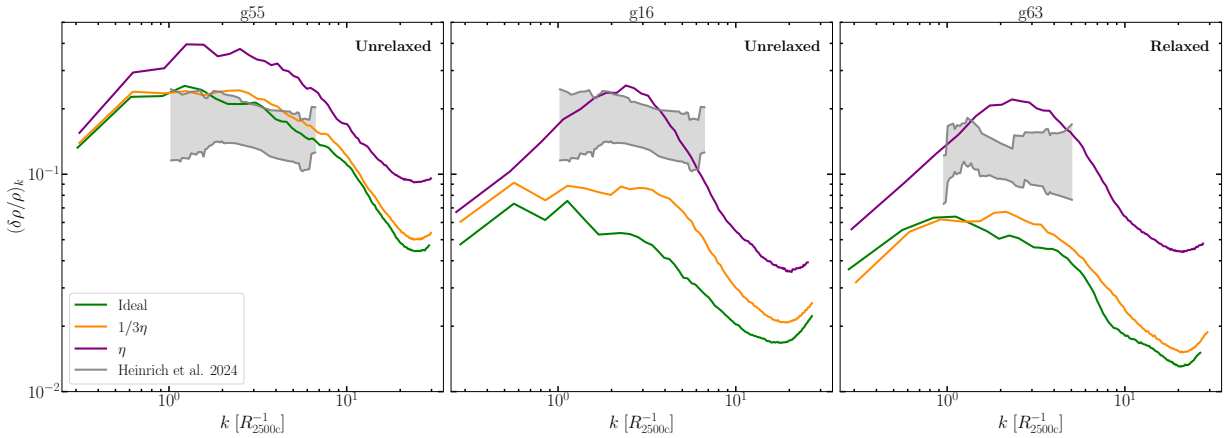

Figure 6.7: Comparison between density fluctuations obtained from our simulations with different viscosities (solid lines) and observations from Heinrich et al. (2024) (gray areas) as a function of the scale within R_{2500c}. *From left to right*: clusters g55, g16 and g63 for each one of the configurations. The unrelaxed clusters (g55 and g16) are compared with the observational data of unrelaxed clusters, and the relaxed cluster (g63) with the observational data of relaxed clusters.

steeper 3D density amplitude fluctuations. This was probed by comparing Coma observations with direct numerical simulations (DNS) of hydrodynamic turbulence. They found a level of suppression of at least a factor of 10 with respect to the Spitzer value, depending on the Prandtl number[5].

Assuming that the motions are subsonic and driven at large scales, one can assume that the fluctuations in the ICM are passively advected by the velocity field (Kunz et al., 2022). Therefore, a comparison with a hydrodynamic turbulence simulation is somewhat reasonable. However, the DNS simulations employed in Zhuravleva et al. (2019) use a rather idealised setup, where compressible fluids (important mainly for unrelaxed clusters) or magnetic fields are not considered. They also assumed an isothermal fluid of $T_e \sim 8$ keV ($\sim 9.28 \times 10^7$ K) for Coma. And, since viscosity is highly dependent on the temperature (see equation (2.2)), that means that they used a constant value of viscosity. This might produce the sharp viscous cutoff observed in their results. However, in cosmological simulations, we observe a range of temperatures from 3.3×10^6 K to 2.5×10^8 K, and therefore, a big range of values for viscosity. This range of values for viscosity at different scales prevents the power spectrum from having a sharp cutoff, as observed in Fig. 6.7 for density and Fig. J1 for the velocity power spectrum. As a consequence, the slope of the 3D amplitude of density fluctuations is insensitive to the amount of viscosity. This is investigated in more detail in §6.6.

It is important to note the maximum observed at $k \sim 2.5 R_{2500c}^{-1} \sim 175$ kpc in the viscous runs of clusters g16 and g63 in Fig. 6.7. This feature is not found either in observations or in the other simulations, where the amplitude of density fluctuations decreases monotonically with k. The reason is the value of $f_{\rm cut}$ used in equation (6.1), where we used a value of $f_{\rm cut} = 2.5$,

[5]The Prandtl number is defined as the ratio of momentum to thermal diffusivity (i.e., the ratio between viscosity and thermal conduction).

the minimum value suggested in Zhuravleva et al. (2012). This value was reasonable for our cluster g55, where we have a clear separation of bulk gas following a log-normal distribution and a high-density tail (see Fig. 6.3). However, there is no clear separation between the bulk gas and high-density regions in the density PDF of cluster g16 (see appendix H) and g63, which looks more like a log-normal plus power law distribution. Due to its broad PDF, the median value is large, and a value of $f_{\rm cut} = 2.5$ sets a threshold at a large density value, causing very few or no particles to be considered as high-density (see Fig. H1). The small fraction of particles removed due to the choice of $f_{\rm cut}$ increases the amplitude density fluctuations at the scale of the high-density clumps (50 kpc - 200 kpc). A more reasonable value for this cluster would be $f_{\rm cut} = 0.5$, where the split between bulk and high-density gas is more appropriate, as shown in the top panel of Fig. H2. With a lower value of $f_{\rm cut}$, the maximum observed in the middle panel of Fig. 6.7 disappears, as can be seen in Fig. H3. However, the same value should be applied to all the analyses for consistency, and that would imply that in cluster g55, a lot of bulk gas would be considered as high-density gas (see bottom panel of Fig. H2). For this reason, we perform our analysis with a value of $f_{\rm cut} = 2.5$, acknowledging that it has an impact on the viscous runs of clusters g16 and g16, leading to a factor of ~ 2 larger amplitude at the scales of the high-density clumps ($\sim$ 175 kpc). However, the slope of the density fluctuations is not affected by the choice of $f_{\rm cut}$ (see Fig. H3), indicating that the method to constrain viscosity is still robust regardless of the value of $f_{\rm cut}$.

The code VORTEX-P also allows us to interpolate the velocity fluctuation field calculated from v_{rms} as shown in equation (6.5) and the soundspeed of each particle. Then we calculate the power spectrum of the velocity fluctuations in an analogous way as shown in equation (6.8)

$$\left(\frac{\delta v}{c_s}\right)_k = \sqrt{4\pi P_{\rm 3D}(k) k^3} = \mathcal{M}_{{\rm 3D},k}\,, \tag{6.9}$$

where $P_{\rm 3D}(k) = P_x(k) + P_y(k) + P_z(k)$. To obtain the 1D velocity fluctuations we do $\mathcal{M}_{{\rm 1D},k} = \mathcal{M}_{{\rm 3D},k}/\sqrt{3}$. Fig. 6.8 shows the velocity fluctuations for the three different clusters.

Since viscosity reduces the velocity of the particles (Marin-Gilabert et al., 2022, §4) and, at the same time, increases the temperature (see §6.3) and, therefore, the soundspeed, one could expect that the $\mathcal{M}_{{\rm 1D},k}$ decreases with viscosity. However, Fig. 6.8 shows very similar results among the simulations or even larger amplitude fluctuations in the viscous cases. This apparently counter-intuitive result might be due to the lack of mixing in the viscosity runs. This causes the most massive structures in the cluster to keep their mass for a longer time compared to the non-viscous runs, experiencing a larger gravitational pull and accelerating as they fall into the gravitational well of the cluster before being stripped. This can also be observed in the kinetic energy spectrum in appendix J, where at large scales the runs with viscosity lead to larger values of the energy spectrum.

Considering density and velocity fluctuations, we can study the relationship between the density and velocity fluctuations of equation (1.31). In Fig. 6.9 we show the value of $\eta_{\rho,k}$ calculated as $\eta_{\rho,k} = (\delta\rho/\rho)_k/\mathcal{M}_{{\rm 1D},k}$ for different scales. The runs with greater viscosity tend to have larger values of $\eta_{\rho,k}$. This means that, even though both density and velocity fluctuations are higher in the viscous runs, they do not compensate for each other, and the ratio between the two is

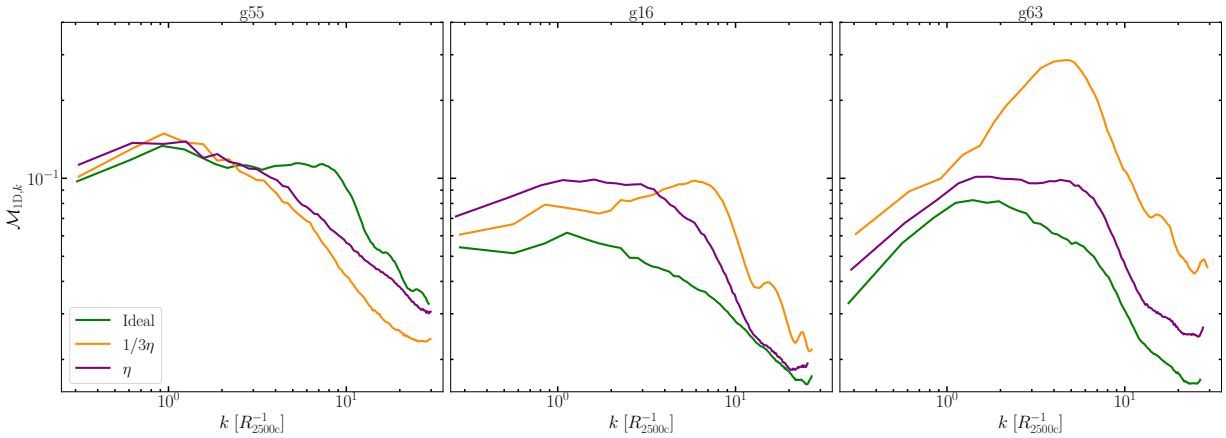

Figure 6.8: Comparison of velocity fluctuations obtained from our simulations with different viscosities as a function of the scale within R_{2500c}. *From left to right*: clusters g55, g16 and g63 for each one of the configurations.

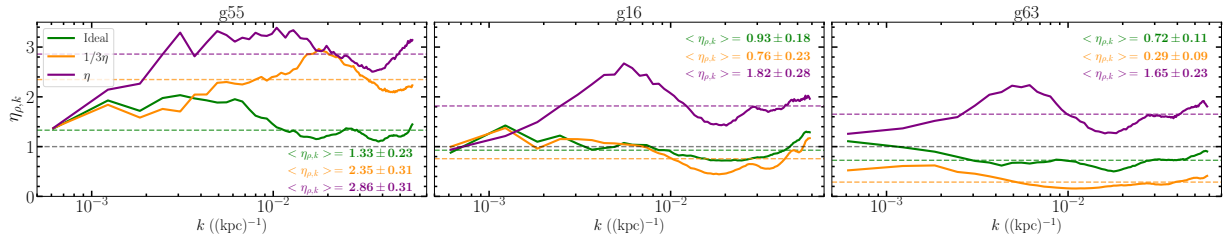

Figure 6.9: Ratio between density fluctuations and velocity fluctuations as a function of the scale within R_{2500c}. The solid lines indicate the data from the simulations, while the dashed lines indicate the mean value in each case along the different scales. The mean value and the standard deviation in each run are indicated in each panel. *From left to right*: clusters g55, g16 and g63 for each one of the configurations.

still larger than for the non-viscous runs. The cluster g55 has values larger than 1, however, this is in agreement with previous work for unrelaxed clusters (Gaspari et al., 2014; Simonte et al., 2022). The cluster g16 shows a relation very close to 1, as expected theoretically (Zhuravleva et al., 2014, 2023), although in the case with full viscosity we still see the maximum analyzed in appendix H. In cluster g63, we observe a value close to, but lower than 1, also consistent with previous work for a very relaxed cluster.

6.6 Thermodynamical Structure

For a better understanding of the gas dynamics of the clusters, in this section, we study the thermodynamical structure of the different clusters. For a better comparison with observations, we focus only on the inner regions of the cluster (within R_{2500c}), as we did in previous sections. To visualize the thermodynamical structure of the clusters, Fig. 6.10 shows 2D histograms of the

line-of-sight velocity ($v_{\rm LoS}$) as a function of the temperature, color-coded by the emissivity. For the calculation of the emissivity, we assume it to be $\propto \rho^2\sqrt{T}$, expected for thermal bremsstrahlung (Sarazin, 1986). We also overplot the mass distribution of the particles as a contour for the different $v_{\rm LoS}$ and temperatures.

The unrelaxed dynamical state of cluster g55 (top row) can be identified by analyzing the $v_{\rm LoS}$, where the mass is distributed over a larger range of velocities. The emissivity is also distributed over a larger range of velocities, and there is no clear emissivity peak, as can be seen in the other two clusters. Although cluster g16 is unrelaxed and g63 is relaxed, the distributions of $v_{\rm LoS}$ look very similar, being approximately $v_{\rm LoS} \in [-1000, 1000]$ km/s in both cases. The peak of emissivity in both g16 and g63 is localized around $v_{\rm LoS} = 0$ km/s for all the configurations in the two clusters.

In all cases, the peak of emissivity is approximately between 10^7 and 10^8 K, within the range expected for galaxy clusters (Biffi et al., 2012). However, cluster g55 exhibits a broader temperature distribution due to its unrelaxed state, reaching temperatures of 5×10^8 K. The cases with full viscosity tend to have more mass at larger temperatures, as can also be seen in Fig. 6.2.

It is important to note that cluster g16 exhibits a narrower mass-weighted temperature distribution in the three configurations. The majority of the mass is concentrated in a narrow range of temperatures, meaning that this cluster is closer to being isothermal for the three runs than the other two clusters. This is similar to the case analyzed by Zhuravleva et al. (2019), where they assumed an isothermal fluid of $T \sim 9.28 \times 10^7$ K for Coma. The narrower the temperature distribution is, the narrower is the range of viscosities as well (see equation (2.2)). This would imply a sharper cutoff in the turbulent cascade, leading to steeper 3D amplitude density fluctuations. Although cluster g16 is not perfectly isothermal, these steeper 3D amplitude density fluctuations can be seen in the middle panel of Fig. 6.7 by comparing the non-viscous and the viscous case. The maximum produced by the choice of $f_{\rm cut}$ might affect the results; however, the steeper spectrum can also be seen in Fig. H3 for different values of $f_{\rm cut}$. The difference in slope is not as prominent as the one suggested by Zhuravleva et al. (2019), however, it indicates that their criterion to constrain viscosity might be applicable only to isothermal galaxy clusters. The consequence of the narrower temperature distribution can also be seen in the middle panel of Fig. J1, where the dynamical range of the spectrum reaches smaller scales in the non-viscous than in the viscous case.

Fig. 6.10 shows how a more isothermal cluster produces a steeper slope in the density fluctuations amplitude for the cases with viscosity compared to the inviscid cases. However, the differences in the slope vanish if the temperature distribution within the cluster is broader.

6.7 Conclusions

In this Chapter, we performed a set of cosmological simulations using the code OpenGadget3 of three different galaxy clusters, each with three different values of viscosity, to quantify the effect of viscosity in the ICM. First, we compared the results of these simulations at redshift zero in order to understand the effect that viscosity has in the ICM. Then we tried to constrain the amount of viscosity in the ICM by comparing with X-ray observations of density fluctuations.

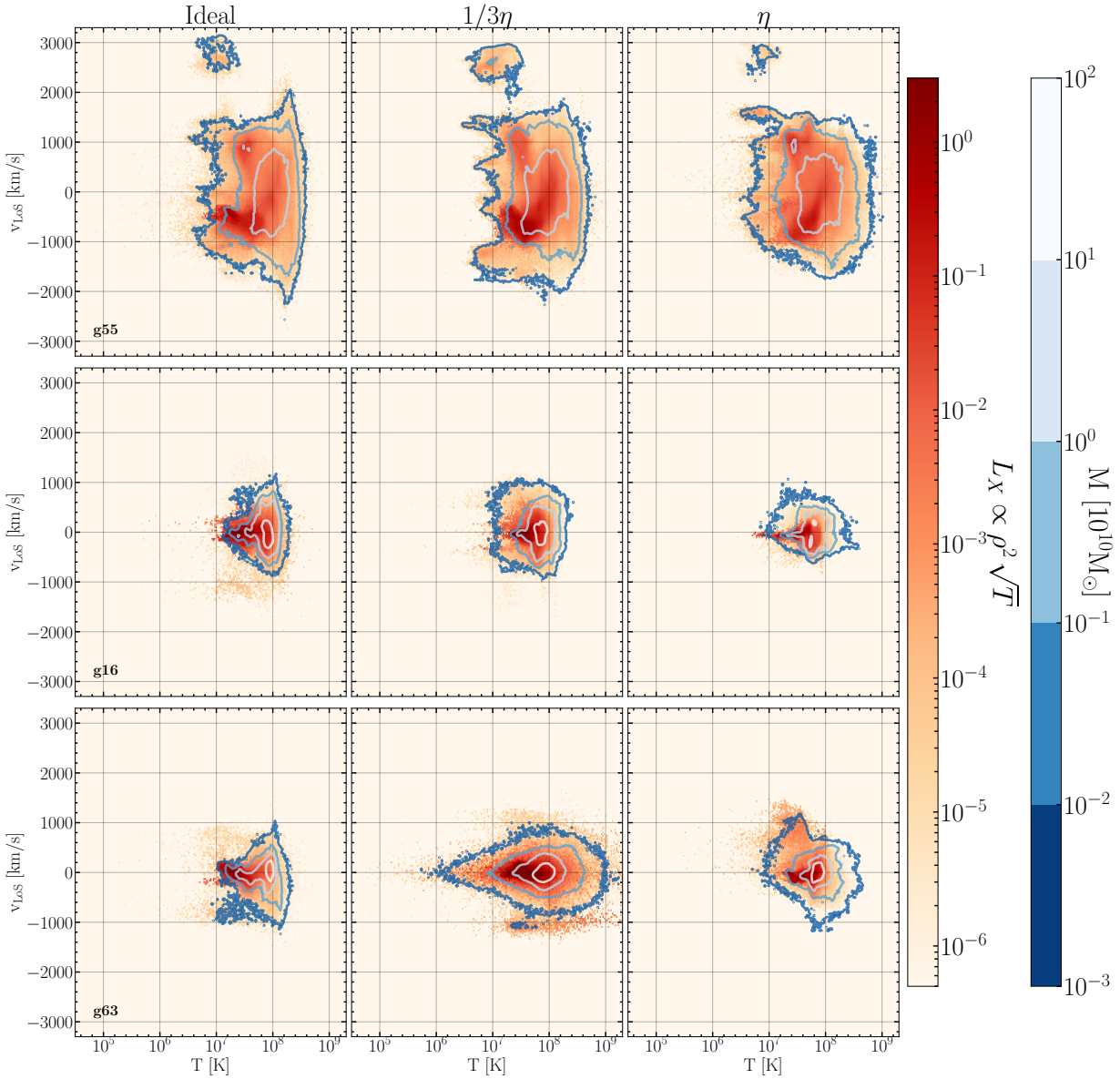

Figure 6.10: 2D histograms of the v_{LoS} as a function of the temperature, color-coded by emissivity. The contours indicate the mass distribution of the particles within the cluster. *From left to right*: MHD only, MHD with 1/3 of Spitzer viscosity, and full Spitzer viscosity at redshift zero. *From top to bottom*: clusters g55, g16 and g63.

Although the overall morphology remains the same, by visual inspection, one can identify morphological differences produced by viscosity due to the suppression of instabilities on small scales. The runs with more viscosity show a larger amount of small clumps that have not been disrupted by instabilities; a more filamentary structure produced by the gas stripped from infalling structures towards the center of the cluster; and more gas concentrated in the denser regions, rather than the more mixed and homogeneous gas seen in the non-viscous cases. The kinetic energy transformed into internal energy by viscosity leads to the heating of the less dense regions, although the denser regions remain as cold as in the inviscid runs. This is translated into a higher virial temperature in the runs with viscosity by ∼5% - 10%.

The lack of mixing in the viscous case produces a broader density PDF of the bulk gas of the cluster, which can be interpreted as larger density fluctuations. The density fluctuations are consistently larger along the cluster radius, the more viscous the medium is, increasing towards longer distances from the center.

Using a fixed value of $f_{\rm cut}$, used to divide the bulk and high-density gas, works well for inviscid simulations of galaxy clusters. However, the results with full viscosity (where the density PDF is broader) are slightly dependent on the choice of $f_{\rm cut}$. Therefore, a more accurate method to separate bulk and high-density gas should be investigated in the future to avoid the dependence on the shape of the density PDF.

The density and velocity fluctuations are directly proportional to one another, and both increase with the distance from the center. However, in all three clusters, the slope of the relationship between velocity and density fluctuations decreases with increasing viscosity. This linear relation is translated into a density-to-velocity fluctuations ratio of the order of unity for distances up to R_{200c}.

The runs with viscosity tend to have larger amplitudes of density fluctuations as a function of the scale. However, the density fluctuations obtained from our simulations are consistent with observations, even in the case with full viscosity. This is due to the large range of temperature distribution. In isothermal clusters, the slope of the amplitude of density fluctuations is affected by viscosity. This means that the method suggested by Zhuravleva et al. (2019) to constrain the amount of viscosity in the ICM by measuring the slope of the amplitude of density fluctuations is only applicable to isothermal clusters.

The amplitude of velocity fluctuations also appears to increase with viscosity, mainly at large scales. This behavior can also be observed when computing the velocity power spectrum, where viscosity leads to more power at large scales but decreases at smaller scales. The ratio of density to velocity fluctuations tends to be higher for cases with full viscosity, while remaining close to unity for all cases regardless of the amount of viscosity.

In summary, the cosmological simulations with viscosity show some morphological differences as well as temperature differences. We can quantify these morphological differences by measuring the fluctuations in density, which become larger in the cases with higher viscosity. This can be compared with observational measurements of the amplitude of density fluctuations. Our results are consistent with observations, making it difficult the task of constrain the amount of viscosity in the ICM solely from density fluctuations. The velocity fluctuations also happen to be larger at large scales in the cases with viscosity, although the ratio of density to velocity fluctuations is larger with viscosity, but close to one.

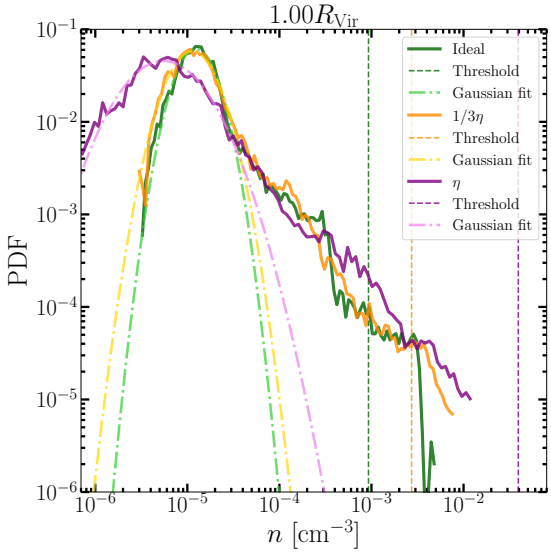

Figure H1: Density PDF of a 5 kpc shell centered around the virial radius of cluster g16 using a value of $f_{\rm cut} = 2.5$. The solid lines show the data obtained from the simulations; the dashed lines show the calculated threshold to split bulk and high-density gas; and the dashed-dotted lines show the fit of the bulk gas to a log-normal distribution.

Appendix H: Dependence on $f_{\rm cut}$

Viscosity broadens the density PDF due to the lack of mixing. As a result, it becomes difficult to define a dividing line between the bulk and the high-density gas. The median value of density is displaced towards larger values of density, causing the threshold defined in equation (6.1) to be a poor choice for the division between bulk and high-density gas. In the most extreme cases, this threshold lies outside the range of densities for certain shells of the cluster, as can be seen in Fig. H1 for cluster g16 for $f_{\rm cut} = 2.5$.

This signifies that some high-density clumps are not removed, leading to a maximum in the density fluctuations spectrum, as shown in Fig. 6.7. This can be solved by reducing the value of $f_{\rm cut}$ in equation (6.1) to lower values than 2.5. By doing this, we can successfully split bulk and high-density gas, as can be seen in the upper panel of Fig. H2, where we used $f_{\rm cut} = 0.5$. As a consequence, the maximum observed in the amplitude of the density fluctuations is reduced (see Fig. H3). However, if we use $f_{\rm cut} = 0.5$ in other clusters, the split of bulk and high-density gas is not properly done (see bottom panel of Fig. H2 to observe the effect in cluster g55). This value of $f_{\rm cut}$ would consider part of the bulk gas as high-density gas and would remove more gas than only high-density clumps. For consistency we use the same value of $f_{\rm cut}$ in all our clusters, choosing the value suggested in Zhuravleva et al. (2012) of $f_{\rm cut} = 2.5$ and acknowledging the spurious effects that it can have in the amplitude of density fluctuations.

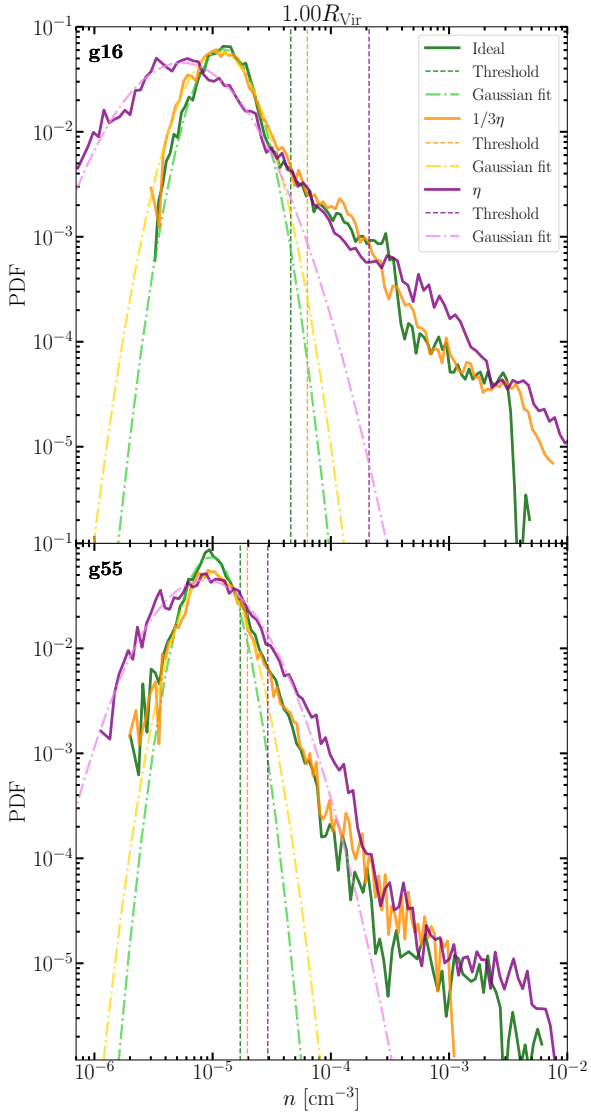

Figure H2: Density PDF of a 5 kpc shell centered around the virial radius using a value of $f_{\rm cut}$ = 0.5. The solid lines show the data obtained from the simulations; the dashed lines show the calculated threshold to split bulk and high-density gas; and the dashed-dotted line shows the fit of the bulk gas to a log-normal distribution. *Top panel*: cluster g16. *Bottom panel*: cluster g55.

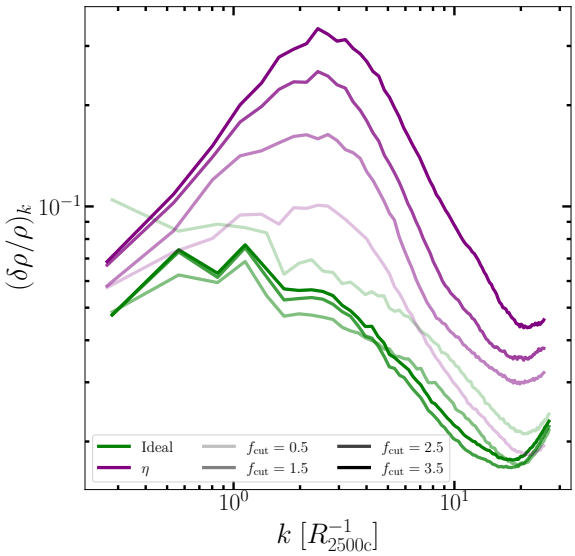

Figure H3: Comparison of the amplitude of density fluctuations in cluster g16 for different values of $f_{\rm cut}$ with and without viscosity.

Appendix I: Density Profile

If we look at the radial density profile of each one of the clusters (Fig. I1), we do not observe any clear trend among the cases with different viscosities. This shows how, at large scales, the viscosity effects do not significantly affect the cluster morphology. We need to study the density fluctuations ($\sim$ 5%-10% of the total density, Churazov et al., 2012; Sanders & Fabian, 2012) to see bigger differences between the cases with and without viscosity. When making a radial profile, using the mean density for each shell hides the main impact of the viscosity, which is seen in the fluctuations about the mean. Fig. 6.3 shows how, even though the density distribution is broader with viscosity, the mean value remains more or less the same, leading to very similar radial density profiles.

Appendix J: Velocity Power Spectrum

We can make use of the code VORTEX-P to interpolate the particles into a grid and compute the velocity power spectrum for each cluster and each amount of viscosity in each case. Fig. J1 shows the power spectrum normalized to Kolmogorov for each cluster within R_{2500c}. In all cases, the slope is steeper than Kolmogorov, however, the slope is the same in each cluster regardless of the amount of viscosity. At larger scales, the runs with viscosity appear to be more energetic, although at intermediate and small scales, the viscosity runs become less energetic (except for the cluster g16).

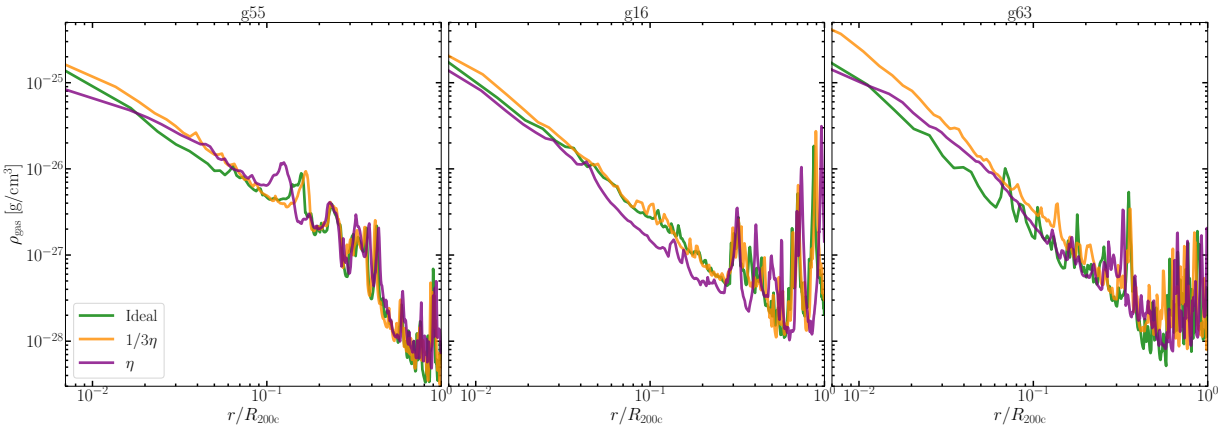

Figure I1: Radial profile of the density computed from spherical shells of 10 kpc. *From left to right*: clusters g55, g16 and g63 for each one of the configurations.

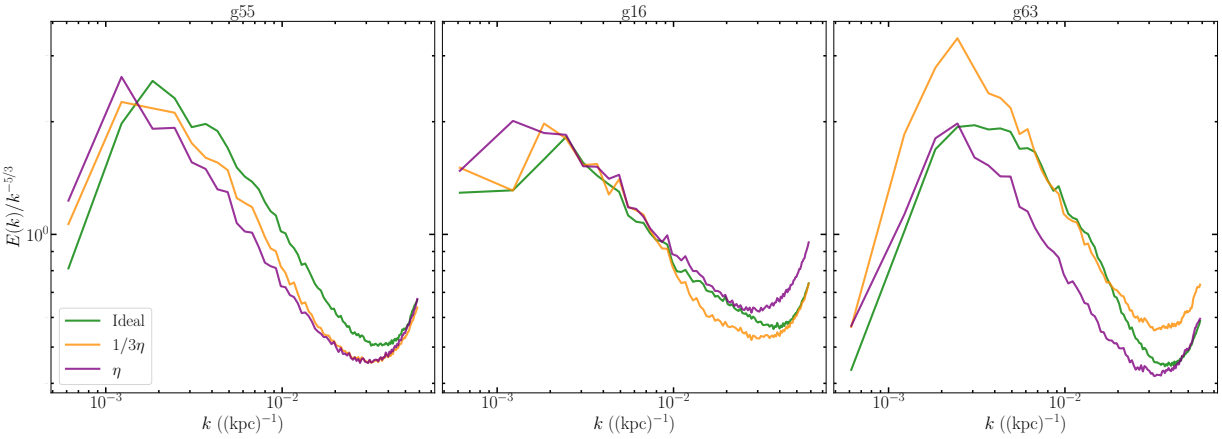

Figure J1: Velocity power spectrum normalized to Kolmogorov. *From left to right*: clusters g55, g16 and g63 for each one of the configurations.

7 | The Effect of Viscosity on the Dynamics of Galaxy Clusters[1]

After having attempted to quantify the impact of viscosity in the ICM and to constrain its value from the power spectrum of density fluctuations, in this Chapter we analyze how viscosity influences the dynamical evolution of galaxy clusters. Although there is no current method to constrain the amount of viscosity quantitatively from cosmological simulations besides the comparison with density fluctuations, investigating the effect of viscosity in individual processes in detail is still valuable. It allows for a more comprehensive understanding of how viscosity shapes not only observable cluster characteristics but also their long-term evolution.

7.1 Turbulent Pressure Support

Viscous forces damp the turbulent motions in the ICM, which has a direct impact on the dynamics of galaxy clusters. A direct consequence of this, together with the dissipative effect of viscosity, might be to reduce the turbulent pressure support, leading to the lower values observed recently (see §1.5.1). The decrease of turbulent velocity, together with an increase of temperature, might potentially lead to a lower turbulent to total pressure ratio ($P_{\rm turb}/P_{\rm tot}$).

7.1.1 Measurement of Turbulence

Astrophysical turbulent flows display an intrinsically multi-scale nature, making their numerical simulation and the subsequent analysis of simulated data a complex problem. In particular, the study of turbulent velocity fields can be done by performing a Helmholtz-Hodge decomposition (compressive + solenoidal) and a Reynolds decomposition (bulk + turbulent). This problem is relatively simple to perform numerically in uniform grids, such as the one emerging from Eulerian, fixed-grid simulations, but its computation is remarkably more complex in the case of non-uniformly sampled data, such as the one stemming from particle-based or meshless simulations. This can be done using the code VORTEX-P (Vallés-Pérez et al., 2021b,a, 2024, §3.3), which creates an ad-hoc AMR mesh hierarchy from the velocity field with the ultimate goal of providing a multi-resolution Helmholtz-Hodge and Reynolds decomposition.

[1]This Chapter is expected to be published by Marin-Gilabert et al, in prep.

Table 7.1: Volume-weighted average of the $\mathcal{M}_{3D}$ within R_{200c} and R_{2500c} and the turbulent pressure fraction within R_{2500c} depending on the amount of viscosity, for a direct comparison with observations (see Table 1.1 for comparison). Clusters g55 and g16 (first and second rows) are unrelaxed, while cluster g63 (third row) is relaxed.

	$\mathcal{M}_{3D}\|_{R_{200c}}$			$\mathcal{M}_{3D}\|_{R_{2500c}}$			$P_{turb}/P_{tot}\|_{R_{2500c}}$		
	Ideal	1/3 η	η	Ideal	1/3 η	η	Ideal	1/3 η	η
g55	0.44	0.40	0.29	0.50	0.53	0.53	0.13	0.14	0.14
g16	0.44	0.40	0.26	0.26	0.30	0.24	0.04	0.06	0.04
g63	0.33	0.38	0.25	0.18	0.19	0.18	0.02	0.03	0.02

To measure the turbulent velocity field in galaxy clusters, we perform a Reynolds decomposition in our galaxy cluster after having removed the high-density clumps (see §6.4.1). We then use the turbulent field and compute the turbulent pressure support as

$$P_{turb} = \frac{1}{3}\rho v_{turb}^2 , \tag{7.1}$$

and the total pressure as the sum of the thermal pressure of the gas, the turbulent pressure, and the magnetic pressure:

$$P_{tot} = P_{th} + P_{turb} + P_{mag} , \tag{7.2}$$

although the magnetic pressure has a negligible effect. Then the turbulent pressure fraction is calculated as P_{turb}/P_{tot}. The results of turbulent pressure fraction, as well as $\mathcal{M}_{3D}$ for our three clusters and the three levels of viscosity can be seen in Table 7.1. The calculation has been done within R_{2500c}, to be comparable with observations (see Table 1.1), as well as within R_{200c}, by volume-weighted averaging over the particles.

While cluster g55 shows a larger turbulent pressure support due to its recent activity[2], clusters g16 and g63 show a very low turbulent pressure in the cluster core, although g16 is considered unrelaxed, consistent with recent observations (see Table 1.1). Although both g55 and g16 are active clusters, the discrepancy is due to a recent merger in cluster g55, which produces an increase of a factor of three with respect to g16. Overall, viscosity seems to have a small effect on the turbulent to total pressure ratio within R_{2500c}. Viscosity does not show a significant effect in the averaged Mach number within R_{2500c} either. However, when averaging within R_{200c}, the effect of viscosity is remarkable, leading to a factor 1.3-1.7 lower $\mathcal{M}_{3D}$ in the most viscous cases compared to the ideal ones.

For a more detailed study of the turbulent pressure support in our clusters, we plot the ratio of the turbulent to total pressure as a function of the radius (see Fig. 7.1). Although P_{turb}/P_{tot} is expected to increase towards the outskirts of galaxy clusters (Groth et al., 2025), in the case of g55 it decays with the radius, as a consequence of a recent merger, which increases P_{turb} in the center. In both g16 and g63, the turbulent to total pressure ratio increases with the radius, reaching a $P_{turb}/P_{tot} \sim 0.1$ at R_{200c}. Although the radial profile of g16 shows consistently larger turbulent to

[2]There was a recent merger in cluster g55 just before $z = 0$.

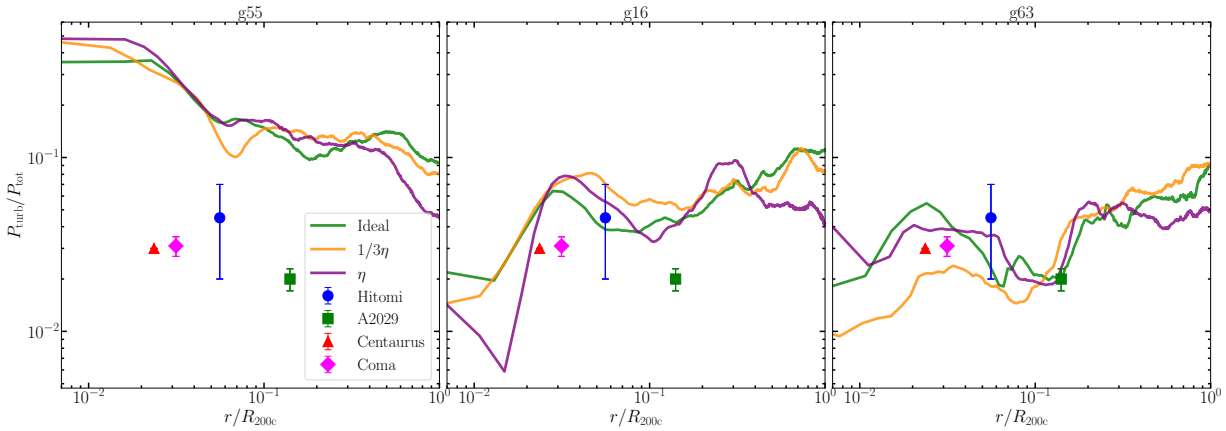

Figure 7.1: Volume-weighted radial profile of the turbulent pressure support ($P_{\rm turb}/P_{\rm tot}$) of our three clusters within R_{200c}, depending on viscosity (solid lines). The data points correspond to different observations shown in Table 1.1: Hitomi (Hitomi et al., 2018), A2029 (XRISM, 2025), Centaurus (Audard et al., 2025), and Coma (XRISM et al., 2025). *From left to right*: clusters g55, g16 and g63 for each one of the configurations.

total pressure values compared to g63, both g16 and g63 are in agreement with the observations. While the impact of viscosity appears minimal in the central regions of the cluster, its influence becomes more evident at larger radii, resulting in a reduced $P_{\rm turb}/P_{\rm tot}$ ratio in the outskirts of the galaxy cluster. Note that these simulations are non-radiative, and the contribution of AGN feedback might increase the turbulent to total pressure ratio in the cluster centers, therefore, these results should be understood as lower limits.

7.2 Magnetic Fields

Although the ICM is weakly magnetized, magnetic fields have a crucial effect in several astrophysical processes, such as cosmic ray acceleration and non-thermal emission (Brunetti & Lazarian, 2007; Böss et al., 2024), energy transport and cooling flows (Carilli & Taylor, 2002), or structure formation and evolution (Feretti et al., 2012). Therefore, understanding the magnetic field structure, magnitude, and evolution is key for a proper description of the physics of the ICM.

Magnetic fields are amplified over time due to a dynamo effect, until an (approximately) equipartition is reached between the turbulent and magnetic energy. This continuous process amplifies the magnetic fields to the order of $\sim 1-10\,\mu$G at $z = 0$ in the cluster center. The dynamo effect relies on the amplification due to small-scale turbulence. Therefore, the interplay between viscosity and turbulence might significantly influence the dynamo processes within clusters, as viscosity can suppress the small-scale eddies of the turbulent cascade where magnetic fields are amplified (see §1.4.2). To measure the impact of viscosity in the magnetic field amplification, Fig. 7.2 shows the magnetic field strength for our three different clusters and viscosities at $z = 0$.

In all cases, the magnetic field reaches a strength of the order of $\sim 10\,\mu$G, consistent with observations (Feretti et al., 2012), and then decays when increasing the distance from the cluster

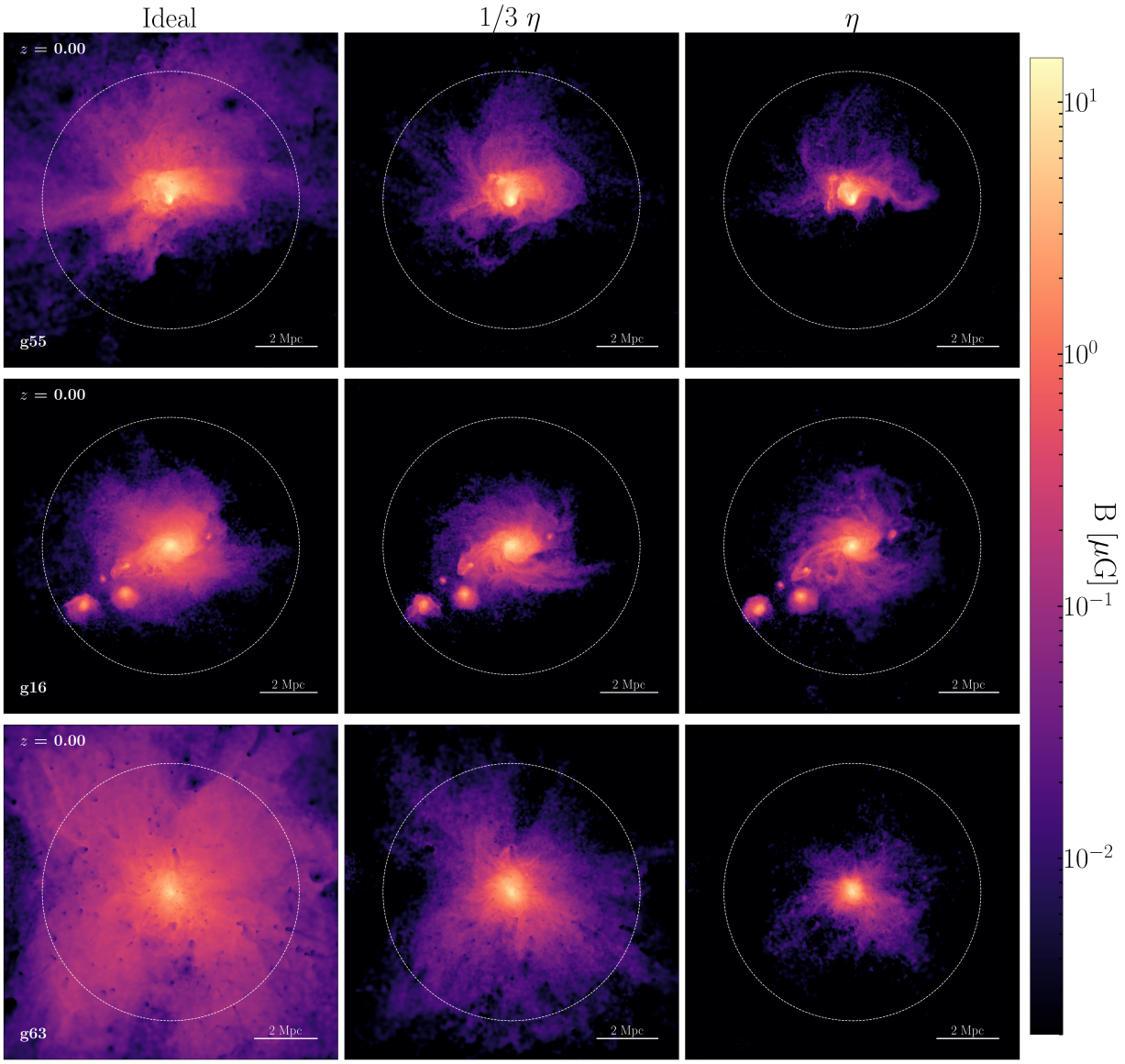

Figure 7.2: Magnetic field strength projections for all of our simulations listed in Table 6.1. *From left to right*: MHD only, MHD with $1/3$ of Spitzer viscosity, and full Spitzer viscosity at redshift zero. *From top to bottom*: clusters g55, g16 and g63.

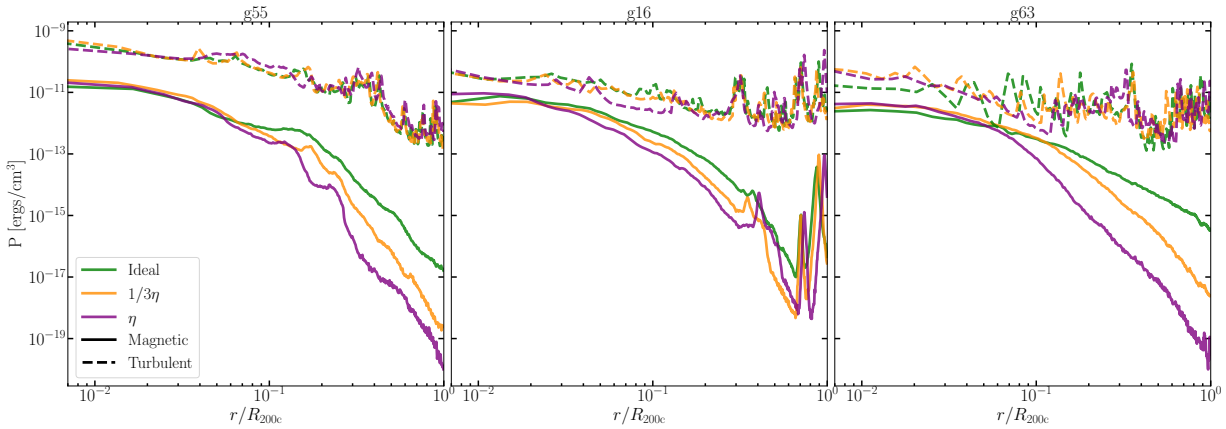

Figure 7.3: Radial profile of the magnetic pressure (solid lines) and turbulent pressure (dashed lines) at redshift zero. *From left to right*: clusters g55, g16 and g63 for the different runs.

center. While viscosity appears to have little influence on the magnetic field strength near the core, it leads to a noticeably weaker magnetic field in the outskirts compared to the non-viscous scenario. This effect can be seen in more detail by plotting the magnetic field radial profile. Fig. 7.3 shows the magnetic pressure (solid lines) and the turbulent pressure[3] (dashed lines) as a function of the radius. The reduced magnetic field in the outskirts is a direct consequence of the lower turbulent velocities shown in Table 7.1, indicating that viscosity plays a more significant role at larger radii. The suppression of turbulence by viscosity results in a less efficient amplification of the magnetic field in these outer regions, as it was already shown in Fig. 7.2. The high activity of cluster g55 produces a turbulent pressure that is more than an order of magnitude larger than the magnetic pressure, probably because the energy injection due to a recent merger has not been able to amplify the magnetic field yet. In contrast, g16 and g63 exhibit a turbulent and magnetic pressure of the same order of magnitude, as expected from dynamo theory (see §1.4.2).

Although no big effects can be seen in the turbulent pressure profile due to viscosity, the continuous viscous effect over cosmological times has a significant impact on the magnetic field evolution. Fig. 7.4 shows this effect, where the magnetic pressure (solid lines) and turbulent pressure (dashed lines) are plotted as a function of the scale factor (time) by averaging over R_{200c}. In all cases, the magnetic field grows exponentially regardless of the level of viscosity, although in the viscous cases, this growth is slower. The growth rate of the dynamo depends on the smallest eddies' turnover time (see §1.4.2). Therefore, since viscosity suppresses the small-scale turbulence, the smallest eddies' turnover time is larger. This leads to a slower amplification, although it eventually saturates when an equipartition with the turbulent pressure is reached. In all clusters, the magnetic field saturates at the same magnetic field strength ($B \sim 10\ \mu$G). From our three clusters, we can observe that the saturation is reached at $z \sim 1.5 - 1$, although this saturation is reached later the more viscous the medium is. At $z = 0$, the magnetic field strength is dominated by the strength at the center, which is several orders of magnitude larger than in the

[3]In this case, we use the solenoidal component of velocity as a proxy of turbulence, to account also for bulk motions.

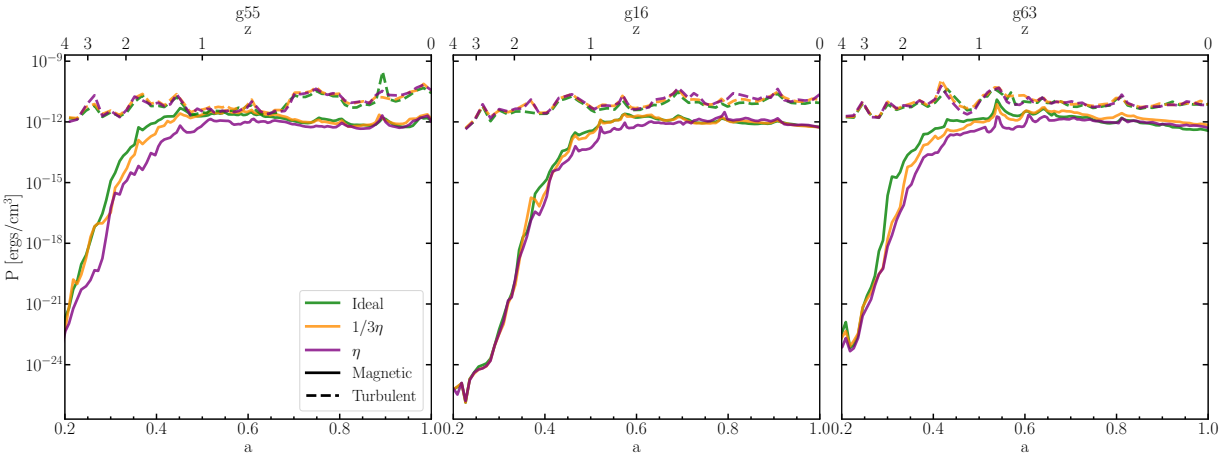

Figure 7.4: Magnetic pressure (solid lines) and turbulent pressure (dashed lines) evolution from $z = 4$ until $z = 0$. *From left to right*: clusters g55, g16 and g63 for the different runs.

outskirts.

These results show that even a modest level of viscosity can have a measurable impact on the evolution of galaxy clusters, particularly at large radii and over cosmological timescales. While the impact of viscosity in the inner regions of the cluster seems to be limited, the effect becomes significantly stronger in the outskirts. This leads to a clear suppression of small-scale turbulent motions, resulting in a reduced turbulent pressure support and, consequently, a lower efficiency in the amplification of magnetic fields. The slower growth of magnetic energy and the delayed onset of saturation observed in the more viscous runs are a direct consequence of the reduced turbulent cascade, especially at the smallest scales where magnetic amplification operates. Although the central magnetic field strength at $z = 0$ eventually reaches similar values across all models, the buildup is noticeably delayed in the viscous cases, highlighting the cumulative nature of viscous damping in the outer regions. This highlights the importance of accurately modeling microphysical processes when aiming to capture the long-term thermodynamical and magnetohydrodynamical evolution of the ICM, especially accounting for its weakly collisional and magnetized nature, where the assumption of isotropy may no longer hold.

8 | Braginskii Viscosity – A More Accurate Treatment of Viscosity[1]

The isotropic (Spitzer) viscosity treatment shown in previous sections represents a simplification of the plasma conditions present in the ICM (see §2.1 and 2.5). In reality, the ICM behaves as a weakly collisional plasma, and its viscosity is governed by anisotropic transport processes due to the suppression of particle motion perpendicular to magnetic field lines (Schekochihin et al., 2005; Squire et al., 2023). Therefore, a more physically consistent description of viscosity in such environments is achieved by adopting the Braginskii viscosity formalism, which accounts explicitly for the anisotropic nature of momentum transport along magnetic fields (Braginskii, 1965). In this section, we present the initial tests of the anisotropic (Braginskii) viscosity implementation in OpenGadget3, described in §3.1.8, following the setups described by Berlok et al. (2019). These tests serve to validate the numerical approach and explore the fundamental differences arising from anisotropic transport relative to the isotropic approximation.

8.1 Soundwave Test

The first test is the propagation of a simple soundwave in a 3D setup of sizes $L = L_{x,y,z}$ with an initial velocity of

$$v_x = A \sin(\mathbf{k} \cdot x)\hat{x}\,, \tag{8.1}$$

where A is the initial amplitude of the perturbation and $\mathbf{k} = 2\pi\hat{x}$ is the wavenumber. We start with a constant density ρ and a resolution of 128^3, given by the number of particles per unit length placed in a regular grid. We include a constant static magnetic field $\mathbf{B}$, first in the x-direction (parallel to the velocity gradient) and then in the y-direction (perpendicular to the velocity gradient).

Fig. 8.1 shows the velocity profile at $ct/L = 1$ for B_x on the left, and B_y on the right. In both cases, the inviscid run keeps the initial amplitude, showing that it has not been damped due to numerical viscosity, while the isotropic run suppresses the soundwave by the same amount regardless of the magnetic field direction. In the soundwave with a parallel magnetic field ($B_x \parallel \Delta v$, left panel), the isotropic and the anisotropic cases have the same amplitude, showing that, in the direction of the magnetic field lines, the overall effect of the anisotropic viscosity is

[1] This Chapter is expected to be published by Marin-Gilabert et al, in prep.

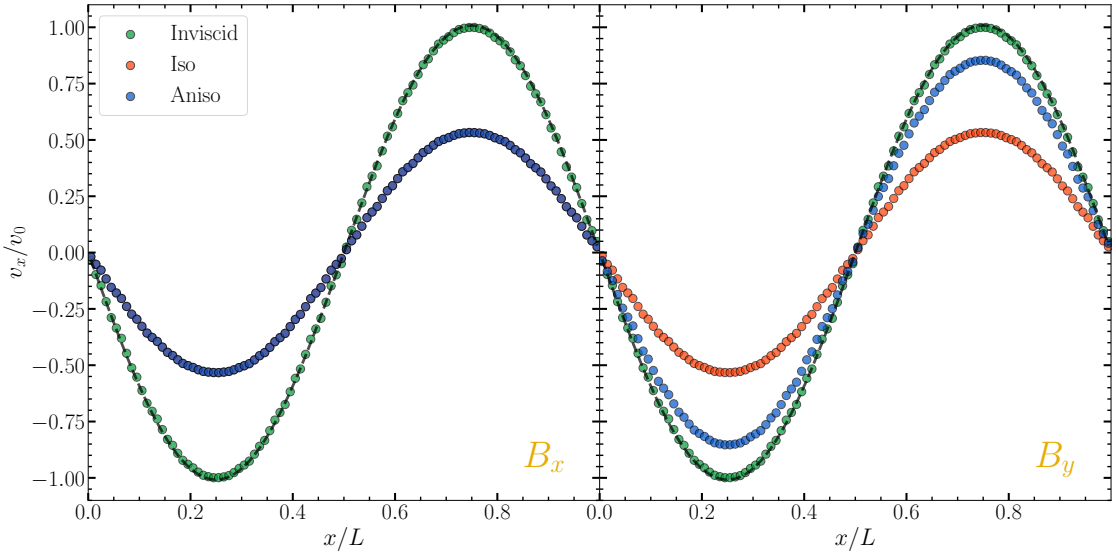

Figure 8.1: Velocity profile of the soundwave described by equation (8.1) after $ct/L = 1$. *Left panel*: Magnetic field in the x-direction, parallel to the velocity gradient. The inviscid case (green) follows the initial soundwave amplitude, while the isotropic case (red) and anisotropic case (blue) have been damped due to viscosity by the same factor. *Right panel*: Magnetic field in the y-direction, perpendicular to the velocity gradient. The inviscid and isotropic runs remain unchanged compared to the parallel case, but the amplitude in the anisotropic case has been reduced due to the compression of the wave.

equal to the isotropic one. In contrast, when the magnetic field is perpendicular to the velocity gradient ($B_y \perp \Delta v$, right panel), the anisotropic case does not mimic the isotropic case, although there is still some suppression. This suppression corresponds exactly to $\Delta p = \eta \nabla \cdot v$, the second term of the RHS in equation (2.8). This means that, although the magnetic field is perpendicular to the velocity gradient, viscosity has some effect due to the compression (or expansion) of the fluid. In an incompressible fluid, the overall effect of anisotropic viscosity should be zero, although this is not the case in a compressible fluid.

8.2 KHI Test

To perform the second test, we use the KHI setup described in §4.2, although in this case we add a magnetic field **B**. With this setup, the velocity gradient has only a y component, therefore, we would see the maximum viscous effects when $\mathbf{B} = B\,\hat{y}$. However, in the case of a magnetic field in the y-direction, the fluids' motion leads to a shear amplification due to the compression of the magnetic field lines, thus suppressing the instability (see Das & Gronke, 2023). For this reason, we can only include a magnetic field in the z-direction ($B_z \perp \nabla v$) and in the x-direction ($B_x \perp \nabla v$). In the presence of magnetic fields in the shear direction ($\hat{x}$), the KHI is fully suppressed due to magnetic tension when

$$B_\mathrm{h}^2 + B_\mathrm{c}^2 > 4\pi \frac{\rho_\mathrm{h}\rho_\mathrm{c}}{\rho_\mathrm{h} + \rho_\mathrm{c}} \Delta v_\mathrm{shear}^2 \,, \tag{8.2}$$

where B_h and B_c are the magnetic field of the hot and cold medium, respectively (Vikhlinin et al., 2001). In our setup, where $B_\mathrm{h} = B_\mathrm{c}$, the KHI is suppressed when $\beta \lesssim 16$, therefore we use a $\beta = 10^3$ to be able to study the growth of the instability depending on viscosity without suppression due to magnetic tension. Fig. 8.2 shows the results after $t = 1.5\tau_\mathrm{KH}$ of the simulation with B_z in the top row, and B_x in the bottom row.

The left panel of Fig. 8.2 shows the density colormap normalized to the hot medium density. In the run with B_z (upper row), the KHI can grow in a similar way to the non-viscous (or low viscosity) case shown in the bottom row of Fig. 4.2, where the characteristic rolls of the KHI are fully developed[2]. The magnetic field remains similar to the initial one after $1.5\tau_\mathrm{KH}$ (middle panel), while the pressure anisotropy remains close to zero (right panel). The growth of the instability can be quantified by measuring the growth rate, as we did in §4.4.2, although now we compare the growth rate of the inviscid, isotropic, and anisotropic cases. Note that in the isotropic and anisotropic case, the same value of the Spitzer coefficient is used: $\eta = 0.05\eta_\mathrm{Sp}$, assuming a $T = 3 \cdot 10^7$ K (a viscosity much higher than the critical viscosity found in §4 to highlight the differences, see Table §4.1). The left panel of Fig. 8.3 shows the growth rate of the instability for the different cases. The isotropic case strongly suppresses the growth of the KHI, while the inviscid and anisotropic cases behave very similarly, allowing the growth of the instability. This kind of behavior is expected, since $B_z \perp \nabla v$, therefore, the effect of the anisotropic viscosity should be almost zero.

[2]Note that the version of the code used here is different than the one used in §4, therefore the results might be slightly different.

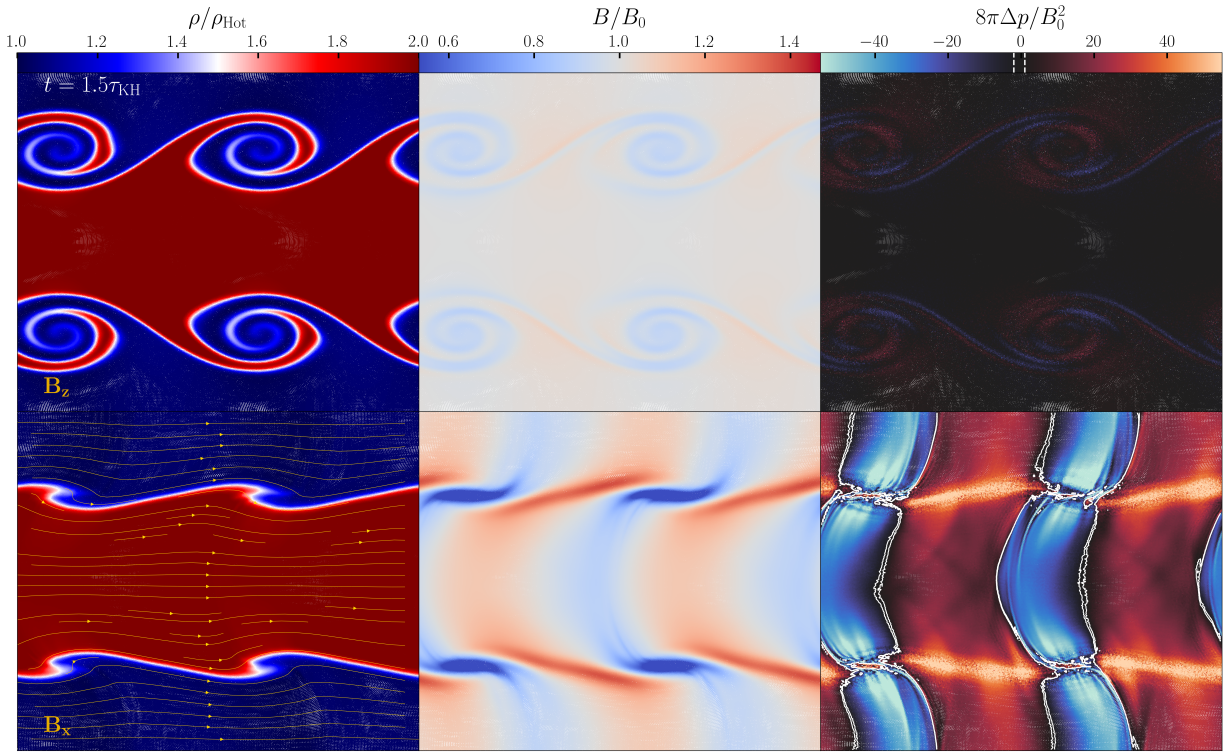

Figure 8.2: Colormaps of the KHI with anisotropic viscosity. *Top row*: Magnetic field in the z-direction. *Bottom row*: Magnetic field in the x-direction. *Left column*: Density colormap, normalized to the hot gas density. *Middle column*: Magnetic field strength colormap, normalized to the initial magnetic field. *Right column*: Pressure anisotropy, normalized to $B_0^2/8\pi$, where the white dashed line in the colorbar indicates the limits for the firehose and mirror microinstabilities (left and right, respectively).

In the run with B_x (bottom row of Fig. 8.2), although the magnetic field and the velocity gradient are initially perpendicular, the density colormap (left panel) shows a clear suppression of the instability. The reason is the bend of the magnetic field lines due to the growth of the KHI. Due to the fluid motions, the magnetic field lines (indicated by the yellow vector field in the colormap) are bended in the y-direction (parallel to the velocity gradient), producing a non-zero pressure anisotropy that results in a strong suppression of the growth (note that $\eta \gg \eta_{\rm Crit}$). The plasma motions also lead to an increase in the magnetic field strength in areas where the magnetic field lines are compressed, or decrease where they are decompressed (middle panel). These processes lead to a non-zero pressure anisotropy (right panel), with a positive value in regions where the field strength increases and a negative value where the field strength decreases (see §2.5). The pressure anisotropy colormap shows regions where the firehose instability is triggered ($8\pi\Delta p/B_0^2 < -2$, blue colors) and regions where the mirror instability is triggered ($8\pi\Delta p/B_0^2 > 1$, yellow colors), where the limits are indicated by white-dashed lines in the colorbar. These white lines are plotted over the colormap, highlighting that only the gas inside the white lines lies within the limits set by the plasma microinstabilities. This means that, if we set the limit for plasma microinstabilities, the value of Δp of the vast majority of the plasma will be limited by the microinstabilities (see §2.5.1). Due to the weak magnetic field used ($\beta = 10^3$), the magnetic field lines are bent more easily. This has three effects: *i*) the KHI is able to grow; *ii*) the bend of the lines produces a strong effect of anisotropic viscosity; *iii*) the plasma microinstabilities are triggered easily.

The growth rate of the instability with B_x can be seen in the right panel of Fig. 8.3. While the isotropic case strongly suppresses the KHI, as in the B_z case, the inviscid case allows the growth. However, the maximum y-velocity reached is lower than the B_z case, since the magnetic field itself slightly suppresses the growth of the instability. In the anisotropic case, there is an initial growth; however, as soon as the magnetic field lines are bent, viscosity suppresses the growth, reaching a much lower amplitude than the non-viscous case. As described above, the pressure anisotropy values exceed the limits set by the plasma microinstabilities. If we set these limits, the growth of the instability follows a similar growth as the inviscid case, since the Δp of the majority of the gas is limited by these microinstabilities.

To analyze in detail the amount of particles affected if we switch on the plasma microinstabilities limits, Fig. 8.4 shows a histogram of Δp of all the particles in the setup with $\beta = 10^3$ (left column) and $\beta = 10^2$ (right column), together with the values of the limits set by the microinstabilities (dashed lines). The top-left panel shows the histogram of the simulation without the limits after $t = 0.5\tau_{\rm KH}$, allowing Δp to go beyond the limits. It shows how the vast majority of particles are found outside the limits set for $\beta = 10^3$. If we switch on the limits (bottom-left panel), the range allowed for Δp is much smaller, thus, the viscous effect is largely reduced, which explains why the KHI behaves similarly to the inviscid case in Fig. 8.3.

In the case of $\beta = 10^2$, the magnetic field lines have a larger tension, thus they are more difficult to bend. This leads to a stronger suppression of the KHI due to magnetic fields, as can be seen in Fig. 8.5 by measuring the growth rate in the case with $\mathbf{B} = B\,\hat{x}$ and $\beta = 10^2$. The inviscid case grows (the slope is positive within $1\tau_{\rm KH}$), but much less than the case with $\beta = 10^3$. Since the field lines are more difficult to bend, this means that the contribution to anisotropic viscosity is also lower than in the case of $\beta = 10^3$, although the effect is still noticeable. Since the

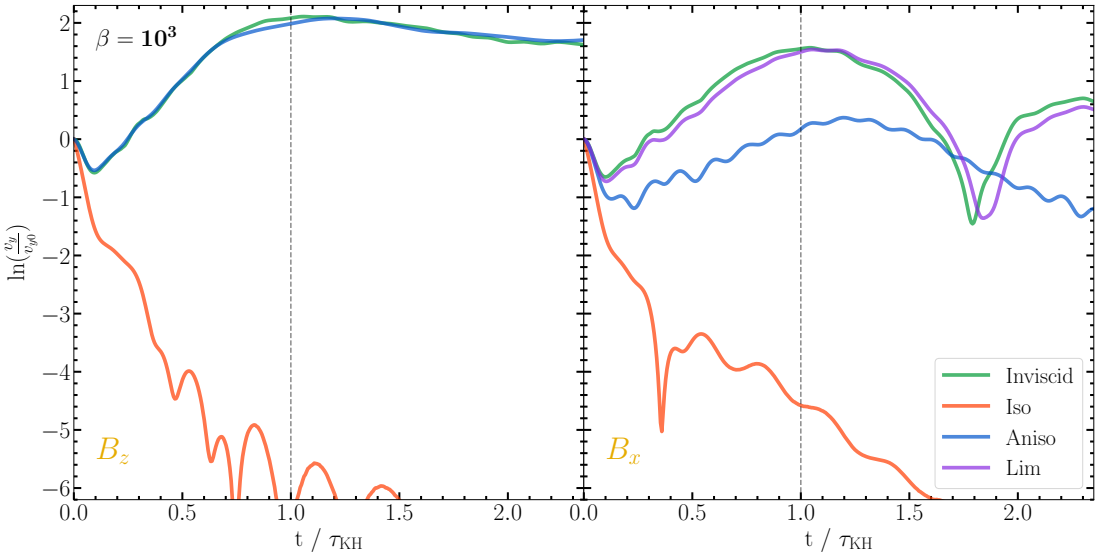

Figure 8.3: Growth rate of the KHI of a setup with $\beta = 10^3$ for different viscosity treatments: inviscid (green), isotropic (red), anisotropic (blue), and anisotropic with plasma microinstabilities limits (purple). *Left panel*: Runs where the initial magnetic field has only a z-component. *Right panel*: Runs where the initial magnetic field has only x-component.

magnetic component parallel to ∇v is smaller compared to the case with $\beta = 10^3$, the range of values of Δp is narrower (see top-right panel of Fig. 8.4), producing that the majority of particles are found within the plasma microinstabilities limits for $\beta = 10^2$. This translates into a smaller overall effect of anisotropic viscosity. Additionally, the stronger magnetic field sets the plasma microinstability limits to larger values of Δp, therefore, if we switch on the limits (bottom-right panel in Fig. 8.4), the behavior is similar to the anisotropic case without the limits (see Fig. 8.5).

These initial tests constitute an important step toward a more accurate modeling of viscosity in the ICM, capturing the inherently anisotropic nature of momentum transport in magnetized, weakly collisional plasmas. The results show that, unlike the isotropic treatment, anisotropic viscosity responds to the orientation and evolution of the magnetic field, allowing or suppressing instabilities depending on the local field geometry and fluid dynamics. While configurations aligned with the velocity gradient reproduce similar damping to the isotropic case, perpendicular or evolving field geometries reveal substantial differences, including directional suppression of instabilities and the emergence of pressure anisotropies that can exceed microinstability thresholds. These effects, although explored here in controlled setups, have clear implications for realistic astrophysical environments, where magnetic fields are neither static nor homogeneous. These tests set a first step toward a more comprehensive understanding of anisotropic transport in the ICM, requiring further development, testing, and eventual integration into cosmological simulations.

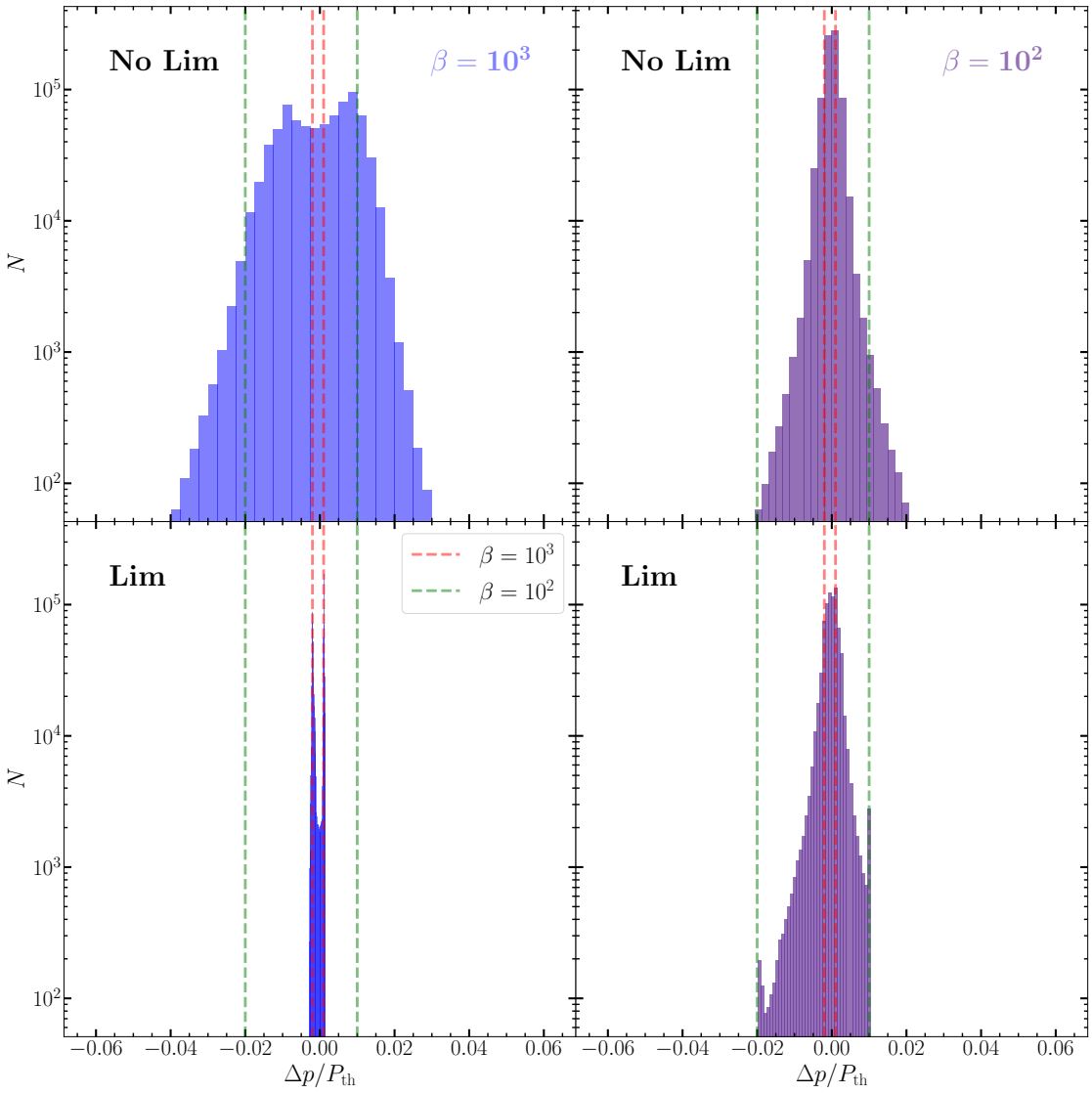

Figure 8.4: Histogram of the pressure anisotropy of all the particles of the simulation, normalized to the thermal pressure. *Top row*: Runs where Δp can evolve without setting the plasma microinstabilities limits. *Bottom row*: Runs where Δp is limited to the mirror and firehose instabilities limits, for $\beta = 10^3$ (red dashed line) and $\beta = 10^2$ (green dashed line). *Left column*: Cases with $\beta = 10^3$. *Right column*: Runs with $\beta = 10^2$.

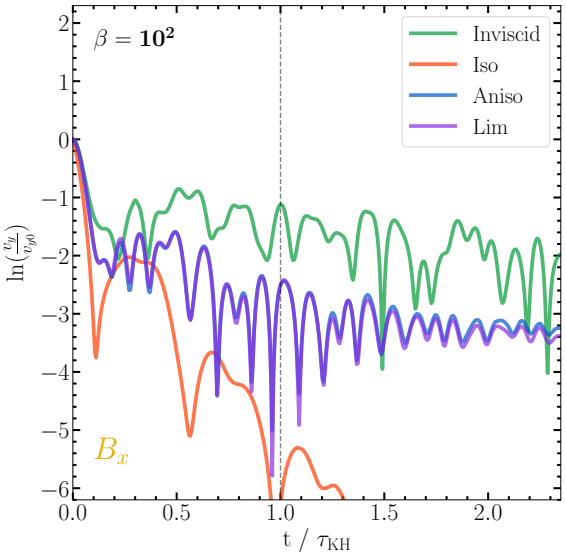

Figure 8.5: Growth rate of the KHI of a setup with $\beta = 10^2$ and initial B_x for different viscosity treatments: inviscid (green), isotropic (red), anisotropic (blue), and anisotropic with plasma microinstabilities limits (purple).

9 | Conclusions

In this thesis, we have presented a detailed investigation of the physical processes governing the evolution of the ICM and CGM, with particular emphasis on the roles of turbulence, isotropic viscosity, and multiphase gas dynamics. Utilizing both idealized setups and cosmological simulations, we quantified how these mechanisms influence observable characteristics of galaxy clusters and galactic halos.

Detailed simulations of the KHI under realistic conditions relevant to galaxy clusters showed that physical viscosity substantially suppresses instability growth below a well-defined threshold. This threshold corresponds to a small fraction (approximately 10^{-3}) of classical Spitzer viscosity in our setup, although this threshold depends on the overdensity, Mach number, and wavelength of the instability. The numerical viscosity in our implementation in OpenGadget3 was explicitly quantified and found negligible relative to physical values in cluster-like environments, reinforcing the validity of our numerical approach for astrophysical applications.

The role of viscosity in multiphase systems and its effect on cooling has also been thoroughly explored. Our simulations confirm that physical viscosity suppresses turbulent velocities in the weak cooling regime, while keeping cooling efficiency intact, thus modifying previously established inviscid relations between cooling and turbulence. In contrast, in the strong cooling regime, viscosity was found to (slightly) enhance the surface brightness by smoothing temperature gradients, thereby increasing intermediate-temperature gas fractions and overall cooling efficiency. In this regime, cooling dominates over viscosity, allowing the system to develop turbulence, thus keeping the scaling relations in TRMLs largely intact. We derived analytical criteria predicting when viscosity would minimally impact cooling processes, validated through our numerical simulations. These results have direct implications for understanding observations of multiphase systems like galactic outflows, or the interaction between ISM-CGM-ICM, and it will be important for the implementation of subgrid models in large-scale simulations.

In our cosmological simulations, we found that viscosity significantly modifies turbulence and mixing in galaxy clusters, leading to a hotter ICM, as well as morphological differences. Specifically, viscosity enhances velocity fluctuations at large scales while suppressing small-scale mixing. This scale-dependent behavior directly impacts the amplitude and morphology of density fluctuations. Importantly, the ratio of density to velocity fluctuations increases with viscosity but remains close to unity, as theoretically expected. The power spectrum of density fluctuations increases with viscosity, although the slope remains the same regardless of the amount of viscosity. This was expected to be used as a method to constrain the amount of viscosity from observations,

however, our results are consistent with observational constraints from X-ray studies for all levels of viscosity. The reason for this is the large distribution of temperatures found in the gas of galaxy clusters, which ultimately sets the dissipation scale. This broad distribution does not set a unique dissipation scale, therefore keeping the slope of the power spectrum unchanged. These findings imply that current observations alone face challenges in constraining viscosity due to its subtle yet measurable morphological signatures.

The lack of turbulence found in galaxy clusters due to viscosity directly influences the dynamo effect needed for the magnetic field amplification. Viscosity leads to weaker magnetic fields in the outskirts of galaxy clusters, a consequence of the reduced turbulence compared to the non-viscous case. This result, however, is still consistent with both theory and observations, reaching a mean magnetic strength of $\sim 10\ \mu$G within the virial radius.

Finally, the first tests with anisotropic viscosity show promising results, where the simulations can reproduce the expected behavior in the weakly collisional ICM. These tests confirm the accuracy and robustness of our numerical implementation of Braginskii viscosity. So far, these tests have demonstrated the capability of our simulations to capture the subtle physical effects of anisotropic viscosity, crucial for ensuring the reliability of future studies. This implementation, however, still needs a more careful and detailed study before we can fully trust the results in a cosmological simulation.

Collectively, the findings of this thesis establish a link between microscopic plasma processes and macroscopic observables in galaxy clusters and galactic halos. Through a combination of idealized and cosmological simulations, we have systematically shown how isotropic viscosity, turbulence, and multiphase gas dynamics shape the evolution of the ICM and CGM. We demonstrated that even a small fraction of Spitzer viscosity can suppress the growth of instabilities and affect turbulent motions, with direct consequences for mixing, cooling, and magnetic field amplification. Our results highlight how viscosity modifies the morphological and spectral properties of the gas, including density fluctuations and velocity fields, while remaining broadly consistent with current observational constraints. The scale-dependent nature of these effects explains why current X-ray observations struggle to provide precise constraints on viscosity, despite its measurable impact on cluster structure. Moreover, the first successful tests of our implementation of anisotropic (Braginskii) viscosity in OpenGadget3 open the door to more realistic modeling of the weakly collisional ICM. Altogether, the work presented here advances our understanding of the baryonic physics in galaxy clusters and halos and provides a solid foundation for improving subgrid models in future large-scale simulations, as well as for interpreting upcoming high-resolution observations.

10 | Outlook and Future Work

While this work has provided a comprehensive analysis of isotropic viscosity and its influence on the ICM, several important physical regimes remain to be explored. In particular, the role of anisotropic viscosity, expected in magnetized, weakly collisional plasmas, requires deeper investigation. This extension is not only theoretically motivated but also numerically and observationally relevant, as recent high-resolution simulations and X-ray spectroscopic data point toward phenomena that might be explained through anisotropic transport mechanisms.

In addition to cluster-scale dynamics, future work will benefit from examining the impact of viscosity on smaller-scale processes such as ram pressure stripping in galaxies. Systems like jellyfish galaxies, which exhibit strong ICM-ISM interactions, provide a unique test for understanding how viscosity shapes gas morphology, mixing, and star formation in dynamic environments. Incorporating a physically accurate viscosity model in such contexts is crucial for improving subgrid physics and for connecting small-scale processes with large-scale galaxy evolution.

10.1 Anisotropic Viscosity in Cosmological Simulations

Having studied in detail the effects of isotropic viscosity within the ICM, the next natural step of this research is to extend the analysis to the more realistic scenario of anisotropic viscosity. Anisotropic viscosity, governed by the magnetic field orientation within the ICM, differs significantly from isotropic viscosity due to its directional dependence, thus potentially impacting the cluster dynamics in different ways.

Although a Braginskii viscosity is already implemented in OpenGadget3, it is still under testing to understand the limits and accuracy of the scheme. This treatment must ensure an accurate modeling of the complex plasma behavior governed in the weakly collisional ICM. Preliminary tests show promising results so far; however, extensive validation and optimization remain necessary to guarantee the robustness and accuracy of future simulations.

The state-of-the-art high-resolution cosmological simulations achieve a spatial resolution high enough to resolve the Coulomb collision scale (Steinwandel et al., 2024), entering the kinetic-aware regime (see Fig. 10.1, taken from Steinwandel et al., 2024). At this resolution, a simple isotropic treatment of viscosity becomes inadequate. Instead, a detailed Braginskii implementation is needed to properly capture the anisotropic nature of momentum transport along magnetic field lines. This is particularly crucial for understanding turbulence and instabilities in

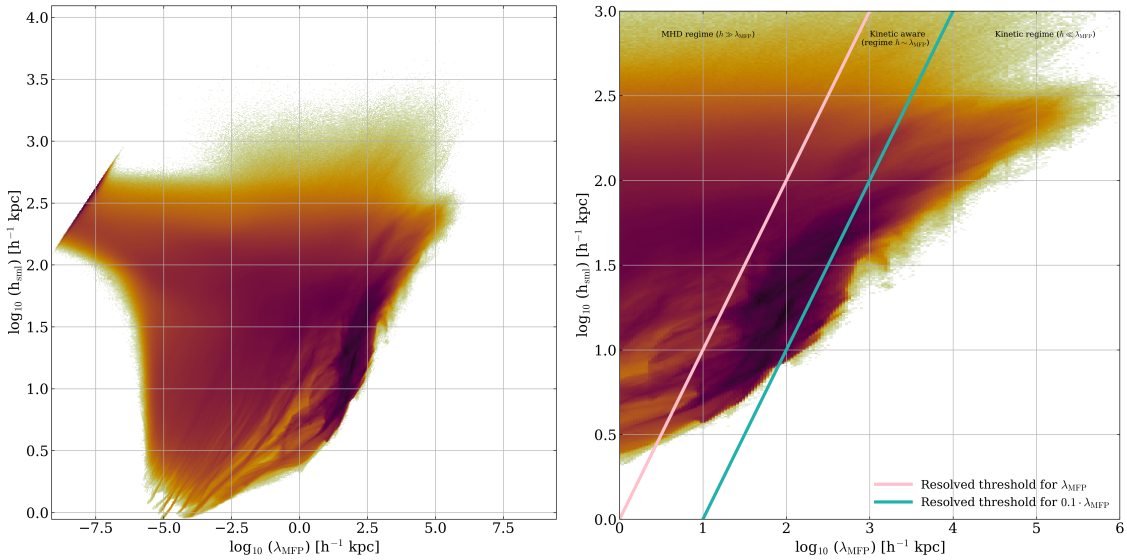

Figure 10.1: *Left panel*: Global distribution of the resolution (h_{sml}) as a function of the electron mean free path (λ_{MFP}). *Right panel*: Resolution as a function of the electron mean free path as a measure for the Coulomb diffusion length scale. This shows the region in the ICM that carries most of the mass in the ICM, densities above 10^{-7} cm^{-3} and temperatures above 10^6 K. The resolution in this regime resolves the Coulomb mean free path over a broad density and temperature regime in the ICM. The oink and turquoise lines mark the transition regions at which the smoothing length $h_{\mathrm{sml}} \approx \lambda_{\mathrm{MFP}}$ and $h_{\mathrm{sml}} \approx 0.1 \times \lambda_{\mathrm{MFP}}$ respectively, indicating that the resolution transits into a regime where kinetic-aware MHD becomes relevant. To the right of the turquoise line, one should consider a fully kinetic treatment. Figure taken from Steinwandel et al. (2024).

the ICM at scales relevant for observational comparisons.

The recent observations provided by XRISM (XRISM et al., 2025; XRISM, 2025; Audard et al., 2025) underline the importance of incorporating accurate viscosity models into simulations. These measurements show unexpectedly low turbulence levels in cluster cores, which could be explained by viscous damping effects, potentially arising from anisotropic viscosity. These observational constraints offer a unique opportunity to validate simulation outputs, reinforcing the importance of accurate viscosity modeling. Furthermore, the combination of simulations with isotropic and anisotropic viscosity with observations can be used to constrain the overall level of viscosity expected in galaxy clusters.

10.2 Pressure Stripping Galaxies

Another interesting aspect for future investigation involves the morphology and dynamical evolution of jellyfish galaxies. As galaxies move through the ICM, their cold ISM and CGM gas is stripped away, forming extended tails of gas that mix with the hot ICM. In these systems, the

cooling of the hot ICM in the interaction of the ISM might enhance the star formation (Müller et al., 2021). In this process, not only does mixing become important, but also cooling efficiency, which accounts for the amount of cold gas available to form stars.

The suppression of instabilities and consequent lack of mixing due to viscosity leads to morphological differences in the tails of these jellyfish galaxies moving through the ICM (see §6.3). Previous studies have analyzed the effect of isotropic viscosity in the morphology of stripped galaxies, showing longer tails the more viscous the ICM is (Roediger et al., 2015; Kraft et al., 2017), however, the effect of an anisotropic viscosity has never been studied in this context.

Viscosity reduces the total mixing of the hot and cold phases, decreasing the amount of intermediate-temperature gas entering the regime where the cooling curve peaks. Additionally, viscosity might (slightly) modify the cooling efficiency (see §5.2.3), directly affecting star formation in the tails of jellyfish galaxies. A deeper study with an idealized setup, combined with a thorough comparison with observations, might help us understand the overall effect of viscosity in such environments.

Understanding all these complex processes happening in the tails of jellyfish galaxies in more detail will enhance our ability to accurately model the intricate physics governing the ICM. Moreover, they will not only provide valuable insights into ram pressure stripping but will also aid the development of more accurate subgrid models, such as star formation, for larger cosmological simulations. These models are essential for capturing the complex interactions between galaxies and their environments, ultimately improving our understanding of galaxy evolution on both small and large scales.

In summary, this work provides a solid foundation for understanding the role of isotropic viscosity in the ICM, while highlighting the importance of extending this analysis to the more realistic regime of anisotropic viscosity. The implementation and validation of a Braginskii-type viscosity scheme in high-resolution cosmological simulations will be a crucial step forward, particularly as we enter a regime where the Coulomb mean free path is resolved and kinetic effects become increasingly relevant. Exploring the impact of anisotropic viscosity across different environments — from cluster-wide turbulence to the gas dynamics of ram pressure stripped galaxies — will allow us to probe the role of microphysical transport processes in shaping observable structures. Ultimately, this line of investigation will not only advance our theoretical understanding of the ICM but also help develop more accurate subgrid models for galaxy formation and evolution.

Bibliography

Agertz, O., Moore, B., Stadel, J., et al. (2007), *Fundamental differences between SPH and grid methods*, Monthly Notices of the Royal Astronomical Society, 380(3), 963–978

Allen, S. W., Evrard, A. E., and Mantz, A. B. (2011), *Cosmological Parameters from Observations of Galaxy Clusters*, Annual Review of Astronomy and Astrophysics, 49(1), 409–470

Anderson, M. E. and Bregman, J. N. (2010), *DO HOT HALOS AROUND GALAXIES CONTAIN THE MISSING BARYONS?*, The Astrophysical Journal, 714(1), 320

Armillotta, L., Fraternali, F., and Marinacci, F. (2016), *Efficiency of gas cooling and accretion at the disc-corona interface*, Monthly Notices of the RAS, 462(4), 4157

Arrigoni Battaia, F., Obreja, A., Costa, T., et al. (2023), *The Luminosity-Area Relation of $z > 2$ Quasars' Lyα Nebulae*, Astrophysical Journal, Letters, 952(1), L24

Arth, A., Dolag, K., Beck, A. M., et al. (2017), *Anisotropic thermal conduction in galaxy clusters with MHD in Gadget*

Arzamasskiy, L., Kunz, M. W., Squire, J., et al. (2023), *Kinetic Turbulence in Collisionless High-β Plasmas*, Phys. Rev. X, 13, 021014

Arévalo, P., Churazov, E., Zhuravleva, I., et al. (2012), *A Mexican hat with holes: calculating low-resolution power spectra from data with gaps: Power spectrum of data with gaps*, Monthly Notices of the Royal Astronomical Society, 426(3), 1793–1807

Audard, M., Awaki, H., Ballhausen, R., et al. (2025), *The bulk motion of gas in the core of the Centaurus galaxy cluster*, Nature, 638(8050), 365–369

Balsara, D. S. (1995), *von Neumann stability analysis of smoothed particle hydrodynamics—suggestions for optimal algorithms*, Journal of Computational Physics, 121(2), 357

Barnes, J. and Hut, P. (1986), *A Hierarchical O(N Log N) Force-Calculation Algorithm*, Nature, 324, 446

Barret, D., den Herder, J. W., Piro, L., et al. (2013), *The Hot and Energetic Universe: The X-ray Integral Field Unit (X-IFU) for Athena+*, arXiv e-prints, arXiv:1308.6784

Beck, A. M., Murante, G., Arth, A., et al. (2016), *An improved SPH scheme for cosmological simulations*, Monthly Notices of the RAS, 455(2), 2110

Begelman, M. C. and Fabian, A. C. (1990), *Turbulent mixing layers in the interstellar and intracluster medium.*, Monthly Notices of the RAS, 244, 26P

Begelman, M. C. and McKee, C. F. (1990), *Global Effects of Thermal Conduction on Two-Phase Media*, Astrophysical Journal, 358, 375

Beresnyak, A. (2015), *ON THE PARALLEL SPECTRUM IN MAGNETOHYDRODYNAMIC TURBULENCE*, The Astrophysical Journal, 801(1), L9

Beresnyak, A. (2019), *MHD turbulence*, Living Reviews in Computational Astrophysics, 5(1)

Berger, M. and Colella, P. (1989), *Local adaptive mesh refinement for shock hydrodynamics*, Journal of Computational Physics, 82(1), 64

Berlok, T., Pakmor, R., and Pfrommer, C. (2019), *Braginskii viscosity on an unstructured, moving mesh accelerated with super-time-stepping*, Monthly Notices of the Royal Astronomical Society, 491(2), 2919–2938

Biffi, V., Dolag, K., and Böhringer, H. (2012), *Investigating the velocity structure and X-ray observable properties of simulated galaxy clusters with PHOX*, Monthly Notices of the Royal Astronomical Society, 428(2), 1395–1409

Binney, J. and Tremaine, S. (2008), *Galactic Dynamics: Second Edition*

Birkinshaw, M. (1999), *The Sunyaev–Zel'dovich effect*, Physics Reports, 310(2–3), 97–195

Bîrzan, L., Rafferty, D. A., Brüggen, M., et al. (2020), *LOFAR observations of X-ray cavity systems*, Monthly Notices of the RAS, 496(3), 2613

Bode, P., Ostriker, J. P., and Xu, G. (2000), *The Tree Particle-Mesh N-Body Gravity Solver*, The Astrophysical Journal Supplement Series, 128(2), 561–569

Böhringer, H. and Werner, N. (2010), *X-ray spectroscopy of galaxy clusters: studying astrophysical processes in the largest celestial laboratories*, Astronomy and Astrophysics Reviews, 18(1-2), 127

Bonafede, A., Dolag, K., Stasyszyn, F., et al. (2011), *A non-ideal magnetohydrodynamic gadget: simulating massive galaxy clusters: A non-ideal magnetohydrodynamic gadget*, Monthly Notices of the Royal Astronomical Society, 418(4), 2234–2250

Bonafede, A., Vazza, F., Brüggen, M., et al. (2013), *Measurements and simulation of Faraday rotation across the Coma radio relic*, Monthly Notices of the Royal Astronomical Society, 433(4), 3208

Bond, J. R. and Myers, S. T. (1996), *The Peak-Patch Picture of Cosmic Catalogs. I. Algorithms*, Astrophysical Journal, Supplement, 103, 1

Boselli, A., Fossati, M., and Sun, M. (2022), *Ram pressure stripping in high-density environments*, The Astronomy and Astrophysics Review, 30(1)

Bourne, M. A. and Sijacki, D. (2017), *AGN jet feedback on a moving mesh: cocoon inflation, gas flows and turbulence*, Monthly Notices of the RAS, 472(4), 4707

Braginskii, S. I. (1965), *Transport Processes in a Plasma*, Reviews of Plasma Physics, 1, 205

Brandenburg, A. and Lazarian, A. (2013), *Astrophysical Hydromagnetic Turbulence*, Space Science Reviews, 178(2-4), 163

Brandenburg, A. and Subramanian, K. (2005), *Astrophysical magnetic fields and nonlinear dynamo theory*, Physics Reports, 417(1–4), 1–209

Bregman, J. N., Anderson, M. E., Miller, M. J., et al. (2018), *The Extended Distribution of Baryons around Galaxies*, The Astrophysical Journal, 862(1), 3

Breuer, J. P., Werner, N., Mernier, F., et al. (2020), *The mergers in Abell 2256: displaced gas and its connection to the radio-emitting plasma*, Monthly Notices of the Royal Astronomical Society, 495(4), 5014–5026

Brunetti, G. and Jones, T. W. (2014), *Cosmic Rays in Galaxy Clusters and Their Nonthermal Emission*, International Journal of Modern Physics D, 23(4), 1430007

Brunetti, G. and Lazarian, A. (2007), *Compressible turbulence in galaxy clusters: physics and stochastic particle re-acceleration*, Monthly Notices of the Royal Astronomical Society, 378(1), 245

Bryan, G. L., Norman, M. L., O'Shea, B. W., et al. (2014), *ENZO: An Adaptive Mesh Refinement Code for Astrophysics*, Astrophysical Journal, Supplement, 211(2), 19

Brüggen, M. and Ruszkowski, M. (2005), *Viscosity in cosmological simulations of clusters of galaxies*

Brüggen, M. and Scannapieco, E. (2016), *THE LAUNCHING OF COLD CLOUDS BY GALAXY OUTFLOWS. II. THE ROLE OF THERMAL CONDUCTION*, The Astrophysical Journal, 822(1), 31

Brüggen, M., Scannapieco, E., and Grete, P. (2023), *The Launching of Cold Clouds by Galaxy Outflows. V. The Role of Anisotropic Thermal Conduction*, The Astrophysical Journal, 951(2), 113

Butsky, I. S., Hummels, C. B., Hopkins, P. F., et al. (2024), *Cold Gas Subgrid Model (CGSM): a two-fluid framework for modelling unresolved cold gas in galaxy simulations*, Monthly Notices of the Royal Astronomical Society, 535(2), 1672

Bykov, A. M., Vazza, F., Kropotina, J. A., et al. (2019), *Shocks and Non-thermal Particles in Clusters of Galaxies*, Space Science Reviews, 215(1)

Böss, L. M., Dolag, K., Steinwandel, U. P., et al. (2024), *Simulating the LOcal Web (SLOW): III. Synchrotron emission from the local cosmic web*, Astronomy & Astrophysics, 692, A232

Caprioli, D., Brunetti, G., Jones, T. W., et al. (2019), *Plasma 2020 - Intracluster Medium Plasmas*

Carilli, C. L. and Taylor, G. B. (2002), *Cluster Magnetic Fields*, Annual Review of Astronomy and Astrophysics, 40(1), 319–348

Carlstrom, J. E., Holder, G. P., and Reese, E. D. (2002), *Cosmology with the Sunyaev-Zel'dovich Effect*, Annual Review of Astron and Astrophys, 40, 643

Cavaliere, A. G., Gursky, H., and Tucker, W. H. (1971), *Extragalactic X-ray Sources and Associations of Galaxies*, Nature, 231(5303), 437

Chandrasekhar, S. (1961), *Hydrodynamic and hydromagnetic stability*, Clarendon Press

Chevalier, R. A. and Clegg, A. W. (1985), *Wind from a starburst galaxy nucleus*, Nature, 317(6032), 44

Chew, G. F., Goldberger, M. L., and Low, F. E. (1956), *The Boltzmann Equation and the One-Fluid Hydromagnetic Equations in the Absence of Particle Collisions*, Proceedings of the Royal Society of London Series A, 236(1204), 112

Cho, J. and Lazarian, A. (2003), *Compressible magnetohydrodynamic turbulence: mode coupling, scaling relations, anisotropy, viscosity-damped regime and astrophysical implications*, Monthly Notices of the RAS, 345(12), 325

Churazov, E., Vikhlinin, A., Zhuravleva, I., et al. (2012), *X-ray surface brightness and gas density fluctuations in the Coma cluster: X-ray surface brightness fluctuations in the Coma cluster*, Monthly Notices of the Royal Astronomical Society, 421(2), 1123–1135

Cimatti, A., Fraternali, F., and Nipoti, C. (2019), *Introduction to Galaxy Formation and Evolution: From Primordial Gas to Present-Day Galaxies*, Cambridge University Press

Clarke, T. E., Kronberg, P. P., and Böhringer, H. (2001), *A New Radio-X-Ray Probe of Galaxy Cluster Magnetic Fields*, Astrophysical Journal, Letters, 547(2), L111

Clowe, D., Bradač, M., Gonzalez, A. H., et al. (2006), *A Direct Empirical Proof of the Existence of Dark Matter*, Astrophysical Journal, Letters, 648(2), L109

Cowie, L. L. and McKee, C. F. (1977), *The evaporation of spherical clouds in a hot gas. I. Classical and saturated mass loss rates.*, Astrophysical Journal, 211, 135

Cox, D. P. (2005), *The Three-Phase Interstellar Medium Revisited*, Annual Review of Astron and Astrophys, 43(1), 337

Cox, D. P. and Tucker, W. H. (1969), *Ionization Equilibrium and Radiative Cooling of a Low-Density Plasma*, Astrophysical Journal, 157, 1157

Cui, W., Power, C., Borgani, S., et al. (2016), *On the dynamical state of galaxy clusters: insights from cosmological simulations – II.*, Monthly Notices of the Royal Astronomical Society, 464(2), 2502

Cullen, L. and Dehnen, W. (2010), *Inviscid smoothed particle hydrodynamics*, Monthly Notices of the Royal Astronomical Society, 408(2), 669–683

Damköhler, G. (1940), *Der einfluss der turbulenz auf die flammengeschwindigkeit in gasgemischen*, Zeitschrift für Elektrochemie und angewandte physikalische Chemie, 46(11), 601

Das, H. K. and Gronke, M. (2023), *Magnetic fields in multiphase turbulence: impact on dynamics and structure*, Monthly Notices of the Royal Astronomical Society, 527(1), 991

Das, H. K., Gronke, M., and Weinberger, R. (2024), *MOGLI: Model for Multiphase Gas using Multifluid hydrodynamics*

Dedner, A., Kemm, F., Kröner, D., et al. (2002), *Hyperbolic Divergence Cleaning for the MHD Equations*, Journal of Computational Physics, 175(2), 645

Dehnen, W. and Aly, H. (2012), *Improving convergence in smoothed particle hydrodynamics simulations without pairing instability*, Monthly Notices of the Royal Astronomical Society, 425(2), 1068–1082

Dekel, A., Birnboim, Y., Engel, G., et al. (2009), *Cold streams in early massive hot haloes as the main mode of galaxy formation*, Nature, 457(7228), 451–454

Dimopoulos, K. and Davis, A.-C. (1997), *Evolution of primordial magnetic fields*, Physics Letters B, 390(1), 87

Dodelson, S. (2003), *Modern Cosmology*

Dolag, K. and Stasyszyn, F. (2009), *An MHD gadget for cosmological simulations*, Monthly Notices of the Royal Astronomical Society, 398(4), 1678–1697

Donnert, J., Vazza, F., Brüggen, M., and ZuHone, J. (2018), *Magnetic Field Amplification in Galaxy Clusters and Its Simulation*, Space Science Reviews, 214

Dopita, M. A. and Sutherland, R. S. (2003), *Astrophysics of the diffuse universe*

Draine, B. T. (2011), *Physics of the Interstellar and Intergalactic Medium*

Drazin, P. G. and Riley, N. (2006), *The Navier-Stokes Equations: A Classification of Flows and Exact Solutions*, London Mathematical Society Lecture Note Series, Cambridge University Press

Dupourqué, S., Clerc, N., Pointecouteau, E., et al. (2024), *CHEX-MATE: Turbulence in the intra-cluster medium from X-ray surface brightness fluctuations*, Astronomy & Astrophysics, 687, A58

Efstathiou, G., Bond, J. R., and White, S. D. M. (1992), *COBE background radiation anisotropies and large-scale structure in the Universe*, Monthly Notices of the Royal Astronomical Society, 258(1), 1P

Einstein, A. (1916), *Die Grundlage Der Allgemeinen Relativitätstheorie*, Annalen der Physik, 354, 769

Einstein, A. and de Sitter, W. (1932), *On the Relation between the Expansion and the Mean Density of the Universe*, Proceedings of the National Academy of Science, 18(3), 213

El-Badry, K., Ostriker, E. C., Kim, C.-G., et al. (2019), *Evolution of supernovae-driven superbubbles with conduction and cooling*, Monthly Notices of the Royal Astronomical Society, 490(2), 1961

Elmegreen, B. G. and Scalo, J. (2004), *Interstellar Turbulence I: Observations and Processes*, Annual Review of Astronomy and Astrophysics, 42(1), 211–273

Esch, R. E. (1957), *The instability of a shear layer between two parallel streams*, Journal of Fluid Mechanics, 3(3), 289–303

Evans, C. R. and Hawley, J. F. (1988), *Simulation of Magnetohydrodynamic Flows: A Constrained Transport Model*, Astrophysical Journal, 332, 659

Fabian, A. C. (1994), *Cooling Flows in Clusters of Galaxies*, Annual Review of Astron and Astrophys, 32, 277

Fabian, A. C. (2012), *Observational Evidence of Active Galactic Nuclei Feedback*, Annual Review of Astron and Astrophys, 50, 455

Fabian, A. C., Reynolds, C. S., Taylor, G. B., and Dunn, R. J. H. (2005), *On viscosity, conduction and sound waves in the intracluster medium*, Monthly Notices of the Royal Astronomical Society, 363(3), 891

Fabian, A. C., Sanders, J. S., Allen, S. W., et al. (2003), *A deep Chandra observation of the Perseus cluster: shocks and ripples*, Monthly Notices of the RAS, 344(3), L43

Faltenbacher, A., Kravtsov, A. V., Nagai, D., and Gottlöber, S. (2005), *Supersonic motions of galaxies in clusters*, Monthly Notices of the Royal Astronomical Society, 358(1), 139

Faucher-Giguère, C.-A. and Oh, S. P. (2023), *Key Physical Processes in the Circumgalactic Medium*, Annual Review of Astronomy and Astrophysics, 61(Volume 61, 2023), 131

Federrath, C. (2016), *The role of turbulence, magnetic fields and feedback for star formation*, Journal of Physics: Conference Series, 719, 012002

Feretti, L., Giovannini, G., Govoni, F., and Murgia, M. (2012), *Clusters of galaxies: observational properties of the diffuse radio emission*, Astronomy and Astrophysics Reviews, 20, 54

Field, G. B. (1965), *Thermal Instability.*, Astrophysical Journal, 142, 531

Fielding, D. B. and Bryan, G. L. (2022), *The Structure of Multiphase Galactic Winds*, The Astrophysical Journal, 924(2), 82

Fielding, D. B., Ostriker, E. C., Bryan, G. L., and Jermyn, A. S. (2020), *Multiphase Gas and the Fractal Nature of Radiative Turbulent Mixing Layers*, The Astrophysical Journal Letters, 894(2), L24

Forman, W., Jones, C., Churazov, E., et al. (2007), *Filaments, Bubbles, and Weak Shocks in the Gaseous Atmosphere of M87*, Astrophysical Journal, 665(2), 1057

Forman, W., Kellogg, E., Gursky, H., et al. (1972), *Observations of the Extended X-Ray Sources in the Perseus and Coma Clusters from UHURU*, Astrophysical Journal, 178, 309

Friedmann, A. (1922), *Über Die Krümmung Des Raumes*, Zeitschrift fur Physik, 10, 377

Friedmann, A. (1924), *Über Die Möglichkeit Einer Welt Mit Konstanter Negativer Krümmung Des Raumes*, Zeitschrift fur Physik, 21, 326

Fujita, Y., Takizawa, M., and Sarazin, C. L. (2003), *Nonthermal Emissions from Particles Accelerated by Turbulence in Clusters of Galaxies*, The Astrophysical Journal, 584(1), 190–202

Gardiner, T. A. and Stone, J. M. (2008), *An unsplit Godunov method for ideal MHD via constrained transport in three dimensions*, Journal of Computational Physics, 227(8), 4123

Gaspari, M. (2015), *Shaping the X-ray spectrum of galaxy clusters with AGN feedback and turbulence*, Monthly Notices of the Royal Astronomical Society: Letters, 451(1), L60–L64

Gaspari, M., Churazov, E., Nagai, D., et al. (2014), *The relation between gas density and velocity power spectra in galaxy clusters: High-resolution hydrodynamic simulations and the role of conduction*, A&A, 569, A67

Gaspari, M., Melioli, C., Brighenti, F., and D'Ercole, A. (2011), *The dance of heating and cooling in galaxy clusters: three-dimensional simulations of self-regulated active galactic nuclei outflows*, Monthly Notices of the RAS, 411(1), 349

Ge, C., Liu, R.-Y., Sun, M., et al. (2020), *Chandra and XMM–Newton observations of A2256: cold fronts, merger shocks, and constraint on the IC emission*, Monthly Notices of the Royal Astronomical Society, 497(4), 4704–4717

Gendron-Marsolais, M., Hlavacek-Larrondo, J., van Weeren, R. J., et al. (2020), *High-resolution VLA low radio frequency observations of the Perseus cluster: radio lobes, mini-halo, and bent-jet radio galaxies*, Monthly Notices of the RAS, 499(4), 5791

Ghosh, R., Dutta, A., and Sharma, P. (2024), *Ram pressure stripping in clusters: gravity can bind the ISM but not the CGM*, Monthly Notices of the Royal Astronomical Society, 531(3), 3445

Gingold, R. A. and Monaghan, J. J. (1977), *Smoothed particle hydrodynamics: theory and application to non-spherical stars*, Monthly Notices of the Royal Astronomical Society, 181(3), 375

Gisler, G. R. (1976), *The fate of gas in elliptical galaxies and the density evolution of of radio sources.*, Astronomy and Astrophysics, 51(1), 137

Goldreich, P. and Sridhar, S. (1995), *Toward a Theory of Interstellar Turbulence. II. Strong Alfvenic Turbulence*, Astrophysical Journal, 438, 763

Govoni, F. and Feretti, L. (2004), *MAGNETIC FIELDS IN CLUSTERS OF GALAXIES*, International Journal of Modern Physics D, 13(08), 1549–1594

Grasso, D. and Rubinstein, H. R. (2001), *Magnetic fields in the early Universe*, Physics Reports, 348(3), 163–266

Gronke, M. and Oh, S. P. (2018), *The growth and entrainment of cold gas in a hot wind*, Monthly Notices of the Royal Astronomical Society: Letters, 480(1), L111

Gronke, M. and Oh, S. P. (2019), *How cold gas continuously entrains mass and momentum from a hot wind*, Monthly Notices of the Royal Astronomical Society, 492(2), 1970–1990

Gronke, M., Oh, S. P., Ji, S., and Norman, C. (2021), *Survival and mass growth of cold gas in a turbulent, multiphase medium*, Monthly Notices of the Royal Astronomical Society, 511(1), 859

Groth, F., Steinwandel, U. P., Valentini, M., and Dolag, K. (2023), *The cosmological simulation code OpenGadget3 – implementation of meshless finite mass*, Monthly Notices of the Royal Astronomical Society, 526(1), 616

Groth, F., Valentini, M., Steinwandel, U. P., et al. (2025), *Turbulent pressure support in galaxy clusters: Impact of the hydrodynamical solver*, Astronomy &; Astrophysics, 693, A263

Gunn, J. E. and Gott, III, J. R. (1972), *On the Infall of Matter Into Clusters of Galaxies and Some Effects on Their Evolution*, Astrophysical Journal, 176, 1

Gursky, H., Kellogg, E., Murray, S., et al. (1971), *A Strong X-Ray Source in the Coma Cluster Observed by UHURU*, Astrophysical Journal, Letters, 167, L81

Harrison, E. R. (1970), *Fluctuations at the Threshold of Classical Cosmology*, Phys. Rev. D, 1, 2726

Heinrich, A., Zhuravleva, I., Zhang, C., et al. (2024), *Merger-driven multiscale ICM density perturbations: testing cosmological simulations and constraining plasma physics*, Monthly Notices of the Royal Astronomical Society, 528(4), 7274

Hitomi, Aharonian, F., Akamatsu, H., et al. (2016), *The quiescent intracluster medium in the core of the Perseus cluster*, Nature, 535(7610), 117

Hitomi, Aharonian, F., Akamatsu, H., et al. (2018), *Atmospheric gas dynamics in the Perseus cluster observed with Hitomi*, Publications of the ASJ, 70(2), 9

Hockney, R. W. and Eastwood, J. W. (1981), *Computer Simulation Using Particles*

Hoffman, Y. and Shaham, J. (1985), *Local density maxima: progenitors of structure.*, Astrophysical Journal, 297, 16

Hopkins, P. F. (2013), *A general class of Lagrangian smoothed particle hydrodynamics methods and implications for fluid mixing problems*, Monthly Notices of the RAS, 428(4), 2840

Hopkins, P. F. (2015), *A new class of accurate, mesh-free hydrodynamic simulation methods*, Monthly Notices of the Royal Astronomical Society, 450(1), 53–110

Hu, C.-Y., Naab, T., Walch, S., et al. (2014), *SPHGal: smoothed particle hydrodynamics with improved accuracy for galaxy simulations*, Monthly Notices of the Royal Astronomical Society, 443(2), 1173–1191

Huang, S., Katz, N., Scannapieco, E., et al. (2020), *A new model for including galactic winds in simulations of galaxy formation – I. Introducing the Physically Evolved Winds (PhEW) model*, Monthly Notices of the Royal Astronomical Society, 497(3), 2586

Hubble, E. (1929), *A Relation between Distance and Radial Velocity among Extra-Galactic Nebulae*, Proceedings of the National Academy of Science, 15(3), 168

Hubble, E. P. (1925), *Cepheids in spiral nebulae*, The Observatory, 48, 139

Hubble, E. P. (1926), *Extragalactic nebulae.*, Astrophysical Journal, 64, 321

Iapichino, L., Adamek, J., Schmidt, W., and Niemeyer, J. C. (2008), *Hydrodynamical adaptive mesh refinement simulations of turbulent flows – I. Substructure in a wind*, Monthly Notices of the Royal Astronomical Society, 388(3), 1079

Iapichino, L., Federrath, C., and Klessen, R. S. (2017), *Adaptive mesh refinement simulations of a galaxy cluster merger – I. Resolving and modelling the turbulent flow in the cluster outskirts*, Monthly Notices of the Royal Astronomical Society, 469(3), 3641–3655

Ignesti, A., Brunetti, G., Gullieuszik, M., et al. (2024), *Investigating the Intracluster Medium Viscosity Using the Tails of GASP Jellyfish Galaxies*, The Astrophysical Journal, 977(2), 219

Jansen, F., Lumb, D., Altieri, B., et al. (2001), *XMM-Newton observatory. I. The spacecraft and operations*, Astronomy and Astrophysics, 365, L1

Jeans, J. H. (1902), *The Stability of a Spherical Nebula*, Philosophical Transactions of the Royal Society of London Series A, 199, 1

Jennings, R. M. and Li, Y. (2021), *Thermal instability and multiphase gas in the simulated interstellar medium with conduction, viscosity, and magnetic fields*, Monthly Notices of the Royal Astronomical Society, 505(4), 5238–5252

Ji, S., Oh, S. P., and Masterson, P. (2019), *Simulations of radiative turbulent mixing layers*, Monthly Notices of the Royal Astronomical Society, 487(1), 737

Junk, V., Walch, S., Heitsch, F., et al. (2010), *Modelling shear flows with smoothed particle hydrodynamics and grid-based methods*, Monthly Notices of the Royal Astronomical Society, 407(3), 1933–1945

Kazantsev, A. P. (1968), *Enhancement of a Magnetic Field by a Conducting Fluid*, Soviet Journal of Experimental and Theoretical Physics, 26, 1031

Klein, R. I., McKee, C. F., and Colella, P. (1994), *On the Hydrodynamic Interaction of Shock Waves with Interstellar Clouds. I. Nonradiative Shocks in Small Clouds*, Astrophysical Journal, 420, 213

Klimov, A. M. (1963), *Laminar Flame in a Turbulent Flow*, Zhurnal Prikladnoy Mekhaniki i Tekhnicheskoy Fiziki, 3, 49

Kneib, J.-P. and Natarajan, P. (2011), *Cluster lenses*, The Astronomy and Astrophysics Review, 19(1)

Kolmogorov, A. (1941), *Local structure of turbulence in incompressible fluid under very high values of Reynolds numbers*, Rep. AS USSR, 30(4), 299

Kolmogorov, A. N. (1962), *A refinement of previous hypotheses concerning the local structure of turbulence in a viscous incompressible fluid at high Reynolds number*, Journal of Fluid Mechanics, 13(1), 82–85

Komatsu, E., Smith, K. M., Dunkley, J., et al. (2011), *Seven-year Wilkinson Microwave Anisotropy Probe (WMAP) Observations: Cosmological Interpretation*, Astrophysical Journal, Supplement, 192(2), 18

Kowal, G., Lazarian, A., Vishniac, E. T., and Otmianowska-Mazur, K. (2009), *Numerical Tests of Fast Reconnection in Weakly Stochastic Magnetic Fields*, Astrophysical Journal, 700(1), 63

Kraft, R. P., Roediger, E., Machacek, M., et al. (2017), *Stripped Elliptical Galaxies as Probes of ICM Physics. III. Deep Chandra Observations of NGC 4552: Measuring the Viscosity of the Intracluster Medium*, The Astrophysical Journal, 848(1), 27

Kravtsov, A. V. and Borgani, S. (2012), *Formation of Galaxy Clusters*, Annual Review of Astronomy and Astrophysics, 50(Volume 50, 2012), 353

Kulsrud, R. M. (2004), *Plasma Physics for Astrophysics*

Kulsrud, R. M. and Anderson, S. W. (1992), *The Spectrum of Random Magnetic Fields in the Mean Field Dynamo Theory of the Galactic Magnetic Field*, Astrophysical Journal, 396, 606

Kunz, M., Schekochihin, A., and Stone, J. (2014), *Firehose and Mirror Instabilities in a Collisionless Shearing Plasma*, Physical Review Letters, 112

Kunz, M. W. (2011), *Dynamical stability of a thermally stratified intracluster medium with anisotropic momentum and heat transport*, Monthly Notices of the Royal Astronomical Society, 417(1), 602

Kunz, M. W., Bogdanović, T., Reynolds, C. S., and Stone, J. M. (2012), *BUOYANCY INSTABILITIES IN A WEAKLY COLLISIONAL INTRACLUSTER MEDIUM*, The Astrophysical Journal, 754(2), 122

Kunz, M. W., Jones, T. W., and Zhuravleva, I. (2022), *Plasma Physics of the Intracluster Medium*, 1–42, Springer Nature Singapore

Kuo, K. K.-y. and Acharya, R. (2012), *Turbulent Premixed Flames*, chapter 5, 283–401, John Wiley & Sons, Ltd

Kwak, K. and Shelton, R. L. (2010), *NUMERICAL STUDY OF TURBULENT MIXING LAYERS WITH NON-EQUILIBRIUM IONIZATION CALCULATIONS*, The Astrophysical Journal, 719(1), 523

Lancaster, L., Ostriker, E. C., Kim, J.-G., and Kim, C.-G. (2021a), *Efficiently Cooled Stellar Wind Bubbles in Turbulent Clouds. I. Fractal Theory and Application to Star-forming Clouds*, Astrophysical Journal, 914(2), 89

Lancaster, L., Ostriker, E. C., Kim, J.-G., and Kim, C.-G. (2021b), *Efficiently Cooled Stellar Wind Bubbles in Turbulent Clouds. II. Validation of Theory with Hydrodynamic Simulations*, Astrophysical Journal, 914(2), 90

Landau, L. (1944), *The instability of moving superposed fluids*, Akad. Nauk. SSSR, Comptes Rendus (Doklady), 44, 139

Landau, L. D. and Lifshitz, E. M. (1987), *Fluid Mechanics*, volume 6 of *Course of Theoretical Physics*, Pergamon

Lau, E. T., Gaspari, M., Nagai, D., and Coppi, P. (2017), *Physical Origins of Gas Motions in Galaxy Cluster Cores: Interpreting Hitomi Observations of the Perseus Cluster*, The Astrophysical Journal, 849(1), 54

Lazio, J. (2009), *The Square Kilometre Array*

Lecoanet, D., McCourt, M., Quataert, E., et al. (2015), *A validated non-linear Kelvin–Helmholtz benchmark for numerical hydrodynamics*, Monthly Notices of the Royal Astronomical Society, 455(4), 4274–4288

Lemaître, G. (1931), *A Homogeneous Universe of Constant Mass and Increasing Radius Accounting for the Radial Velocity of Extra-Galactic Nebulae*, Monthly Notices of the Royal Astronomical Society, 91, 483

Lemaître, G. (1933), *L'Univers En Expansion*, Annales de la Société Scientifique de Bruxelles, 53, 51

Li, Y., Luo, R., Fossati, M., et al. (2023), *Turbulence in the tail of a jellyfish galaxy*, Monthly Notices of the Royal Astronomical Society, 521(3), 4785–4791

Liang, H., Hunstead, R. W., Birkinshaw, M., and Andreani, P. (2000), *A Powerful Radio Halo in the Hottest Known Cluster of Galaxies 1E 0657-56*, Astrophysical Journal, 544(2), 686

Libby, P. A. and Williams, F. A. (1982), *Structure of laminar flamelets in premixed turbulent flames*, Combustion and Flame, 44(1), 287

Lin, X., Wang, J., Staveley-Smith, L., et al. (2025), *FEASTS Combined with Interferometry. III. The Low Column Density H i Around M51 and Possibility of Turbulent-mixing Gas Accretion*, The Astrophysical Journal, 982(2), 151

Lovisari, L., Ettori, S., Rasia, E., et al. (2024), *CHEX-MATE: Characterization of the intra-cluster medium temperature distribution*, A&A, 682, A45

Lucy, L. B. (1977), *A numerical approach to the testing of the fission hypothesis.*, Astronomical Journal, 82, 1013

Mandelker, N., Nagai, D., Aung, H., et al. (2020), *Instability of supersonic cold streams feeding galaxies – IV. Survival of radiatively cooling streams*, Monthly Notices of the Royal Astronomical Society, 494(2), 2641–2663

Mandelker, N., Nagai, D., Aung, H., et al. (2019), *Instability of supersonic cold streams feeding Galaxies – III. Kelvin–Helmholtz instability in three dimensions*, Monthly Notices of the Royal Astronomical Society, 484(1), 1100

Mandelker, N., Padnos, D., Dekel, A., et al. (2016), *Instability of supersonic cold streams feeding galaxies – I. Linear Kelvin–Helmholtz instability with body modes*, Monthly Notices of the Royal Astronomical Society, 463(4), 3921

Mantz, A., Allen, S. W., Rapetti, D., and Ebeling, H. (2010), *The observed growth of massive galaxy clusters – I. Statistical methods and cosmological constraints*, Monthly Notices of the Royal Astronomical Society, 406(3), 1759

Marin-Gilabert, T., Gronke, M., and Oh, S. P. (2025), *The (Limited) Effect of Viscosity in Multiphase Turbulent Mixing*

Marin-Gilabert, T., Steinwandel, U. P., Valentini, M., et al. (2024), *Density Fluctuations in the Intracluster Medium: An Attempt to Constrain Viscosity with Cosmological Simulations*, The Astrophysical Journal, 976(1), 67

Marin-Gilabert, T., Valentini, M., Steinwandel, U. P., and Dolag, K. (2022), *The role of physical and numerical viscosity in hydrodynamical instabilities*, Monthly Notices of the Royal Astronomical Society, 517(4), 5971–5991

Markevitch, M. and Vikhlinin, A. (2007), *Shocks and cold fronts in galaxy clusters*, Physics Reports, 443(1), 1

McKee, C. F. and Ostriker, J. P. (1977), *A theory of the interstellar medium: three components regulated by supernova explosions in an inhomogeneous substrate.*, Astrophysical Journal, 218, 148

McNally, C. P., Lyra, W., and Passy, J.-C. (2012), *A WELL-POSED KELVIN-HELMHOLTZ INSTABILITY TEST AND COMPARISON*, The Astrophysical Journal Supplement Series, 201(2), 18

McNamara, B. and Nulsen, P. (2007), *Heating Hot Atmospheres with Active Galactic Nuclei*, Annual Review of Astronomy and Astrophysics, 45(1), 117–175

McNamara, B. R. and Nulsen, P. E. J. (2012), *Mechanical feedback from active galactic nuclei in galaxies, groups and clusters*, New Journal of Physics, 14(5), 055023

Mo, H., van den Bosch, F. C., and White, S. (2010), *Galaxy Formation and Evolution*

Mohapatra, R., Federrath, C., and Sharma, P. (2020), *Turbulence in stratified atmospheres: implications for the intracluster medium*, Monthly Notices of the Royal Astronomical Society, 493(4), 5838–5853

Monaghan, J. (1997), *SPH and Riemann Solvers*, Journal of Computational Physics, 136(2), 298

Monaghan, J. and Gingold, R. (1983), *Shock simulation by the particle method SPH*, Journal of Computational Physics, 52(2), 374

Monaghan, J. J. (1992), *Smoothed particle hydrodynamics.*, Annual Review of Astronomy and Astrophysics, 30, 543

Moore, D. W. (1979), *The Spontaneous Appearance of a Singularity in the Shape of an Evolving Vortex Sheet*, Proceedings of the Royal Society of London. Series A, Mathematical and Physical Sciences, 365(1720), 105

Mukhanov, V. (2005), *Physical foundations of cosmology*, Cambridge university press

Mukhanov, V., Feldman, H., and Brandenberger, R. (1992), *Theory of cosmological perturbations*, Physics Reports, 215(5), 203

Murante, G., Borgani, S., Brunino, R., and Cha, S. H. (2011), *Hydrodynamic simulations with the Godunov smoothed particle hydrodynamics*, Monthly Notices of the RAS, 417(1), 136

Müller, A., Ignesti, A., Poggianti, B., et al. (2021), *Role of Magnetic Fields in Ram Pressure Stripped Galaxies*, Galaxies, 9(4), 116

Navarro, J. F., Frenk, C. S., and White, S. D. M. (1996), *The Structure of Cold Dark Matter Halos*, Astrophysical Journal, 462, 563

Navarro, J. F., Frenk, C. S., and White, S. D. M. (1997), *A Universal Density Profile from Hierarchical Clustering*, Astrophysical Journal, 490(2), 493

Nelson, K., Lau, E. T., and Nagai, D. (2014), *HYDRODYNAMIC SIMULATION OF NON-THERMAL PRESSURE PROFILES OF GALAXY CLUSTERS*, The Astrophysical Journal, 792(1), 25

Neronov, A. and Semikoz, D. V. (2009), *Sensitivity of gamma-ray telescopes for detection of magnetic fields in the intergalactic medium*, Physical Review D, 80(12)

Neronov, A. and Vovk, I. (2010), *Evidence for Strong Extragalactic Magnetic Fields from Fermi Observations of TeV Blazars*, Science, 328(5974), 73–75

Nulsen, P. E. J. (1982), *Transport processes and the stripping of cluster galaxies.*, Monthly Notices of the RAS, 198, 1007

Obergaulinger, M. and Aloy, M. (2020), *Numerical viscosity in simulations of the two-dimensional Kelvin-Helmholtz instability*, Journal of Physics: Conference Series, 1623, 012018

O'Neill, S. M., Young, D. S. D., and Jones, T. W. (2009), *THREE-DIMENSIONAL MAGNETOHYDRODYNAMIC SIMULATIONS OF BUOYANT BUBBLES IN GALAXY CLUSTERS*, The Astrophysical Journal, 694(2), 1317

Oppenheimer, B. D., Davé, R., Kereš, D., et al. (2010), *Feedback and recycled wind accretion: assembling the $z = 0$ galaxy mass function*, Monthly Notices of the RAS, 406(4), 2325

Ostriker, J. P. and Steinhardt, P. J. (1995), *The observational case for a low-density Universe with a non-zero cosmological constant*, Nature, 377(6550), 600

Overzier, R. (2016), *The realm of the galaxy protoclusters: A review*, The Astronomy and Astrophysics Review, 24

Ozmidov, R. (1992), *ON LENGTH SCALES AND DIMENSIONLESS NUMBERS IN THE STRATIFIED OCEAN*, OKEANOLOGIYA, 32(3), 389

Peacock, J. A. (1999), *Cosmological Physics*

Peebles, P. J. E. (1993), *Principles of Physical Cosmology*

Peeples, M. S., Werk, J. K., Tumlinson, J., et al. (2014), *A BUDGET AND ACCOUNTING OF METALS AT $z \sim 0$: RESULTS FROM THE COS-HALOS SURVEY*, The Astrophysical Journal, 786(1), 54

Penzias, A. A. and Wilson, R. W. (1965), *A Measurement of Excess Antenna Temperature at 4080 Mc/s.*, Astrophysical Journal, 142, 419

Phillips, G. J. and Monaghan, J. J. (1985), *A numerical method for three-dimensional simulations of collapsing, isothermal, magnetic gas clouds*, Monthly Notices of the Royal Astronomical Society, 216(4), 883

Pitaevskii, L. P. and Lifshitz, E. M. (1981), *Physical Kinetics: Volume 10 (Course of Theoretical Physics)*

Pittard, J. M., Dyson, J. E., Falle, S. A. E. G., and Hartquist, T. W. (2005), *Dynamical and pressure structures in winds with multiple embedded evaporating clumps - I. Two-dimensional numerical simulations*, Monthly Notices of the Royal Astronomical Society, 361(3), 1077–1090

Planck Collaboration, Ade, P. A. R., Aghanim, N., et al. (2014), *Planck 2013 results. I. Overview of products and scientific results*, Astronomy and Astrophysics, 571, A1

Planck Collaboration, Aghanim, N., Akrami, Y., et al. (2020), *Planck 2018 results: VI. Cosmological parameters*, Astronomy &; Astrophysics, 641, A6

Poggianti, B. M., Ignesti, A., Gitti, M., et al. (2019), *GASP XXIII: A Jellyfish Galaxy as an Astrophysical Laboratory of the Baryonic Cycle*, Astrophysical Journal, 887(2), 155

Pope, S. B. (2000), *Turbulent Flows*, Cambridge University Press

Porter, D. H., Jones, T. W., and Ryu, D. (2015), *VORTICITY, SHOCKS, AND MAGNETIC FIELDS IN SUBSONIC, ICM-LIKE TURBULENCE*, The Astrophysical Journal, 810(2), 93

Power, C., Knebe, A., and Knollmann, S. R. (2012), *The dynamical state of dark matter haloes in cosmological simulations - I. Correlations with mass assembly history*, Monthly Notices of the RAS, 419(2), 1576

Pratt, G. W., Arnaud, M., Biviano, A., et al. (2019), *The Galaxy Cluster Mass Scale and Its Impact on Cosmological Constraints from the Cluster Population*, Space Science Reviews, 215(2)

Press, W. H. and Schechter, P. (1974), *Formation of Galaxies and Clusters of Galaxies by Self-Similar Gravitational Condensation*, Astrophysical Journal, 187, 425

Price, D. J. (2008), *Modelling discontinuities and Kelvin–Helmholtz instabilities in SPH*, Journal of Computational Physics, 227(24), 10040

Price, D. J. (2012), *Smoothed particle hydrodynamics and magnetohydrodynamics*, Journal of Computational Physics, 231(3), 759–794

Price, D. J., Wurster, J., Tricco, T. S., et al. (2018), *Phantom: A Smoothed Particle Hydrodynamics and Magnetohydrodynamics Code for Astrophysics*, Publications of the Astronomical Society of Australia, 35

Péroux, C., Zwaan, M. A., Klitsch, A., et al. (2019), *Multiphase circumgalactic medium probed with MUSE and ALMA*, Monthly Notices of the Royal Astronomical Society, 485(2), 1595

Qu, Z., Chen, H.-W., Rudie, G. C., et al. (2022), *The Cosmic Ultraviolet Baryon Survey (CUBS) V: on the thermodynamic properties of the cool circumgalactic medium at $z < 1$*, Monthly Notices of the Royal Astronomical Society, 516(4), 4882

Ragone-Figueroa, C., Granato, G. L., Murante, G., et al. (2013), *Brightest cluster galaxies in cosmological simulations: achievements and limitations of active galactic nuclei feedback models*, Monthly Notices of the Royal Astronomical Society, 436(2), 1750–1764

Rahmani, M., Seymour, B., and Lawrence, G. (2014), *The evolution of large and small-scale structures in Kelvin–Helmholtz instabilities*, Environmental Fluid Mechanics, 14, 1275

Randall, S., Nulsen, P., Forman, W. R., et al. (2008), *Chandra's View of the Ram Pressure Stripped Galaxy M86*, The Astrophysical Journal, 688(1), 208–223

Rappaz, Y. and Schober, J. (2024), *The effect of pressure-anisotropy-driven kinetic instabilities on magnetic field amplification in galaxy clusters*, Astronomy &; Astrophysics, 683, A35

Rayleigh, L. (1911), *LXXXII. On the motion of solid bodies through viscous liquid*, The London, Edinburgh, and Dublin Philosophical Magazine and Journal of Science, 21(126), 697

Raymond, J. C., Cox, D. P., and Smith, B. W. (1976), *Radiative cooling of a low-density plasma.*, Astrophysical Journal, 204, 290

Read, J. I., Hayfield, T., and Agertz, O. (2010), *Resolving mixing in smoothed particle hydrodynamics*, Monthly Notices of the Royal Astronomical Society, no–no

Rebusco, P., Churazov, E., Böhringer, H., and Forman, W. (2005), *Impact of stochastic gas motions on galaxy cluster abundance profiles*, Monthly Notices of the Royal Astronomical Society, 359(3), 1041

Riess, A. G., Filippenko, A. V., Challis, P., et al. (1998), *Observational Evidence from Supernovae for an Accelerating Universe and a Cosmological Constant*, The Astronomical Journal, 116(3), 1009

Riess, A. G., Yuan, W., Macri, L. M., et al. (2022), *A Comprehensive Measurement of the Local Value of the Hubble Constant with 1 km s−1 Mpc−1 Uncertainty from the Hubble Space Telescope and the SH0ES Team*, The Astrophysical Journal Letters, 934(1), L7

Rincon, F., Schekochihin, A. A., and Cowley, S. C. (2014), *Non-linear mirror instability*, Monthly Notices of the Royal Astronomical Society: Letters, 447(1), L45–L49

Robertson, H. P. (1935), *Kinematics and World-Structure*, The Astrophysical Journal, 82, 284

Robertson, H. P. (1936a), *Kinematics and World-Structure II.*, The Astrophysical Journal, 83, 187

Robertson, H. P. (1936b), *Kinematics and World-Structure III.*, The Astrophysical Journal, 83, 257

Roediger, E., Kraft, R. P., Forman, W. R., et al. (2013a), *KELVIN-HELMHOLTZ INSTABILITIES AT THE SLOSHING COLD FRONTS IN THE VIRGO CLUSTER AS A MEASURE FOR THE EFFECTIVE INTRACLUSTER MEDIUM VISCOSITY*, The Astrophysical Journal, 764(1), 60

Roediger, E., Kraft, R. P., Nulsen, P., et al. (2013b), *Viscous Kelvin–Helmholtz instabilities in highly ionized plasmas*, Monthly Notices of the Royal Astronomical Society, 436(2), 1721

Roediger, E., Kraft, R. P., Nulsen, P. E. J., et al. (2015), *STRIPPED ELLIPTICAL GALAXIES AS PROBES OF ICM PHYSICS. II. STIRRED, BUT MIXED? VISCOUS AND INVISCID GAS STRIPPING OF THE VIRGO ELLIPTICAL M89*, The Astrophysical Journal, 806(1), 104

Ruszkowski, M., Lee, D., Brüggen, M., et al. (2011), *COSMOLOGICAL MAGNETOHYDRODYNAMIC SIMULATIONS OF CLUSTER FORMATION WITH ANISOTROPIC THERMAL CONDUCTION*, The Astrophysical Journal, 740(2), 81

Ruszkowski, M. and Oh, S. P. (2010), *Shaken and Stirred: Conduction and Turbulence in Clusters of Galaxies*, Astrophysical Journal, 713(2), 1332

Ryden, B. (2003), *Introduction to cosmology*

Ryu, D., Kang, H., Cho, J., and Das, S. (2008), *Turbulence and Magnetic Fields in the Large-Scale Structure of the Universe*, Science, 320(5878), 909

Sanders, J. S. and Fabian, A. C. (2012), *Deep Chandra and XMM–Newton X-ray observations of AWM 7 – I. Investigating X-ray surface brightness fluctuations*, Monthly Notices of the Royal Astronomical Society, 421(1), 726

Sarazin, C. L. (1986), *X-ray emission from clusters of galaxies*, Rev. Mod. Phys., 58, 1

Sayers, J., Sereno, M., Ettori, S., et al. (2021), *CLUMP-3D: the lack of non-thermal motions in galaxy cluster cores*, Monthly Notices of the Royal Astronomical Society, 505(3), 4338–4344

Schekochihin, A. A. and Cowley, S. C. (2006), *Turbulence, magnetic fields, and plasma physics in clusters of galaxies*, Physics of Plasmas, 13(5)

Schekochihin, A. A., Cowley, S. C., Kulsrud, R. M., et al. (2005), *Plasma Instabilities and Magnetic Field Growth in Clusters of Galaxies*, The Astrophysical Journal, 629(1), 139

Schekochihin, A. A., Maron, J. L., Cowley, S. C., and McWilliams, J. C. (2002), *The Small-Scale Structure of Magnetohydrodynamic Turbulence with Large Magnetic Prandtl Numbers*, The Astrophysical Journal, 576(2), 806–813

Schneider, E. E. and Robertson, B. E. (2017), *HYDRODYNAMICAL COUPLING OF MASS AND MOMENTUM IN MULTIPHASE GALACTIC WINDS*, The Astrophysical Journal, 834(2), 144

Schuessler, I. and Schmitt, D. (1981), *Comments on smoothed particle hydrodynamics*, Astronomy and Astrophysics, 97(2), 373

Shchelkin, K. (1943), *O sgoranii v turbulentnom potoke (Combustion in a Turbulent Flow)*, Zhurnal Eksperimental'noi i Teoreticheskoi Fiziki, 13(9-10)

Sijacki, D. and Springel, V. (2006), *Physical viscosity in smoothed particle hydrodynamics simulations of galaxy clusters*, Monthly Notices of the Royal Astronomical Society, 371(3), 1025

Simionescu, A., Werner, N., Urban, O., et al. (2015), *A Uniform Contribution of Core-collapse and Type Ia Supernovae to the Chemical Enrichment Pattern in the Outskirts of the Virgo Cluster*, Astrophysical Journal, Letters, 811(2), L25

Simionescu, A., ZuHone, J., Zhuravleva, I., et al. (2019), *Constraining Gas Motions in the Intra-Cluster Medium*, Space Science Reviews, 215(2)

Simonte, M., Vazza, F., Brighenti, F., et al. (2022), *Exploring the relation between turbulent velocity and density fluctuations in the stratified intracluster medium*, A&A, 658, A149

Slavin, J. D., Shull, J. M., and Begelman, M. C. (1993), *Turbulent Mixing Layers in the Interstellar Medium of Galaxies*, Astrophysical Journal, 407, 83

Smith, M. C., Fielding, D. B., Bryan, G. L., et al. (2023), *<scp>Arkenstone</scp> – I. A novel method for robustly capturing high specific energy outflows in cosmological simulations*, Monthly Notices of the Royal Astronomical Society, 527(1), 1216–1243

Smith, S. (1936), *The Mass of the Virgo Cluster*, Astrophysical Journal, 83, 23

Spitzer, L. (1962), *Physics of Fully Ionized Gases*

Springel, V. (2005), *The cosmological simulation code gadget-2*, Monthly Notices of the Royal Astronomical Society, 364(4), 1105

Springel, V. (2010), *E pur si muove:Galilean-invariant cosmological hydrodynamical simulations on a moving mesh*, Monthly Notices of the Royal Astronomical Society, 401(2), 791–851

Springel, V. (2014), *High performance computing and numerical modelling*

Springel, V., White, S. D. M., Jenkins, A., et al. (2005), *Simulations of the formation, evolution and clustering of galaxies and quasars*, Nature, 435(7042), 629

Springel, V., Yoshida, N., and White, S. D. M. (2001), *GADGET: a code for collisionless and gasdynamical cosmological simulations*, New Astronomy, 6(2), 79

Squire, J., Kunz, M., Arzamasskiy, L., et al. (2023), *Pressure anisotropy and viscous heating in weakly collisional plasma turbulence*, Journal of Plasma Physics, 89(4), 905890417

Squire, J., Schekochihin, A. A., and Quataert, E. (2017), *Amplitude limits and nonlinear damping of shear-Alfvén waves in high-beta low-collisionality plasmas*, New Journal of Physics, 19(5), 055005

Stasyszyn, F. A. and de los Rios, M. (2019), *Faraday rotation measure dependence on galaxy cluster dynamics*, Monthly Notices of the Royal Astronomical Society, 487(4), 4768–4774

Stasyszyn, F. A., Dolag, K., and Beck, A. M. (2013), *A divergence-cleaning scheme for cosmological SPMHD simulations*, Monthly Notices of the RAS, 428(1), 13

Steidel, C. C., Erb, D. K., Shapley, A. E., et al. (2010), *The Structure and Kinematics of the Circumgalactic Medium from Far-ultraviolet Spectra of z ∼= 2-3 Galaxies*, Astrophysical Journal, 717(1), 289

Steinwandel, U. P., Böss, L. M., Dolag, K., and Lesch, H. (2022), *On the Small-scale Turbulent Dynamo in the Intracluster Medium: A Comparison to Dynamo Theory**, The Astrophysical Journal, 933(2), 131

Steinwandel, U. P., Dolag, K., Böss, L. M., and Marin-Gilabert, T. (2024), *Toward Cosmological Simulations of the Magnetized Intracluster Medium with Resolved Coulomb Collision Scale*, The Astrophysical Journal, 967(2), 125

Stokes, G. G. (1851), *On the Effect of the Internal Friction of Fluids on the Motion of Pendulums*, Transactions of the Cambridge Philosophical Society, 9, 8

Stone, J. M., Gardiner, T. A., Teuben, P., et al. (2008), *Athena: A New Code for Astrophysical MHD*, The Astrophysical Journal Supplement Series, 178(1), 137

Stone, J. M. and Norman, M. L. (1992), *ZEUS-2D: A Radiation Magnetohydrodynamics Code for Astrophysical Flows in Two Space Dimensions. I. The Hydrodynamic Algorithms and Tests*, Astrophysical Journal, Supplement, 80, 753

Stone, J. M., Tomida, K., White, C. J., and Felker, K. G. (2020), *The Athena++ Adaptive Mesh Refinement Framework: Design and Magnetohydrodynamic Solvers*, Astrophysical Journal, Supplement, 249(1), 4

Su, K.-Y., Hopkins, P. F., Hayward, C. C., et al. (2017), *Feedback first: the surprisingly weak effects of magnetic fields, viscosity, conduction and metal diffusion on sub-L* galaxy formation*, Monthly Notices of the Royal Astronomical Society, 471(1), 144–166

Subramanian, K., Shukurov, A., and Haugen, N. E. L. (2006), *Evolving turbulence and magnetic fields in galaxy clusters*, Monthly Notices of the Royal Astronomical Society, 366(4), 1437

Sutherland, R. S. and Dopita, M. A. (1993), *Cooling Functions for Low-Density Astrophysical Plasmas*, Astrophysical Journal, Supplement, 88, 253

Syer, D. and White, S. D. M. (1998), *Dark halo mergers and the formation of a universal profile*, Monthly Notices of the Royal Astronomical Society, 293(4), 337

Tan, B., Oh, S. P., and Gronke, M. (2021), *Radiative mixing layers: insights from turbulent combustion*, Monthly Notices of the Royal Astronomical Society, 502(3), 3179

Tavecchio, F., Ghisellini, G., Foschini, L., et al. (2010), *The intergalactic magnetic field constrained by Fermi/Large Area Telescope observations of the TeV blazar 1ES0229+200*, Monthly Notices of the RAS, 406(1), L70

Teyssier, R. (2002), *Cosmological hydrodynamics with adaptive mesh refinement. A new high resolution code called RAMSES*, Astronomy and Astrophysics, 385, 337

Thompson, T. A. and Heckman, T. M. (2024), *Theory and Observation of Winds from Star-Forming Galaxies*

Tonnesen, S., Bryan, G. L., and Chen, R. (2011), *How to Light it Up: Simulating Ram-pressure Stripped X-ray Bright Tails*, Astrophysical Journal, 731(2), 98

Tormen, G., Bouchet, F. R., and White, S. D. M. (1997), *The structure and dynamical evolution of dark matter haloes*, Monthly Notices of the Royal Astronomical Society, 286(4), 865–884

Townsend, R. H. D. (2009), *AN EXACT INTEGRATION SCHEME FOR RADIATIVE COOLING IN HYDRODYNAMICAL SIMULATIONS*, The Astrophysical Journal Supplement Series, 181(2), 391

Tricco, T. and Price, D. (2013), *A Switch for Artificial Resistivity and Other Dissipation Terms*

Tripp, T. M., Lu, L., and Savage, B. D. (1998), *The Relationship between Galaxies and Low-Redshift Weak Ly α Absorbers in the Directions of H1821+643 and PG 1116+215* **, The Astrophysical Journal, 508(1), 200

Tumlinson, J., Peeples, M. S., and Werk, J. K. (2017), *The Circumgalactic Medium*, Annual Review of Astronomy and Astrophysics, 55(1), 389–432

Turok, N. (1997), *Critical Dialogues in Cosmology*, WORLD SCIENTIFIC

Umetsu, K., Medezinski, E., Nonino, M., et al. (2014), *CLASH: Weak-lensing Shear-and-magnification Analysis of 20 Galaxy Clusters*, Astrophysical Journal, 795(2), 163

Valentini, M. and Brighenti, F. (2015), *AGN-stimulated cooling of hot gas in elliptical galaxies*, Monthly Notices of the RAS, 448(3), 1979

Vallés-Pérez, D., Planelles, S., and Quilis, V. (2021a), *Troubled cosmic flows: turbulence, enstrophy, and helicity from the assembly history of the intracluster medium*, Monthly Notices of the Royal Astronomical Society, 504(1), 510–527

Vallés-Pérez, D., Planelles, S., and Quilis, V. (2021b), *Unravelling cosmic velocity flows: a Helmholtz–Hodge decomposition algorithm for cosmological simulations*, Computer Physics Communications, 263, 107892

Vallés-Pérez, D., Planelles, S., Quilis, V., et al. (2024), *vortex-p: A Helmholtz-Hodge and Reynolds decomposition algorithm for particle-based simulations*, Computer Physics Communications, 304, 109305

van Haarlem, M. P., Wise, M. W., Gunst, A. W., et al. (2013), *LOFAR: The LOw-Frequency ARray*, Astronomy and Astrophysics, 556, A2

van Weeren, R. J., Shimwell, T. W., Botteon, A., et al. (2021), *LOFAR observations of galaxy clusters in HETDEX: Extraction and self-calibration of individual LOFAR targets*, Astronomy and Astrophysics, 651, A115

Vazza, F., Angelinelli, M., Jones, T. W., et al. (2018), *The turbulent pressure support in galaxy clusters revisited*, Monthly Notices of the Royal Astronomical Society: Letters, 481(1), L120–L124

Vazza, F., Jones, T. W., Brüggen, M., et al. (2016), *Turbulence and vorticity in Galaxy clusters generated by structure formation*, Monthly Notices of the Royal Astronomical Society, 464(1), 210–230

Vazza, F., Roediger, E., and Brüggen, M. (2012), *Turbulence in the ICM from mergers, cool-core sloshing, and jets: results from a new multi-scale filtering approach*, Astronomy &; Astrophysics, 544, A103

Veilleux, S., Maiolino, R., Bolatto, A. D., and Aalto, S. (2020), *Cool outflows in galaxies and their implications*, Astronomy and Astrophysics Reviews, 28(1), 2

Vikhlinin, A., Kravtsov, A. V., Burenin, R. A., et al. (2009), *Chandra Cluster Cosmology Project III: Cosmological Parameter Constraints*, Astrophysical Journal, 692(2), 1060

Vikhlinin, A., Markevitch, M., and Murray, S. S. (2001), *[ITAL]Chandra[/ITAL] Estimate of the Magnetic Field Strength near the Cold Front in A3667*, The Astrophysical Journal, 549(1), L47–L50

Voit, G. M., Meece, G., Li, Y., et al. (2017), *A Global Model for Circumgalactic and Cluster-core Precipitation*, Astrophysical Journal, 845(1), 80

Wadsley, J. W., Keller, B. W., and Quinn, T. R. (2017), *Gasoline2: a modern smoothed particle hydrodynamics code*, Monthly Notices of the RAS, 471(2), 2357

Wadsley, J. W., Stadel, J., and Quinn, T. (2004), *Gasoline: a flexible, parallel implementation of TreeSPH*, New Astronomy, 9(2), 137

Wadsley, J. W., Veeravalli, G., and Couchman, H. M. P. (2008), *On the treatment of entropy mixing in numerical cosmology*, Monthly Notices of the RAS, 387(1), 427

Walker, A. G. (1937), *On Milne's Theory of World-Structure*, Proceedings of the London Mathematical Society, 42, 90

Walker, S., Simionescu, A., Nagai, D., et al. (2019), *The Physics of Galaxy Cluster Outskirts*, Space Science Reviews, 215(1)

Walker, S. A., Hlavacek-Larrondo, J., Gendron-Marsolais, M., et al. (2017), *Is there a giant Kelvin–Helmholtz instability in the sloshing cold front of the Perseus cluster?*, Monthly Notices of the Royal Astronomical Society, 468(2), 2506

Wang, Q. H. S. and Markevitch, M. (2018), *A Deep X-Ray Look at Abell 2142—Viscosity Constraints From Kelvin–Helmholtz Eddies, a Displaced Cool Peak That Makes a Warm Core, and A Possible Plasma Depletion Layer*, The Astrophysical Journal, 868(1), 45

Weinberger, R. and Hernquist, L. (2022), *Modelling multiphase gases in cosmological simulations using compressible multifluid hydrodynamics*, Monthly Notices of the Royal Astronomical Society, 519(2), 3011

Weisskopf, M. C., Tananbaum, H. D., Van Speybroeck, L. P., and O'Dell, S. L. (2000), *Chandra X-Ray Observatory (CXO): Overview*, in *X-Ray Optics, Instruments, and Missions III*, edited by J. E. Truemper, B. Aschenbach, SPIE

Wendland, H. (1995), *Piecewise polynomial, positive definite and compactly supported radial functions of minimal degree*, Advances in Computational Mathematics, 4, 389

Werner, N., Oonk, J. B. R., Canning, R. E. A., et al. (2013), *The Nature of Filamentary Cold Gas in the Core of the Virgo Cluster*, Astrophysical Journal, 767(2), 153

Wiersma, R. P. C., Schaye, J., and Smith, B. D. (2009), *The effect of photoionization on the cooling rates of enriched, astrophysical plasmas*, Monthly Notices of the RAS, 393(1), 99

Williams, F. (1975), *A review of some theoretical considerations of turbulent flame structure*, in *AGARD Conference Proceeding, 1975*

Wisotzki, L., Bacon, R., Brinchmann, J., et al. (2018), *Nearly all the sky is covered by Lyman-α emission around high-redshift galaxies*, Nature, 562(7726), 229–232

XRISM (2025), *XRISM reveals low non-thermal pressure in the core of the hot, relaxed galaxy cluster Abell 2029*

XRISM, Audard, M., Awaki, H., et al. (2025), *XRISM forecast for the Coma cluster: stormy, with a steep power spectrum*

XRISM Science Team (2020), *Science with the X-ray Imaging and Spectroscopy Mission (XRISM)*, arXiv e-prints, arXiv:2003.04962

Xu, G. (1995), *A New Parallel N-Body Gravity Solver: TPM*, Astrophysical Journal, Supplement, 98, 355

Zeldovich, Y. and Raizer, Y. P. (1967), *Physics of Shock Waves and High Temperature Hydrodynamic Phenomen*, Academic Press

Zel'dovich, Y. B. (1970), *Gravitational Instability: An Approximate Theory for Large Density Perturbations.*, Astronomy and Astrophysics, 5, 84

Zeldovich, Y. B. (1972), *A hypothesis, unifying the structure and the entropy of the Universe*, Monthly Notices of the RAS, 160, 1P

Zhuravleva, I., Chen, M. C., Churazov, E., et al. (2023), *Indirect measurements of gas velocities in galaxy clusters: effects of ellipticity and cluster dynamic state*, Monthly Notices of the Royal Astronomical Society, 520(4), 5157–5172

Zhuravleva, I., Churazov, E., Kravtsov, A., et al. (2012), *Quantifying properties of ICM inhomogeneities*, Monthly Notices of the Royal Astronomical Society, 428(4), 3274–3287

Zhuravleva, I., Churazov, E., Schekochihin, A. A., et al. (2019), *Suppressed effective viscosity in the bulk intergalactic plasma*, Nature Astronomy, 3(9), 832–837

Zhuravleva, I., Churazov, E. M., Schekochihin, A. A., et al. (2014), *THE RELATION BETWEEN GAS DENSITY AND VELOCITY POWER SPECTRA IN GALAXY CLUSTERS: QUALITATIVE TREATMENT AND COSMOLOGICAL SIMULATIONS*, The Astrophysical Journal, 788(1), L13

ZuHone, J. A. (2011), *A PARAMETER SPACE EXPLORATION OF GALAXY CLUSTER MERGERS. I. GAS MIXING AND THE GENERATION OF CLUSTER ENTROPY*, The Astrophysical Journal, 728(1), 54

ZuHone, J. A., Kunz, M. W., Markevitch, M., et al. (2015), *The Effect of Anisotropic Viscosity on Cold Fronts in Galaxy Clusters*, Astrophysical Journal, 798(2), 90

ZuHone, J. A. and Roediger, E. (2016), *Cold fronts: probes of plasma astrophysics in galaxy clusters*, Journal of Plasma Physics, 82(3)

Zwicky, F. (1933), *Die Rotverschiebung von extragalaktischen Nebeln*, Helvetica Physica Acta, 6, 110

List of Figures

List of Tables

Acknowledgements

First of all, I would like to thank my PhD advisor, Prof. Dr. Klaus Dolag, for his support and advice during these three and a half years. Thank you for giving me the opportunity to do my PhD in such an amazing group, and for both the academic and extra-academic support. I truly appreciate your guidance throughout this journey.

I also want to thank Ulrich Steinwandel and Milena Valentini for all the helpful discussions and for being supportive and available despite the distance. None of this would have been possible without you.

I am really grateful to Max Gronke for all the time and discussions we shared. What began as a six-month side project ended up as a two-year-long, endless project that I honestly thought we were not going to be able to finish. But thanks to your support and your patience, together with the help of Peng Oh, we managed to finish it.

Many thanks to all the people at USM for the great moments we shared together over the years, and for all the discussions and advice. You definitely made everything a lot easier. I'm especially thankful to Frederick Groth, with whom I've shared not only valuable scientific exchanges but also countless experiences, travels, and memories.

Thank you as well to all the people at MPA for adopting me and making MPA a place I genuinely enjoyed going to every week. In particular, I want to thank Hitesh Kishore Das for all the time we spent together and all the great discussions we had that really helped me better understand the TRMLs simulations.

I also want to thank all my friends here in Munich for all the amazing moments we have lived together. Even if it's not science-related, you definitely made my PhD years much easier and a lot more fun. A very special thank you to Cristina for all your support and for being there in both the good and the difficult times. This wouldn't have been possible without you.

Ahora quiero pasar al castellano para agradecer todo el apoyo que he tenido de mis amigos en España. Luis, que has sido como un hermano durante todos estos años, desde el colegio hasta aquí, has estado siempre ahí en todo este camino. Fran, Anto y Antonio, que me conocisteis cuando apenas tenía 17 años y estaba empezando la carrera, habéis sido una

parte fundamental de la fuerza que me impulsó a emprender el viaje a Alemania y convertirme en quien soy hoy. De verdad, os agradezco muchísimo todos los momentos que hemos vivido juntos, y todos los que nos quedan todavía por vivir.

Por último, pero no menos importante, quiero agradecer a mi familia. Vosotros sabéis que éste ha sido mi sueño desde pequeño y que he trabajado toda mi vida por conseguirlo. No ha sido un camino fácil: primero dejar Alicante, y luego dejar España, todo por llegar a cumplir el sueño que he tenido desde que tenía 10 años. He trabajado duro, pero sin ninguna duda, esto no habría sido posible sin vuestro apoyo y sin vuestro esfuerzo. Sin vosotros no habría llegado a conseguir todo lo que he conseguido a día de hoy. Os quiero mucho.

I acknowledge support by the COMPLEX project from the European Research Council (ERC) under the European Union's Horizon 2020 research and innovation program grant agreement ERC-2019-AdG 882679. Part of this research was supported in part by grant NSF PHY-2309135 to the Kavli Institute for Theoretical Physics (KITP).